

MICROFABRICATED DEVICES FOR SINGLE CELL ANALYSIS

A Dissertation
presented to
the Faculty of the Graduate School
University of Missouri-Columbia

In Partial Fulfillment
of the Requirements for the Degree
Doctor of Philosophy

by
YUANFANG GAO
Dr. Shubhra Gangopadhyay, Dissertation Supervisor
Dr. Kevin Gillis, Co-Advisor
DECEMBER 2006

The undersigned, appointed by the Dean of the Graduate School, have examined the dissertation entitled

**MICROFABRICATED DEVICES FOR SINGLE CELL
ANALYSIS**

Presented by Yuanfang Gao

A candidate for the degree of Doctor of Philosophy

And hereby certify that in their opinion it is worthy of acceptance.

Professor Shubhra Gangopadhyay

Professor Kevin Gillis

Professor Sheila Grant

Professor Mahmoud Almasri

Professor Jae W. Kwon

DEDICATION

To:

Qingyun Gao and Liangyuan Tan, my dear parents,

Xiaoying Jin, my beloved wife, and

Jason Deli Gao, my little one.

ACKNOWLEDGMENTS

My sincere thanks first go to my advisors, Prof. Shubhra Gangopadhyay and Prof. Kevin Gillis, for their intellectual guidance, continuing support and encouragement during my Ph.D. study. Prof. Shubhra Gangopadhyay provided me detailed directions and keen insights in my research together with freedom of methods and thoughts. Many ideas are inspired and enlightened by Prof. Gillis from the talks, discussions which I enjoyed a lot. Without them I wouldn't have finished this work.

I also would like to thank Prof. Sheila Grant, Prof. Mahmoud Almasri, Prof. Jae W. Kwon for serving as members of my doctoral committee, and for their insightful advice on my research and dissertation.

Studying and work in Prof. Gangopadhyay's large research group benefits me a lot, yet I had another chance to work in Prof. Gillis's lab which provided me very good exposure to life science research due to this strong interdisciplinary study. I would like to thank all the faculty members, the staff, the fellow students, and the colleagues in both groups. Overall, studying in the Electrical and Computer Engineering Department and MU has been a wonderful experience.

Specially, I would like to thank my wife Xiaoying for her support and encouragement in every possible way and my son Jason who assigned me another project since he was born in 2004, in the middle of my other projects, which is a lot of fun and joy. I would also thank my parents, parents-in-law for their understanding, support and help.

MICROFABRICATED DEVICES FOR SINGLE CELL ANALYSIS

TABLE OF CONTENTS

Acknowledgements.....	ii
Table of contents.....	iii
List of figures.....	v
Abstract.....	xii
Chapter 1 INTRODUCTION	1
1.1 MEMS technology and BioMEMS.....	1
1.1.1 BioMEMS and biochip technology	2
1.1.2 Objective and goals.....	3
1.2 Overview of Single Cell manipulation and analysis.....	6
1.3 Impedance Based Cell Measurements	14
1.4 Exocytosis Measurement	15
1.5 Dissertation outline	21
Chapter 2 MICROELECTRODE THEORY, MATERIALS AND DIAMOND LIKE CARBON MICROELECTRODE DEVICES	22
2.1 Introduction.....	22
2.2 The Solid - Electrolyte Interface and modeling.....	24
2.2.1 Electrical modeling of the double layer	26
2.3 Microelectrode and their properties	33
2.4 Electrode Noises	38
2.4.1 Thermal Noise.....	38
2.4.2 Shot noise.....	39
2.4.3 $e_n c_t$ noise	39
2.4.4 Interconnect and Parasitics	40
2.5 Electrode Materials and fabrication	41
2.5.1 Metal electrodes and deposition.....	41
2.5.2 Carbon based electrodes	44
2.5.3 Diamond-like Carbon electrode.....	45
2.5.4 Properties of sputtered DLC film.....	51
2.6 Diamond Like Carbon (DLC) Microelectrode and its application for low noise exocytosis measurement in microdevices.....	52
2.6.1 Device design and fabrication.....	55
2.6.2 Experimental setup.....	57
2.6.3 Electrochemical characteristics of the DLC microelectrodes.....	58
2.6.4 The specific capacitance of the DLC microelectrode	62
2.6.5 Amperometric detection of quantal exocytosis of catecholamines from cells	63
2.6.6 Comparison with the Pt microelectrodes	68

2.6.7 Background current and noise analysis.....	71
2.6.8 Comparison with the Pt microelectrodes	72
2.6.9 Reference electrodes	77
2.8 Summary	78
Chapter 3 IMPEDENCE BASED CELL SENSORS	80
3.1 Introduction.....	80
3.2 Literature review of previous impedance based micro sensor work.....	82
3.3 SENSOR DESIGN AND FABRICATION	88
3.3.1 Microsensor Design	88
3.3.2 Mask design considerations	89
3.3.3. Microsensor Fabrication	92
3.4 Experimental setup and test	101
3.4.1 Probe Setup	101
3.4.2 Instrumentation	101
3.4.3 Impedance-frequency Characteristics and modeling	106
3.4.4 Test on microbeads and pulse amplitude distributions	111
3.4.5 Discussion	113
3.5. Summary and Conclusion	115
Chapter 4 MICROCHIP DEVICES FOR HIGH THROUGHPUT ELECTROCHEMICAL ANALYSIS OF EXOCYTOSIS	116
4.1 Introduction.....	116
4.2 Previous work	119
4.3 Device Design comparison and Fabrication process overview	121
4.3.1 Vertical approach, planar electrode with vertical through hole design	122
4.3.2 Horizontal approach with microchannels	128
4.3.3 Fabrication process overview	140
4.3.4 Process integration and device Implementation	153
4.4 Device interface and instrumentation system	157
4.4.1 Hardware Design	159
4.4.2 Software Design.....	163
4.5 Experimental setup and device test.....	164
4.5.1 Experiment setup	164
4.5.2. Cell trapping experiments	166
4.5.3 Amperometric detection of quantal exocytosis of catecholamines.....	168
4.5.4 Further analysis of exocytosis, events density, amplitude and background current	171
4.6 Summary.....	175
Chapter 5 CONCLUSION AND FUTURE WORK	176
5.1 Bettering cell trapping capability.....	177
5.2 A practical instrumentation system for multiple channel recording.....	179
5.3 Further work on DLC and new sensing electrode material	180
List of Publications	181
VITA.....	184
References:	185

List of figures

Fig. 1.1 Cell trapping mechanisms designed along microfluidic channel. Yun et. al, 2005 ..	11
Fig. 1.2 Schematic diagrams and cell docking results by a dam structure by Yang at al. (a) (b) the schematic design, (c) Fluorescence image of the microchannels showing the alignment of mammalian HL-60 cells along the dam structures. (d) picture of a section of the dam with docked cells.....	12
Fig. 1.3 Schematic design of microfluidic based cell culture platform directs axon growth through micro groves(10 μm) between the channels.	13
Fig. 1.4 A typical exocytosis measurement setup based on a patch-clamp system. From left to right is: Faraday cage shielded microscope bench with piezoelectric micromanipulator and head stage preamplifier; instrument rack of patch-clamp amplifier, AD/DA module, monitor etc.; computer control for voltage/current clamp and data acquisition. (Courtesy of Dr. Gillis's electrophysiology lab at Dalton Cardiovascular Research Center).....	16
Fig. 1.5 The schematic setup of electrochemical detection of exocytosis using carbon fiber, a carbon fiber is put close to a chromaffin cell and the faradic current due to oxidation of catecholamines is amplified through A1, a high gain I-V converter and a current spike around 100 pA is shown.....	19
Fig. 1.6 Manual manipulation of cells using a micro pipette and electrochemical detection of exocytosis by carbon fiber.	20
Fig. 1.7 (a) A typical lab setup for patch-clamp experiment and exocytosis measurement using carbon fiber microelectrodes. (b) A miniaturized microchip device for exocytosis measurement.	20
Fig. 2.1 Holmoltz model of the electrody-electrolyte interface. From p6332, Fig. 7.7 Bockris and Reddy, "Modern electrochemistry", Vol. 2, 1970.	24
Fig. 2.2 Diffuse layer and the potential profile across the double layer region. Adapted from http://www.cheng.cam.ac.uk/	26
Fig. 2.3 Circuit model of the electrode-electrolyte interface	30
Fig. 2.4 Schematic of a Goda et. al. circuit model. This is a relatively simple model of a cell-based-biosensor.....	32
Fig. 2.5 Schematic circuit model of Hong et. al.	32
Fig. 2.6 Circuit model proposed by Gawad et. al	33

- Fig. 2.7 Concentration profiles difference at large and small electrodes, adopted from [46]. 36
- Fig. 2.8 Raman spectroscopic analysis of DLC..... 47
- Fig. 2.9 AFM image of DLC deposited on glass substrate, grain size of 5 nm, surface roughness of 1.5 nm, very smooth surface and grain size of the film. 49
- Fig. 2.10 DLC deposited on silicon substrate, grain size average 5 nm, Surface roughness: 1.4 nm 50
- Fig. 2.11 Raman spectroscopic scan of the DLC films on silicon and glass substrates, the broadened G, D peaks indicates that the highly disordered DLC film. 52
- Fig. 2.12 The design of the chip device for cell exocytosis measurement using DLC microelectrodes. (a) First mask layout for the lift-off process to pattern the electrodes traces and contact pads, (b) Second mask for exposing the contacts pads and 30 μm wide microelectrodes while the other portion is covered by photoresist, (c) The fabricated DLC microelectrodes, vertical traces are the 40 μm DLC wires, the horizontal trace is an empty line where photoresist is removed, the white rectangular shapes are the exposed microelectrodes of size 30 μm by 40 μm . (d) The overall picture of a chip device made on a 1 inch by 3 inch glass slide. 56
- Fig. 2.13 The experimental setup for exocytosis measurement using EPC-9 patch-clamp amplifier and HEKA pulse software..... 57
- Fig. 2.14 Cyclic voltammogram of the DLC in 100 mM H_2SO_4 shows a large working window, electrode size is 30 μm by 60 μm 60
- Fig. 2.15 Cyclic voltammogram of the DLC on ITO electrodes shows the oxidation activity of the epinephrine compared to the bath background, the solution used is 100 μM epinephrine in the standard calcium bath solution as describe previously in the paper. Electrode size is defined by an o-ring of diameter of 1/8 inch or 0.3175 cm, scan rate 100 mV/s. 60
- Fig. 2.16 Cyclic voltammogram of DLC microelectrode size of 30 μm by 40 μm , scan rate 100 mV/s, 100 μM epinephrine in bath solution as compared to the background of calcium bath solution..... 61
- Fig. 2.17 Cyclic voltammograms of the DLC on ITO microelectrodes at the size of 30 μm by 40 μm , the solution is 1 mM $\text{K}_3\text{Fe}(\text{CN})_6$ in 0.1 M KCL at PH=3, scan rate (a) 100 mV/s and (b) 500 mV/s 62
- Fig. 2.18 The chromaffin cells settled down onto the DLC microelectrodes electrodes, the active sensing microelectrodes are at the cross section of the horizontal strip (photoresist free) and the vertical dark gray strip (DLC trace of 40 μm)..... 64

Fig. 2.19 One example of current spikes recorded from the DLC on ITO electrodes. (a) An example of a recording of 24 seconds, (b) An enlarged view of one portion of (a). Each current spike indicates a single vesicle release from a single cell due to the oxidation of the catecholamines from the vesicles oxidized on the DLC electrodes..... 66

Fig. 2.20 Histogram data analysis of the current spikes parameters of exocytosis measurement, from top to bottom, the time to peak or rise time of the spikes; charge of the spikes; T half time or the FWHM (Full Width Half Maximum) width of the spikes; Amplitude histogram is the distribution of the spike amplitudes. 67

Fig. 2.21 Cyclic voltammograms of the DLC on ITO and platinum microelectrodes at the size of 30 μm by 40 μm , the solution is 1 mM $\text{K}_3\text{Fe}(\text{CN})_6$ in 0.1 M KCL. 68

Fig. 2.22 Comparison of spike amplitude, peak current, background current and noise level vs background current between DLC and Pt microelectrodes..... 77

Fig. 3.1 Comparison between (a) the Coulter counter design which may have a coincidence problem, and (b) the sensor design studied in this paper for detecting particles one by one. 83

Fig. 3.2 Micro Coulter counter by Larsen et al..... 84

Fig. 3.3 Micro Coulter counter device by M. Koch et. al..... 85

Fig. 3.4 Nano colloid particle sensing device on a microchip by Saleh et al 85

Fig. 3.5 Micro electrical impedance measurement system developed by Ayliffe et al 86

Fig. 3.6 A.C capacitance based device developed by Sohn et al 87

Fig. 3.7 Schematic diagrams of the microsensor prototype: (a) one whole probe, (b) a design using multiple-tip gating electrodes, and (c) cross-sectional view of the sensor structure..... 90

Fig. 3.8 The mask layout of the design on a 3" wafer, maximal devices are laid out on the wafer for better fabrication yield. 91

Fig. 3.9 Crystal planes in silicon wafers 91

Fig. 3.10 the illustration of etching mask design 92

Fig. 3.11 Image reversal process gives a better photoresist profile for lift-off process..... 95

Fig. 3.12 Process flow for fabrication of the impedance microsensor..... 98

Fig. 3.13 The fabricated impedance sensor and sensing aperture with gold electrodes. (a) (b) the overall sensor tip and contact pads. (c), (d), (e) are the fabricated sensing holes: (c) 100

μm , (d) $60\ \mu\text{m}$, and (e) $20\ \mu\text{m}$, respectively. The width of all gold wire lines (except the tips) is $10\ \mu\text{m}$ 99

Fig. 3.14 The overall sensor picture and SEM picture of the etched pyramid through holes in silicon wafer. (a) the overall impedance sensor. (b) the etched through hole array in silicon wafer. (c) an enlarged etched pyramid hole..... 100

Fig. 3.15 Schematic design of the PCB device..... 100

Fig. 3.16 Experimental setup for (a) the microfabricated probe and (b) the PCB probe that allows sample solution to flow through the sensing holes with suction. 104

Fig. 3.17 Schematic diagram of the instrumentation system and the real system with microscope, oscilloscope, function generator and the computer for data acquisition. 105

Fig. 3.18 Equivalent circuit models for the sensor interface (a) without considering the parasitic capacitance and (b) considering the parasitic capacitance. R_s represents the bulk resistance of the electrolyte, C_d the double-layer capacitance, and R_d the leakage resistance across the double layer..... 107

Fig. 3.19 Voltage output across gating electrodes versus frequency curves for (a) the microfabricated sensor and (b) the PCB device..... 108

Fig. 3.20 Pulse amplitude distribution and a typical pulse obtained from (a) the microfabricated sensing aperture of $100\ \mu\text{m}$ and (b) the $1.3\ \text{mm}$ sensing hole of the PCB device. 112

Fig. 4.1 Microfabrication process flow of the micro well chip device. A) $500\ \text{nm}\ \text{SiO}_2$ is deposited by low pressure chemical vapor deposition (LPCVD). b) Following patterning of the SiO_2 , anisotropic etching with KOH creates the microwells. c) SiO_2 is deposited by plasma enhanced chemical vapor deposition (PECVD) to insulate the bulk silicon substrate. d) Following coating and patterning of photoresist, Cr ($20\ \text{nm}$) and Au ($0.5\ \mu\text{m}$) are evaporated. After liftoff, electrodes, conducting traces and bonding pads are formed. E) Deposition of an additional layer of SiO_2 by PECVD passivates the conducting traces. F) SiO_2 is removed from the wells and bonding pads by buffered oxide etching..... 120

Fig. 4.2 The first generation of the micro well electrode device. From the left of top row and clock wise: a) The overall picture of the packaged device in a DIP IC package b) the device die compared to a dime coin c) the electrodes array on the die d) cells manipulated in a well with a patch clamp micropipette e) SEM picture of a fabricated well with gold electrode, f) a close up SEM view of the electrode array. 121

Fig. 4.3 Simplified fabrication process for the second generation of the micro well device, device with a small through hole at the bottom of the well. 124

- Fig. 4.4 Fabrication process for the planar electrodes on thin film design, 1-6 cross section view, the bottom picture is the top view of the patterned sensing ring electrodes with opening in the center. 125
- Fig. 4.5 The schematic design, etching profile of the device on SOI wafer and working principle of automatic positioning by suction..... 128
- Fig. 4.6 Schematic design of parallel channel with cell docking, cell flow channel width 20 μm , cell diameter is about 10 μm and dock width is about 15 μm . there are small channels with 2 μm width connecting the two main channels. (a) Cell trap position with 3 passage channel, (b) simplified design with two reservoirs and the parallel running channel, (c) cell trap with one 2 μm passage channel and a sensing electrode 131
- Fig. 4.7 Cross section view of the simplified fabrication process for design 1. 133
- Fig. 4.8 Schematic design of the dam structure, top view and cross-section view; the profile of the channel shown is after anisotropic etching, the middle green color is the dam channel which connects two main channels, with a much shallower depths(2~3 μm). 135
- Fig. 4.9 Schematic design and electrodes layout of the device. (a) Two pairs of flow channels are designed between the two reservoirs, contact pads are aligned on both sides of the channels. (b) Only one pair of flow and waste channel, sensing electrodes and contact pads are laid out only on one side, the number is only half the right side design..... 138
- Fig. 4.10 Screen shot of the device design from CAD tool L-Edit and the idea of escape channel 139
- Fig. 4.11 Device layout on a 2" wafer, 4 devices are laid out. 140
- Fig. 4.12 The schematic and the actually built oxidation furnace 143
- Fig. 4.13 Plot of Wet oxygen oxidation curve from the Deal-Grove model 144
- Fig. 4.14 Ellipsometry curve fitting data of two oxidized sample..... 146
- Fig. 4.15 The etching process of the "one-step-etching" design where the docking positions, channels and the 2 μm channel are laid out in one mask. (a) channels patterned on silicon wafer, grey blue is the SiO_2 masking layer. (b) After 4 minutes etching at a channel depth about 4 μm . (c) After 10 minutes etching, the docking position and the small channel merged. 147
- Fig. 4.16 Silicon etching simulation by AECS. Silicon wafer orientation is (100). (a), (b) etching mask vertical to $\langle 100 \rangle$ plane, (c), (d) etching mask tilted 45 degrees. (e) etch compensation simulation, left is the etching mask with bottle neck like compensation shapes, the middle part is the simulation etching result after 10 minutes, and the right part is the etching result after 15 minutes. 148

Fig. 4.17 Two-step etching to keep the small channel from widening. (a) the blue is oxide layer, the black line is the etched 2 μm channel after oxidation protection. (b) is the etched channel after dye flow test, the green dye is flowed from the left channel through the small 2 μm channels. 149

Fig. 4.18 Etching mask and the etched channel with cell trapping positions and dam structure in-between in a silicon wafer. Two pairs of channels are shown, the dam lies between the two channels with a deeper color, small notches are the cell trapping positions..... 150

Fig. 4.19 Screenshot of the measurement result from Alpha step 200, the profile of the etched channel with the dam structure. 150

Fig. 4.20 Schematic setup of anodic bonding..... 152

Fig. 4.21 Schematic view in cross section view for the device fabrication process. (1) Start from a bare $\langle 100 \rangle$ silicon wafer, first oxidation to grow a 300 nm oxide layer. (2) First photolithography to pattern the small passage channel. (3) Buffered HF etching, removes SiO_2 to expose Si for KOH etching. (4) KOH etching of Si, create the small passage channel or a shallow dam channel. (5) Second oxidation to protect the etched channel. (6) Second photolithography for the cell and waste channels. (7) Second buffered HF etching to remove SiO_2 to expose Si for KOH etching. (8) KOH etching, create the main channel pair and the docking sites. (9) Third oxidation to insulate channel from the substrate. (10) Metallization using lift-off process, deposit and pattern 20 μm wide electrode into the channel and the docking sites. (11) Channel bonding, seal the channels with a PDMS piece. 156

Fig. 4.22 Fabricated devices on a two inch silicon wafer, total four devices on one wafer. 157

Fig. 4.23 Patterned microelectrodes inside microchannels, electrodes width is 20 μm 157

Fig. 4.24 Schematic circuit design of the small current amplifier or “I-V” converter, it is also used in the patch clamp amplifiers as the pre-amplifier or head stage. 158

Fig. 4.25 The schematic configuration of the instrumentation system..... 159

Fig. 4.26 Single Patch Clamp amplifier cell..... 160

Fig. 4.27 2nd order Filter – Sallen Key Topology 162

Fig. 4.28 Schematic experiment setup of the device, the device was fixed on a PCB board (not shown) and working electrodes are connected to the PCB board by wire bonding and soldered with short wires, short wires then connected to a head stage and EPC-9 patch-clamp amplifier which is controlled by HEKA pulse software. 165

Fig. 4.29 The fabricated microchip device in silicon. (a) Device mounted onto a PCB board and working electrodes are connected to the small wires through wire bonding. (b) A cut

device die with microchannels, reservoirs and working electrodes. (c) A whole board view of the prototype of the device with integrated amplifiers and filters on PCB board. 167

Fig. 4.30 Cell trapping experiment on different size of channels. (a) 20 μm cell flow microchannel. (b) 30 μm cell flow microchannel. Device in (a) and (b) have no working electrodes, cells are stained with Methylene blue for easier visualization. (c) cell trapped in 20 μm channel. (d) cell trapped in 70 μm channel..... 168

Fig. 4.31 Exocytosis recording example from the microchip device. (a) A typical exocytosis recording for a period of 4 seconds. (b) An expanded view of the dashed square region of (a) showing a spike with a clear foot signal. 170

Fig. 4.32 Exocytosis recordings from the trapping device for a period of 30 minutes, each last for 4 seconds. (a) At the beginning. (b) A few minutes later. (c) After about 10 minutes (d) After around 30 minutes. 174

Fig. 5.1 Possible design improvement to count for undercut and widen problem in silicon anisotropic wet etching process for better cell trapping. 178

MICROFABRICATED DEVICES FOR SINGLE CELL ANALYSIS

Yuanfang Gao

Advisor: Dr. Shubhra Gangopadhyay**Co-Advisor: Dr. Kevin Gillis****ABSTRACT**

BioMEMS or lab-on-a-chip technology is promising technology and enables the possibility of microchip devices with higher throughput or better performance for single cell analysis. We have designed and fabricated microdevices for single cell analysis, with impedance based device for fast cell screening and microchannel based flow systems for high throughput, high time resolution quantal exocytosis measurement with automatic cell positioning and reusability. The automatic cell positioning is realized by differential forces of fluidic dynamics. Microelectrodes are patterned at automatic trap positions for electrochemical detection quantal release of hormones like catecholamines secreted by cells.

We also developed diamond-like carbon (DLC) microelectrodes onto chip device for low noise exocytosis measurement. The DLC microelectrodes were deposited by magnetron sputtering process with nitrogen doping and a bottom ITO conductive layer. Test results show the developed DLC can detect exocytosis with low noise and a stable background current which are comparable to that of carbon-fiber electrodes. They are batch producible at low cost and can realize high-throughput on-chip measurement of quantal exocytosis. The technology developed in this research can have wide ranging applications in fields such as electrophysiology, cell based sensors, high throughput screening of new drug development.

Chapter 1 INTRODUCTION

1.1 MEMS technology and BioMEMS

Micro-Electro-Mechanical Systems (MEMS) are systems made at the microscopic length scale for useful technological applications. MEMS technology integrates mechanical elements, sensors, actuators, and electronics on various substrates with silicon being used the most. MEMS devices are fabricated using either same, compatible or similar micromachining processes borrowed from the semiconductor industry. Such processes may include selective etching of silicon wafers or adding new structural layers to form the mechanical and electromechanical devices. In simple words, MEMS is a technology to miniaturize existing systems or to create entirely new microdevices. For example, miniaturization has been demonstrated before by creating integrated circuits of the relatively large printed circuit board technology. It has great potential to revolutionize a lot of products by bringing together silicon-based microelectronics and micromachining technology. The goal of MEMS is the realization of complete systems on a single chip. Before the complete integration of any system is achieved, many of the constitutive subsystems are developed and commercialized. Products such as pressure sensors, accelerometers, inkjet nozzles, digital light processors etc. are very successful. There is a significant amount of funding in this area from both government and private industry. It is a highly multidisciplinary field, involving various fields such as Mechanical MEMS, Optical MEMS, RF MEMS, and BioMEMS. In particular, BioMEMS is a new area of research to explore MEMS device applications in medicine and life sciences.

1.1.1 BioMEMS and biochip technology

BioMEMS followed MEMS, as described earlier, mainly because of a strong need of miniaturization in the fields of biotechnology, pharmaceuticals and medical applications. The field of BioMEMS can be related to the development of the microminiaturized analyzers in the analytical field also known as micro total analytical systems (μ TAS). This technology is more recently known as the “lab-on-a-chip” technology. BioMEMS technology promises the possibility of mass production of miniaturized, smart, and low-cost biomedical devices that could revolutionize research and clinical practice in our everyday life. The interdisciplinary nature of BioMEMS enables its easy fusion with many other technologies such as nanotechnology, clinical applications, surgical instruments, tissue repair, artificial organs, diagnostic tools, drug delivery systems etc.

There are several prominent advantages of BioMEMS. like miniaturization of a lab scaled down to a chip size, low energy consumption, realization of an easy batch production process resulting in reduced cost, minimal sample volumes, an increased heat and mass transport. The miniaturization makes many bulky instruments portable by reducing their overall size and weight. In many cases, where sensing has to be performed at the point-of-care such as clinical testing for biowarfare monitoring, these devices are particularly handy. The miniaturization in the overall size and weight also reduces energy consumption. Secondly, due to powerful techniques like microfabrication and rapid prototyping, their batch production is easily realized resulting in reduced prices and making complicated instruments more affordable. These devices only need very small amount of sample volumes which enhances their sensitivity. The advantage of smaller sample size is less

consumption of expensive or limited reagents and reduction in the production of toxic waste, thus making these devices more environmentally friendly. The miniaturization can make complex systems in a compact structure and highly integrated thus making their interface with sensors and electronics easier. The scaling down of sizes in general to the microscopic regime provides many other significant advantages such as increased heat exchange and faster mass transport across diffusion boundaries. Thus, BioMEMS is an enabling technology for greater functionality and cost reduction of micron scale devices for improved medical diagnostic and therapeutic applications.

1.1.2 Objective and goals

The recent development of BioMEMS or lab-on-a-chip technologies enables the possibility of microchip devices with higher throughput or better performance for single cell analysis^{1,2,3,4,5,6,7,8}. Our objective in this research is (1) to apply existing and develop new microfabrication strategies and processes for design, fabrication and testing of novel sensory devices. In addition, we also plan to explore the advanced sensing and transducing capabilities from these devices and apply them to the biological/biomedical field. In many biological and biomedical experiments, there is a strong need to manipulate single cells and carry out measurement or study their properties in-vitro in order to understand their in-vivo behavior more appropriately. This is usually a quite challenging task for researchers. The single cell detection and manipulation area still remains by and large unexplored. Some initial studies have been proposed by researchers for cell by cell manipulation although an integrated sensing scheme has not been applied to these cells in isolation^{9,10}. Most of the current technology of sensing cell behavior on single cell basis uses dielectrophoresis on

chip platforms for cell positioning and electrochemical or other detection on the same platform. However, dielectrophoretic platforms have several disadvantages like using high electric fields which may affect the physiological behavior of the cells and also create a lot of noise in the measurements. In order to improve the efficiency of single cell manipulation and provide better tools on the same integrated platform, we have developed a microfluidic assay which positions single cells on docking sites and electrochemically measures cellular signals through sensing microelectrodes. These devices can not only detect and manipulate single cells but also can perform further analysis on the basis of cell size, type such as cell secretion measurements. Microfluidic systems with reservoirs and micro channels are etched onto silicon wafers to manipulate fluids with cells and reagents to trigger physiological responses within those cells. An array of microelectrodes is fabricated in this fluidic system for impedance sensing and electrochemical detection. The design of instrumentation is carried out with ultra-low current sensing circuits, small impedance change detection schemes, signal amplification and filtering mechanisms, and a data acquisition and analysis system.

In order to study the versatility of the microfabricated designs for cell detection and measurement, different designs have been explored. Some of them have been implemented into real devices by a series of microfabrication processes. The first project describes a micro sensing probe for detection and counting individual cells. It is a microsensor with coplanar electrodes for detecting individual cells based on impedance sensing. The essence of this work is to explore silicon processing to miniaturize existing bulkier instruments like Coulter counter and study the possibility of hand held and point of care instruments. The second project is the development of microchip devices to assay quantal exocytosis

processes where we explore different designs of devices for single cell automatic positioning and electrochemically measuring the exocytosis. Our design allows cells to be trapped and positioned onto microelectrodes for amperometric detection of pA range currents from a set of 64 channels each with millisecond resolution. The conventional method to study cellular exocytosis process has been the use of patch clamp setup with or without a carbon fiber. It detects the capacitance change of the cell membrane or directly measures the oxidation current electrochemically by means of carbon fiber with size around 10 microns. The accessories and facilities required to perform measurements include expensive equipments such as microscopes, micro manipulators, patch clamp amplifiers, AD/DA converters, computers and most importantly well-trained personnel. All these put together may still necessitate substantial amount of time for single cell measurements making the process throughput extremely low. The target of this project is the development of an on-chip system with high throughput and high resolution in which many cells can be measured in a few minutes. The significance of this project is that it will greatly increase the efficiency and accuracy of exocytosis measurement processes, thus accelerating the process of research work in life sciences, biosafety, drug development etc. This platform will also have a secondary purpose of being used as a cell-based biosensor to detect toxins which can inhibit the cellular exocytosis process and to screen potential weapons of bioterrorism.

In addition, we will study new electrode materials for the micro chip devices. Electrochemical detection in micro scale has specific requirements on electrode materials. It also requires microfabrication compatibility. Carbon fiber by far is the most commonly used electrode in this field. But it can not be integrated on a chip. Diamond like carbon

films will be studied as an alternate to carbon fiber as the microelectrode material. Nitrogen doped DLC film deposited at high density plasma sputtering has shown great potential as an electrode material. DLC film deposition is performed using a sputtering system under various conditions and film properties are characterized by Raman spectroscopy, atomic force microscopy and cyclic voltammetry to find the best film for electrochemical detection.

1.2 Overview of single cell manipulation and analysis

Single cell analysis is of great importance in neuroscience and cell biology. In many cases, analysis of single cells is more informative than the study of a cell population, for example, the study of ion channels on the cell membrane and cellular secretion. Techniques like centrifugation, filtration, cell sorting etc. are commonly used for manipulating single cells and their diagnosis is carried out using microscopes and micromanipulators. Currently, research focuses on other complicated techniques using Atomic Force Microscopy, Scanning Electrochemical Microscopy, Confocal Microscopy etc. However the conventional equipment setup is not only bulky and expensive, but also labor intensive. Following the paths set by MEMS research and technology, laboratories have been trying to develop new devices and protocols which can detect or manipulate single cells. Some of these new technologies include dielectrophoresis platforms, optical tweezers and magnetic tweezers. The advent of new miniaturization technologies create new opportunities for developing devices which confine single cells in micron-size docking stations/traps and microchannels. This scaling down to the cellular level can offer enhanced performance and new opportunities. These microfabricated devices or probes are designed to manipulate and trap single cells, measure their properties, perform reduction-oxidation reactions/ electron

transfer processes, and in general study the broader kinetics of all biochemical processing within the cell cytosol and outside the cell.

Single cell manipulation has attracted many researchers from various disciplines of science and engineering. The first thing that comes to our mind regarding cell manipulation is cytometry. Cytometry is a general term that may apply to any technology used to measure, count, compare, or otherwise characterize biological cells although most cytometry study is based on flows. Flow cytometry is a powerful diagnostic tool which uses laser scattering, fluorescence or electrical impedance measurements for rapid analysis of entire cell populations and this data has been effectively used to predict single-cell characteristics. Multiple characteristics, including cell count, cell size or content, and responses to fluorescent probes diagnostic of cell function may be collected simultaneously by this method. During measurements, the cells flow in a liquid stream through a tube or an orifice individually where an intensity change of light or electrical signals are observed due to phenomena like scattering, absorption fluorescence or impedance change due to the passing cells. Detailed analyses of populations of interest can be obtained instantly or offline by using a number of analysis packages.

Micromanipulation is a common method to put a single cell to a specific position in a liquid medium and hold it in position to examine its properties. Micromanipulation techniques allow the stable positioning of cells for observation purpose during single-cell assaying for pharmacological or biochemical activities. For example, in a patch-clamp setup, micromanipulators are used to make a patch using micro pipette and depending on

the overall configuration, drugs can be injected to the cell, ion channels can be studied on a small patch or on a whole cell attachment and cell secretion activities can be measured electrically by monitoring the cell membrane capacitance change or by adding a carbon fiber electrode close to the cell electrochemically. Apart from methods of physical separation or positioning, micromanipulation may permit the direct measurement of the physical or structural characteristics of an individual cell. Piezoelectric effect is often used in micromanipulators but many other methods such as mechanical, optical, or electrokinetic micromanipulation can also be used to manipulate or measure the forces or interactions exerted by a microorganism on its environment.

The overall technology of single cell manipulation can be divided into four categories: mechanical, optical, electrical and the very recently developed BioMEMS methods. BioMEMS devices use pressure, heat, acoustic energy, dielectrophoresis, or electroosmotic flow or microflow to realize precise control over very small particles. The manipulation of single cells, adding and mixing of reagents, thermal cycling, and analyte detection can be carried out within the same device.

The mechanical method is probably is the earliest method used to manipulate single cell. As early as 1951, Zele et. al used a microscope mounted mechanical manipulator to study individual *E. coli* cells¹¹. The latest technique uses the AFM (Atomic Force Microscope) where the microprobe-based force transduction in AFM enables direct measurements of the physical or structural properties of individual cells. Strictly speaking, AFM is not a pure mechanical method since it usually involves laser and optic measurement, but it can be

used to measure mechanical properties of single cells. AFM technology uses piezoelectric crystals to operate the cantilever probe and an optical method to measure the force due to the interaction between the probe and the sample. Optical method uses laser to exert a focused radiation pressure that is big enough to manipulate particles, including microbial cells. Optical forces can be used to trap, move, pull or even twist cells and the technology is called “optical tweezers”^{12,13,14,15}. The optical tweezers for trapping and manipulation of neutral particles by lasers provided a unique means to control small particles. Following the development of the MEMS technology, many other forms of micro devices are demonstrated for micromanipulation capability. Examples are mechanical, electrothermally activated microgripper¹⁶, thermal gelation¹⁷ Polymer MEMS-based microgripper for single cell manipulation, Ionic Conduction Polymer Films (ICPF) micro actuators^{18,19}, single-cell manipulation supporting robot (SMSR)⁵, microrobots^{20,21} etc.

Microfluidics, a subset of MEMS technology, is another important way to trap, or sort cells while maintaining cell cultures automatically. By careful design and integration of components like micropumps, electrodes and by interfacing all this with electronics, micro total-analysis systems (lab-on-a-chip) devices can be realized. This way a complete bio/chemical experiment can be carried over a single chip. This greatly reduces the size of the devices and make many portable instruments affordable with quick data read outs. Microfluidics also reduces the sample or reagent volumes and other the waste products generated from chemicals used to maintain a cell culture. According to a recent study (NEXUS) (<http://www.microfluidics-roadmap.com/>), microfluidic systems had a net global market size of around 15 billion US dollars in year 2002. Among them, around 5

billion was attributed to the life sciences application. Going small is becoming increasingly big business as the strong need for smaller, faster and cheaper products are realized.²²

Using microdevice to study cells can be dated back to 1991 when Ogura et al., developed a microfabricated device to study human red blood cell deformity by small microchannels (pores) down to 1 μm .²³ Many other devices were designed after this for the study of blood rheology and blood cell deformability to mimic capillary conditions of blood cells.^{24,25,26} Researchers next tried to use microfluidic devices for cell counting and sorting [more detailed review is in Chapter 3]. However, the use of microfluidic devices for single cell trapping and positioning is relatively new. Glasgow et al [2001] reported a device to handle individual mammalian embryos using microfluidic channels with relatively large size (cell size 100~150 μm in diameter and channel size of 250~400 μm wide, 160~200 μm deep)²⁷, Huang et al. has reported a microfluidic chip for single cell analysis and manipulation with electrodes which make an electrical interface with single cells [2003]²⁸. The main purpose of this device is to analyze and alter biochemical state of cells. An integrated cell processor for the automatic handling of individual embryo cells has been demonstrated by Park et al. in [2005]²⁹. The authors have claimed important functions of the integrated processor like cell transport, isolation, orientation, and immobilization. The isolation of cell was performed using polypyrrole (PPy) valves in a microchannel. The orientation of cells was controlled by electro-rotation (ER), and the target cell was immobilized by suction from a micro-hole. A more recent microfluidic device with single cell trapping capability has been reported by Yun et al. for single cell based assays³⁰ as shown in Fig. 1.1.

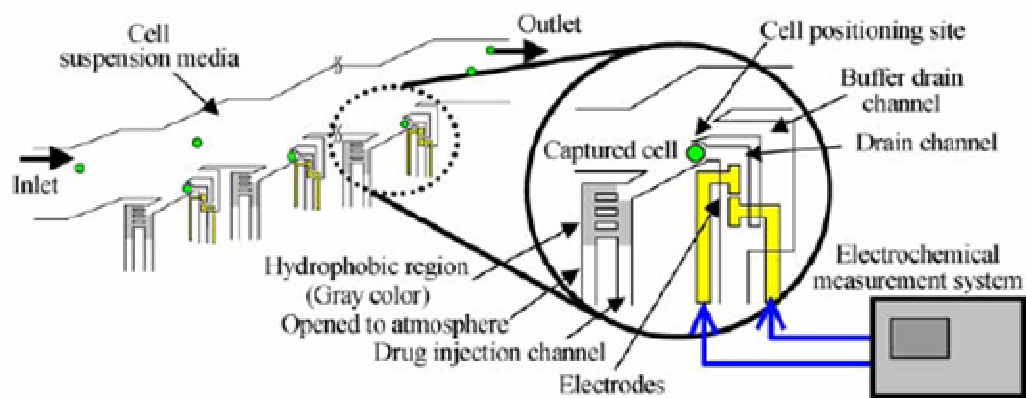


Fig. 1.1 Cell trapping mechanisms designed along microfluidic channel. Yun et. al, 2005

Another cell trapping mechanism using two parallel microfluidic channels with a dam structure in-between was demonstrated by Yang, et al in 2002³¹. This design used the lateral pushing force created by the lateral flow between the two channels to align a row of cells at one side of the cell flow channel as shown in Fig. 1.2. This design did not demonstrate single cell trapping or docking, but did show results of cells aligned in a row which is close to one cell by one cell as shown in Fig. 1.2. The authors state that, when liquid pressure in channel 5 is higher than in channel 4, a fraction of the fluid flows over the dam structure to channel 4. The hydrodynamic pressure difference will bring the cells in channel 5 to dock along the dam. After complete cell docking, the fraction of flow across the dam is reduced so that excessive cells become more difficult to approach the laminas of slower velocities near the dam and are driven away along the main flow route. A single line of cells will be docked along the dam without multilayer formation.

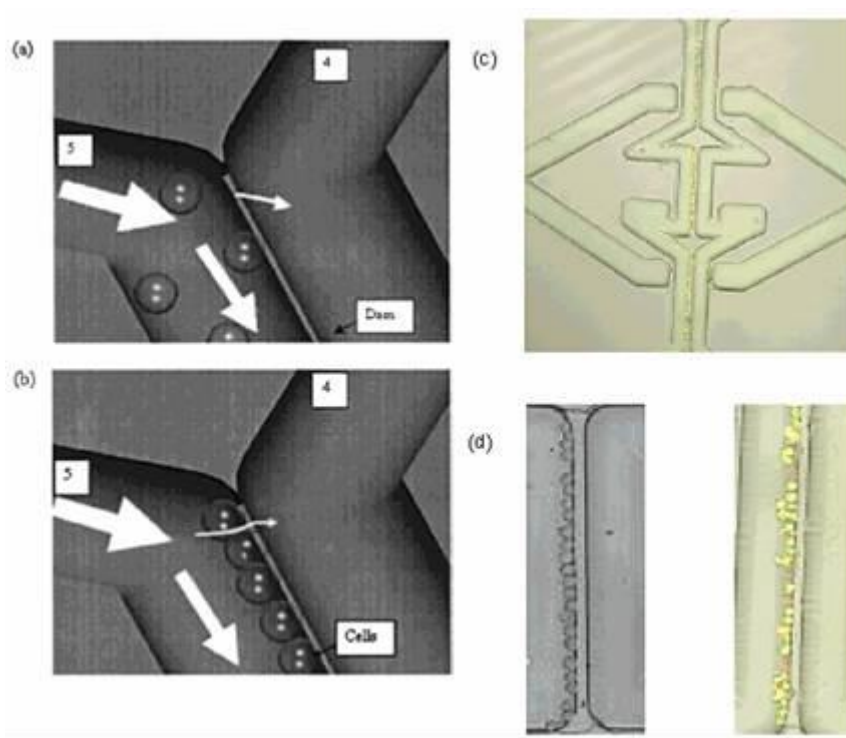


Fig. 1.2 Schematic diagrams and cell docking results by a dam structure by Yang et al. (a) (b) the schematic design, (c) Fluorescence image of the microchannels showing the alignment of mammalian HL-60 cells along the dam structures. (d) picture of a section of the dam with docked cells.

Similar structure was designed for in-vitro neuron cell culturing by Taylor et al in 2005³². The author designed a pair of parallel channel with very small channels in-between so that the neuron axon can grow through the small channel to the other channel. This design method enables one to culture single neuron cells with isolated soma and dendrites as shown in Fig. 1.3. Although this design was intended for static cell culture, it could be used for cell docking if there is a flow from one channel to the other, a similar lateral force will be applied on the cells flowing in the channel.

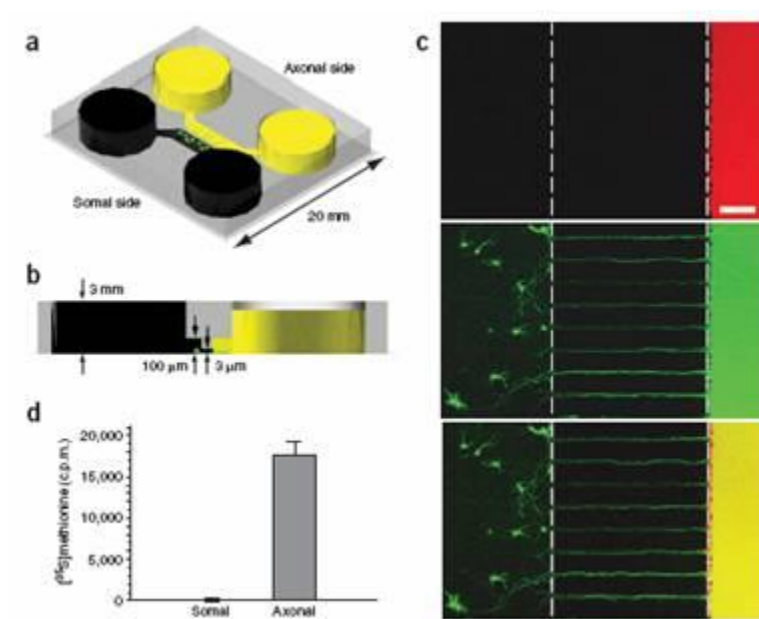


Fig. 1.3 Schematic design of microfluidic based cell culture platform directs axon growth through micro grooves(10 μm) between the channels.

Electronic manipulation of cells on a chip

AC electrokinetic effects including dielectrophoresis (DEP) and electrorotation can be used to manipulate cells. Due to non-uniform AC electrical fields and cell dielectric properties, a dielectrophoretic (DEP) force can be exerted on cells. If the electrical field is rotating, then a rotation force can be applied to cells too and thus the name electrorotation. It is believed that the dielectrophoresis and AC electrokinetic forces are produced by the interaction of induced field in the particles or cells with the applied electrical field. Cells usually have different dielectric properties and may experience different forces even for identical AC signals. In addition, the DEP force is frequency dependent and the distribution of the electric field varies according to the electrode design. This complicates the use of electronic manipulation applications. Although with the complications, many researchers have demonstrated microfabricated devices using DEP to manipulate single cells^{2,33,34}. DEP has great potential to be used for cell manipulation and cell sorting, and also for the

purpose of electrophysiology measurement such as exocytosis, although there are still many issues that need to be addressed such as the need for relative immobilization of cells, the applied electrical field's effect to the response of cells, the difficulties of single cell trap etc.

Recently people even proposed a static way to isolate single cells, culturing cells on a surface patterned by certain adhesion molecules, cells will only like to stay on those patterned islands but not on the other portion of the surface so that cells can be separated from each other. This technology usually need soft lithography to create the micro sites where special adhesion molecules are coated similar to printing and molding. Although isolate cells one by one is very challenging, people already demonstrated that cells do like certain surfaces and dislike some others^{35,36,37}.

In summary, there are many possible ways to manipulate single cells. Some of them are very complicated such as microrobots and optical tweezers. One goal of our research here is to study alternative ways of trapping or positioning cells and also perform cell measurements on the same device. We will use the most natural way to trap the cells and automatically position the cells to multiple sensing spots by passive trapping in flow dynamics. Cells will be kept in their original medium environment and automatically positioned to the sensing spots where microsensing electrodes are already patterned.

1.3 Impedance based cell measurements

Biological impedance measurement has been a simple, straight forward method to characterize tissues for a fairly long amount of time. It has been used to monitor cell

growth and change and a new technology has been developed in 1986 with the name ECIS (Electrical Cell Impedance Sensor). This is a non-invasive way to monitor the activity of a population of cells rather than a single cell. Using similar technology but smaller electrodes on glass substrate, Connelly, et al. was able to examine the impedance characteristics of individual BHK cells³⁸ [Connelly, et al., 1989]. Electric Impedance Spectroscopy is another technique which can be used to measure the properties of tissue and organ, and also to measure single cells using MEMS technology^{39,40}. In flow cytometry, electrical impedance has been successfully used to measure/count particles passing through an orifice due to the impedance change. This technology was developed into the 'Coulter counter' for counting blood cells.

Many micro devices have been designed and fabricated to detect or measure particles/cells by monitoring electrical impedance. By designing microelectrode comparable to that of a cell, more detailed information can be obtained of cell sizes and even the cell growth cycles. The microfabricated devices opened a new aspect of view to study the cells one by one or even probe metabolism event inside a cell.

1.4 Exocytosis measurement

Exocytosis is a process of cellular secretion or excretion which is a very important biological phenomenon for signaling or life regulation. For example, hormones stored within vesicles inside endocrine cells as are released when a rise in intracellular Ca^{2+} concentration triggers the fusion of vesicles with the outer membrane of the cell. Similarly, release of neurotransmitter from nerve terminals is another example of an exocytosis process for signaling. Exocytosis is quantal in nature since the process involves single

vesicles. During an exocytosis process, individual vesicles loaded with chemicals are formed, docked and fused to the cell membrane and finally release the chemicals inside the vesicle to the extracellular environment. It is also commonly referred as vesicle exocytosis due to this reason. The measurement of quantal release provides detailed information about the mechanics and regulation of exocytosis processes which is important for life science research and drug discovery as detailed earlier. However, the current method to measure exocytosis is very time consuming, labor intensive and needs a complicated setup and well trained personnel. It is typically done by researchers at a very low throughput (one hour or more per cell). The typical setup to measure exocytosis is shown in Fig. 1.2, which is based on a patch clamp setup.



Fig. 1.4 A typical exocytosis measurement setup based on a patch-clamp system. From left to right is: Faraday cage shielded microscope bench with piezoelectric micromanipulator and head stage preamplifier; instrument rack of patch-clamp amplifier, AD/DA module, monitor etc.; computer control for voltage/current clamp and data acquisition. (Courtesy of Dr. Gillis's electrophysiology lab at Dalton Cardiovascular Research Center)

Basically, there are three common techniques to measure exocytosis at the single-cell level, namely, the cell membrane capacitance based method, post-synaptic response based method and electrochemical based method. Among them, the electrochemical way is most suitable to be used in a microfabricated device.

1.4.1 Capacitance based exocytosis measurement

The Exocytosis process involves the fusion of vesicles with the cell membrane. The fusion of vesicles with the cell membrane increases the surface area and so the electrical capacitance of the membrane. The measurement needs a patch-clamp setup whereby a micro pipette is attached to a cell. Then a sinusoidal voltage signal is applied through the pipette and the cell membrane and the resulting sinusoidal current is used to calculate the membrane capacitance. Although the capacitance method can provide high time resolution measurement, it is an indirect measurement method, so the capacitance change may not be due to the vesicle release. It could be any other event that can change the membrane capacitance; for example, the reverse of exocytosis, the endocytosis may occur simultaneously and cause capacitance change too.

1.4.2 Post-synaptic response measurement

The post-synaptic response is an electrophysiological measurement of the electrical response of a post-synaptic method in which the electrical response of either voltage or current of the post-synaptic cell acts as a sensitive bioassay of the release from the presynaptic cell. This measurement is fast and closer to natural response and thus more “physiological”. The drawback of this method is that the postsynaptic cell to

neurotransmitter is nonlinear and subject to dynamic modulation. The change in synaptic transmission could be caused by the release or just the sensitivity change of the cell.

1.4.3 Electrochemical based exocytosis measurement

Electrochemical measurement of exocytosis is the most suitable method for microchip device. It is sensitive, can provide high time resolution and high temporal resolution and can be easily integrated onto microchip devices by patterning microelectrodes. Catecholamines are electroactive materials and can be oxidized on the surface of an electrochemical electrode with sufficiently high potential. The oxidation process involves in electron transfer between the chemicals and the sensing electrode which result in a current. Since the exocytosis is quantal release from single vesicles, the current due to exocytosis process is spike like. Each resultant oxidation current spike corresponds to a single vesicle release and it is a direct measurement of the transmitter release. Conventional electrochemical measurement of exocytosis uses carbon fiber as the sensing electrode as shown in Fig. 1.5 schematically and an real case picture in Fig. 1.6 where the setup uses a patch-clamp micro pipette with a carbon fiber tip under a microscope. An insulated carbon fiber with a diameter of about 10 μm is placed close to a cell with the help of a micro manipulator, with only the circular end or the radial cross-section is exposed to constitute the working electrode surface ($\sim 10 \mu\text{m}$). A constant potential of 700 mV is held at the sensing electrode and current is monitored. At such a high potential, catecholamines are readily oxidizable at the electrode surface. Obviously, this method is all manual, and only one cell can be measured at a time. In addition, the CFE are usually manually prepared in small quantities before the experiment and need to be cut for a fresh surface for multiple

uses or replaced frequently. For the high throughput microchip device applications, we need to find alternative materials or processes to fabricate microelectrodes which are comparable or even better than CFE yet can be batch producible at a lower cost, it either can be easily reused or can be disposable after a single measurement.

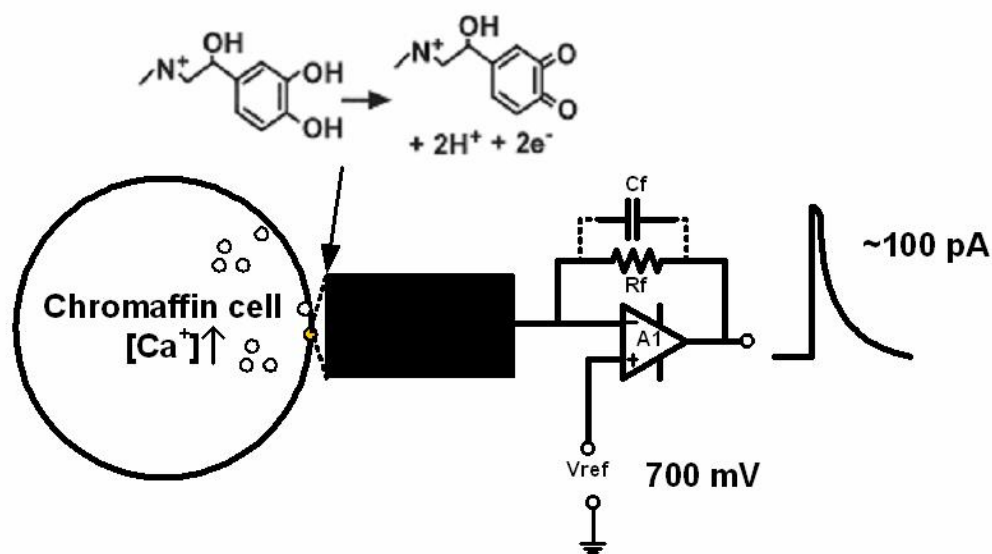


Fig. 1.5 The schematic setup of electrochemical detection of exocytosis using carbon fiber, a carbon fiber is put close to a chromaffin cell and the faradic current due to oxidation of catecholamines is amplified through A1, a high gain I-V converter and a current spike around 100 pA is shown.

In an exocytosis measurement, the sensing electrode needs to be put as close to the cell as possible for the high time and temporal resolution. In addition, the dilution of the chemical released due to diffusion can also be alleviated since the chemical contents inside the tiny vesicles released into the extracellular space and are quickly diluted into the external media by free diffusion. A significant decrease in signal and spatio-temporal resolution of exocytosis has been shown theoretically^{41,42} (Schroeder et al., 1992; Wightman et al., 1995)

and experimentally^{43,44} (Jankowski et al., 1993; Wightman et al., 1995) when the electrodes are placed more than even a few microns away from the cell surface.

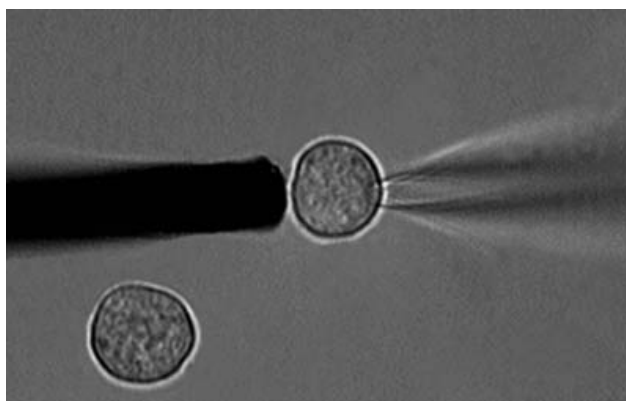


Fig. 1.6 Manual manipulation of cells using a micro pipette and electrochemical detection of exocytosis by carbon fiber⁴⁵.

In order to improve the efficiency and throughput, it is desirable to design microchip devices that can automate this tedious measurement process. One of the main purposes of our research is to miniaturize this whole complicated exocytosis measurement setup to a hand held micro-chip. Our goal is to shrink the whole lab on to a chip as shown in Fig. 1.7 in which (b) is the prototype microchip device we developed.

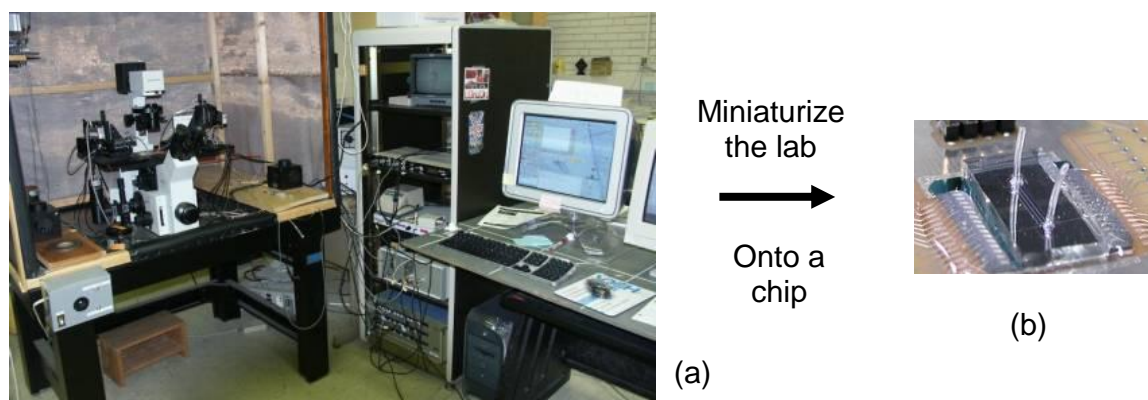


Fig. 1.7 (a) A typical lab setup for patch-clamp experiment and exocytosis measurement using carbon fiber microelectrodes. (b) A miniaturized microchip device for exocytosis measurement.

1.5 Dissertation outline

The purpose of this dissertation is to study new microfabricated devices for single cell assay. The discussion starts from chapter 1 with the introduction and objectives of this project and also the current potential of MEMS technology to fabricate compact and smart systems. A brief overview of the current technologies on cell manipulation and measurement is also provided. In chapter 2, we will discuss some theoretical background of microelectrodes and the fabrication and test of the microelectrodes in different materials. In chapter 3 we will explore the design, fabrication and characterization of a micro device for cells/particles sensing based on electrical impedance. Chapter 4 is focused on the microchip device for single cell exocytosis measurement. Beginning with some previous work in this topic a list of possible improvements in the previous device designs are presented and some new designs are discussed and compared. Then, the fabrication of a selected design is detailed followed by its testing and characterization. Chapter 5 provides the conclusions, discussions and possible future directions for this research work. Some problems and limitations of the current technology are also discussed with possible improvements.

Chapter 2 MICROELECTRODE THEORY, MATERIALS AND DIAMOND LIKE CARBON MICROELECTRODE DEVICES

2.1 Introduction

Electrochemical biosensors use electrochemical methods for transduction and can be divided into three types. The first type is potentiometric sensors which measures the potential of an electrochemical cell at zero current. The second type is the amperometric sensors where a current is measured when certain potential is applied to the cell until oxidation (reduction) of the substance to be analyzed occurs. The simplest excitation is to apply a constant potential, the sensor then monitors the current-time or *i-t* curve, and many other kinds of excitation could be applied, for example, in cyclic voltammetry, linear increasing and decreasing potential is commonly used. The third type is the conductimetric sensors which use the relationship between the conductance and ionic species concentration to measure the concentration of the substrate. All of the electrochemical sensors need certain kind of electrodes and microelectrodes used in microdevices have different properties from that of the macro electrodes. It is necessary to discuss some of their special properties of the microelectrodes.

Microelectrodes are very small electrodes. There is no definite size how small an electrode can be classified as microelectrodes, but usually we refer to an electrodes size at the micron level. For example, the carbon fiber electrode used to measure exocytosis is usually around 10 μm in diameter. Microelectrodes are often used to study electrical characteristics of

living cells and tissues. They can be fiber/needle like or planar in structure. Due to scaling, there are some unique properties when compared to big electrodes. Microelectrode can provide dramatic improvements in the quality of electrochemical data. For example, they can provide better temporal resolution, increased current density, and fewer problems due to solution resistance. The electrochemical response at microelectrodes can be very different from that seen at conventional millimeter or bigger electrodes. The main reason is due to the reduced size such that the dimensions of the electrode are much smaller than the diffusion distance of the molecules in solution. This means that the diffusion at microelectrodes is not planar diffusion as is commonly seen at conventional electrodes. The mass transport from the bulk of solution toward the electrode conditions is also changed. This leads to a decreased ohmic drop of potential, fast establishment of a steady-state signal, increased current density due to enhanced mass transport at the electrode boundary, and increased signal-to-noise ratio. These effects make microelectrodes advantageous in many areas of electroanalytical chemistry.

In this chapter, we begin with the discussion about the solid/electrolyte interface, some models will be introduced. Properties of microelectrode especially at voltammetry are followed. Then, we will discuss electrode noise. Electrode materials such as metals like gold and platinum will be discussed and compared with carbon based electrodes. Among the new electrode materials, we will focus on the fabrication of diamond-like carbon(DLC) and their application for low noise exocytosis measurement in micro devices.

2.2 The solid - electrolyte interface and modeling

A solid-electrolyte interface will be formed when a solid is placed into an *electrolyte*. An electrolyte usually refers to a solution with free ions to produce an electrically conductive medium. Because they generally consist of ions in solution, electrolytes are also known as ionic solutions. Some molten substance has similar properties and can be called an electrolyte too but this is beyond the scope of this work. Our discussion will focus on the solid-electrolyte interface of metal or other conductive materials, as the other non-conductive material is not relevant to this research. While the primary ions of electrolytes are sodium, potassium, calcium, magnesium, chloride, phosphate, and bicarbonate in physiology, our interest is the detection of catecholamine hormones which has very important regulatory effect.

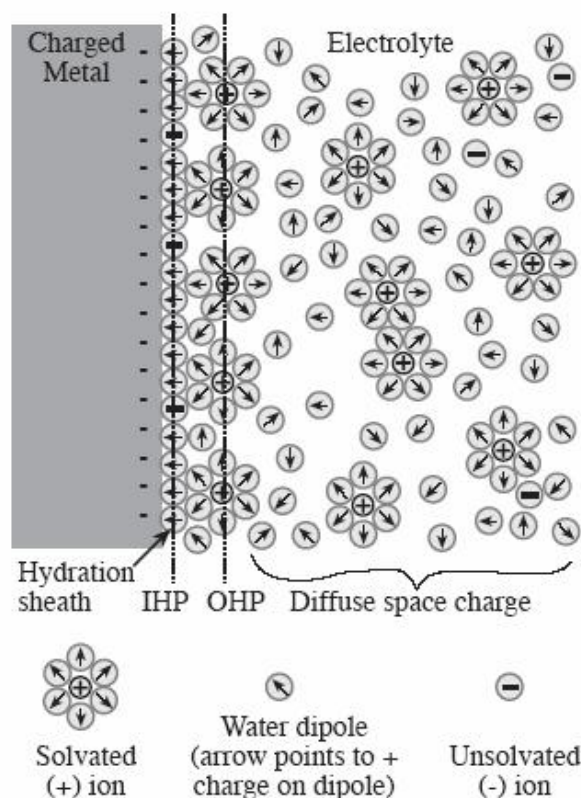


Fig. 2.1 Helmholtz model of the electrody-electrolyte interface. From p6332, Fig. 7.7 Bockris and Reddy, "Modern electrochemistry", Vol. 2, 1970.

A metal and an ionically conducting solution are electroneutral themselves. When a metal is placed in the solution, some new forces arise at the electrode-electrolyte interface due to physical absorption, chemical absorption, or chemical reaction. The new forces will rearrange the solvent dipoles and charged species at the interface. Thus the previously random orientation of dipoles and equal distribution of positive and negative charges in the electrolyte is no longer valid at the interface. This results in the formation of an electric field between the electrode and the electrolyte, the electroneutrality has broken down on the electrolyte side of the phase boundary, the interface has become charged or electrified. Water dipoles orient themselves in the field in a layer at the metal surface forming what is known as the *hydration sheath*. The locus of the electrical centers of the specifically adsorbed ions is called the inner Helmholtz plane (IHP) which is at a distance around 5-20 angstroms. Ions of opposite charge from the solution form a counter layer adjacent to the electrode surface which is known as the *outer Helmholtz plane* (OHP) as shown in Fig. 2.1. There is also specific adsorption of ions (cations or anions) at the electrode surface interspersed with the orientated water dipoles. The net result of these reactions, adsorptions and orientations is the creation of the *electrical double layer* (or simply *double layer*), an electrified interface describing the interphase region at the boundary of an electrolyte. The non-specifically adsorbed solvated ions interact with the charged metal electrodes with only long-range electrostatic forces, their interaction is essentially independent of the chemical properties. Because of thermal agitation in the solution, the nonspecifically adsorbed ions are distributed in a three dimensional region called the diffuse layer, which extends from the OHP into the bulk of the solution. The thickness of the diffuse layer

depends on the total ionic concentration and the potential profile across the double layer region is shown in Fig. 2.2.

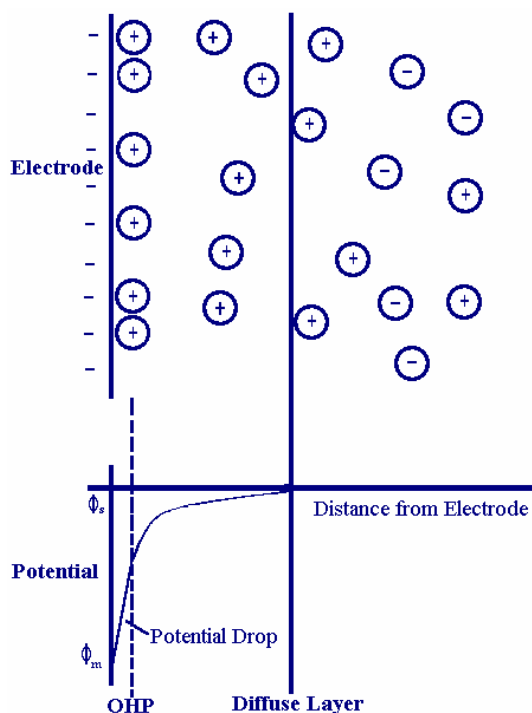


Fig. 2.2 Diffuse layer and the potential profile across the double layer region. Adapted from <http://www.cheng.cam.ac.uk/>

Arbitrary case of positive ions at the OHP and electrons at the metal surface has been assumed as illustrated in Fig. 2.2. The choice of an unsolvated negative ion for specific adsorption was also arbitrary and independent of the other charges in the system. The space charge region shown has a graded profile with the strongest field at the interface, diminishing to zero in the bulk electrolyte.

2.2.1 Electrical modeling of the double layer

The earliest model of the electrical double layer is usually attributed to Helmholtz (1879). In Helmholtz's model, the double layer is treated as a simple capacitor, based on a simple

physical model assumption that a single compact layer of ions is adsorbed at the surface as illustrated in Fig. 2.1. Later Gouy and Chapman (1910-1913) made significant improvements by introducing a diffusion model of the electrical double layer, in which the potential at a surface decreases exponentially due to adsorbed counter-ions from the solution. The current classical electrical double layer is the Gouy-Chapman-Stern model, which combines the Helmholtz single adsorbed layer with the Gouy-Chapman diffuse layer. Important approximations used in this model are (1) ions are effectively point charges (2) the only significant interactions are columbic. (3) electrical permittivity is constant throughout the double layer. (4) the solvent is uniform at the atomic scale. Helmholtz assumed the charge of solvated ions was confined to a rigid sheet at the OHP which was equal and opposite to that in the metal. A simple capacitor is modeled with the orientated water dipole layer acting as a dielectric layer, this capacitance in the Helmholtz model can be determined by the dielectric permittivity of electrolyte ($\epsilon_0 \epsilon_r$), the area of the interface

(A), and the distance of the OHP from the metal electrode (d_{OHP}):

$$C_H = \frac{\epsilon_0 \epsilon_r}{d_{OHP}} \quad (2.1)$$

where C_H is the capacitance per unit area (F/m^2), ϵ_0 is the permittivity of free space (8.85419×10^{-12} F/m) and ϵ_r is the relative permittivity of the electrolyte. Then, the Helmholtz capacitance can be estimated by some value of ϵ_r and d_{OHP} which can be obtained from experimental values. Obviously, the simple model of Helmholtz is not accurate enough, the capacitance is not constant and is dependent on potential, i.e. C_H is a function of potential as observed experimentally. Since the OHP was determined by the closeness of the solvated ions getting to the electrode, which could be affected by the electrical potential, the proposed simple capacitor model is not accurate. Gouy and

Chapman modified the simple Helmholtz model by considering mobile solvated ions at the electrode surface [Gouy, 1910; Chapman, 1913]. These mobile ions were influenced by thermal forces in addition to the electrical forces. The result was an *ion cloud* near the interface where the combined effects of thermal and electrical forces equilibrated to form a time-averaged ionic distribution. This extended the space charge layer extend to the bulk electrolyte while maintaining the same total charge. The distribution of this space charge was concentrated at the OHP, tending toward zero in the bulk solution. This model allowed the change of capacitance by movement of ions in response to an applied potential. The resulting relationships for the potential distribution and the capacitance for relatively small applied voltages (<50 mV) the voltage drop through the space charge region can be estimated as an exponential decay:

$$V_x = V_0 e^{-kx} \quad (2.2)$$

Detailed mathematical derivations of the model about the nonlinear distribution of the mobile ions can be found in several texts [Bard and Faulkner⁴⁶, 2001; Bockris and Reddy⁴⁷, 1970]. While the Gouy-Chapman model was an improvement over that of Helmholtz, it overestimates the interfacial capacitance as it varies more strongly with applied potential than is observed experimentally and it is too dependent on ionic concentration. Stern rectified this inconsistency by combining the Gouy-Chapman model with that of Helmholtz. He combined a layer of bound ions at the OHP with a diffuse ion layer [Stern, 1924]. Thus, the total interfacial capacitance was the series combination of both capacitances:

$C_I = \frac{1}{C_H} + \frac{1}{C_G}$, where C_I is the total interfacial capacitance, C_H is the Helmholtz capacitance and C_G is the Gouy-Chapman capacitance due to the diffuse ion cloud as described in the Gouy-Chapman model respectively. The Stern model results in a linear

potential drop between the electrode and the OHP with a near exponential decay from the OHP to the bulk solution as shown in Fig. 2.2.

The above analysis of the interfacial capacitance is assumed at equilibrium in an electrolyte without a net current. When an external DC potential is applied, then a current may start to flow at certain conditions. Obviously, there will be additional resistive part in the solution which we define as R_s . The flow of current through this metal-electrolyte interface requires the net movement of charge in response to the applied electrical field. The applied voltage will break the equilibrium value (V_0) across the interface. This potential difference ($V - V_0$) responsible for the net flow of charge is termed as overpotential η and is defined as the sum of four different components:

$$h = h_t + h_d + h_r + h_c \quad (2.3)$$

where η_t is due to *charge transfer* through the double layer; η_d is due to the *diffusion* of reactants to and from the electrode; η_r is due to *chemical reactions* at the electrode; and η_c is due to exchange of metal atoms with corresponding ions in solution. A potential high enough can drive charge transfer, diffusion, chemical reactions and crystallization respectively. Thus, three parallel currents in series with the diffusion current may exist, each driven by a percentage of the total overpotential. For operation of an electrode near its equilibrium condition, the charge transfer overpotential (η_t) tends to dominate the overall current. As the applied potential is pushed further from equilibrium, diffusion of reactants may become a limiting factor, making the diffusion overpotential (η_d) more significant. The overpotentials due to chemical reactions (η_r) and crystallization (η_c) are not of significance in biological applications [Cobbold, 1974]⁴⁸.

In order to study a system involving electrode-electrolyte electrochemical system, it will be very helpful to introduce circuit model so that the system can be analyzed electrically. However, the actual system is a very complicated system which at least related to the electrode double layer capacitance, the electrode kinetics, the diffusion layer and the solution resistance. After the simple capacitor electrical model of the double layer, the complete circuit model including the electrodes and the solution would be a capacitor and a solution resistance R_s in series. Many other circuit models have been proposed for closer estimation. Among them, the commonly accepted model is shown in the right circuit in Fig. 2.3.

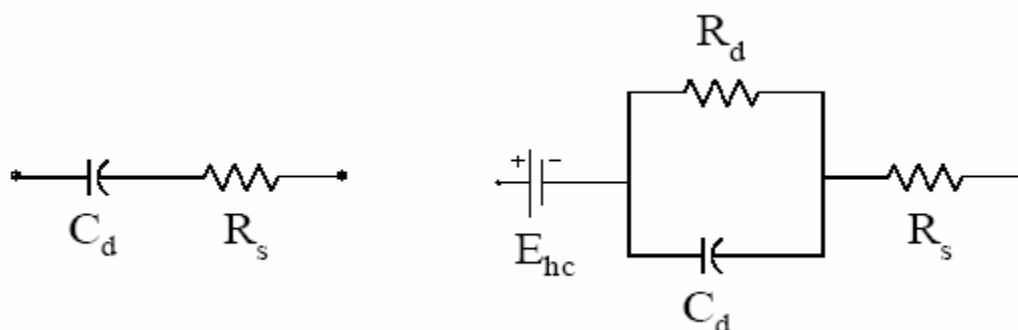


Fig. 2.3 Circuit model of the electrode-electrolyte interface

As shown in Fig. 2.3, E_{hc} is the half cell potential, the equilibrium value (V_0) across the interface, R_s is the series resistance of the resistance by the electrolyte, C_d represents the double layer capacitance. R_d represents the leakage resistance across this double layer of charge. The values of the circuit elements are, however, determined by the material of the electrode, the material of the electrolyte and its concentration. This simple model can give a good approximation of the interface properties yet without too much complication. We have to note here that, due to different properties of electrode-electrolyte, the system may produce

very complicated response in many cases. The values of the circuit component are not constant and dependant on time or frequency.

Electrodes can be theoretically classified into two categories based on the electrochemical properties of the electrode material, namely perfectly polarizable and those that are perfectly non-polarizable. Perfectly polarizable electrodes are those in which there is no actual charge crossing the electrode-electrolyte interface when current is applied, strictly following the Helmholtz capacitance model. Perfectly non-polarizable electrodes on the other hand are those in which current flows freely across the electrode-electrolyte interface with direct electron transfer. Practically neither of these two electrodes can be found in practice and all material presents the property somewhere in-between. However many noble metal electrodes such as platinum and gold show very similar characteristics of perfectly polarized electrodes owing to their relatively inert nature. The electrical characteristics of such electrodes show a strong capacitance effect.

As for cell based sensors which measures the impedance, the sensing circuit model may be a little different and some other relatively more complicated circuit models have been proposed. For example, in the model proposed by Goda et. al.,⁴⁹ there are three capacitors and two resistors. The capacitor C_e represents the capacitance between the two electrodes. The first resistance in this model is due to the electrolyte solution and the second resistance in this model is the parasitic resistance, referring to the resistance from the cables, wires, and the electrodes themselves. Fig. 2.4 shows the complete circuit schematic for this model of the biosensor.

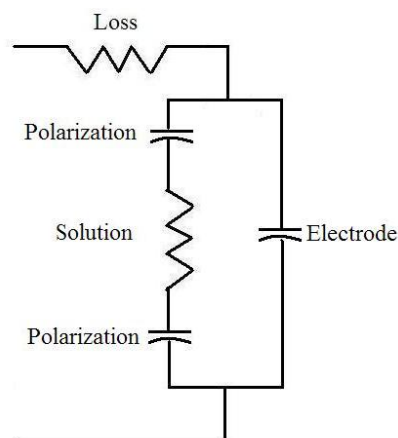


Fig. 2.4 Schematic of a Goda et. al. circuit model. This is a relatively simple model of a cell-based-biosensor.

Hong et. al. proposed a somewhat simpler model as shown in Fig. 2.5⁵⁰.

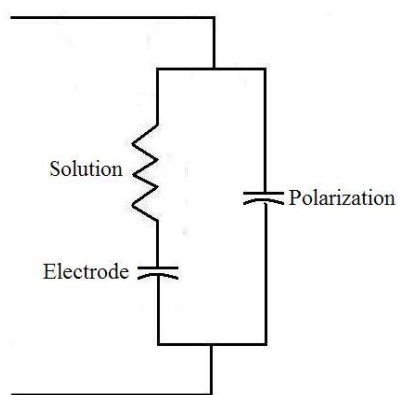


Fig. 2.5 Schematic circuit model of Hong et. al.

Gawad et. al proposed a very complicated circuit model as shown in Fig. 2.6.⁵¹ Both the solution and cell impedance consist of a parallel resistance and capacitance, and the polarization impedance is made of a series resistance and capacitance. The impedance of the solution and cell are in parallel because the current takes two paths when it reaches the electrode.

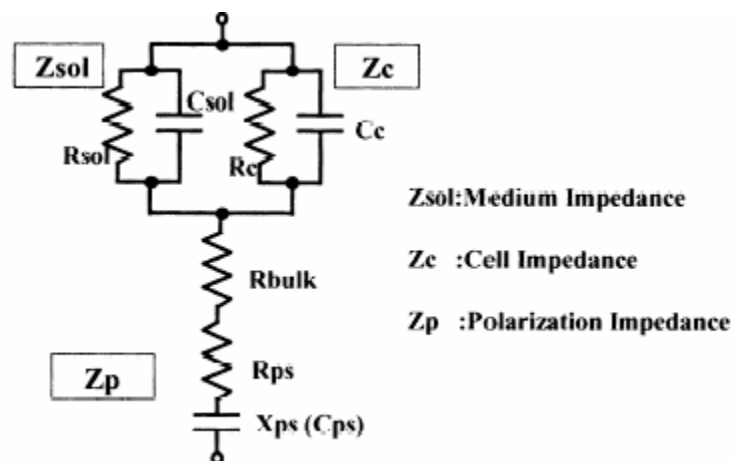


Fig. 2.6 Circuit model proposed by Gawad et. al

In summary, although we discussed so much on the interface and the double layers, the interfacial capacitance from double layer introduces problems to electroanalytical measurements. First, charging current of the capacitor results in background current which is superimposed on and independent of the analytical current from the electrochemical redox couple. Second, it limits the electrode and instrument response time and scan rate. Third, it may also distort the analytical signal.

2.3 Microelectrode and their properties

When the dimensions of the electrode decrease down to the microscale, many changes occur in the electrode properties, especially the voltammetric behavior. Due to the specific features of microelectrodes, sensors using them can provide unique solutions to many situations where large electrodes are not suitable.

When an electrochemical reaction occurs at the electrodes, a concentration gradient is generated between the electrodes surface and solution. The electrode current measured thus

depends on the mass transport to and from the electrodes. At microelectrodes, the predominant mode is diffusion, the effects of convection is much less apparent than diffusion because the flux due to diffusion is very large. Because of this reason, the theoretical study of currents at microelectrodes is usually treated as diffusion limited process⁵². Although the magnitude and time dependence of the diffusion processes are partly determined by the geometry of the electrode, usually the conditions of semi-infinite diffusion are assumed.

We can do an analysis of the diffusion at spherical electrodes with the geometry of r_0 , r is the radial distance from the center of the electrode. The boundary conditions for the reduction of species O, of bulk concentration C_o^* , are

$$\begin{aligned}\lim_{r \rightarrow \infty} C_o(r, t) &= C_o^* \\ C_o(r, 0) &= C_o^*, (r > r_0) \\ C_o(r_0, t) &= 0, (t > 0)\end{aligned}\quad (2.4)$$

To evaluate the faradaic current (i), we should find the solution to the gradient of the concentration at the electrode surface:

$$\frac{i}{nFA} = D_o \left[\frac{\partial C_o(r_0, t)}{\partial r} \right], \quad (2.5)$$

where D_o is the diffusion coefficient of the species being analyzed, A is the area of the electrode, F is the Faraday constant, n is the number of electrons transfer per molecule. Since the situation here a non-steady or continually changing state diffusion, i.e. the concentration within the diffusion volume changes with respect to time, we have to apply

Fick's second law ($\frac{\partial f}{\partial t} = D_o \frac{\partial^2 f}{\partial x^2}$) in a spherical coordinate system, the concentration is

$$\frac{\partial C_o(r,t)}{\partial t} = D_o \left[\frac{\partial^2 C_o(r,t)}{\partial r^2} + \frac{(2/r)\partial C_o(r,t)}{\partial r} \right] \quad (2.6)$$

The solution of this second-order differential equation, with appropriate boundary conditions, gives the concentration profile:

$$C_o(r,t) = C_o^* \left(1 - \frac{r_0}{r}\right) \operatorname{erfc} \left[\frac{r - r_0}{(4D_o t)^{1/2}} \right] \quad (2.7)$$

For large electrodes, r_0 can be considered as infinite, then

$$C_o(r,t) = C_o^* \operatorname{erfc} \left[\frac{x}{(4D_o t)^{1/2}} \right], \quad (2.8)$$

Where $x = r - r_0$, equation (2.8) is the concentration profile at large planar electrodes. If time is long enough, we have

$$C_o(r,t) = C_o^* \left(1 - \frac{r_0}{r}\right) \quad (2.9)$$

For comparison purposes, we can plot out the concentration profiles for the large and small electrodes, as shown in Fig. 2.7. Here we assume $r_0 \rightarrow \infty$ for large electrodes and $r_0 = 1 \mu\text{m}$ for the small electrodes, and also assume that a sufficient potential is applied to the electrodes so that the electroactive species concentration at the electrode surface is driven to zero.

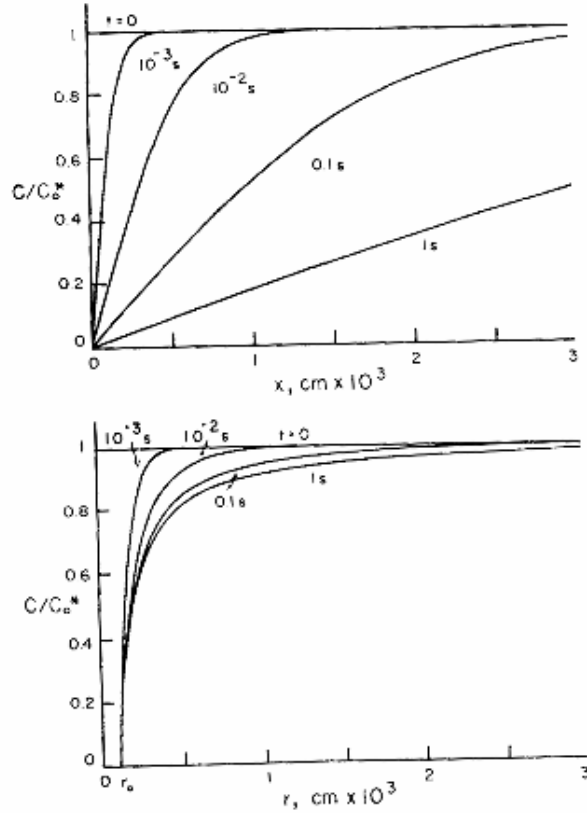


Fig. 2.7 Concentration profiles difference at large and small electrodes, adopted from [52].

If the value of $D_0 t / r_0^2$ is large enough, the limiting current under diffusion-controlled conditions will not change with the potential excitation. For example, at a sufficient slow scan rate for cyclic voltammetry, the limiting current for a spherical electrode is

$$i_{\text{lim}} = 4pr_0 nFC_0^* D_0 \quad (2.10)$$

and for a disk electrode, the limiting current is

$$i_{\text{lim}} = 4rnFC_0^* D_0 \quad (2.11)$$

It needs to be pointed out that the limiting current for a planar microelectrodes is not proportional to the area but to the radius as shown in equation 2.11.

There are two major factors that affect the current magnitude arising from electrooxidation of solution species: mass transport and the rate of electron transfer at the electrode surface. The electron transfer rate depends on the material and properties of the electrode material and the target chemical, and of course the potential applied. For a redox reaction, an equilibrium potential may be reached thermodynamically as shown in the Nernst equation:

$$E = E^0 + \frac{RT}{nF} \ln \frac{C_{ox}}{C_{red}} \quad (2.12)$$

where E is the potential applied to the electrode, E^0 is the standard half cell equilibrium potential as found in standard tables, R is the gas constant, T is the temperature, n is the number of electrons transferred, and F is the Faraday constant. The electron transfer kinetics can be described by the Butler-Volmer equation for the effect of potential applied:

$$j = -k_0 C_{red}(0, t) \exp\left[\frac{(1-\alpha)n_a F(E - E_0)}{RT}\right] \quad (2.13)$$

where j is flux of R_{ed} (i.e. epinephrine, dopamine, etc.), k^0 is the standard rate constant for electron transfer, α is the transfer coefficient, n_a is the number of electrons passed in the rate limiting step in the electrochemical reaction, F is the Faraday constant, E is electrode potential, and C_{Red} is expressed as a function of time and distance. Equation (2.13) states that flux is proportional to the electron transfer rate, the concentration of unoxidized species, and the amount of overpotential ($E - E^0$) applied to the electrode surface.

The diffusion profile of microelectrode induces an improved mass transfer compared to that of macro-electrodes. The microelectrode diffusion profile brings much higher current density which renders a high signal to noise ratio. Furthermore, the limiting current can be

reached quickly. Due to small currents and the fact that the ohmic drop is limited to a small area close to the electrode, microelectrodes can be used in high resistive media without loss of sensitivity. In addition, since the sensing is done within the diffusion layer, this induces low dependence on hydrodynamic conditions. Thus, microelectrodes can be used for flow-dependent detection, the smaller microelectrode diameters the better. As for cell secretion, then there is a requirement that the cell should be as close as possible to the electrode, otherwise, due to diffusion, the secreted chemical may diluted too much beyond detection limit or diffused away.

2.4 Electrode noises

2.4.1 Thermal noise

There is an intrinsic noise associated with the electrode-electrolyte interface, as with most circuit elements, regardless of any applied voltage, since this noise is due to the random thermal motion of the charge carriers (the electrons) in any conductors. At small signal level, the noise is more significant and we have to treat noise carefully to attain proper signal to noise ratio to extract useful signal. This noise has been known as Johnson thermal noise.

$$S_{v,rms} = \sqrt{4kTRB} \quad (2.14)$$

Since the current is what we actually sensing, the current noise can be written as (2.15) when (2.14) is divided by R:

$$S_{I,rms} = \sqrt{\frac{4kTB}{R}} \quad (2.15)$$

$$S_{I,th}^2 = \frac{4kTB}{R} \quad (2.16)$$

where k is Boltzman's constant ($1.38 \times 10^{-23} \text{ J/K}$), T is the absolute temperature in Kelvin, R is the real part of the electrode impedance in ohms, and B is the signal bandwidth. The electrode impedance is measured in the bandwidth of interest. The obtained resistance is then used in equations (2.14) ~ (2.16) to estimate the thermal noise in root mean square of voltage, current or current variance. In our application, we care more about current than voltage, so we usually use current variance $S^2_{I,th}$ to estimate the overall noises. Although from the recording techniques and circuit configurations point of view, reduced electrode impedance is desirable whereas in low current sensing and amplification, a bigger resistance is desirable.

2.4.2 Shot noise

Shot noise is due to random fluctuations of the electric current in an electrical conductor, but shot noise is different from current fluctuations in equilibrium and are independent from any external applied voltage, it happens anywhere when a current is flowing. The main reason is due to the fact that the current is carried by discrete charges (electrons). Shot noise here we usually refer to the current noise due to input bias current and can be expressed by equation (2.17).

$$S^2_{I,shot} = 2I_b e B \quad (2.17)$$

For an amplifier, I_b is the bias current, e is the electron charge in Coulomb, and B is the bandwidth.

2.4.3 $e_n c_t$ noise

The $e_n c_t$ noise is due to the voltage together with the capacitance loading, namely the charging effect at the amplifier input and it can be calculated by

$$S^2_{I,encr} = \int_0^B (2pfC_t)^2 e_n^2 df \quad (2.18)$$

The above three kinds of noise is the main source of noises, there are also other sources of noises, namely dielectric noise, excess noise, etc.

2.4.4 Interconnect and parasitics

Microelectrodes created by thin film deposition technology have the basic “sandwich structure”. While there is no significant problem when the substrate is an insulator (glass or plastic), in cases where the substrate is conductive (here in our case is silicon), there usually is an insulation layer between the electrodes and the substrate. Then a capacitive parasitic path (Cs) exists between the metal conductors (electrodes, interconnects and bond-pads) and the substrate. This capacitance can result in cross-talk between adjacent elements if the substrate is not grounded or a reduction in signal if the substrate is held at ground. These parasitic capacitances are determined by the geometrical area of the metal as well as the dielectric thickness. They may be calculated using the standard parallel plate model for a capacitor, but this underestimates the capacitance due to fringing fields due to the small scale. More complicated calculation other than the parallel plate has been proposed to account for the effects. In low frequency and low current applications, the parasitic capacitance may not be that significant, especially when the electrode spacing is much larger than the wire width.

Other parasitic capacitances associated with the packaging of the device and the electronics circuit configuration such as interconnect and layout plays a role too. Interconnect

resistance and bond-wire inductance may be neglected in the total microelectrode model since their effects are negligible compared to the other components.

2.5 Electrode Materials and fabrication

Metals especially noble metals are commonly used as electrode. The electrodes have different shapes and configuration such as wire, disks, rings, pellet, cylinders, etc.

2.5.1 Metal electrodes and deposition

The most commonly used thin film deposition processes are by evaporation and sputtering. They all belong to physical vapor deposition (PVD) method since usually the process does not involve chemical reactions. This is compared to chemical vapor deposition (CVD) process, though there could be reactive evaporation and reactive sputtering processes which are combined process of both CVD and PVD.

There are two kinds of evaporation, thermal evaporation and E-beam evaporation. In thermal evaporation, electric resistance heater is used to melt the material and raise its vapor pressure so that the material is evaporated to a useful range for deposition. A high vacuum is needed for evaporation, the vaporized material should not react with any gases before reaching the substrate. High vacuum also reduce the incorporation of impurities from the residual gas in the vacuum chamber. The heating element should have a much lower vapor pressure than the material to be deposited for a contamination free film. Tungsten is commonly used as the heating element. The E-beam evaporator uses a high-energy electron beam from an electron gun to heat the material to be evaporated in a crucible for better control of the process.

Sputtering is another physical process whereby atoms in a solid target material are ejected into the gas phase due to bombardment of the material by energetic ions from plasma. The target is at a much lower temperature than evaporation, due to heat generated from the bombardment, usually cooling is needed for the target to keep cooled. Sputtering is one of the most flexible deposition techniques. Not only commonly used in semiconductor industry for metal deposition, it is especially useful for compounds or mixtures/alloys, where different components would otherwise tend to evaporate at different rates.

Sputtering effect is largely driven by energetic ion collision with the target atoms. The momentum exchange between the ions and atoms in the material vaporizes the target material into atoms. The process is similar to the billiard, where the energetic ion (cue ball) striking a large cluster of close-packed atoms (billiard balls). The number of atoms ejected from the surface per incident ion is called the sputter yield and is an important measure of the efficiency of the sputtering process. Other things the sputter yield depends on are the energy of the incident ions, the masses of the ions and target atoms, and the binding energy of atoms in the solid.

One important advantage of sputtering as a deposition technique is that the deposited films have the same composition as the source material, thus makes sputtering a very versatile thin film deposition method. It can virtually deposit any kinds of materials. Sputter deposition rate is comparable with evaporation. In production equipment, the deposition rate may be much higher than other methods when a huge power is used. According to

Angstrom Science Inc. the sputtering target have certain power density limit per unit area according to different cooling mechanism. When the target area is large enough, a huge power in tens of kilowatts can be used to gain a very fast deposition rate. The higher rate of deposition results in lower impurity incorporation because fewer impurities are able to reach the surface of the substrate in the same amount of time. Sputtering methods are consequently able to use process gases with far higher impurity concentrations than the vacuum pressure that MBE methods can tolerate. During sputter deposition, the substrate may be bombarded by energetic ions and neutral atoms. Ions can be deflected with a substrate bias and neutral bombardment can be minimized by off-axis sputtering, but only at the cost of deposition rate. Plastic substrates cannot tolerate the bombardment and are usually coated via evaporation.

Types of sputter deposition

Modern Sputter guns are usually magnetrons that incorporate a strong magnetic fields to concentrate the ions around the target such that higher density plasma and higher deposition rate can be achieved. The sputter gas is inert, typically argon. The sputtering process can be disrupted by other electric or magnetic fields in the vicinity of the target. Charge build-up on insulating targets can be avoided with the use of RF sputtering where the sign of the anode-cathode bias is varied at a high rate. RF sputtering works well to produce highly insulating oxide films but only with the added expense of RF power supplies and impedance matching networks.

2.5.2 Carbon based electrodes

Carbon electrodes are widely used in electrochemistry due to their low cost, wide working window, stable and low background current. Stable and low background current is extremely important in the small signal electrophysiology measurements since the signal is very small in this case. As carbon fiber has been considered a “gold standard” for measuring quantal exocytosis, it is not practical to use it at a chip level since the carbon fiber is not compatible to any microfabrication process thus making the integration to chip level almost impossible.

Carbon-based electrode material preparation

The microelectrode material for electrochemical detection requires high speed, high sensitivity, and microfabrication compatibility. While carbon fiber microelectrodes are considered as the “gold standard”, the doped diamond films show great potential as superior electrode materials in the field of electroanalysis and electrophysiology. But diamond film is difficult to fabricate at microelectrode level. This issue can be addressed by two approaches: 1) Immobilize doped diamond nanoparticles to modify the surface properties of electrode materials. For example, the immobilization of fullerenes, diamond nanoparticles, carbon nanotubes, and graphite nanoparticles on various substrates may provide us the desirable properties. 2) Deposit nitrogen doped DLC (Diamond-like carbon) film by PECVD or sputtering to get conductive carbon-based film with similar properties of carbon fiber. We have started investigation on approach 1); but in this dissertation, we focus on approach 2).

2.5.3 Diamond-like carbon electrode

I. Diamond-like carbon film deposition by PECVD

Diamond-like carbon (DLC) films are hard, amorphous films with a significant fraction of sp^3 -hybridized carbon atoms and which could contain a significant amount of hydrogen.⁵³ Depending on the deposition conditions, these films can be fully graphitic with sp^2 bonding configuration or contain diamond like sp^3 configuration. DLC has been used for applications like wear and tribological protection layers on top layer of magnetic recording films due to its high hardness, low coefficient of friction and good chemical inertness^{54,55}. DLC can be prepared by ion beam deposition, ion-assisted sputtering from graphite or by laser ablation of graphite. DLC with significant amount of hydrogen are prepared by chemical vapor deposition (CVD). The hydrogen content is usually over 25% with deposition parameters of low total pressure, precursor molecules and plasma ionization.⁵⁶ In our DLC film fabrication, plasma activation is by radio frequency. Others can be microwave or Ar^+ ions. The higher the atomic hydrogen content favors diamond like structure formation and high ionization favors graphitic thin films.

Silicon and glass substrates were used for DLC film deposition. The deposition method is based on radio frequency PECVD (plasma-enhanced chemical vapor deposition). When the objective temperature is reached, the gases were flowed into the reactor. The acetylene gas as reactant decomposed on the surface of the substrate to form carbon coated layer. Table 1 summarizes the conditions used to obtain a conductive DLC thin film. Fig. 2.8 shows the Raman spectroscopic analysis of DLC. The two detached peaks around 1590 and 1320 cm^{-1} which can be respectively assigned to sp^2 bonded carbon (G line) and disordered carbon

(D-line) indicating an amorphous film. Although promising, due to the limitation of our current process, the resistivity is too high for practical use of low current sensing.

II. Diamond-like carbon film deposition by Sputtering

Sputtering is a common way of thin film deposition in the IC industry, especially for aluminum metal processes. Diamond Like carbon deposition by sputtering makes the process compatible with general microfabrication. Compare to PECVD, sputtering is a physical process or physical vapor deposition (PVD). For depositing DLC, we use a high purity graphite as the target material, the control is more straight forward and the quality of the film is better controlled. The graphite sputtering process of DLC for microelectrode has the advantage of low cost, robustness and reusability, optical transparency, good electrochemical properties such as large working potential window, low and stable background current and higher sensitivity. A disadvantage of sputtering deposition of DLC is the deposition speed, which is usually slower than PECVD. For example, in one sputtering system with a 3 inch target and 8 inch substrate holder, at a DC power rate of 300 Watts applied to the graphite target or with a power density of 6.6 W/cm^2 , the deposition rate is about 1.2 nm/min.

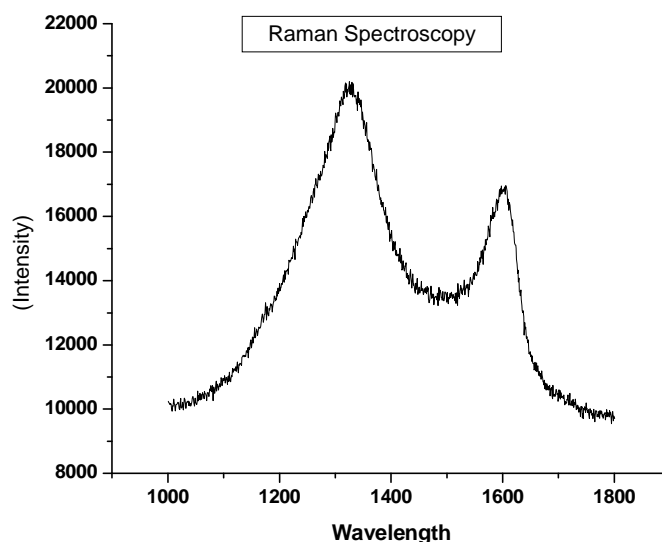


Fig. 2.8 Raman spectroscopic analysis of DLC.

Table 2.1. PECVD (plasma-enhanced chemical vapor deposition) conditions for the preparation of DLC thin films.

Process parameters	Conditions
rf power	10W
Base pressure	9×10^{-6} torr
Working pressure	0.2 torr
Argon flow rate	5 sccm
Nitrogen flow rate	20 sccm
Acetylene flow rate	5 sccm
Substrate temperature	400°C
Deposition time	1 hour

The diamond like carbon film is deposited in a magnetron sputtering system ATC2000 from AJA International Inc, North Scituate, MA 02060 USA. A graphite sputter target (from Williams Advanced Materials Inc, Buffalo NY, USA.) with 99.99% purity, three inch diameter and a thickness of 1/8" is used for DLC deposition. Microscope glass slides size of 1 inch by 3 inch with a thickness of 0.9 mm were purchased from Fisher Scientific Inc, Silicon wafers were obtained from MEMC (St. Charles, MO USA). All substrates were organically cleaned by soaking in acetone for about 5 minutes then rinse with methanol, isopropanol and DI water in sequence and then blow dried. Prior to film deposition, the

substrates were also sputter cleaned by biasing the substrate holder for about 1-2 minutes at a pressure of 4 mTorr and power of RF power of 40 Watts. The chamber base pressure was about 5×10^{-7} Torr. The gas flows were controlled by two mass flow controllers (MFC), 10 sccm Ar and 10 sccm N₂ were fed into the chamber and a deposition pressure of 2 mTorr were maintained for the DLC deposition. The deposition time lasted for 2 hours at the power of 300 Watts for the single layer of DLC film deposition with a result thickness around 200 nm. For the two-layer film deposition to increase the conductivity, an ITO layer was deposited first, the ITO target (In₂O₃/SnO₂, SnO₂ is 10% by weight, 3" diameter with 1/8" thickness, purity is 99.99%, from Williams Advanced Materials Inc.) were used. The two-layer sputtering is sequential without breaking vacuum in-between since the sputtering system is a multi-target source with independent power supplies. RF sputtering was used for ITO deposition at a radio frequency (RF) of 13.56 MHz and power was set at 180Watts. The 20 sccm argon gas flow was controlled by computer through MFC and maintained at a working pressure of 4 mTorr for the deposition of ITO. The deposition temperature was set to be 50 °C and the deposition time was 20 minutes. The ITO film as deposited is about 100 nm in thickness. The second DLC layer was deposited at the similar condition as the single layer DLC film mentioned above but at a temperature of 50 °C and a film thickness of 100 nm. In both cases, the final film thickness is 200 nm. The thickness of the films was measured by a profiler (Alpha step 200, Tencor, San Jose, CA USA).

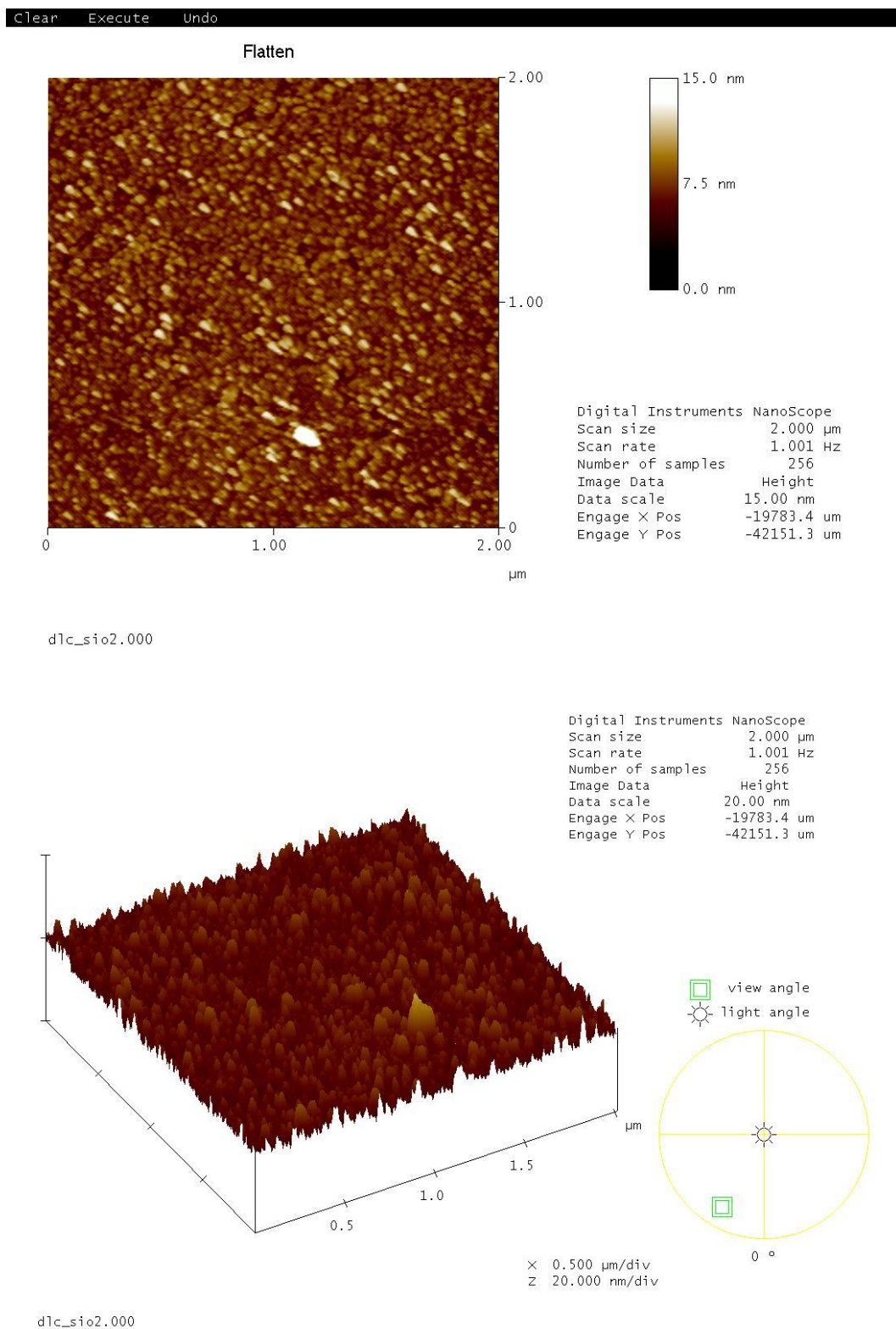


Fig. 2.9 AFM image of DLC deposited on glass substrate, grain size of 5 nm, surface roughness of 1.5 nm, very smooth surface and grain size of the film.

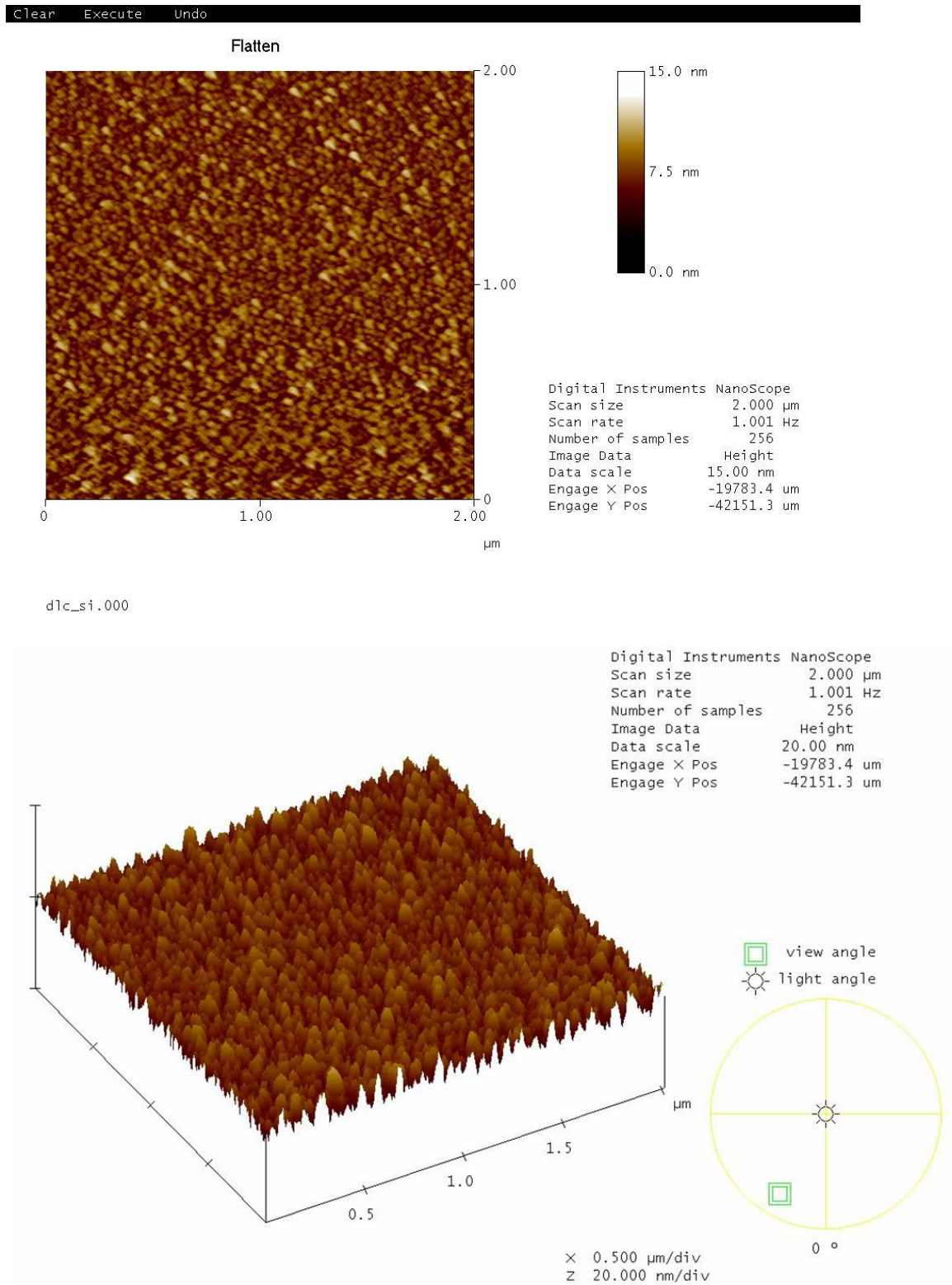


Fig. 2.10 DLC deposited on silicon substrate, grain size average 5 nm, Surface roughness: 1.4 nm

2.5.4 Properties of sputtered DLC film

Surface properties by AFM. Atomic force microscopy (Dimension 3100 Atomic Force Microscope, Veeco Metrology, Inc. Santa Barbara, CA, USA) was performed to analyze the surface properties of the deposited DLC films. Fig.2.9 shows the results of the AFM image. The as-deposited DLC film on glass has an average grain size of 5 nm and surface roughness of 1.5 nm from the analysis of the AFM data. The DLC film deposited on silicon wafer is slightly better with the same average grain size of 5 nm and surface roughness of 1.4 nm as shown in Fig. 2.10. This excellent surface smoothness close to atomic scale explains the mirror-like shiny surface of the deposited DLC film and partial reason for the low specific capacitance of the electrodes.

Raman spectroscopy of the DLC film. Raman spectroscopy is widely used for studying carbon materials. A Raman spectroscopic scan is obtained from a Renishaw double grating spectrometer (RM1000 series, Gloucestershire, UK) and the spectrum is shown in Fig. 2.11. The structure properties can usually be derived from the characteristics of the D peak (1355 cm^{-1}) and the G peak (1550 cm^{-1}). The broadened D peak and G peak indicate that the DC magnetron sputtered DLC film appears to be highly disordered⁶⁴. The increase in the conductivity of the nitrogen doped film has been reported due to reasons like a downward shift of the Fermi level or the widening of the conduction band, and the density of states increase at Fermi level and in the band tails^{57,58}. Although post-annealing can further increase the conductivity, we do not need this process in our case since the highly conductive ITO layer has increased the conductivity by about a thousand times which is good enough in electrochemical detection.

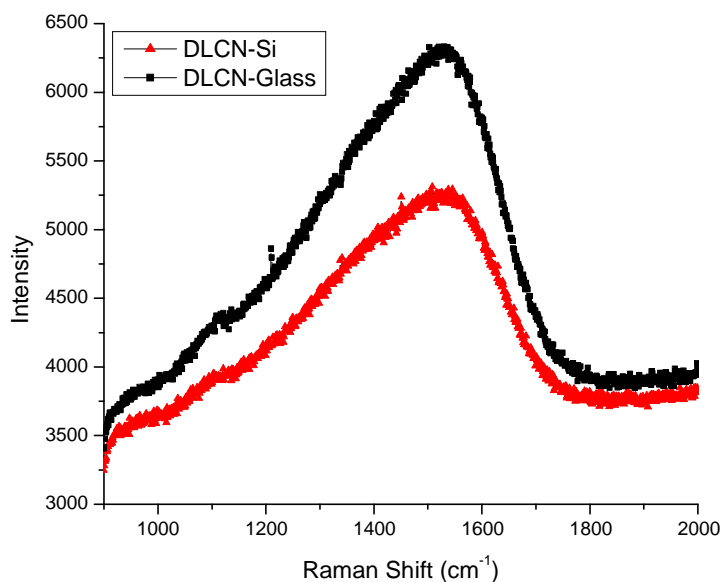


Fig. 2.11 Raman spectroscopic scan of the DLC films on silicon and glass substrates, the broadened G, D peaks indicates that the highly disordered DLC film.

2.6 Diamond like carbon (DLC) microelectrode and its application for low noise exocytosis measurement in microdevices

Although carbon-fiber electrodes (CFE) have been widely used and often being considered as the “gold standard” for measuring quantal exocytosis, it is almost impossible to integrate CFE onto a microchip with a microfabrication compatible process. The recent drive of electrophysiology lab-on-a-chip makes it desirable to integrate carbon based microelectrodes into microchip devices to increase sensitivity and performance. In order to find a process which is compatible with microfabrication and yet can provide microelectrodes with comparable performance of CFE, we probably are the first to develop the sputtering DLC process and prototype micro device for low noise exocytosis measurement. In this section, we report the development of nitrogen doped diamond-like carbon (DLC) microelectrodes on a chip to monitor quantal catecholamines release from

cells during the process called exocytosis. The DLC microelectrodes were prepared by a microfabrication compatible magnetron sputtering process with nitrogen doping. The 30 μm by 40 μm DLC microelectrodes were patterned onto normal microscope glass slides by photolithography and lift-off technology. The properties of the DLC microelectrodes were characterized by AFM, Raman spectroscopy and cyclic voltammetry. Actual cell secretion was recorded from bovine adrenal chromaffin cells on the DLC microelectrodes. A small reservoir was created by a hole into a piece of poly-(dimethylsiloxane) (PDMS) and then put onto the glass substrate by reversible bonding. Bovine adrenal chromaffin cells were loaded into the reservoir and allowed to settle down onto the DLC electrodes on the bottom. “High-K” solution with 100 mM K^+ was used to stimulate cell secretion. Current spikes due to oxidation of catecholamines released from the cells onto the DLC microelectrode were recorded using amperometry at a potential of 700 mV. Amperometric spikes due to quantal release of catecholamines range from 20 to 200 pA were recorded with a stable background current around 180 pA and noise level of less than 1 pA which are comparable or better than that of carbon-fiber electrodes. Further comparison with platinum microelectrodes is also presented. In addition, the DLC microelectrodes have very smooth surface and are transparent. They are batch producible at low cost and can realize high-throughput on-chip measurement of quantal exocytosis with parallel simultaneous recording with the proposed on-chip method.

The commonly used noble metals such as gold and platinum material themselves are not ideal electrochemical material due to a large background current near the formal potential for catecholamines¹. Other efforts of integrating carbon material with microchip devices like carbon paste^{59,60,61}, screen-printed carbon^{62,63} as electrodes are not compatible with

standard batch processing capable processes either. Diamond-like carbon (DLC) electrodes have the greatest potential to solve this problem.

Although many methods including all sputtering techniques have been reported for the deposition of DLC films, very limited efforts on electroanalytical applications of DLC films has been reported⁶⁴. Only recently, people began to explore these applications. For example, cyclic voltammetry studies have demonstrated good electrochemical properties of sputtered DLC films by Zeng. et. al⁶⁴. Undoped DLC films prepared by sputtering are not highly conductive because of the presence of diamond like sp^3 hybridized states. It is important to have low resistivity for electrochemistry applications because high series resistance leads to a loss of control of the working electrode surface potential as a potential drop. The potential drop can be significant if the series resistance R_s is very large. We proposed two ways to reduce the series resistance. One way is to use nitrogen doping in-situ during the deposition process. The other is to deposit a highly conductive bottom layer such as the commonly used adhesion layer Chromium or ITO (Indium Tin Oxide, commonly used as transparent electrode). ITO is preferred because it can maintain the transparency property since inverted microscopes are more common than upright microscopes in cell studies where light go through the substrate from the bottom. Annealing can further reduce the resistivity of the DLC film but on glass substrate due to high temperature stress, the film adhesion can be peeled off after annealing. Silicon substrate can sustain high temperature annealing and keep good adhesion of the DLC film but silicon substrate is opaque and again loses the transparency property.

The DLC microelectrodes we developed have many of the desirable properties especially for cell electrophysiology studies. First, they can be fabricated by the common sputtering process which is microfabrication compatible and can sustain many other microfabrication processes such as photolithography. Second, they exhibit excellent shiny, mirror like surface smoothness close to atomic level, which would provide lower capacitance charging current; Lower double layer capacitance is ideal for electrochemical detection. Third, they are much cheaper than the CFE electrodes and the other noble metal electrodes. Finally and most importantly, they have excellent electrochemical properties such as large working window, low noise level, small double layer capacitance and low, stable background current and higher sensitivity. In addition, the DLC electrodes are transparent and can be deposited onto normal glass slides; this is a desirable property as it enables the capability to view the cells through the glass substrate from an inverted microscope at the same time of electrochemical measurement. The above mentioned properties of the developed DLC microelectrodes are especially ideal for monitoring cell exocytosis on-chip.

2.6.1 Device design and fabrication

The device design, mask layouts and the final device are shown in Fig. 2.9(a)-(d). Eight microelectrodes are designed on a 1 inch by 3 inch glass substrate. For each electrode there are two contact pads at each side of the glass slide, i.e. the electrodes are a complete trace from one side to the other. Only 4 mm of center portion of the wire trace is set at the width of 40 μm , the other portions are wider to reduce the overall resistance of the electrode. The microelectrode will be defined by a second mask with a center line with width of 30 μm so that microelectrodes of 30 μm by 40 μm are defined. The paired contact pads with a complete trace run through the substrate will simplify the fabrication process and alignment

requirement. This design only requires a minimum alignment can even be done without a mask aligner.

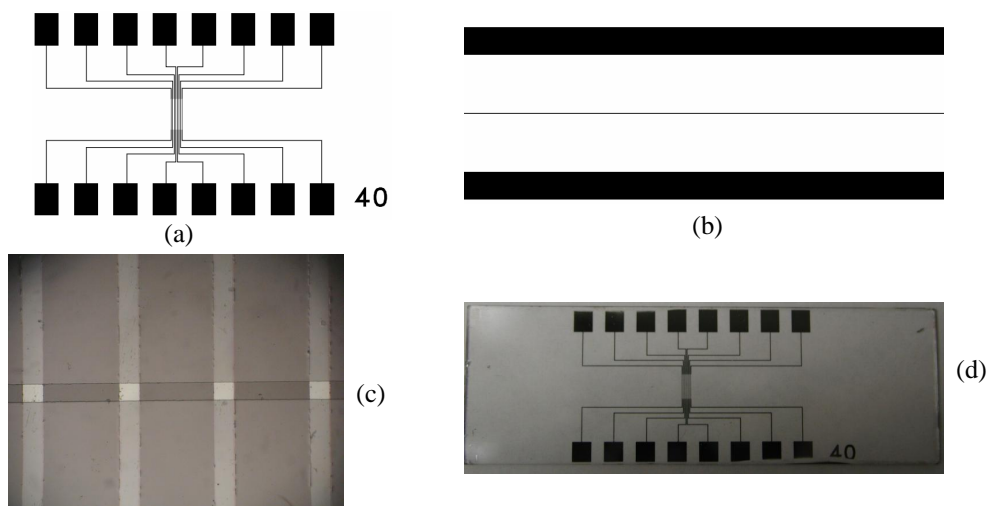


Fig. 2.12 The design of the chip device for cell exocytosis measurement using DLC microelectrodes. (a) First mask layout for the lift-off process to pattern the electrodes traces and contact pads, (b) Second mask for exposing the contacts pads and $30\ \mu\text{m}$ wide microelectrodes while the other portion is covered by photoresist, (c) The fabricated DLC microelectrodes, vertical traces are the $40\ \mu\text{m}$ DLC wires, the horizontal trace is an empty line where photoresist is removed, the white rectangular shapes are the exposed microelectrodes of size $30\ \mu\text{m}$ by $40\ \mu\text{m}$. (d) The overall picture of a chip device made on a 1 inch by 3 inch glass slide.

For the lift-off process, positive photoresist Shipley S1813 was spin-coated onto the glass slides at 2000 rpm first, and then the model 200IR contact aligner from OAI (San Jose, CA, USA) was used to do the UV exposure using the first transparency mask. After development, the substrates were rinsed under DI water and blow dry. Then the substrates were loaded into the Sputtering chamber for the two-layer film deposition as mentioned in the previous section, ITO layer first, followed by DLC layer. The as-deposited substrate then was soaked into acetone for lift-off. After about half an hour, gentle sonication may be needed to help the lift-off process and clean up some small debris. Another layer of photoresist is spun onto the substrates and patterned by the second mask following the same procedure, after development and rinse dry, the substrates are ready to use. Now most

of the substrates are covered and insulated by the photoresist layer, only the contact pads and the center microelectrodes are exposed for electrical connection and sensing.

2.6.2 Experimental setup

The setup for measuring cell exocytosis is shown schematically in Fig. 2.10 A small reservoir was created by cutting a hole of 2 mm by 4 mm into a piece of PDMS and then put onto the glass substrate by reversible bonding. A copper clip with a short wire was used to connect the contact pads on the chip to the head stage of the EPC-9 patch-clamp amplifier (HEKA, Lambrecht, Germany) and HEKA Pulse software was used for the amplifier control and data acquisition. A Ag/AgCl electrode were put into reservoir as the reference electrode, for amperometric recording, a +700 mV potential was added to the sensing microelectrode relative to the Ag/AgCl reference, and current from the sensing electrode is monitored and recorded by the computer. To minimize external electrical noise, the chip and the head stage were put into a Faraday cage.

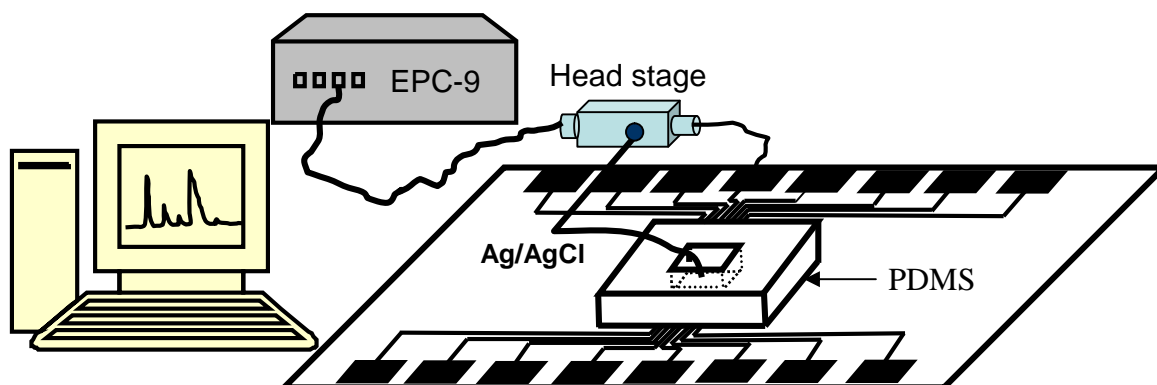


Fig. 2.13 The experimental setup for exocytosis measurement using EPC-9 patch-clamp amplifier and HEKA pulse software.

Chromaffin cell preparation. Chromaffin cells were harvested from fresh bovine adrenal gland as described before⁶⁵. Harvested cells were put into polystyrene 25 cm² cell culture flasks of about 10⁶ cells in 5 mL of culture media (Dulbecco's modified Eagles medium supplemented with 10% (v/v) fetal bovine serum and 1% penicillin/streptomycin). Cells were kept in a 37 °C incubator in a humidified environment with 5% CO₂ and for a period of 1-4 days after preparation. Right before experiments, cells are removed from the culture flask by using a rigorous pipette washing using the original cell medium and put into a 10 mL plastic tube. After a gentle centrifuge for about 4 minutes, the cell medium was sucked out and the standard calcium bath solution (150 mM NaCl, 5 mM KCl, 5 mM CaCl₂, 2 mM MgCl₂, 10 mM glucose, and 10 mM HEPES titrated to pH 7.2 with NaOH.) was added for experiments. The "high-K⁺" solution used to stimulate exocytosis consisted of 100 mM KCl, other chemicals including 55 mM NaCl, 5 mM CaCl₂, 2 mM MgCl₂, 10 mM HEPES, and 10 mM glucose. All reagents were obtained from Sigma Aldrich, unless otherwise stated. The final cell concentration in the standard calcium bath solution is about 10⁶ cells/mL. A 10 μL of the cell suspension was then loaded the reservoir on the chip for experimentation. About 10-20 μL of the "high-K⁺" stimulation solution were added to the reservoir after the cells were allowed to settle down for about 5-10 minutes.

2.6.3 Electrochemical characteristics of the DLC microelectrodes

Cyclic voltammetry of the DLC film Cyclic voltammetry experiment is performed on the DLC electrodes. First, the working window is checked in 100 mM H₂SO₄ as shown in Fig. 2.14. It shows the potentials of hydrogen and oxygen evolution are -0.8 V and +1.5 V respectively. Next, one of our target analytes, 100 μM epinephrine in the standard calcium

bath solution were tested. This is the same buffer solution used for the chromaffin cells after they were extracted from the cell culture medium. Thus we can mimic the condition of the cell secretion environment. As we can see from Fig. 2.15, there is a very obvious oxidation peak at around 0.4 V, but, there is no reduction peak and the curve takes off at around 0.2 V which is the starting point of the oxidation process of epinephrine. These characteristics are similar to the previous report⁶⁶. Although cyclic voltammetry is an effective way to characterize the electrochemical properties of electrodes, we need to be careful, especially when dealing with microelectrodes. We found that for the same electrode material from the same batch of production, the cyclic voltammogram will be very different as seen from Fig. 2.16. There is a very obvious oxidation peak for the bigger DLC electrodes, but at a micro scale, the peak is hardly observable, though we can still see the curve takes off at the same oxidation start point of epinephrine at around 0.2 volts and with a sharp increase in current. The sharp increase in oxidation current indicates higher sensitivity. Since epinephrine does not show reversible properties, we also use potassium ferricyanide commonly used to further characterize the electrodes. We found the similar phenomenon even in the typically almost symmetrical cyclic voltammogram of the $K_3Fe(CN)_6$ for the micro level electrodes of DLC. The perfect is observed when the PH is around 3 as shown in Fig 2.17, the solution is 1 mM $K_3Fe(CN)_6$ in 0.1 M KCL.

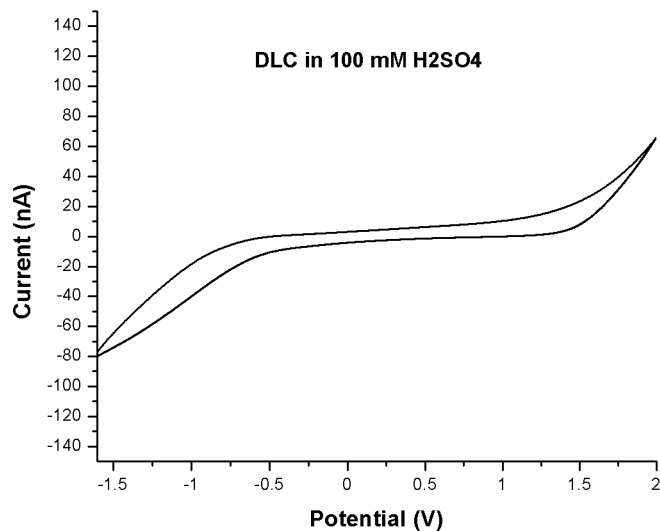


Fig. 2.14 Cyclic voltammogram of the DLC in 100 mM H₂SO₄ shows a large working window, electrode size is 30 μ m by 60 μ m.

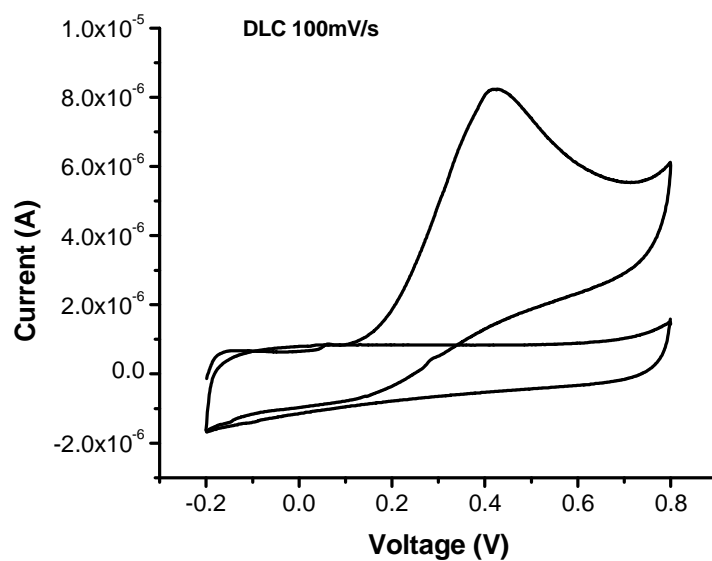


Fig. 2.15 Cyclic voltammogram of the DLC on ITO electrodes shows the oxidation activity of the epinephrine compared to the bath background, the solution used is 100 μ M epinephrine in the standard calcium bath solution as describe previously in the paper. Electrode size is defined by an o-ring of diameter of 1/8 inch or 0.3175 cm, scan rate 100 mV/s.

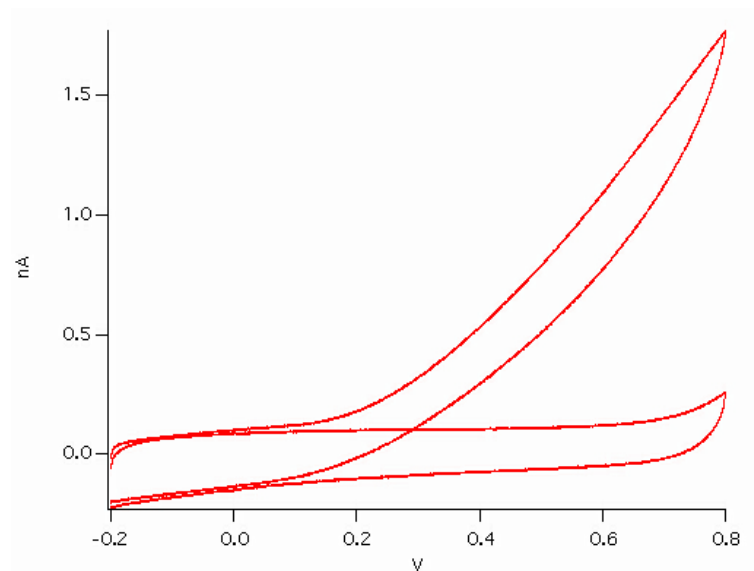


Fig. 2.16 Cyclic voltammogram of DLC microelectrode size of 30 μm by 40 μm , scan rate 100 mV/s, 100 μM epinephrine in bath solution as compared to the background of calcium bath solution.

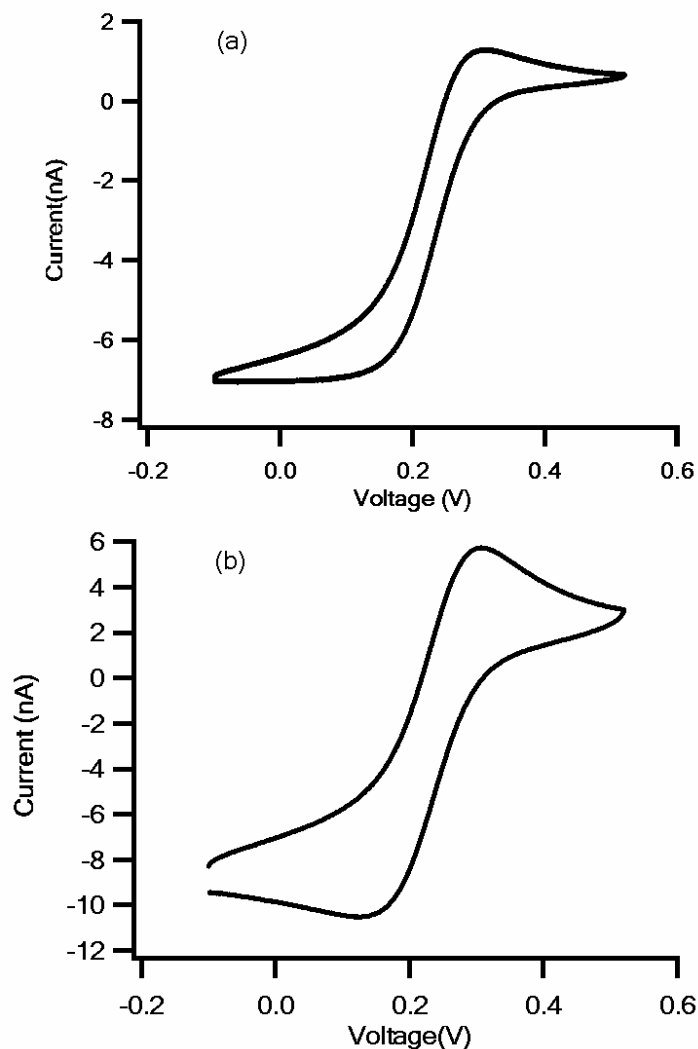


Fig. 2.17 Cyclic voltammograms of the DLC on ITO microelectrodes at the size of 30 μm by 40 μm , the solution is 1 mM $\text{K}_3\text{Fe}(\text{CN})_6$ in 0.1 M KCL at PH=3, scan rate (a) 100 mV/s and (b) 500 mV/s .

2.6.4 The specific capacitance of the DLC microelectrode

There are two methods to measure the specific capacitance of a microelectrode. One way is to find the capacitive current of the DLC electrode through the cyclic voltammetry at the transient point where the voltage scan changes its direction. Using the equation $I_c = CdV/dt$, where (dV/dt) is twice the scan rate and C is the electrode capacitance. Another method is

to use the lock-in amplifier in the EPC-9 patch-clamp amplifier by applying a sine wave excitation, and calculate the capacitance as proposed by Gillis et.al⁶⁷. The average capacitance measured from the EPC-9 lock-in amplifier is 126 pF and divided by the electrode area of 1200 μm^2 , we get the specific capacitance as 10.5 $\mu\text{F}/\text{cm}^2$. This value is lower than the reported values of that of a beveled carbon-fiber electrode encased in a glass pipette⁶⁸ and the ITO microelectrode developed previously at our lab (50 $\mu\text{F}/\text{cm}^2$).⁶⁶ It is also lower than that of the Pt electrode (25 $\mu\text{F}/\text{cm}^2$) deposited and patterned by the similar process in our lab. The lower capacitance and stable background current could be due to the presence of graphitic clusters embedded in the sp^3 matrix. This creates surfaces with electrochemically active sites separated by more insulating regions thus causing a reduction in the background current.

2.6.5 Amperometric detection of quantal exocytosis of catecholamines from cells

About 10 μL drop of solution with bovine adrenal chromaffin cells at a cell density of 10^6 cells/mL were pipetted into the cell reservoir on the chip. The cells were allowed to settle down to the bottom of the reservoir for about 5-10 minutes with a uniform distribution as shown in Fig.2.18. This photo was taken through an inverted microscope(Olympus, model IX51), cells on top of the electrodes seen through the electrodes. The surface of the DLC electrode are very cell friendly, the cells tend to stick to the electrode such that we do not need any cell adhesion promotion treatment material such as poly (l-Lysine) used by Sun et.al⁶⁶. This is a desirable property since it can provide the highest temporal and time resolution for the quantal release of catecholamine from the cells. As we can see that there are cells at almost each electrode. After cells settled down to the electrodes, exocytosis

events were stimulated by adding a high-K⁺ solution. Due to the potassium ion concentration difference across the cell membrane, the cell are depolarized which subsequently will open the voltage-gated Ca²⁺ channels on the cell membrane to allow considerable Ca²⁺ influx from the extracellular calcium bath solution and the rise of intracellular Ca²⁺ concentration will trigger exocytosis. The release of an individual vesicle causes a current spike as catecholamines are oxidized on the electrode surface. The amperometric data was acquired at a sampling frequency of 4 kHz with a low pass digital filter at a cut-off frequency of 1 kHz. To have good temporal time resolution, the cell should be close enough to the sensing electrodes, in our case, we can see cells are directly sitting on top the electrode and we can see the high time resolution from the fast rise times of the current spikes.

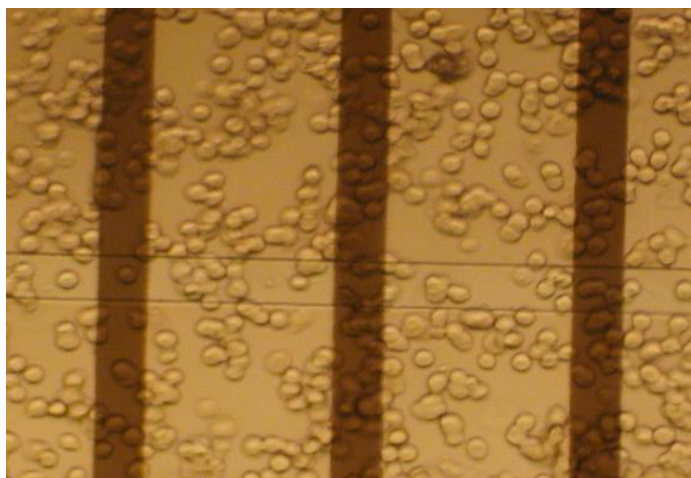


Fig. 2.18 The chromaffin cells settled down onto the DLC microelectrodes electrodes, the active sensing microelectrodes are at the cross section of the horizontal strip (photoresist free) and the vertical dark gray strip (DLC trace of 40 μm)

A typical recording is shown in Fig. 2.19. We can see from Fig. 2.19 that the background current offset is around 180 pA, (b) is a enlarged view of a small portion from (a) where

the current spike clearly indicate a foot signal before the sharp rise to the main pulse. This foot signal is unique for exocytosis and is generally believed due to the fusion pore opens before the large release of the vesicle content to the extracellular environment and is also called pre-spike foot. With the help of a spike data analysis programs by F. Segura et al.⁶⁹, we can measure spike parameters such as amplitude, rise time, charge etc. For example, the biggest spike during this recording is the 5th peak, with an amplitude of 133 pA, charge of 3.14 pC, FWHM (Full Width Half Maximum) width 9.97 ms, rise time 3.19 ms, The average rise time of the 66 current spikes from a continuous recording of 144 seconds was measured to be 2.87 ± 0.26 ms with a median value of 2.41 ms, and the average charge per spike is 1.20 ± 0.13 pC, which is comparable to the value of 1-2 pC from carbon fiber recordings^{70,71,72}. The mean width of the spikes was measured as 12.34 ± 1.29 ms with a median value of 8.22 ms from the software. From these values we can see that the cells are very close to the electrodes and we believe there is a very good cell adhesion to the electrode surface. In addition, the variation of the charge per vesicle is smaller than what was reported in a microchip device with gold electrodes previously done in our lab. The average spike amplitude is 34.10 ± 3.32 pA. Most of the spikes are from 20-150 pA, a common range from carbon fiber recordings. We did not observe many broadened current spikes which usually are from cells not close by and usually lower in amplitude. For a better view of the current spike data, we also plot the distribution of different parameters of the spikes pulses in Fig. 2.20. From top to bottom in Fig. 2.20 shows the time to peak t_p or rise time of the spikes; then charge of the spikes by integration of the spike pulse and time it covered; half time t_h or the FWHM (Full Width Half Maximum) width of the spikes.

Amplitude histogram is the distribution of the spike amplitudes. We can see that the distribution of the parameters is not normal distribution, but they follow similar trends.

In summary, the statistics of the current spikes from our DLC electrodes are similar to that reported from experiments using carbon fiber microelectrodes. As explained previously, the noise of our measurements is also comparable or better than that of carbon-fiber microelectrodes although a more systematic study may be necessary.

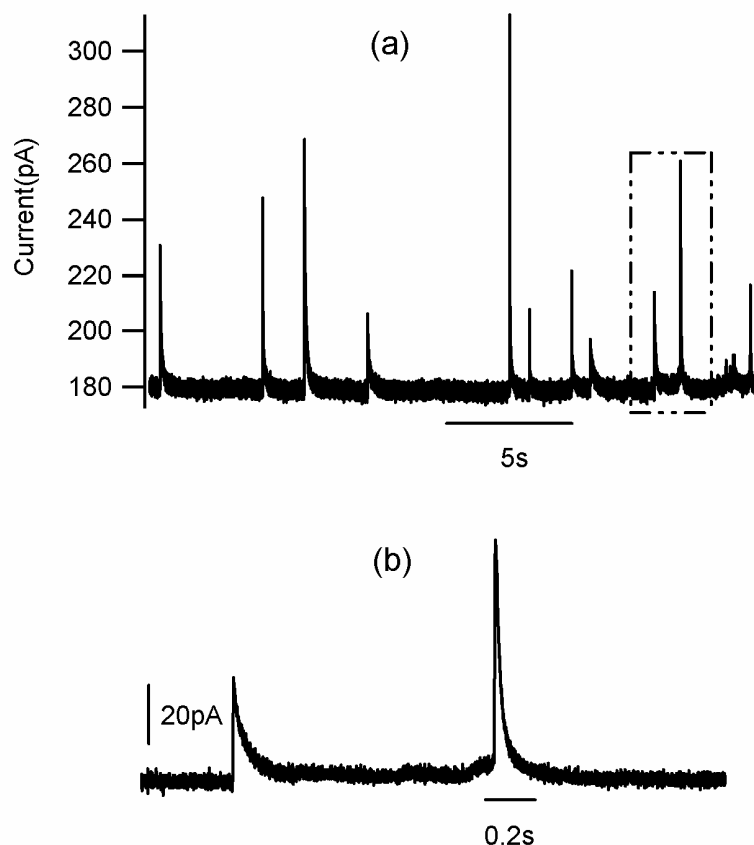


Fig. 2.19 One example of current spikes recorded from the DLC on ITO electrodes. (a) An example of a recording of 24 seconds, (b) An enlarged view of one portion of (a). Each current spike indicates a single vesicle release from a single cell due to the oxidation of the catecholamines from the vesicles oxidized on the DLC electrodes.

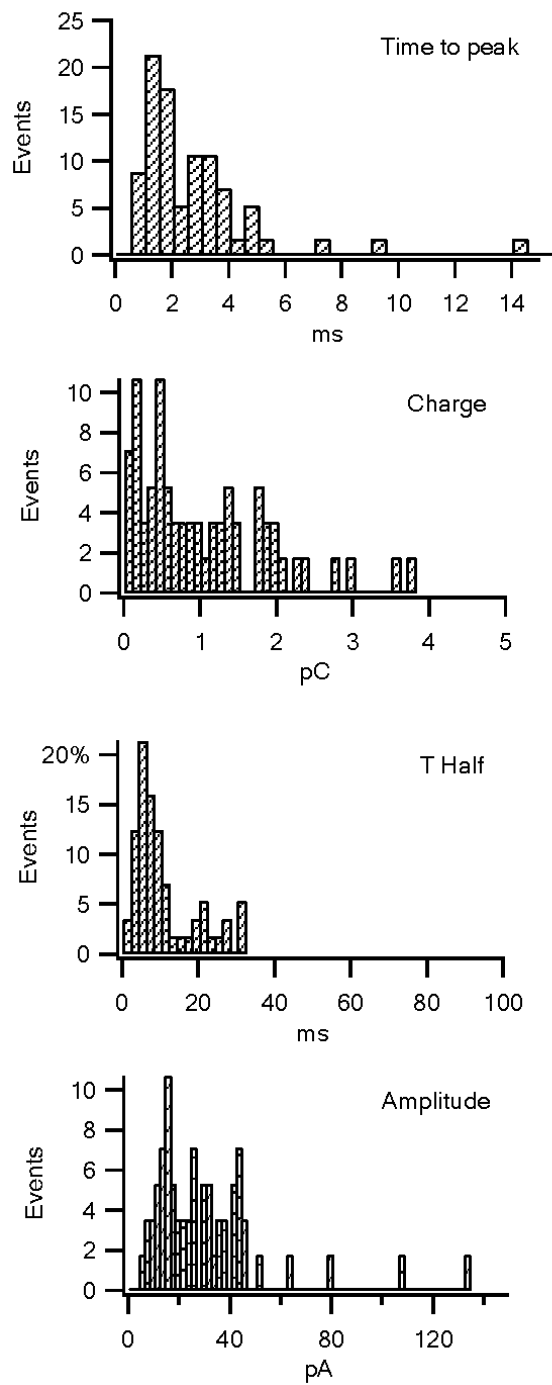


Fig. 2.20 Histogram data analysis of the current spikes parameters of exocytosis measurement, from top to bottom, the time to peak or rise time of the spikes; charge of the spikes; T half time or the FWHM (Full Width Half Maximum) width of the spikes; Amplitude histogram is the distribution of the spike amplitudes.

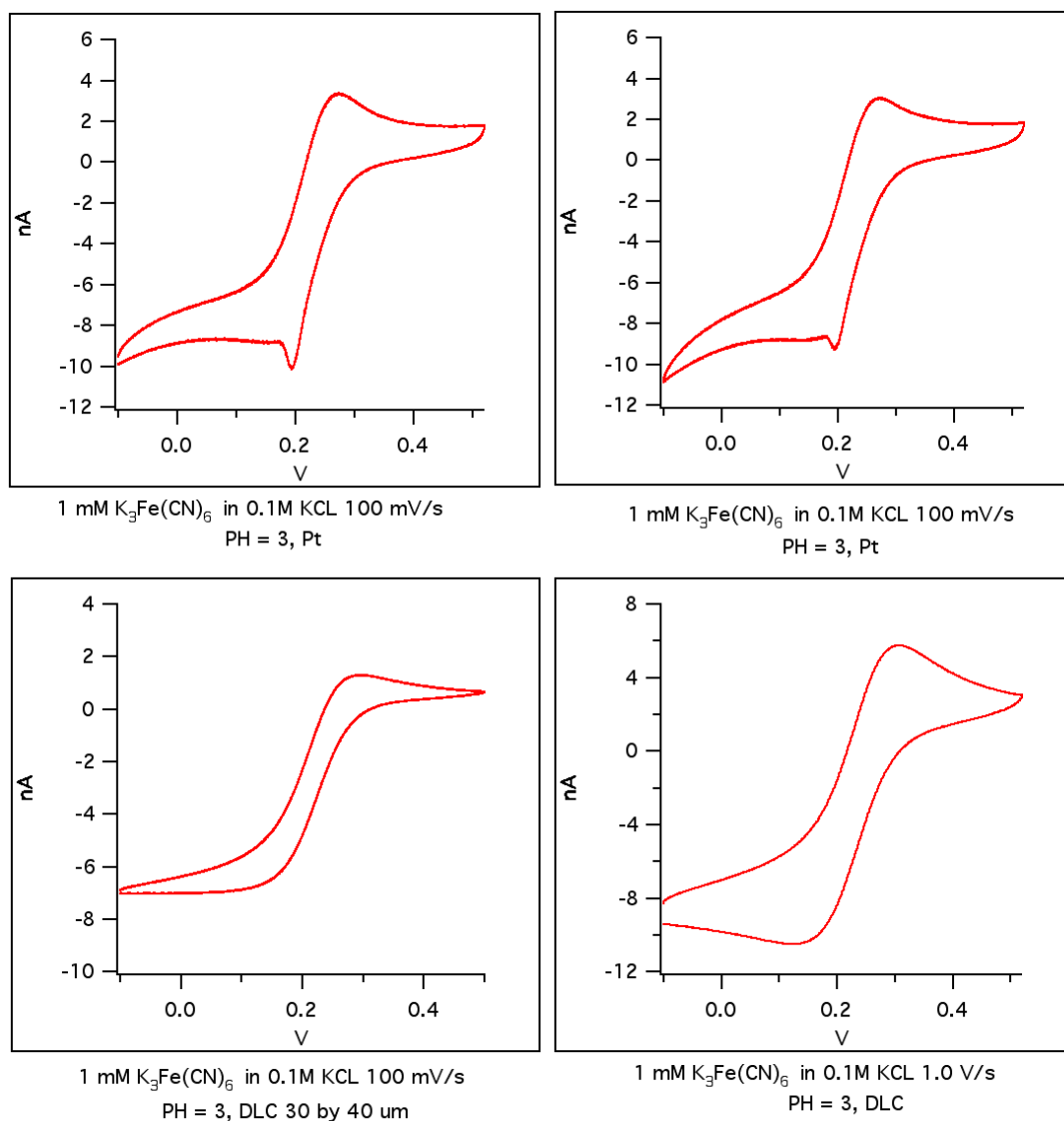


Fig. 2.21 Cyclic voltammograms of the DLC on ITO and platinum microelectrodes at the size of 30 μm by 40 μm , the solution is 1 mM $K_3Fe(CN)_6$ in 0.1 M KCL.

2.6.6 Comparison with the Pt microelectrodes

In order to compare the properties of the DLC electrodes, we fabricated platinum microelectrodes using the same design and same size for a fair comparison. The platinum microelectrodes were prepared using the same sputtering system and lift-off process on the same kind of glass slides. First from the cyclic voltammogram of both DLC and Pt electrodes as shown in Fig.2.21, we can see that the peak current of Pt is bigger than that of

the DLC. The ΔE_p of Pt is about 70 mV which is smaller than the 120 mV for DLC. But the peak current ratio i_{pa}/i_{pc} of DLC is very close to 1 while Pt shows a little shift. The reasons for these observations probably are due to faster electron transfer kinetics in platinum. There is fewer electron transfer sites on DLC electrodes surface as the sp^2 matrix is embedded into those sp^3 inert sites.

We also used the Pt microelectrode for quantal exocytosis measurement. We found a higher average current spike of 175.4 ± 12.5 pA for the Pt electrodes from the 130 spikes for a continuous recording of 124 seconds, compared to 34.10 ± 3.32 pA of the DLC electrode in the previous experiments. In the mean time we found a longer rise time of 10.07 ± 1.99 ms for Pt microelectrodes compared to that of DLC as 2.87 ± 0.26 ms. While in a sense that electrode material should not change biological phenomenon, there must be certain reasons for the observed discrepancies. The average amplitude of the spikes and charge are related to the amount and size of the vesicles of the cells. Although the amplitude of current spike may vary due to different reasons such as vesicle size distribution and cell to cell differences, we suspect that the higher amplitude could be due to possible reasons like faster electron transfer kinetics in Pt electrodes, catalytic effects of Pt material, local PH value change around the working electrode surface. A deeper study on materials may be needed to dig this out. The longer rise time on the other hand may indicate that the cells are further away from the cells as this has been observed that cells hardly sticks to Pt electrodes. In contrast, DLC is more biocompatible and cells like the surface and tend to stick to it. However, the Pt electrodes have larger background current and bigger noise level than that of DLC. We choose a mostly flat portion where there are

no spikes from a number of recordings from the Pt microelectrodes for our comparison after the electrode stabilized in the cell solution. The initial background current for the Pt electrode can be as high as 1500 pA and gradually drops to a lower value; but even recording after about 15 minutes, the background current is still as high as 431 pA. As shown in table 2, for the same size of the electrodes, the noise of the Pt is 9 pA which is almost nine times bigger than DLC. The noise range (maximum-minimum) is 58.4 pA for Pt and only 7.19 pA for DLC. The specific capacitance of Pt is larger than DLC too. We have designed eight electrodes capable of parallel amperometric recording if we use eight amplifiers and eight A/D channels. It is also possible to record exocytosis events sequentially one electrodes after another, as we observed that the recording can last as long as one hour after adding the stimulation solution.

Single cell isolation and single cell recording. Our current prototype design cannot guarantee single cell isolation on the electrodes to realize the strict definition of single cell recording due to larger electrodes size than a single cell and the planar design of the electrodes. But, by a minor modification in design, it is very possible that we could realize single cell isolation of single cell trapping. First, we can reduce the sensing electrodes to be the size close to a single cell, such as 15 μm by 15 μm . To create 3-D trap, the second improvement is to use thick photoresist up to 15 μm such that we can create 15 μm cube well. With a microfluidic channel on top of those single deep traps, cells can flow slowly over them, and cells may fall into this size close to single cell traps to realize single cell trapping and single cell analysis. The similar idea for cell docking by microwell was demonstrated by Khademhosseini A et. al.⁷³

2.6.7 Background current and noise analysis

The background current measured from our DLC microelectrodes is around 180 pA as can be seen from Fig. 2.19. This background current is higher than the small carbon fiber microelectrodes (diameter usually around 10 μm) but we need to point out that the background current is usually proportional to the electrode surface area in the same solution, and our electrode surface area here is 1200 μm^2 , which is much larger than the mentioned carbon fiber microelectrodes. As can be seen from Fig. 2.19, the background current is very stable with a straight and flat baseline. We believe this stable background current is due to the good properties of the DLC electrodes. To analyze the background noise level, we choose a portion (250 ms duration, 1001 data points) from the recording where there are no spikes, and perform a statistical analysis as shown in table 2. The overall noise from the electrodes can be evaluated by the standard deviation of the data or $\sigma_I = 1.07$ pA. From the statistics, we can see that, for the DLC electrodes, the mean value and the median value are very close with the same digits up to the one thousandth level. In order to get an overall noise level of the recording system, we can calculate all three main noise sources, namely the Johnson thermal noise, shot noise, and $e_n C_t$ noise as discussed in section 2.4 of this chapter. Then the total noise can be added together in current variance is the sum of all the three:

$$S^2_{I,total} = S^2_{I,th} + S^2_{I,shot} + S^2_{I,enet} = \frac{4kTB}{R} + 2I_b eB + \int_0^B (2pfC_t)^2 e_n^2 df \quad (2.19)$$

If we put the following values into equation (2.19, $T = 300$, $B = 1000$ Hz, $R = 500$ M Ω , $I_b = 180$ pA, $C_t = 126$ pF, $e_n = 8$ nV / $\sqrt{\text{Hz}}$, we have,

$$S^2_{I,th} = 3.312e-26 \text{ (RMS 0.18 pA),}$$

$$S^2_{I,shot} = 6.4e-26 \text{ (RMS 0.25 pA),}$$

$S^2_{I,encr} = 1.34e-26$ (RMS 0.116pA), the total current noise in RMS value is the square root of the total current variance from equation (2.19), which is 0.332 pA. The recorded current noise is 1.07 pA. With better shielding, we believe the noise level could be further decreased.

2.6.8 Comparison with the Pt microelectrodes

In order to further study the properties of the DLC electrodes, we fabricated platinum microelectrodes using the same design and same size for further comparison. The platinum microelectrodes were made using the same sputtering system and lift-off process on the same kind of glass slides. First from the cyclic voltammogram of both DLC and Pt as shown in Fig. 2.21, we can see that the peak current of Pt is bigger than that of the DLC. The ΔE_p of Pt is about 70 mV which is smaller than the 120 mV for DLC. But the peak current ratio i_{pa}/i_{pc} of DLC is very close to 1 while Pt shows a little shift. The reasons for these observations probably are due to faster electron transfer kinetics in platinum. There is fewer electron transfer sites on DLC electrodes surface as the sp^2 matrix was embedded into those sp^3 inert sites. While potassium ferricyanide is usually considered as a reversible redox process in cyclic voltammetry, the shape of the curve will always have a small shift in practical experiments and also affected by the size of the electrodes and solution PH values. We have noticed that at PH around 7, the redox peak pair is hardly observable. The cyclic voltammogram could be very different at a microelectrode compare to a macro

electrode too, as shown in Fig. 2.15 and Fig. 2.16, there is a very obvious oxidation peak in macro DLC electrodes for the epinephrine in Fig. 2.15 but no peak showed up on the microelectrodes in Fig. 2.16.

We also used the Pt microelectrode for quantal exocytosis measurement. While we found a higher average current spike of 175.4 ± 12.5 pA for the Pt electrodes from the 130 spikes for a continuous recording of 124 seconds, we also found a longer rise time of 10.07 ± 1.99 ms for Pt microelectrodes. Although the amplitude of current spike may vary from cell to cell, this is a good indication that the higher amplitude could be due to the faster electron transfer kinetics in Pt electrodes. The longer rise time on the other hand may indicate that the cells are not so close to the electrodes as this has been observed that cells hardly sticks to Pt electrodes.

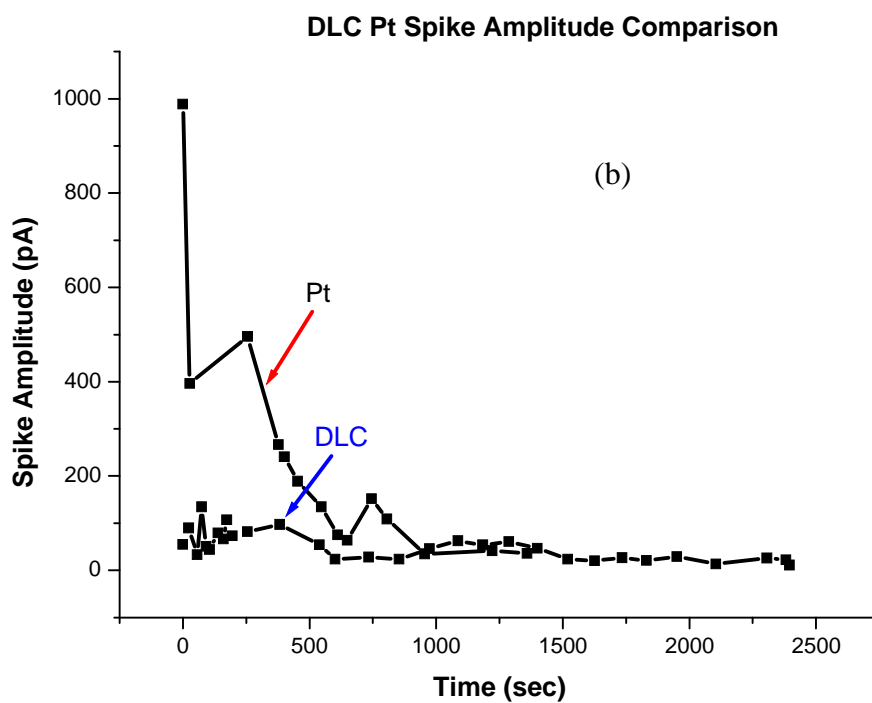
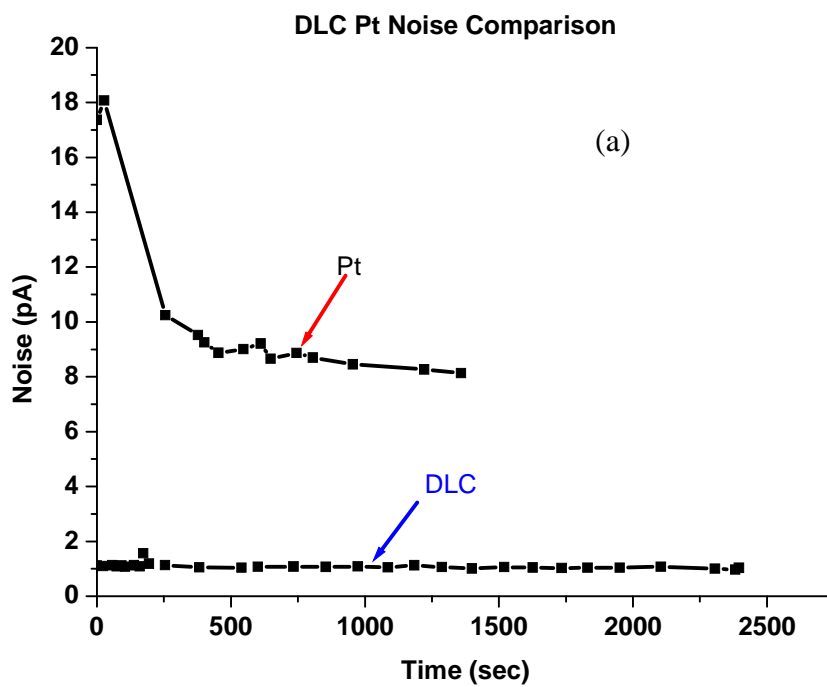
However the Pt electrodes have larger background current and bigger noise level than that of DLC. To calculate the noise level for comparison between DLC and Pt microelectrodes, we chose 1000 data points at a flat portion from a recording where there is no spike, but the other portion of that recording should contain at least one spike. All recordings have the same duration of 4 seconds. The initial background current for the Pt electrode can be as high as 1500 pA and gradually drops to a lower value, but even recording after about 15 minutes, the background current is still as high as 431 pA. As shown in table 2.2, for the same size of the electrodes, the noise of the Pt is 9 pA which is almost nine times bigger than DLC. The noise range (maximum-minimum) is 58.4 pA for Pt and only 7.19 pA for DLC. The specific capacitance of Pt is larger than DLC too. The lower capacitance and

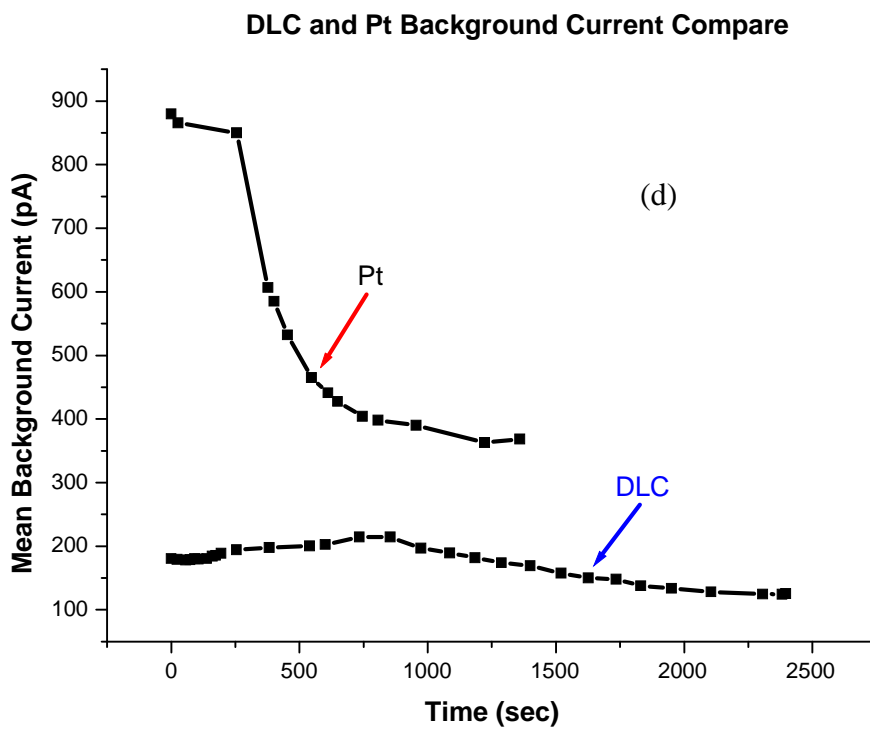
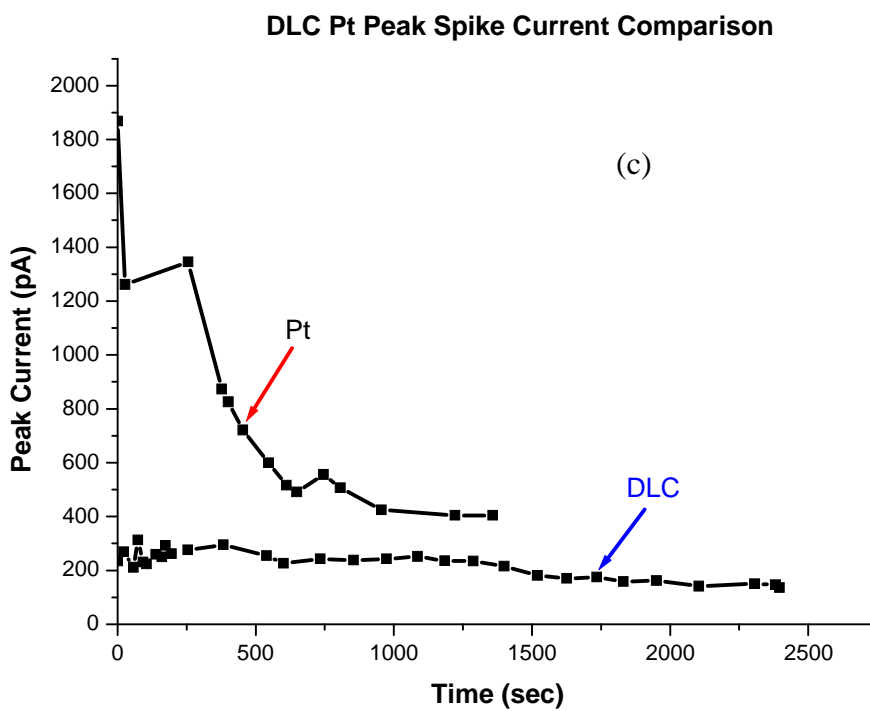
stable background current could be due to the presence of graphitic clusters embedded in the sp^3 matrix. This creates surface with electrochemically active sites separated by more insulating regions which causes a reduction in the background current. Table 2.3 summarizes the comparison results.

Table 2.2 comparison of parameters of current spikes from exocytosis events

Electrode	I_B (pA)	Noise (pA)	Spike amplitude (pA)	Average charge per spike (pC)	FWHM (ms)	Rise time (ms)
DLC	180	1	34.10±3.32	1.20±0.13	12.34±1.29	2.87±0.26
Platinum	430	9	175.4± 12.5	3.89±4.35	10.31±11.51	10.07±1.99

For a better comparison, we plot some statistical parameters of two long-duration recording from both DLC and Pt microelectrodes. The duration is about 20-40 minutes, the parameters we are interested to compare are the noise vs time, peak spike amplitude, peak current, background current and noise level vs background current. These parameters are plotted in Fig. 2.22 (a), (b), (c), (d), (e) respectively. From the figure we can see that the noise level of Pt microelectrodes are much higher than that of DLC and it drops dramatically with time. But the DLC noise level is very stable. The same trends are observed on the other parameters: spike amplitude, peak current, background current and noise level vs background current. All the parameters of DLC are more stable than that of Pt, this indicates that DLC could be a more suitable working electrode material than Pt.





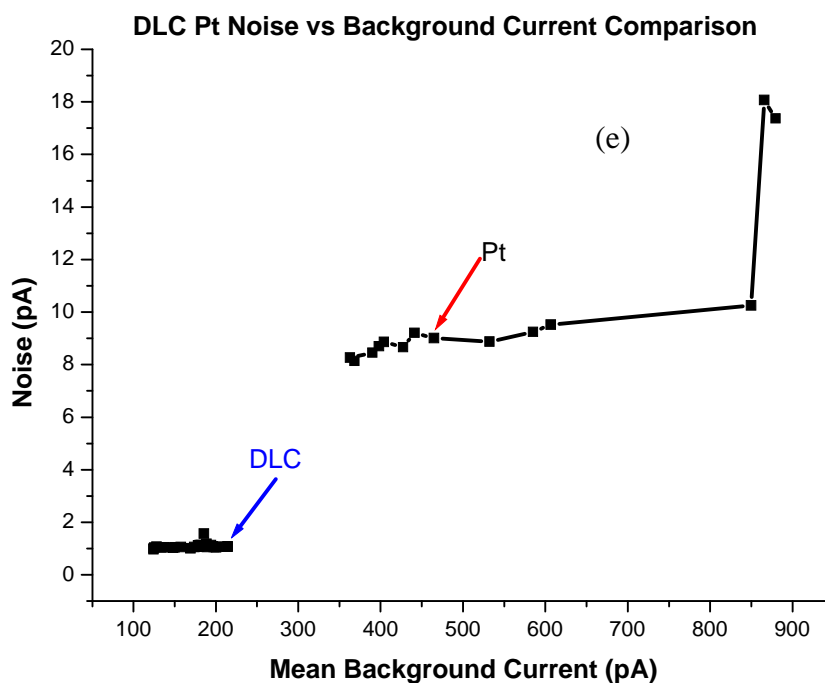


Fig. 2.22 Comparison of spike amplitude, peak current, background current and noise level vs background current between DLC and Pt microelectrodes

2.6.9 Reference electrodes

In electrochemical sensor applications, we usually require a reference electrode. As we have mentioned, a potential will be built up when an electrode is immersed in a solution. When we measure a potential, we need a good reference. So, the major requirement for a reference electrode is a stable and well known potential that does not change with time. Since the passage of current through an electrode can alter the potential, a three electrode system should be used where there is a counter electrode, acting specially as a current sink to minimize potential change for the reference electrode. Commonly used reference electrodes are Ag/AgCl and saturated calomel electrodes. These reference electrodes are similar and consist of a redox reaction between a sparingly soluble chloride and the

metallic element in an aqueous chloride solution. They can be used interchangeably; but, one needs to specify which one is used, since their potentials are different. Actually, the potential of the silver/silver chloride reference electrodes is -35 mV relative to the saturated calomel electrodes. Since all potential values are relative to the reference electrode, any measured potential without a specified reference electrode is meaningless.

The counter or auxiliary electrode is typically a platinum wire that provides a current sink for a redox reaction to balance the one occurring at the surface of the working electrode. In order to support the current generated at the working electrode, the auxiliary electrode should be put to the working electrode as close as possible, and the surface area of the auxiliary electrode should be equal to or larger than that of the working electrode.

2.8 Summary

Electrical models of electrode-electrolyte interface have been described. The effects of microelectrode were discussed compared to macro electrodes. Electrode noises were measured and analyzed. Finally, several electrode materials were discussed and the fabrication processes were described and the characterization method was presented. Nitrogen doped diamond-like carbon (DLC) electrodes have been developed and integrated onto glass slide microchip through DC magnetron sputtering and lift-off process. The DLC microelectrodes exhibit excellent electrochemical properties such as low noise, stable and low background current. Amperometric measurement was performed on the microchip device developed based on the DLC microelectrodes and showed similar results to that of the

carbon fiber electrodes. The integration of DLC onto glass microchip devices provide high performance and low cost solution with the capability of high throughput electrochemical measurement of quantal exocytosis through multi-channel and simultaneous parallel recording.

Chapter 3 IMPEDENCE BASED CELL SENSORS

3.1 Introduction

The electrical impedance has been used as an indicator for many biological properties such as tissue or organ impedance measurement. Although the impedance method has been successfully used to detect and count blood cells in a diluted solution as in the Coulter counter from the early 50's, the study of living biological cell's impedance is relatively recent. The first reported study of impedance based sensors for monitoring living cell behaviors in-vitro was by Giaever and his coworkers in 1986.⁷⁴ Cells are cultured onto microelectrodes fabricated on substrates and impedance is used to monitor cell proliferation, morphology, and motility. under an ac excitation. This technology later was named Electrical Cell Impedance Sensor(ECIS) and a company called Applied Biophysics Inc. is marketing a commercial instrument for this. Cell impedance measurements provide important insight into cell metabolism and are therefore helpful in such medical applications as cell cycle, abnormal cell detection and cancer diagnosis.

ECIS technology is usually used to monitor cell growth over a long time period usually in hours and even days since cells need to settle down onto the microelectrode array, flatten out and grow on the surface. Under low frequency ac excitation, cell membranes are basically insulators and the impedance increases following cell growth and more electrode surface area are covered by cells. ECIS experiment is a long process and it monitors a

group of cells. In many cases, manipulation and measurement of single cells are desirable. For faster analysis, flow-based cell sensing technology needs to be developed.

The detection of single cells rather than a population of cells is of great importance in medical, biological, and pharmaceutical research, especially in the field of genomics and proteomics^{75,76,77}. Major medical advances such as gene therapies and cloning require the capability of isolating and processing an individual cell. In some special cases, like stem cell research and cell cloning research, only a few cells can be harvested. Manually identifying a single cell under microscope is labor intensive even for well-trained personnel⁷⁸; automatic detection of single cells would greatly facilitate research involving single-cell analysis, processing, or manipulation. For example, resolving metabolic activities at the single-cell level would provide more precise understanding of cell life cycles and basic cellular processes, which could not be achieved by observing a group of cells⁷⁹. Measurement of DNA contents inside individual cells may allow early identification of abnormal cell growth before they develop into a full-fledged tumor⁸⁰. One may also envision a cell production line with integrated sensing that can detect and process single cells automatically for tasks such as microinjection of drugs or fabrication of cell-based biosensors.^{81,82}

In this chapter, a brief review of the literature on particle sensing is provided first, which include capacitance-based particle sensor and the effort on the miniaturization of the Coulter counter. Then, we will introduce the design, fabrication and testing of our new microdevice-based impedance sensing with planar electrodes and vertical aligned sensing aperture. The

modeling of the electrical properties of the sensor and discussion on the device test results are then followed by a short summary.

3.2 Literature review of previous impedance based micro sensor work

Cell sensing capability has been available in hematology analyzers or cytometers⁸³, which are traditionally utilized to obtain blood cell counts for diagnosis of hematological disorders. These instruments also serve the medical community as tools for measuring cell concentrations and assessment of cellular DNA contents^{84,85}. However, they are bulky and expensive equipment typically found in central laboratories. With emerging MEMS technology, much effort has been placed on miniaturization of cell counters^{86,87,88} in order to create low-cost handheld cytometric instrument for on-site and point-of-care applications. In addition, utilizing MEMS technology offers the potential to further integrate microsensors, microactuators, and microelectronics together toward a lab-on-a-chip microsystem⁸⁹.

The most common cell diagnosis method probably is the blood cell count which has been used in practical clinical applications for a long time. Blood consists of plasma and blood cells which consist of red blood cells, white blood cells, and platelets. In addition to primitive manual cell counting methods, many other different transducing approaches have been implemented for cell sensing, including electrical^{86,87,88,90,91,92}, optical^{76,93,94} and ultrasonic⁹⁵ detection methods. Compared with optical detection that may require a large number of well-aligned optical components such as laser sources, lenses, detectors, etc., electrical detection allows direct acquisition of electronic sensing output and permits

integration and miniaturization of the entire transducer in less complex microstructures. A typical design for electrical detection in microscale is a micro Coulter counter featuring a narrowed orifice in a microchannel made parallel on a silicon or glass substrate covered by a glass plate. Two electrodes are integrated on the inlet and outlet of the orifice to detect resistive change of the orifice due to displacement of fluidic volume by particles/cells. However, the Coulter counter is subject to the coincidence problem, due to multiple particles/cells present within the orifice. As illustrated in Fig. 3.1(a), the sensor will detect multiple particles within the orifice as one, even if they are moving one after another in a single profile inside the channel. Thus, when coincidence occurs, the Coulter counter design will not be able to distinguish individual particles one by one.

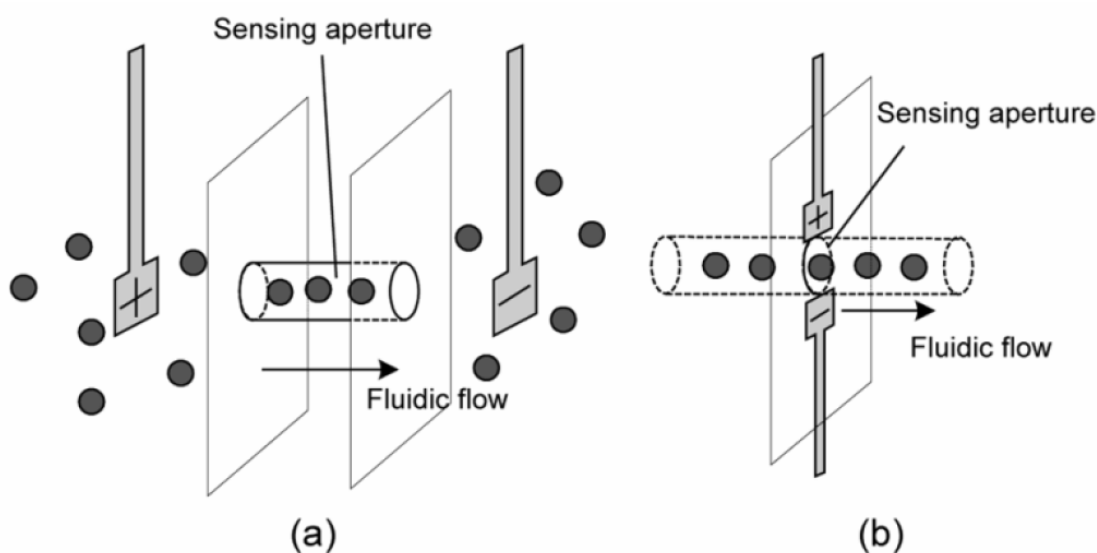


Fig. 3.1 Comparison between (a) the Coulter counter design which may have a coincidence problem, and (b) the sensor design studied in this paper for detecting particles one by one.

Following the development of the MEMS technology, research on the miniaturized versions of the cell sensing devices and analyzers has been ongoing since the 1990s. As a successful electrical impedance based commercial instrument, the Coulter counter was used as a

miniaturization prototype. The first micro Coulter counter device was reported by Larsen et al in 1997.⁸⁶ Figure 3.2 shows the fabricated device which follows the similar principle with the conventional coulter counter. The device has been fabricated on a silicon substrate and the design has been modified to adapt the principle into a planar micro channel system. This device employs hydrodynamic focusing to concentrate the sample fluid and a pulse resistive technique for particle detection. Hydrodynamic focusing uses two outer sheath flows on each side of a central sample flow to laterally constrain the sample flow to the center of the fluidic channel and thus minimizes interaction between the sample and the channel walls. Dynamic focusing was demonstrated with no practical particle sensing data is shown in this design.

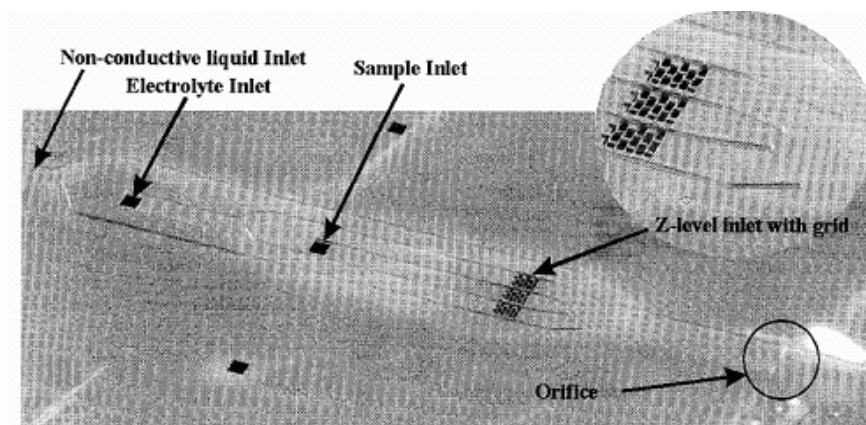


Fig. 3.2 Micro Coulter counter by Larsen et al.

Another report on the micro device on the Coulter counter is reported by M. Koch et. al in 1999⁸⁷. They also used silicon to build the device and resistive pulse method was used without focusing. Channels were etched on silicon and titanium electrodes were patterned for detection and electrical sensing. The silicon device is bonded with Pyrex glass for a sealed device as shown in Fig. 3.3.

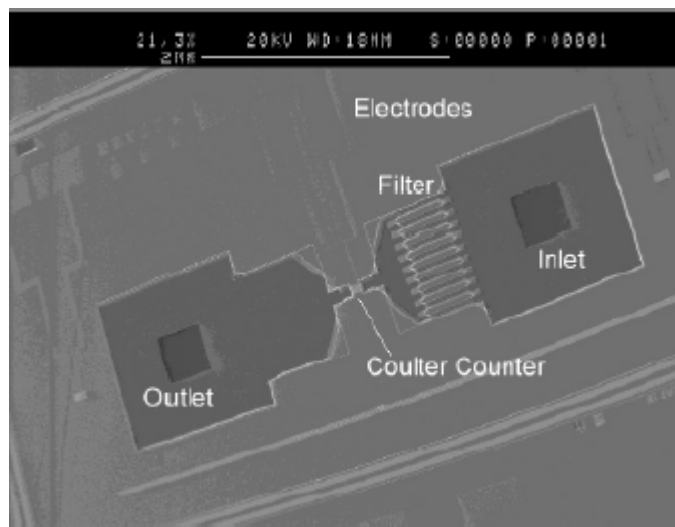


Fig. 3.3 Micro Coulter counter device by M. Koch et. al

The smallest particle sensing device probably was reported by Saleh et al in 2001⁸⁷. Fig. 3.4 shows this device. The device works on the same principle as the conventional Coulter counter. The authors claim that the device can be used for quantitative sensing of nanoscale colloids. The device is fabricated on top of a quartz substrate with no hydrodynamic focusing and it contains two reservoirs with a channel (pore) connecting them as shown in Fig. 3.4.

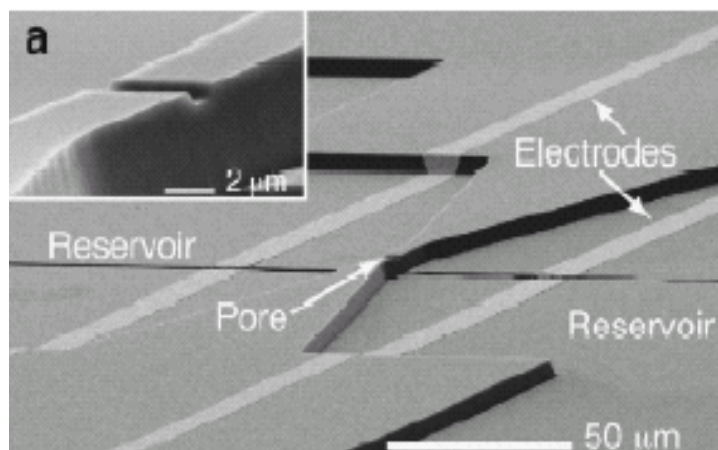


Fig. 3.4 Nano colloid particle sensing device on a microchip by Saleh et al

Another micro device based on electrical impedance measurement was reported by Ayliffe et al in 1999 which makes use of impedance spectroscopy⁹¹. They use a wide frequency range

from 100 Hz to 200 MHz on samples of liquid or gas and record the resulting impedance spectrum. This device features a microchannel with integrated gold microelectrodes perpendicular to the micro fluidic channel which has the same height with the channel depth such that the electrodes works as a horizontal gating electrode. Except for particles sensing, the applications of this device can be extended to determining the electrical properties of isolated biological materials. Fig. 3.5 shows the design of the device.

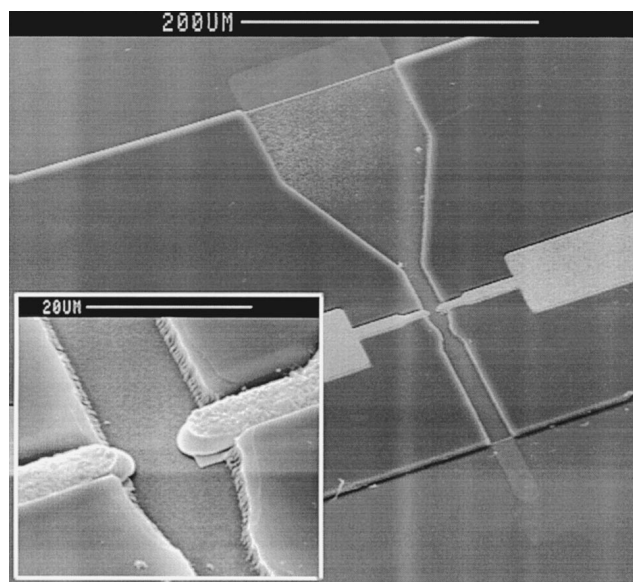


Fig. 3.5 Micro electrical impedance measurement system developed by Ayliffe et al

Sohn et al reported a capacitance technique in measuring biological cells one by one and analyzing the DNA content of the cells³. The device is shown in Fig. 3.6 and is a similar design as Fig. 3.5 but uses planar electrodes and AC capacitance measurements. It measures the capacitance change across a pair of microelectrodes as individual cells suspended in buffer solution flow one by one through a micro fluidic channel. The author claimed that capacitance measurements can detect and quantify the polarization response of DNA within the nucleus of a cell when monitoring the cell cycle. They demonstrated their integrated microfluidic device could replicate the DNA histograms of standard laser flow cytometry.

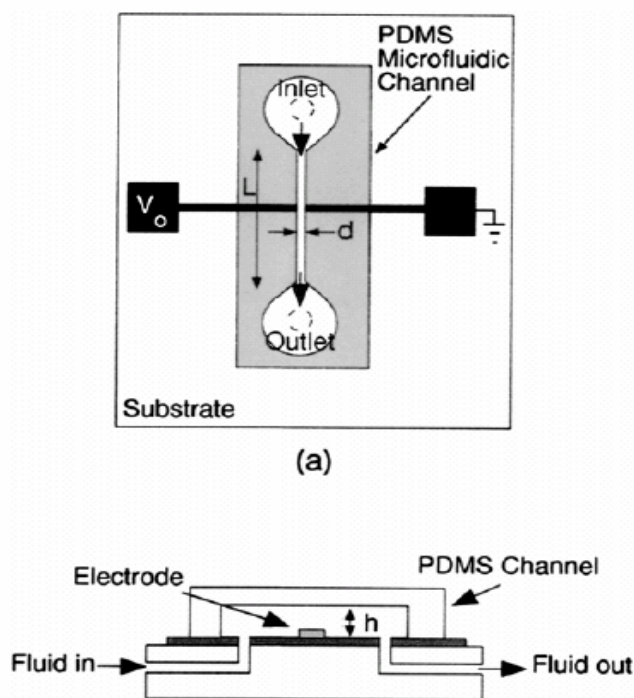


Fig. 3.6 A.C capacitance based device developed by Sohn et al

All the above mentioned microdevices use a microchannel as the carrier of sample fluid with floating particles. As we know, the particles may get clogged inside a microchannel and cells may stick to the bottom of the channel. This may limit the practical application of those devices. In addition, the flow speed inside microchannel may also be limited due to the small size and increased surface tension, thus affecting the sensing or measurement speed of the device. We propose an alternative robust design of an impedance based microsensors consisting of a vertically aligned sensing aperture and a pair of gating electrodes around the edge of the aperture. The sensing mechanism may potentially minimize coincidence errors by arranging interrogating electrodes in a plane perpendicular to the particle/cell flow, as shown in Fig. 3.7(b). The electrical field between the two sensing electrodes is localized to the entrance of the sensing hole. When a particle/cell passes, it interferes with the current paths between the two electrodes and causes the

impedance change due to different electrical property of particles/cells in comparison with the electrolyte solution. The change in impedance can be detected by using AC excitation across the two gating electrodes. Since the particles pass through the sensing aperture and gated sensing electrodes in a very thin plane, this sensing approach would allow detection of single cells one by one without coincidence errors. In addition, the device does not include microchannels, and there will be no cell clogging problem. The device could be inserted between two vertically aligned tubes with good sealing, so that it could be reused and easily cleaned.

3.3 SENSOR DESIGN AND FABRICATION

3.3.1 Microsensor design

The sensing mechanism in Fig. 3.7(b) was implemented using micromachining with planar gating microelectrodes across the entrance of an orifice vertically etched into a silicon substrate. As sketched in Fig. 3.7(a), the microsensor prototype is in the shape of a probe 20 mm long, 2 mm wide at the narrow end, and 10 mm wide at the other end. Nine sensing holes of different size in diameters of 20, 60, and 100 μm are designed near the narrow end. For the 60 μm and 100 μm holes, each electrode has multiple tips as illustrated in Fig. 3.7(b) to achieve more uniform distribution of the electrical field between paired electrodes. The wide end of the probe is utilized for the bonding pads, which have a trace width of 0.25 mm and a pitch of 0.5 mm, allowing interconnections from gating electrodes to a circuit board via flexible heat-seal connectors (Elform Inc., Reno, NV). As sketched in the cross-sectional view in Fig. 3.7(c), the gold metal layer is insulated from the substrate by a silicon nitride dielectric layer. Another Si_3N_4 insulation layer is deposited over the metal

layer to protect the wires with only the tips of electrodes exposed for contact with a sample solution.

3.3.2 Mask design considerations

The mask design of the device is for 3” wafers. In order to make full use of the silicon area multiple probes in inverted pairs in the center of the wafer are designed as shown in Fig. 4.8. A total number of 14 devices can be fabricated on one wafer. The through hole will be etched by KOH anisotropic etching of the (100) Silicon wafer. The anisotropic etching of silicon is a very important silicon bulk micromachining method where the etch rate depends upon the orientation of the crystalline planes. In anisotropic etching, the lateral etch rate can be much larger or smaller than the vertical etch rate, depending upon the orientation of mask edge to crystalline axes. The orientation of the mask edge and the details of the mask pattern determine the final etched shape. In contrast, the etching rate of isotropic etching is the same in all direction and does not depend upon the orientation of the mask edge. The reason for the anisotropic etching is due to the atom density difference on different crystal planes as shown in Fig. 4.9 (Adapted from: S.M. Sze, Semiconductor Devices⁹⁶). The detailed chemical reaction is very complicated; but, the overall redox reaction is as follows:



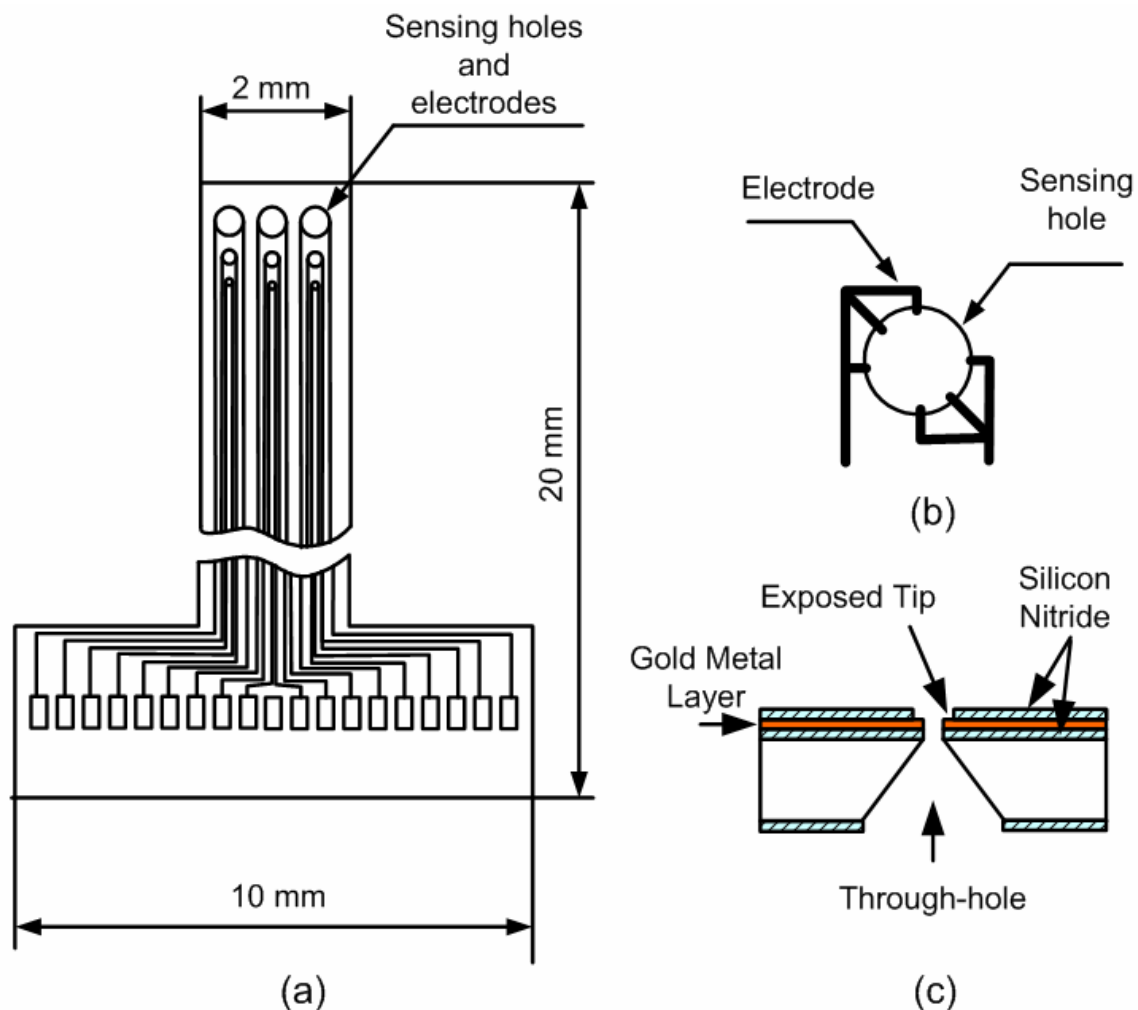


Fig. 3.7 Schematic diagrams of the microsensor prototype: (a) one whole probe, (b) a design using multiple-tip gating electrodes, and (c) cross-sectional view of the sensor structure.

The selectivity between different crystal planes are $(111):(110):(100) \sim 1:600:400$. We can see that (111) can be a very good etch stop as the etch rate on it can be neglected compared to the other two planes.

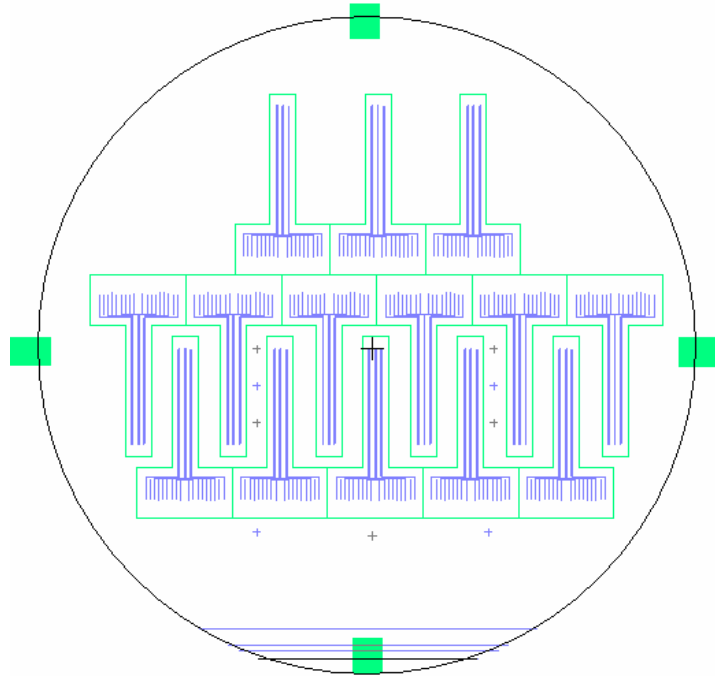


Fig. 3.8 The mask layout of the design on a 3" wafer, maximal devices are laid out on the wafer for better fabrication yield.

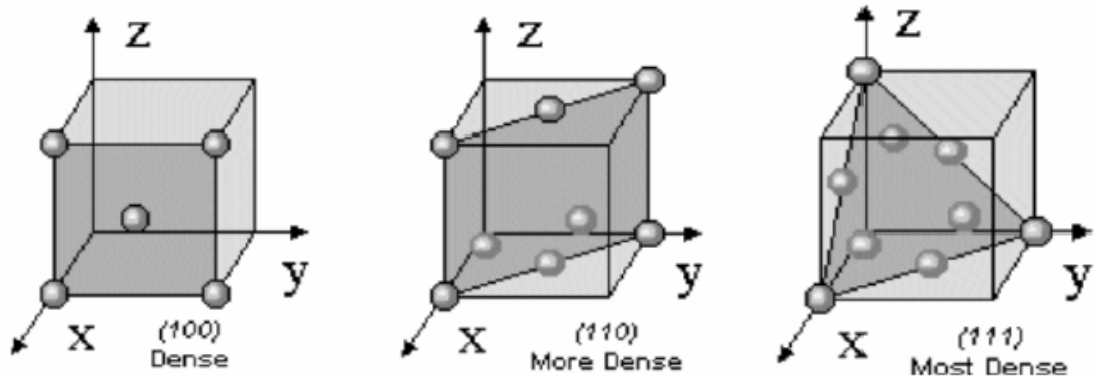


Fig. 3.9 Crystal planes in silicon wafers

From the Fig. 3.9, assume the lattice constant of the silicon crystal cube is a , we can calculate the angle between (111) plane and (100) plane by the following equation:

$$\tan \alpha = \frac{a}{\frac{\sqrt{2}}{2}a} = \sqrt{2} = 1.414, \text{ so } \alpha = \tan^{-1}(\sqrt{2}) = 54.74^\circ \quad (3.1)$$

The ideal case to control the sensing orifice opening for the through hole would be that the silicon opening is exactly same as the designed size d . This requires the thickness of the

wafer should be a known constant value, say t . Then the etching mask size L can be calculated by equation 3.1 and the picture illustration is shown in Fig. 3.10, where L is the mask size(square), d is the the desired opening size, t is the thickness of the wafer and α is the angle between (111) plane and (100) plane, $\alpha = 54.74^\circ$

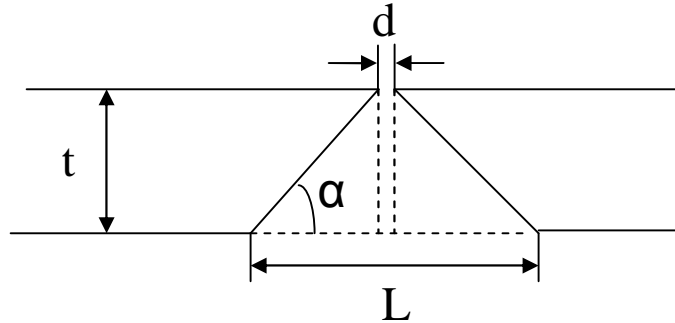


Fig. 3.10 the illustration of etching mask design

$$L = d + 2t \times \cot \alpha \quad (3.2)$$

The wafer thickness could not be constant even in the same production batch where a thickness range is given. In order to maintain a constant opening size, either we have to strictly select a uniform wafer thickness from a bunch of wafers or we can allow a certain variation of the silicon etching opening, but leave the final opening control to the insulation silicon nitride film where the opening size can be precisely controlled by a Reactive Ion Etching (RIE) etching process. The later method is more practical and is adopted for our design and fabrication.

3.3.3. Microsensor fabrication

I. Mask making

All microfabrication starts from mask design and mask making. After the conceptual design of the device, we need to implement the design into mask layout by a CAD tool.

Although there are many CAD tools and file format for mask layout design, the most common file format for the semiconductor industry is the GDSII file format. A pattern generator or laser writer is used to make the masks. We used the L-Edit CAD tool to design our mask and the mask was made by a GCA pattern generator PG3600 at the Cornell Nanofabrication Facility (CNF). Since we need to pattern the backside of the wafer and need to align the features to the other side, one side of the mask should be the mirror image of the other and this can be done on PG3600. If image reversal is needed, the image should be reversed before transferred to PG3600.

The microsensor fabrication is a three-mask process and requires backside alignment. The multiple mask process plus backside alignment capability require a careful alignment marks design on the mask layout. The alignment mark design should also consider the contact aligner requirement. There will be a minimum distance between two alignment marks if the contact aligner uses two objective lenses, the EV620 contact aligner require a minimum distance of 30 mm. The two objective lenses enable you to see two symmetric alignment marks at the same time so that you can easily align x, y direction and the rotation error between the mask and features on the wafer. The simplest design of the alignment marks are a pair of cross. Some other alignment key pairs like a cross embedded into a square with openings at four sides where the ends of the cross fit are also very common.

II. LPCVD silicon nitride deposition

Double-side-polished silicon wafers were used for fabrication of the microsensor. The substrate was first coated with a 2000 Å thick silicon nitride layer on both sides of the

wafer using low-pressure chemical vapor deposition (LPCVD) in a thermal furnace at 900 °C. The LPCVD process produces a low stress nitride film with excellent uniformity of thickness and is a very good mask layer long-duration KOH etching. The process gases used are SiH_2Cl_2 , and NH_3 with a deposition rate about 2-3 nm/min. The overall reaction is as follows:



This LPCVD process is CMOS compatible, a strict RCA clean is required prior to loading wafers to the furnace.

III. Image reversal, metal deposition and lift-off process:

Image reversal process is used to create a desirable photoresist profile for better lift-off effect after metal deposition. As shown in Fig. 3.11, ammonia (NH_3) gas is used to reverse the tone of positive photoresist. After the initial exposure, the sample is put into a chamber filled with 600 Torr of NH_3 vapor. The NH_3 reacts with the acid in the exposed resist changing it to be insoluble in developer. This can create an undercut profile in the photoresist. The following flood exposure causes acid to form in the previously unexposed areas allowing it to be removed in development, leaving behind the negative image of the first exposure and thus reverse the pattern at the initial exposure. The overall process is as follows: a) First pre-bake (dehydrate) wafer on hot plate for 1 min at 110 °C. b) Spin coat photoresist and bake on 110 °C hot plate for 1 min. c) Expose the wafer with the mask with metal wire pattern. d) Reversal bake in YES oven with NH_3 flow at 60 °C for 80 minutes. e) Flood exposure, 30-60 seconds. f) Develop the wafer using MF321 developer for about 2 minutes. Then, the wafer is ready for metal deposition.

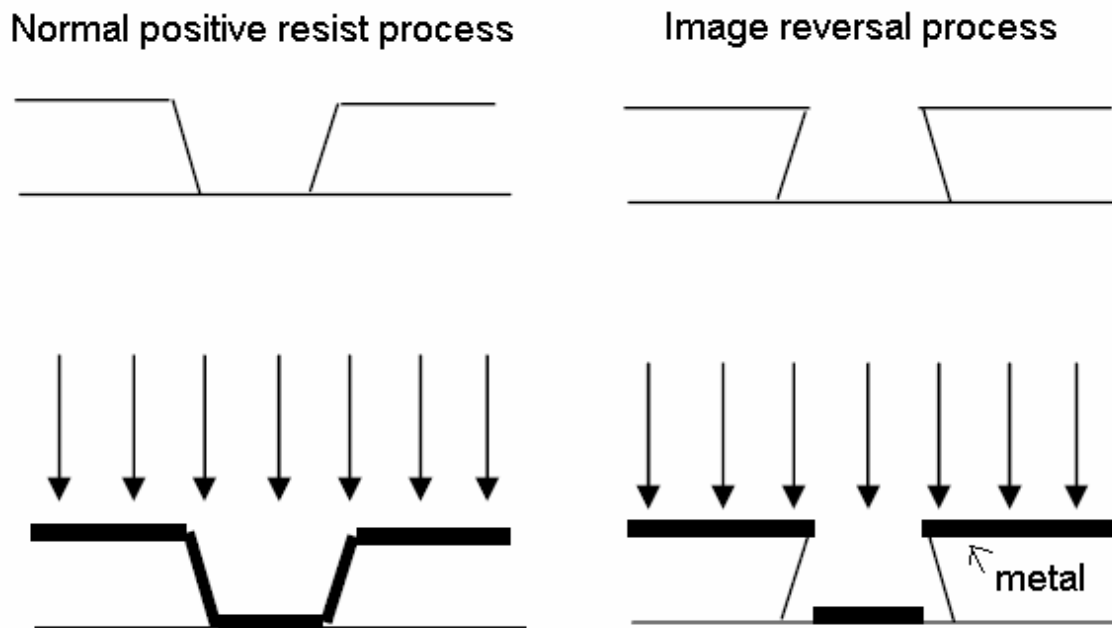


Fig. 3.11 Image reversal process gives a better photoresist profile for lift-off process

Then, Cr and Au in thickness of 1000 and 1500 Å, respectively, were evaporated onto the topside of the wafer under high vacuum. Chromium is used as the adhesion layer. Here we choose Cr not Ti for adhesion layer is because Ti could not sustain long time KOH etching while Cr and Au are very good KOH etching masks. The lift-off process is then done by soaking the sample into acetone for a certain amount of time. If the profile is good enough, it could be finished in less than half an hour and gentle ultrasonic agitation may be added to accelerate the lift-off process. From observation, lift-off process after image reversal is much easier than normal positive resist process, especially for fine patterns.

IV. PECVD nitride deposition

Another insulation layer of silicon nitride was then deposited over the metal layers using plasma enhanced chemical vapor deposition (PECVD) at 300 °C. Although PECVD nitride film's quality is not as good as LPCVD, we have to use PECVD since the film can be

deposited under a lower temperature to protect the metal layer. IPE 1000 PECVD system was used for PECVD silicon nitride deposition and the reactive gases are silane ammonia.

The chemical reaction is:



Silicon nitride is a very common dielectric film and can be used for passivation layer. In MEMS processes it is also commonly used as a masking layer. The only effective wet etching method is to etch at boiling phosphoric acid. More common patterning method is reactive ion etching RIE where plasma energy will be used and it is more environmentally friendly.

V. KOH etching

To pattern the silicon nitride on the backside for subsequent anisotropic etching of through-holes, a contact aligner with “see through” IR light source was utilized for the backside alignment. Silicon wafer is transparent to IR light while the metal pattern on the wafer is not. The IR light illumination method could not provide a good resolution (>2 μm). So, if the alignment is critical, a better aligner with bottom side optics is needed such as the EV620. After the backside nitride layer was patterned with RIE, the through-holes were created in the silicon substrate in a 40% (by weight) KOH solution for about 3 hours, with an etching rate approximately 2.15 $\mu\text{m}/\text{min}$ at 90 °C. The KOH etching of silicon will generate large amount of hydrogen bubbles which may accumulate on the etched surface and affect the further etching reaction and the surface roughness. Magnetic stirrer should be used to quickly remove the bubbles and some additive such as isopropanol may be used to improve the surface roughness. Since the etching process will consume KOH, so the

etching rate may not be constant. Another RIE process was performed on the top nitride layer to expose the sensing electrode tips and the bonding pads. Even though KOH bulk etching resulted in square pyramidal through-holes and the size of the openings on the topside may vary slightly depending on the wafer thickness, the round shape and size of the holes were actually defined in the top silicon nitride layer by the final RIE. The entire schematic fabrication process is shown in Fig. 3.12 in cross section view. Enlarged pictures of microfabricated sensing apertures of different size are shown in Fig. 3.13 and Fig. 3.14. The exposed metal tips of each gating electrode extend into its sensing hole by 1-3 μm .

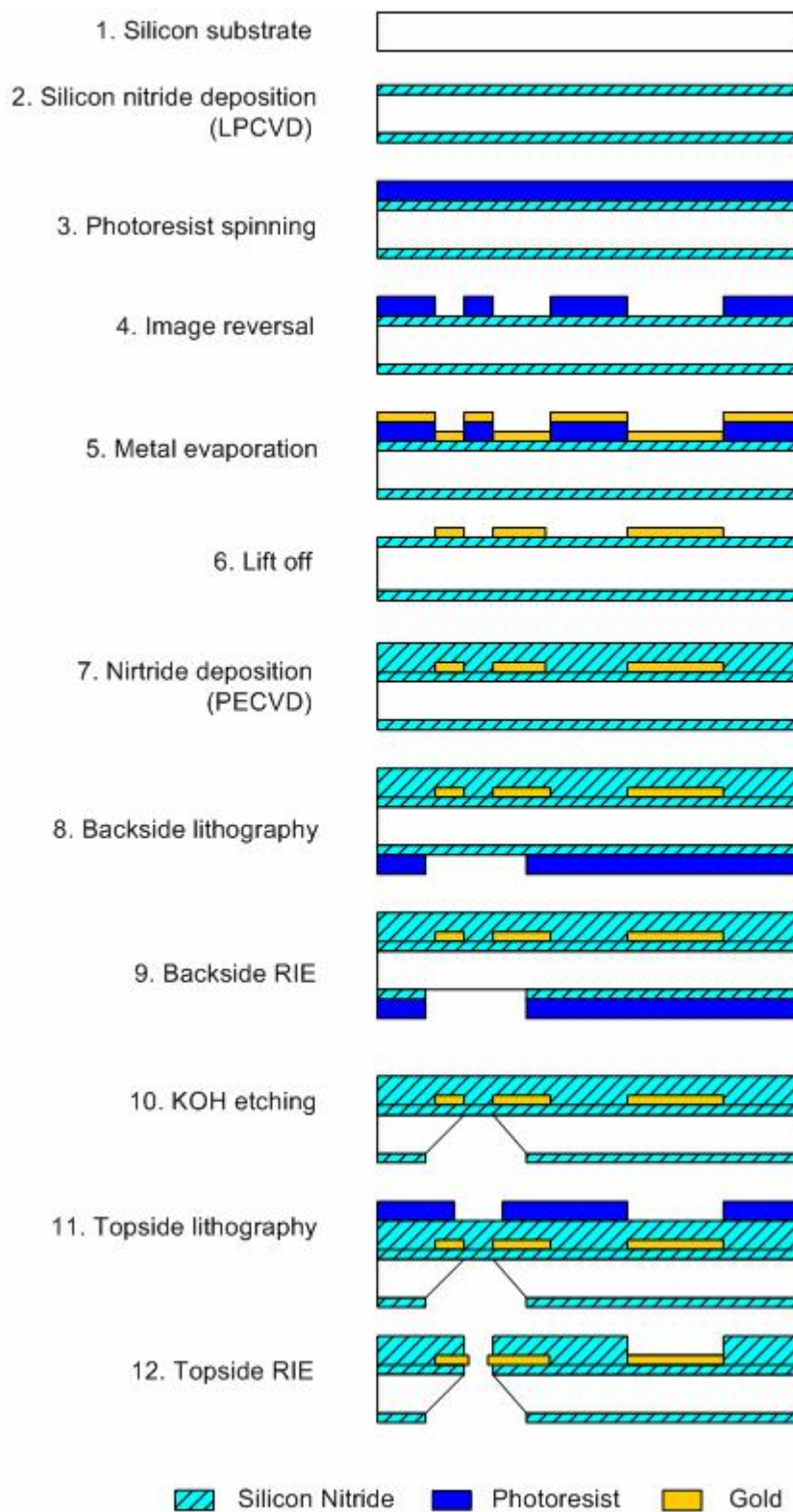


Fig. 3.12 Process flow for fabrication of the impedance microsensor.

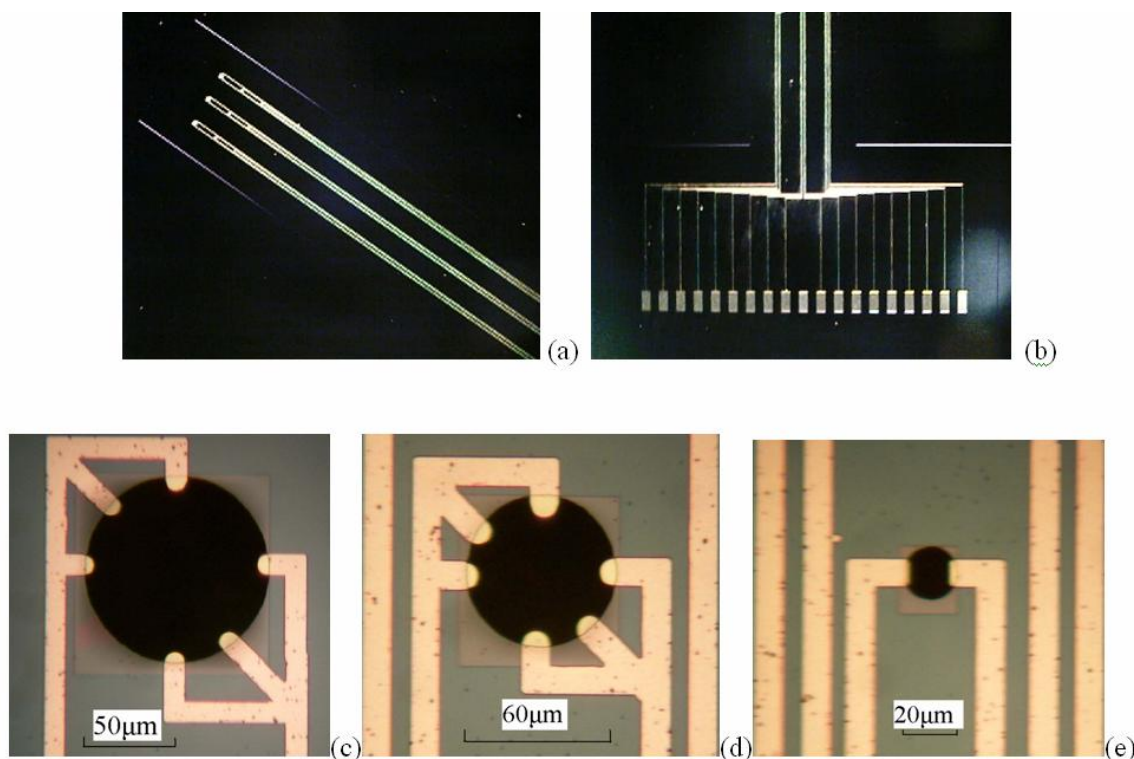


Fig. 3.13 The fabricated impedance sensor and sensing aperture with gold electrodes. (a) (b) the overall sensor tip and contact pads. (c), (d), (e) are the fabricated sensing holes: (c) 100 μm , (d) 60 μm , and (e) 20 μm , respectively. The width of all gold wire lines (except the tips) is 10 μm .

VI. PCB device

For initial testing, the sensing mechanism was also implemented on a printed circuit board (PCB) with copper gating electrodes. The PCB device has the same working principle as the microfabricated probe except for the size of the sensing electrodes and the holes. As shown in Fig. 3.15, the PCB device is 5 cm long, 2.5 cm wide at the narrow end, and 7 cm wide at the wide end. The width of the electrode lines is set at 0.5 mm. While four sensing holes were designed on the PCB device, only the smallest sensing hole with diameter of 1.3 mm was used for testing.

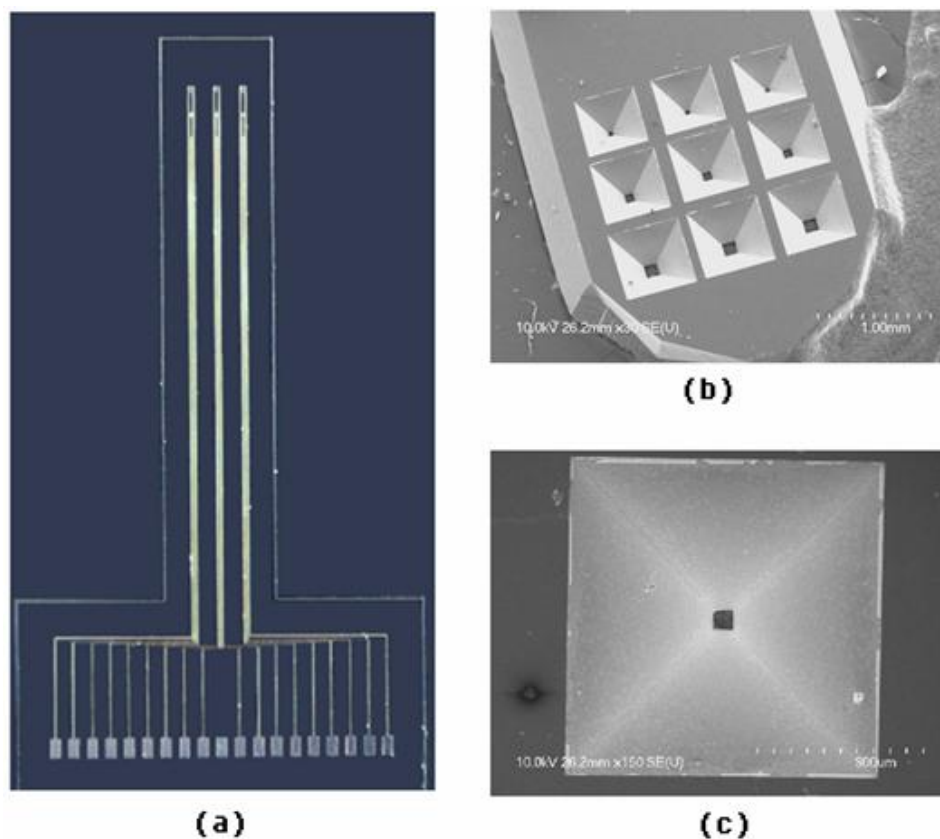


Fig. 3.14 The overall sensor picture and SEM picture of the etched pyramid through holes in silicon wafer. (a) the overall impedance sensor. (b) the etched through hole array in silicon wafer. (c) an enlarged etched pyramid hole.

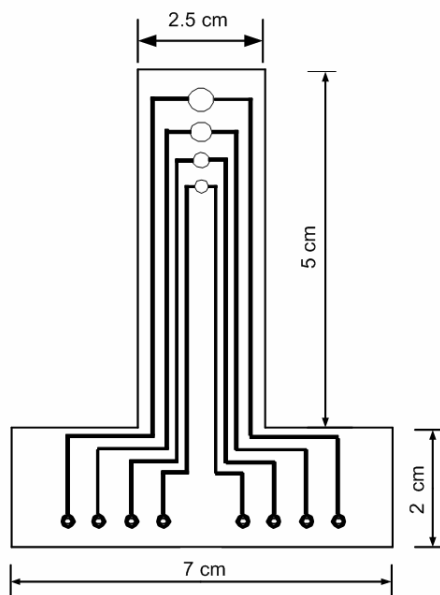


Fig. 3.15 Schematic design of the PCB device.

3.4 Experimental setup and test

3.4.1 Probe setup

The experimental setup for testing the microfabricated sensor as well as the PCB device is shown in Fig. 3.16. For the microfabricated probe, a plastic holder was made from a block of Plexiglas material so that the probe could be placed on the top surface. A chamber (1.4 x 0.6 x 0.8 cm) was made on top of the holder and connected to an outlet tube on the side, as shown in Fig. 3.16(a). The surface of the holder is flat and smooth and the probe can be tightly sealed over the chamber under small pressure with some vacuum grease applied around the edge of the chamber. Droplets of sample solution were pipetted onto the sensing site without using a reservoir, as the reservoir trapped air in initial trials. By applying suction from the side tube with a syringe, solution on top of the probe may flow through the sensing holes under pressure. For the PCB device, tubes were glued to the top and bottom sides with the top one used as a sample reservoir and the bottom one connected to a syringe to move the fluid through the sensing aperture, as shown in Fig. 3.16(b). The saline (NaCl) solution of strength 0.9% with suspended microbeads was used for preliminary testing on the devices.

3.4.2 Instrumentation

An instrumentation system is implemented as shown in Fig. 3.17 to convert the impedance change into pulses and to measure relevant parameters (pulse amplitude and width) from the detected pulses. The system is based on LabView (National Instruments, Austin, Texas) and includes sensing circuitry, signal processing hardware, data acquisition, and data analysis. The sensing circuit is a simple voltage divider that transforms change of the

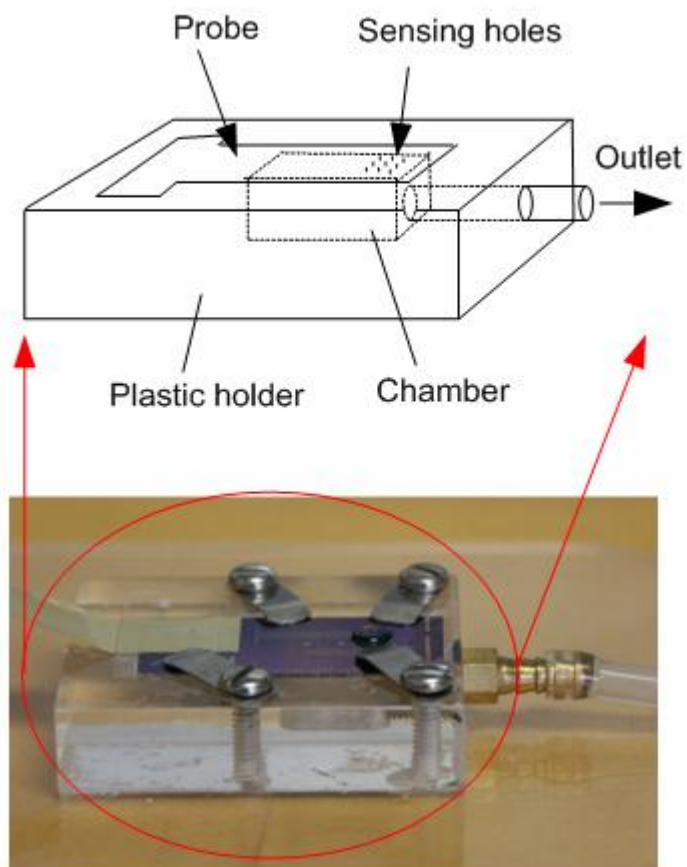
overall impedance Z_x between the electrodes into a voltage output. The sensitivity of the sensing circuit in response to the change of Z_x can be written as:

$$\frac{dV_o}{dZ_x} = \frac{1/R}{(1 + Z_x/R)^2} V_{in} \quad (3.3)$$

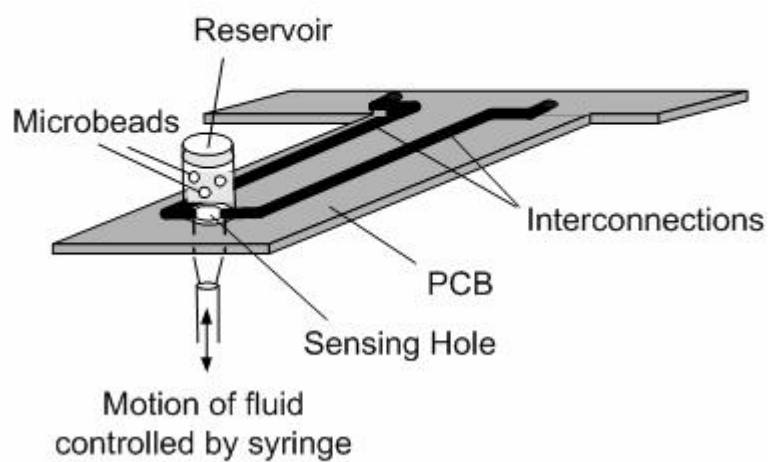
From equation 3.3, we can see that both values of R and Z_x affect the sensitivity of the circuit. For a chosen R , Z_x should be reduced to increase sensitivity. If Z_x is known and fixed, the sensitivity can be further increased with R approaching to the value of Z_x . when R is equal to Z_x , we get the maximum sensitivity, and if R is smaller, overall sensitivity will be higher. As a result, a small Z_x is preferable for good sensitivity.

With AC excitation, the output of the sensing circuit is an amplitude-modulated signal. This amplitude-modulated signal is then demodulated by a demodulator (AD630), followed by a bandpass filter to remove the DC and high-frequency components. The low and high cut-off frequencies of the bandpass filter were set at 0.2 Hz and 1000Hz respectively. As some of the high-frequency components leaks through the bandpass filter, a high-pass filter and an inverter are utilized to subtract the high-frequency component, and only the low-frequency signal is amplified with the differential amplifier with a large gain of 800. The additional inverter is used to create a reference signal which has similar time delay so that the final amplifier works in differential mode. The output of the instrumentation circuit is in the form of pulses corresponding to passage of particles through the aperture. This completely removes DC and high frequency components in the signal, only the low frequency signal change was amplified. When no particles pass through the sensing electrodes, there will be no signal change and the output is zero. The voltage change in its nature is in a pulse shape due to the short impedance transition time when a particle passes

through the electrodes and the important parameters of the pulse such as the pulse width and amplitude are related to the flow rate and size of the passing particle. Such conditioned and amplified signal is then acquired into a PC computer for data analysis. A program implemented in LabView automatically detects the pulses, measures the pulse amplitude and width, displays waveforms and test results.



(a)



(b)

Fig. 3.16 Experimental setup for (a) the microfabricated probe and (b) the PCB probe that allows sample solution to flow through the sensing holes with suction.

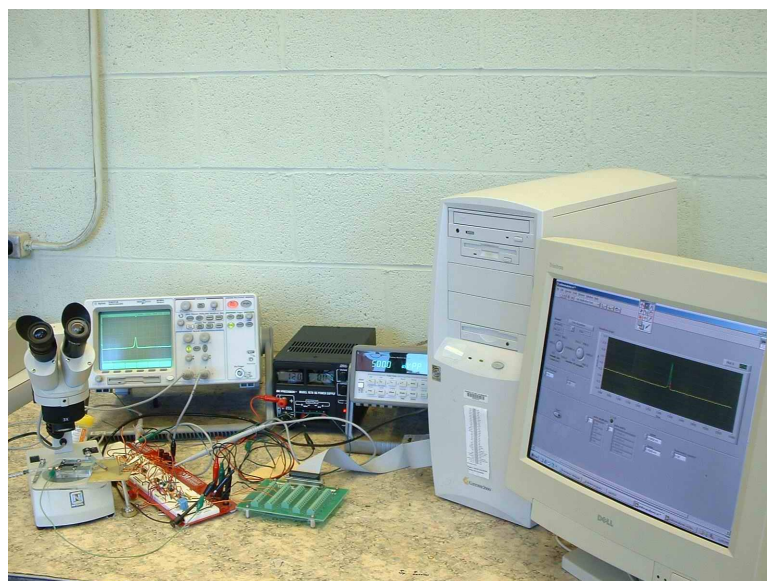
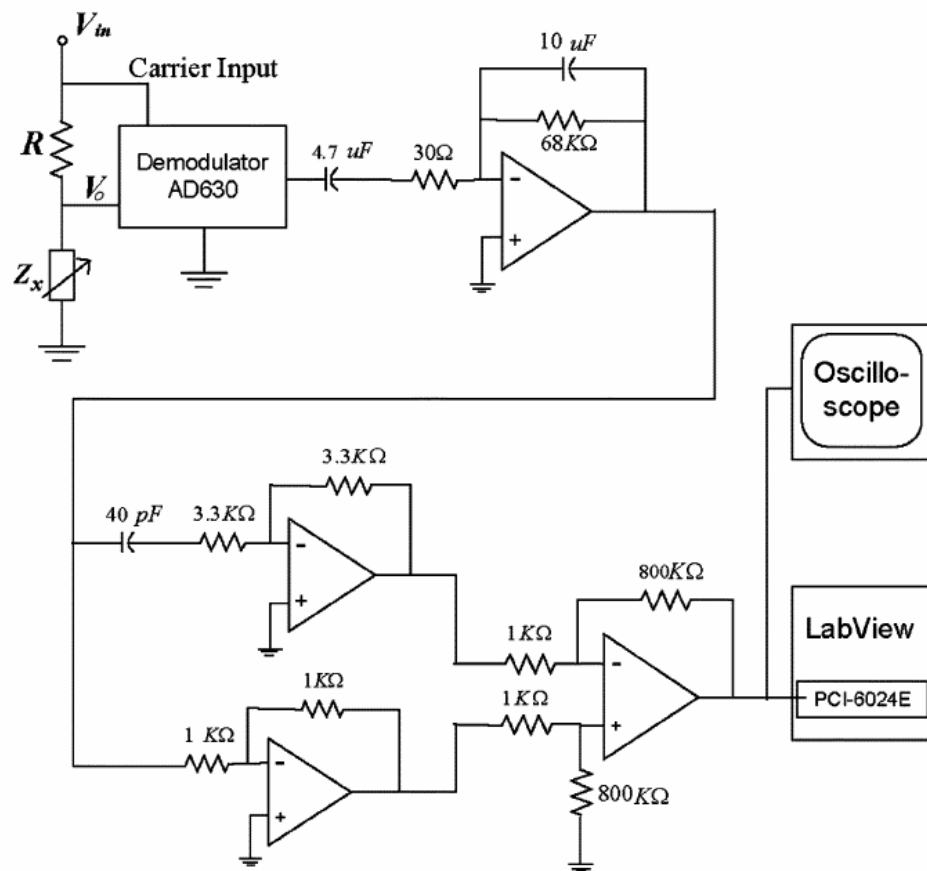


Fig. 3.17 Schematic diagram of the instrumentation system and the real system with microscope, oscilloscope, function generator and the computer for data acquisition.

3.4.3 Impedance-frequency characteristics and modeling

In general, for two electrodes submerged in solution, the impedance Z_x can be decomposed into two components in serial connection: the impedance of electrode-electrolyte interface Z_e and the bulk electrolyte resistance Z_s , as shown in the expanded circuit model in Fig.3.18. In this simplified model, Z_e is composed of a parallel RC circuit was utilized for the electrode-electrolyte impedance, where R_d and C_d represent the resistive and capacitive components respectively⁹⁷. Based on this model, R_d and C_d forms the commonly used simplified electrode-electrolyte interface model, and change of Z_e causes fluctuation of Z_x , which can be written as:

$$Z_x = Z_s + \frac{2R_d}{1 + j\omega R_d C_d} \quad (3.4)$$

Since the overall impedance is frequency-dependent, utilization of AC excitation will reduce the effect of the double-layer capacitance at the electrode-electrolyte interface. Ideally, the excitation frequency should be high enough so that $\omega \gg 1/R_d C_d$. However, the excitation frequency is limited by the characteristic frequency of a cell, which is about 2-3 MHz⁹². Within this range, little current flows through the cytoplasm and the cell behaves more like a non-conductive object. The aperture size should be comparable to the cell size so that the cell blocks as much as the current path to maximize change in Z_e . In addition, the parasitic capacitance between the metal electrodes and the silicon substrate should also be considered for the microsensor prototype. The electrodes are separated from the substrate by a LPCVD silicon nitride layer only 0.2 μm thick, which prevents KOH etching from the front side and is also used as an insulation layer between the metal wires and the substrate. This structure would introduce parasitic capacitance between the

electrodes (including their interconnections) and the substrate, and the parasitic capacitance is in parallel connection with the impedance between the sensing electrodes. To include the effect of the parasitic capacitance, the model for can be modified as shown in Fig. 3.18(b)

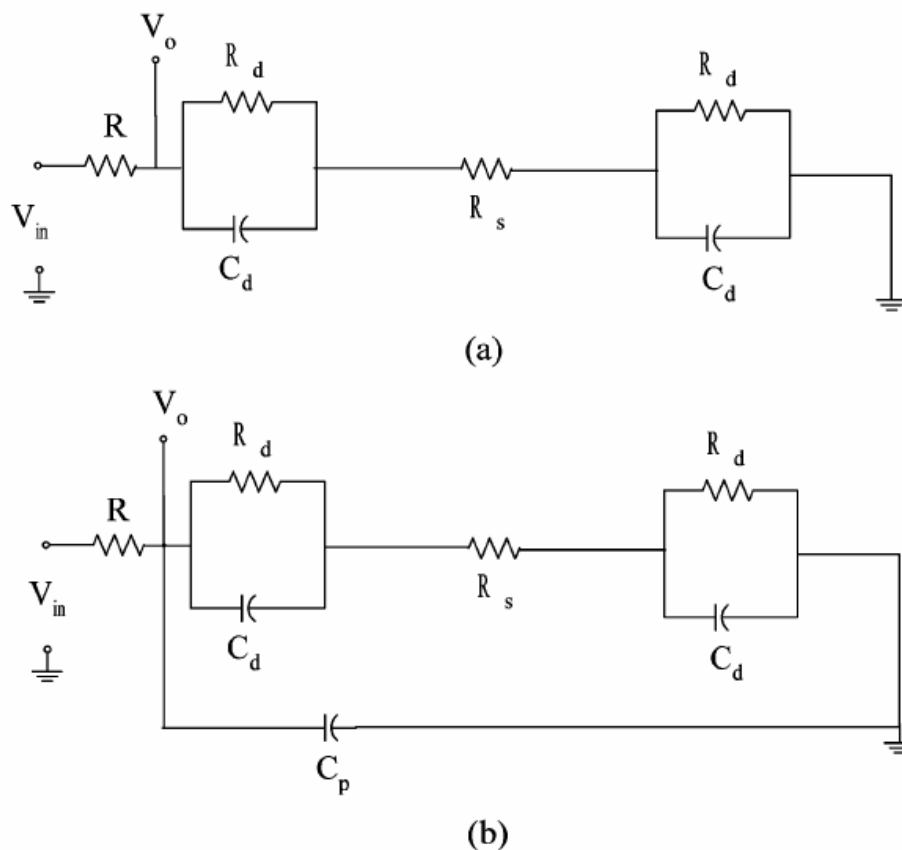


Fig. 3.18 Equivalent circuit models for the sensor interface (a) without considering the parasitic capacitance and (b) considering the parasitic capacitance. R_s represents the bulk resistance of the electrolyte, C_d the double-layer capacitance, and R_d the leakage resistance across the double layer.

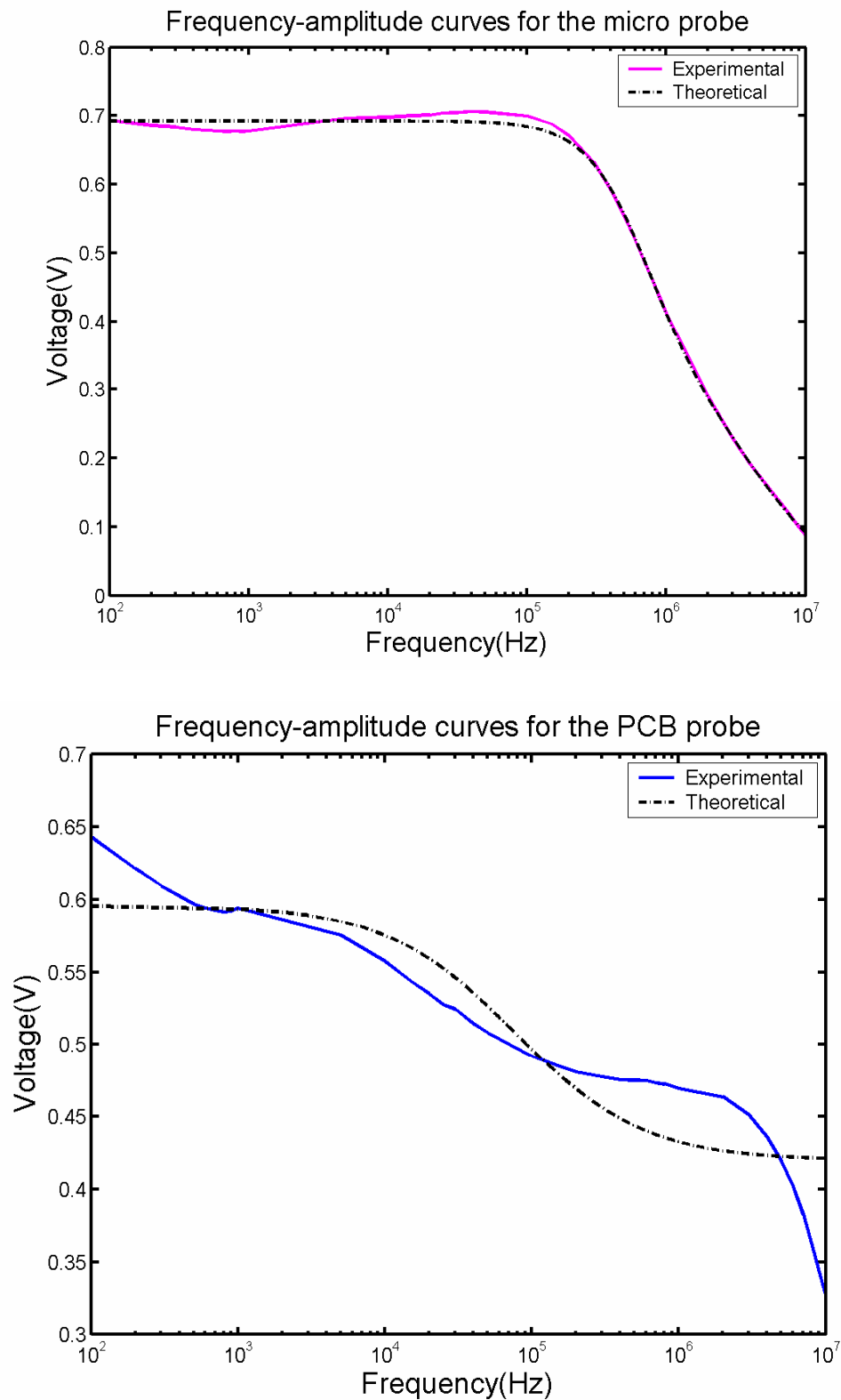


Fig. 3.19 Voltage output across gating electrodes versus frequency curves for (a) the microfabricated sensor and (b) the PCB device.

Fig. 3.19 shows the output voltage from the sensing electrodes vs frequency and the approximate impedance-frequency curves of the 100 μm sensing hole of the microfabricated sensor and the PCB sensor. The figure indicates decreased impedance with increased frequency for both devices as expected. However, the two impedance-frequency curves are significantly different in their shape and this is attributed to the scaling of the size and material of the electrodes. While the impedance of the PCB device decreases quickly with a cutoff frequency close to zero, the impedance of the 100 μm sensing hole does not drop significantly until a relatively high frequency, about 100 kHz. This is due to the small exposed electrode area of the microfabricated sensor causing a low double-layer capacitance. As a result, much higher frequency needs to be utilized to reduce the overall impedance of the microfabricated sensor. For the microfabricated probe, a frequency of 500 kHz was utilized for the AC excitation signal. This frequency also takes into consideration of the working frequency range of the demodulator chip AD630 (Analog Device Inc), which should be below 600 KHz. Beyond this range, the signal output from the AD630 will be greatly attenuated. For the PCB device, the excitation frequency can be much lower; and the actual frequency used is 50 KHz. Based on the model in Fig. 3.18, we can do a nonlinear curve fitting of the modeled components value. As a voltage divider and

consider complex value, we can use the equation $|V_o| = \left| \frac{Z_s + \frac{2R_d}{1 + j\omega R_d C_d}}{R + Z_s + \frac{2R_d}{1 + j\omega R_d C_d}} \right|$ to calculate

the output voltage and model by least-square estimates for the experimental values. We got a group of parameter as follows: [$R_s = 13.5\text{k}\Omega$, $R_d = 19.1\text{k}\Omega$, $C_d = 20.8\text{pF}$, and $C_p = 7.1\text{pF}$] for the microfabricated device, and the result for the PCB is [$Z_s = 723.8\Omega$, $R_d = 374.9\Omega$,

$C_d = 2.39 \mu\text{F}]$, where the series R used were $22 \text{ k}\Omega$ for the microsensor and $1 \text{ k}\Omega$ for the PCB device. With these values, we can calculate the Z_x and the theoretical output from the circuit. The calculated theoretical curve based on the estimated parameters is plotted as the dashed line in Fig. 3.19(a) for the microsensor circuit, which fits the experimental data very well. If using the model in Fig. 3.18(a) without the parasitic capacitance, the theoretical curve will deviate from the experimental data at high frequency range, which verifies the existence of the parasitic capacitance. Curve fitting for the microsensor shows that R_d and C_d are independent of frequency, which is in accordance with Cobbold's theory⁹⁸. Since the gold electrodes are essentially polarizable electrodes, the current flowing across the electrode interface is mainly due to displacement current, not Faradaic electron transfer during a redox reaction. This charge transfer mechanism can be modeled as parallel and that are frequency independent. In contrast, modeling using constant values did not match the experimental data for the PCB device. This is because the copper electrodes are essentially nonpolarizable electrodes, which conduct current through reaction across the interface. As a result, R_d and C_d can be dependent on both frequency and the current density⁹⁹. Further, when the current density is high, and may not obey the power law, i.e. both vary approximately inversely as the square root of frequency. The fitting for the PCB device data shows big deviation when treat the parameters constant. Instead if we follow Cobbold's theory and treat C_d as frequency dependent with a approximate relation of

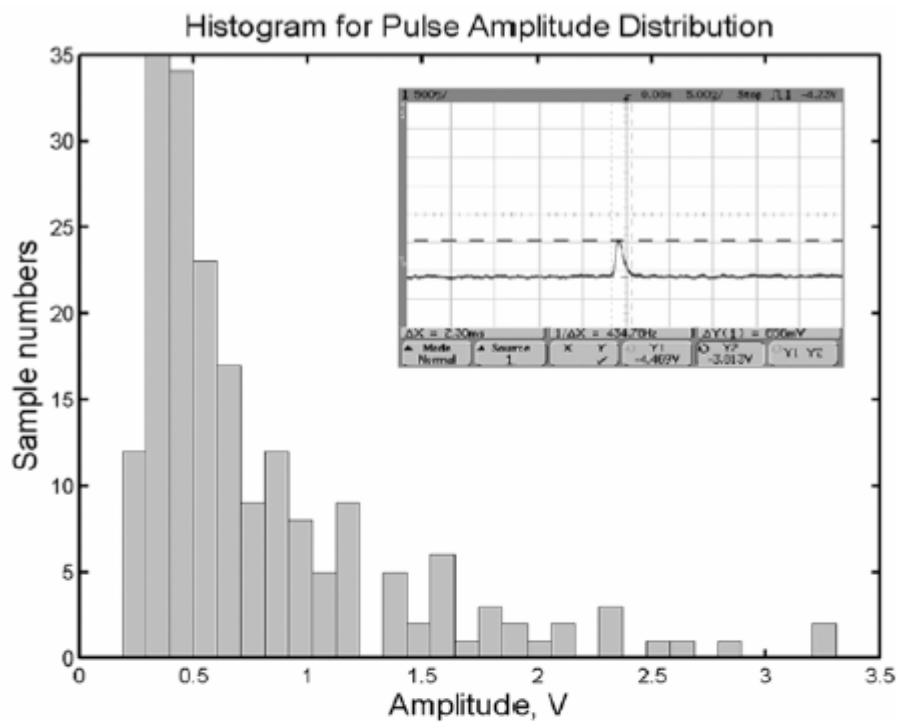
$C_d = \frac{C_0}{\sqrt{f}}$, the curve fitting generates a relatively better fitting shown as the dashed line in

Fig. 3.19(b), where f is the frequency in Hz.

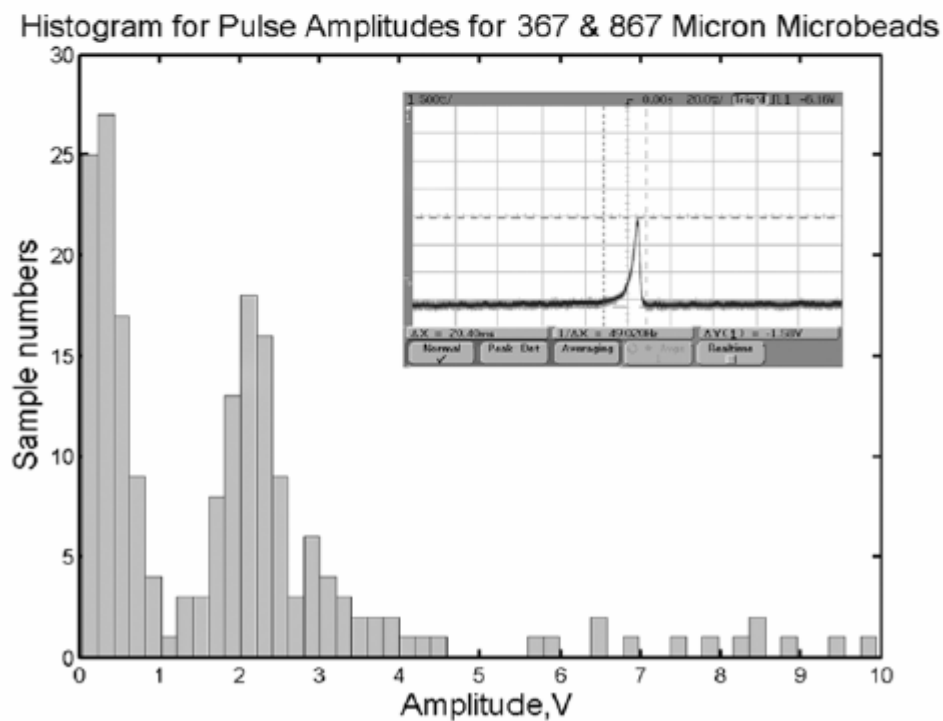
3.4.4 Test on microbeads and pulse amplitude distributions

Polystyrene microbeads with diameter of 45.6 μm have been used for testing the biggest sensing hole of the probe. Microbeads are suspended in 0.9% saline solution to mimic the ionic cellular environment. The excitation voltage was 1.0 V peak-to-peak. The sample solution was controlled to flow up and down the sensing hole with a manually operated syringe. The histogram of the pulse amplitude distribution is shown in Fig. 3.20 (a), together with a typical pulse captured from the oscilloscope. Of the 200 pulses collected for the 45 μm beads, the mean value of the amplitude is 0.79 V and standard deviation is 0.58 V.

Polystyrene microbeads of 367 μm and 867 μm in diameter were used to test the PCB device. The excitation voltage was a sine wave with a frequency of 50 kHz and an amplitude of 1.0 V peak-to-peak. The histogram of the pulse amplitude and a typical pulse captured from the oscilloscope are shown in Fig. 3.20 (b). The histogram showed two peaks for beads of two different sizes. Of the 200 pulses collected for the 867 μm beads, the mean amplitude value is 2.89V with a standard deviation of 0.77V; of the 100 pulses collected for the 367 μm beads, the mean amplitude value is 0.91V with a standard deviation of 0.49V. The results show that the pulse amplitude is distributed over a certain range for beads of the same size.



(a)



(b)

Fig. 3.20 Pulse amplitude distribution and a typical pulse obtained from (a) the microfabricated sensing aperture of 100 μm and (b) the 1.3 mm sensing hole of the PCB device.

3.4.5 Discussion

A cell sensing mechanism using coplanar electrodes has been implemented into a microsensor as well as a PCB device. Comparison between the PCB device and the microsensor indicates that the sensitivity of a sensing hole is clearly related to the hole size. In order to detect smaller particles, smaller sensing holes should be used, allowing smaller spacing between the two gating electrodes. For typical blood cells in the size of 8-15 μm , we anticipate that the size of the sensing hole should be around 20-25 μm . However, smaller electrode area may increase the contribution of the electrode double layers in the base impedance, causing the sensitivity to decrease. While higher excitation frequency may reduce the effect of the electrode double layers, the use of electrode area comparable to the size of cells to be detected is expected to improve the sensitivity of the device. More surface area brings a lower resistance and higher double-layer capacitance that contributes to lower overall impedance for AC excitation. Another approach is to reduce the effect of electrode polarization by using four electrodes, with two outer electrodes for AC excitation, and two inner electrodes for voltage pickup. The inner electrodes would experience much smaller voltages across the electrode-electrolyte interface as compared with the outer excitation electrodes. This approach would require a different design of the sensor and its sensing circuit.

The histogram in Fig.3.20 (b) shows two peaks for beads of two different sizes, suggesting that pulse amplitude correlates with the bead size. There are variations, as expected, in the measured results for beads of the same size. While the coplanar-electrode sensor design is

capable of detecting single particles, the pulse amplitude corresponding to microbeads of the same size distributes around a peak value, as demonstrated in Fig.3.20. The variations can be attributed to lack of flow control in the sensing structure despite its advantage in fabrication. Observations under microscope indicate that microbeads move down to the hole in random positions instead of at the center of the hole. If the electrical field is not uniform due to the fringe effect of the electrodes, the impedance change will vary depending on the position of the bead. The effect of positional difference may be improved by adopting flow control such as hydrodynamic focusing and constant flow rate so that the beads pass through the sensing hole at the center. Whether this modification is necessary depends on how important the information about the cell size is related to subsequent manipulation.

In testing of the microsensor prototype, we also found that there was parasitic capacitance from the electrodes (including their interconnections) to the substrate. As the microsensor scales down, this parasitic capacitance may compromise the overall sensitivity. With the current design, the electrodes are separated from the substrate by a LPCVD silicon nitride layer, which is only 0.2 μm thick. The thin silicon nitride layer prevents KOH etching from the front side and is also used as an insulation layer between the metal wires and the substrate. The parasitic capacitance between the metal and substrate is in parallel connection with the impedance between the sensing electrodes, as shown in Fig. 3.18(b). Possible solutions to eliminate the parasitic capacitance include using thermally grown field oxide for insulation or completely replacing the silicon substrate with a glass substrate.

3.5. Summary and conclusion

An impedance microsensor using coplanar electrodes around vertically etched sensing holes has been fabricated using micromachining and tested on microbeads. The sensor design allows detection of single particles through the sensing hole by using localized electrical field perpendicular to the fluidic flow direction. The sensing mechanism has also been implemented into a PCB device for comparison. While both devices are capable of detecting microbeads with dimensions comparable to the corresponding sensing holes, the micro version enables the detection of much smaller particles by scaling down the spacing between the two gating electrodes. As the two electrodes on each device are utilized for both signal excitation and impedance sensing, AC excitation is necessary to reduce the electrode impedance and increase the sensitivity to impedance change due to passage of particles, with significantly higher excitation frequency for the microsensor. Modeling using a parallel RC circuit for the electrode interface shows that the microsensor has a parallel electrode resistance of 19 k Ω and a parallel electrode capacitance of 20.8 pF, as well as a parasitic capacitance of 7.1 pF to the substrate. Preliminary experiments on microbeads indicate that the pulse amplitude is correlated with the bead size. However, the pulse amplitude is distributed around a certain range for beads of the same size, suggesting the need of a fluidic control mechanism to focus microbeads to the center of the sensing hole.

Chapter 4 MICROCHIP DEVICES FOR HIGH THROUGHPUT ELECTROCHEMICAL ANALYSIS OF EXOCYTOSIS

4.1 Introduction

As we have discussed in chapter 1, exocytosis is a process of cellular secretion that is very important for signaling or life regulation. While the measurement of quantal release provides detailed information about the mechanics and regulation of exocytosis, the current method to measure exocytosis is very time consuming, expensive and labor intensive. To change this situation, we are using microfabrication technology to fabricate microchip devices, which can automatically position single cells onto micro sensing electrodes and do parallel multi-channel data recording of exocytosis. We will fabricate microfluidic channels with microelectrodes to realize automatic cell positioning and amperometric detection of small amount of chemical release such as catecholamine, a group of amines derived from catechol that have important physiological effects as neurotransmitters and hormones. This technology will enable high throughput, high accuracy and high time resolution of exocytosis measurement. It and can also greatly improve the efficiency of research and accelerate the scientific discoveries in life sciences and new drugs. This bioMEMS technology or lab-on-a-chip technology will enable us to develop new biosensors or improve the performance of existing sensors. This may bring a profound technology revolution in the field of life sciences.

Single cell analysis without cell destruction is of great importance in neuroscience and cell biology where live cells are kept in a medium and cell activities can be monitored in-vitro. This requires special design of the microfluidic system to isolate and trap single cells. Although microfabricated flow cytometers can separate cells using hydrodynamic focusing, it lacks the capability to hold the cells in a certain position for a certain amount of time. Dielectrophoresis shows great potential for cell sorting and particle trapping using electrokinetic forces^{100,101}, however, the strong electrical fields may affect and even kill the cells¹⁰², in addition, the dielectrophoresis setup requires a complicated control system. Thus a microfluidic system using flow dynamics and physical trap through careful design sounds more attractive in many applications. In chapter one we reviewed work by Yang et al³¹ demonstrating cell alignment using two parallel microfluidic channels with a dam structure in-between and a more recent report on cell trapping by Yun et al³⁰. These reports helped inspire our approach with improved capability.

The purpose of this project is to develop miniaturized microchip devices for low cost, high throughput exocytosis measurement under different stimulus conditions. Our goal is to obtain a quantitative kinetic description of exocytosis upon varying the cellular and environmental conditions (such as intracellular Ca²⁺ concentration, membrane potential, the presence of pharmacological agents, or altered cell temperature etc.). Treatment of the cells with neurotoxins is a common way to perturb exocytosis. Another approach is to introduce peptides that target specific proteins involved in exocytosis or expression of mutated proteins using molecular biology approaches.

Catecholamines are a family of chemicals occurring naturally in the body that serve as hormones or neurotransmitters. The catecholamines include such compounds as epinephrine (also called adrenaline), norepinephrine, and dopamine. They resemble one another chemically in having an aromatic portion (catechol) to which is attached an amine, or nitrogen-containing group. Epinephrine and norepinephrine are the main catecholamines secreted by the adrenal medulla chromaffin cells, and are our main targets for electrochemical measurement. These adrenaline-containing cells are called “chromaffin cells” because they were found to be easily stained with chromium salts. These hormones can stimulate cells in other organs and tissues far away from the adrenal gland. For example, adrenaline influences heart muscle, increasing the force of contraction so more blood can be pumped to the body to response to threatening situations. Release of adrenaline from chromaffin cells in the adrenal medulla can be increased up to 5 times in one response to fear, pain, etc. In the laboratory, chromaffin cells are usually collected from the adrenal glands of cattle which provide a low cost source of experimental materials in a large quantities compared to smaller animals such as mice or rats. One drawback of chromaffin cells is that, as primary tissue, they have a limited lifespan in culture of about one week. Chromaffin cells are obtained by perfusing the adrenal gland through its central blood vessel with a solution of collagenase, which breaks down the extracellular material that holds the chromaffin cells and release them from the adrenal medulla.

In this chapter, we will explore designs capable of cell trapping and select the most feasible design. Then we describe the detailed device fabrication process. Experimental setup and device test on real cell exocytosis are presented and then followed by results and discussion.

4.2 Previous work

The study of exocytosis and ion channels both focus on activities at the single cell level. Development of the patch clamp technique was first used to measure ion channel activities; it led to the first measurements of exocytosis by Neher and Marty in 1982¹⁰³. They measured cell membrane capacitance changes which were believed to be caused by the exocytotic and endocytotic processes. In fact, capacitance measurement of exocytosis is still considered to be of the highest time resolution though it is an indirect measurement and may not differentiate exocytosis from endocytosis. Another single-cell approach to study exocytosis is carbon-fiber electrochemistry. The first direct measurement of catecholamines from bovine adrenal chromaffin cells by cyclic voltammetry is done by Leszczyszyn et al., in 1990. Further study with cyclic voltammetry revealed that the temporally resolved current spikes were due to exocytosis of individual vesicles (Wightman et al., 1991). Amperometry using carbon fiber microelectrodes has become a common tool of exocytosis measurement at the single cell level.

Although the study of exocytosis has been carried out for years, only recently have people begun to develop microfabricated device for exocytosis measurement. One of the first chip devices reported to measure quantal exocytosis was from Dr. Gillis's group at MU¹. At that time, there was no microfabrication facilities at MU, so the actual fabrication of the device was done at the State University of New York at Albany.^{104,105} A 4x4 gold well electrode array was fabricated on a silicon substrate aimed at catching more secretion from a larger detection area, compared to the carbon fiber electrodes which usually only has a diameter of 10 μm . The microwell was fabricated by KOH anisotropic etch resulted in a inverted

hollow pyramid structure, which could hold a single cell with five sides of the well walls such that release capture from a large fraction of surface area is possible. Fig. 4.1 shows the schematic fabrication process of the micro well chip device and Fig. 4.2 shows a fabricated microwell with gold electrodes and the final chip device packaged into a conventional DIP IC package. Although this design has an array of sensing electrode with larger sensing electrode area, there is a need to manually position cells into the wells. This problem limits the practical applications. Obviously, an improved design with automatic cell positioning capability is necessary.

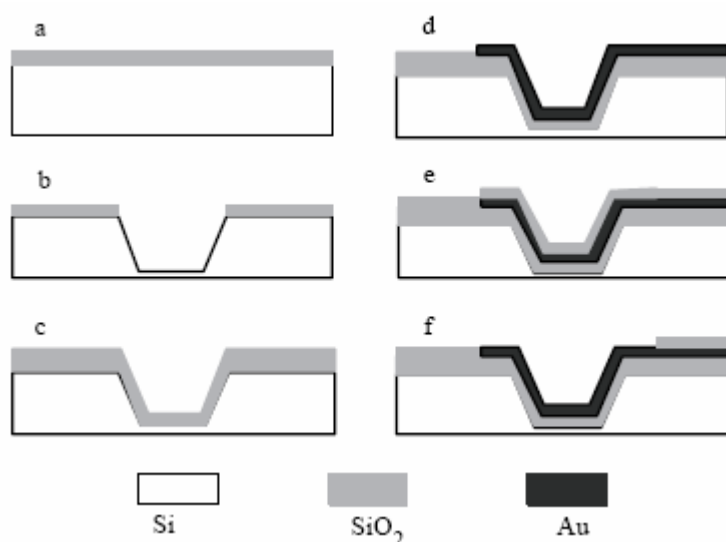


Fig. 4.1 Microfabrication process flow of the micro well chip device. A) 500 nm SiO₂ is deposited by low pressure chemical vapor deposition (LPCVD). b) Following patterning of the SiO₂, anisotropic etching with KOH creates the microwells. c) SiO₂ is deposited by plasma enhanced chemical vapor deposition (PECVD) to insulate the bulk silicon substrate. d) Following coating and patterning of photoresist, Cr (20 nm) and Au (0.5 μm) are evaporated. After liftoff, electrodes, conducting traces and bonding pads are formed. E) Deposition of an additional layer of SiO₂ by PECVD passivates the conducting traces. F) SiO₂ is removed from the wells and bonding pads by buffered oxide etching.

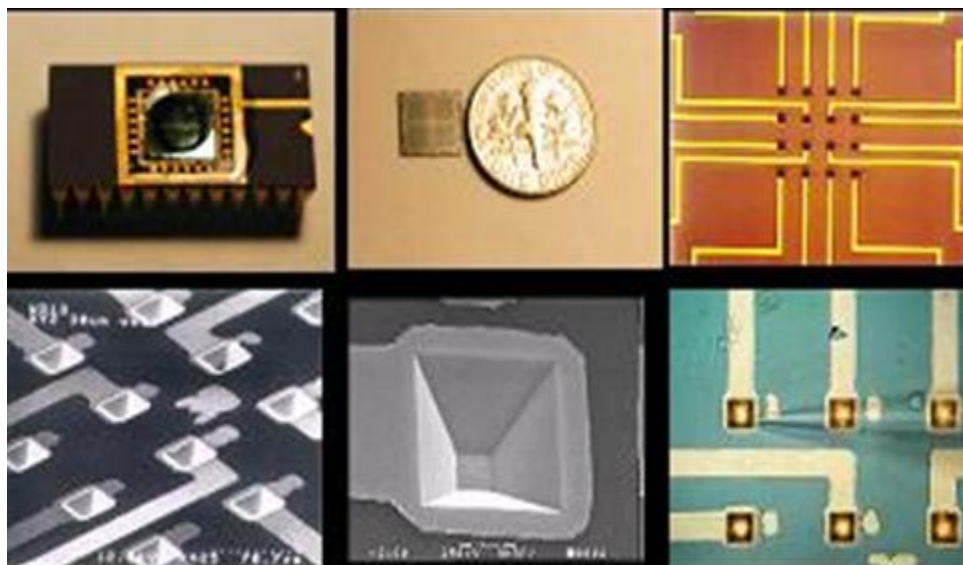


Fig. 4.2 The first generation of the micro well electrode device. From the left of top row and clock wise: a) The overall picture of the packaged device in a DIP IC package b) the device die compared to a dime coin c) the electrodes array on the die d) cells manipulated in a well with a patch clamp micropipette e) SEM picture of a fabricated well with gold electrode, f) a close up SEM view of the electrode array.

4.3 Device design comparison and fabrication process overview

A principle challenge of the device design is automatic positioning of single cells on to microelectrodes. Of course, after the positioning, the cell should remain stable during the stimulation and recording experiment. Ideally, the device should also allow different stimulation methods so that exocytosis can be conveniently stimulated and recorded. In order to explore possible designs satisfying our requirements, we will discuss several possible approaches, sorted into 3 categories, the vertical approach, the horizontal approach and the surface attachment approach. The first approach is a modification of the micro well chip design discussed in section 4.2. Following the fabrication of a 2-3 μm through hole at the bottom of the well, application of suction across the chip could trap cells in the wells by the movement of solution. Another modification could be making the sensing electrode on a planar film, and punch holes on the film. The horizontal approach will use microfluidics

to transport the cells into docking positions where sensing microelectrodes are located. Microchannels and reservoirs can be fabricated onto different substrates. The designs and fabrication processes of all three approaches will be given and pros and cons will be analyzed and compared. Then, we will focus on the horizontal approach of microchannels implemented in a silicon substrate.

4.3.1 Vertical approach, planar electrode with vertical through hole design

Although it appears straightforward, addition of a small suction hole at the bottom of the well electrode is a challenging fabrication process. It is not easy to fabricate the 2-3 μm through hole on a substrate with quite a few hundred μm thickness. First, the through hole size has to be well controlled. If the size is too big then the cells will pass through the hole when suction is applied since the cells are easily deformable. On the other hand, if the hole is too small, then the solution flow may not be enough to attract the cell and trap it in the well. Thus we need a process with very good size control. Second, it is almost impossible to etch 2~3 μm holes through a wafer, available etching processes have limited aspect ratio. Efforts have been tried in the second generation of the micro well chip device. The main idea is to reduce the thickness of the wafer in a small portion to keep the aspect ratio of the through hole. The design idea is to use DRIE to etch silicon wafer from the bottom side for a depth of 300 μm . This deep etch is a big well where the array of micro wells will be etched on the top side in the following steps. Then, it is patterned from the top side and use KOH anisotropic etch from both sides. Timed etch are used to control the etch size. The simplified fabrication process is shown in Fig 4.3. The wet etching process is not easy to

control and give very low yield. The final opening is varied from 1 to 10 μm or even bigger. Another reason is the etching from both sides. When etching from one side using anisotropic etching, the well size could be controlled very well due to etch stop planes in silicon single crystal. Even some over etching will be ok since at the etch stop $\langle 111 \rangle$ planes, the etch rate is very small. But, if etching from both sides, when two sides meet at the sharp edge where all crystal planes converge, the interface is very complicated and the etch stop plane no longer works. The direct result is that the opening size could hardly be controlled during the etching process.

As we can see from the above process, it does not have a good control over the opening. The timed etching and etch from both sides are not able to precisely control the well opening, especially at the sharp edge where the crystal plane meets. We need to find alternative method to control the etching process. When we look carefully into the wet etching mechanism of single crystal silicon, there are a few possible improvement of the process, including other ways to avoid direct control by using anisotropic etching. These possible improvement could be:

- 1) Planar electrodes on thin film
- 2) Planar electrodes on silicon on the top of an upright pyramid well
- 3) SOI design with well controlled silicon layer thickness

I. Planar electrodes on thin film

This method avoids the use of anisotropic etching of silicon to control the small opening. The through hole and sensing electrodes will sit on a thin silicon nitride film. First, a silicon nitride film is deposited on silicon, and then ring shape sensing electrodes are

patterned on the nitride film. Another layer of silicon nitride is deposited on top of the metal electrodes for insulation purpose. The small opening is then controlled by patterned photoresist using photolithography; the hole is in the center of the previously patterned ring electrodes and opened by a following RIE etching process. The RIE etching process opens the through hole and also expose the sensing electrodes. Then the backside of the wafer is patterned with a large square and silicon nitride film is removed for KOH etching. The whole wafer will be etched through until the top layer of silicon nitride film. Thus the sensing electrodes and through holes are all on a thin silicon nitride film with well controlled sensing electrodes and through hole. This can be used for automatic cell positioning when gentle suction is applied from underneath. The simplified fabrication process is shown in Fig. 4.4.

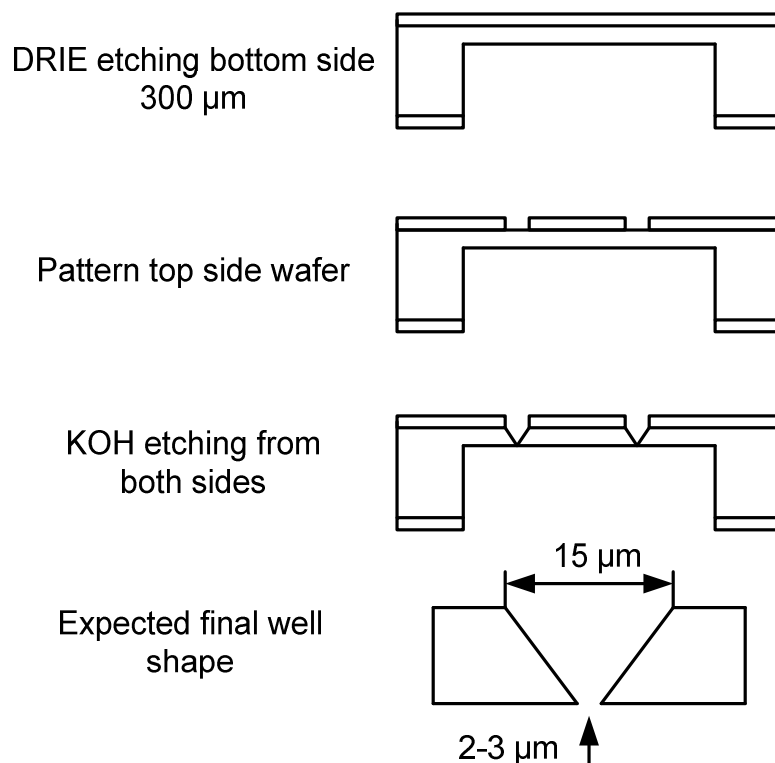


Fig. 4.3 Simplified fabrication process for the second generation of the micro well device, device with a small through hole at the bottom of the well.

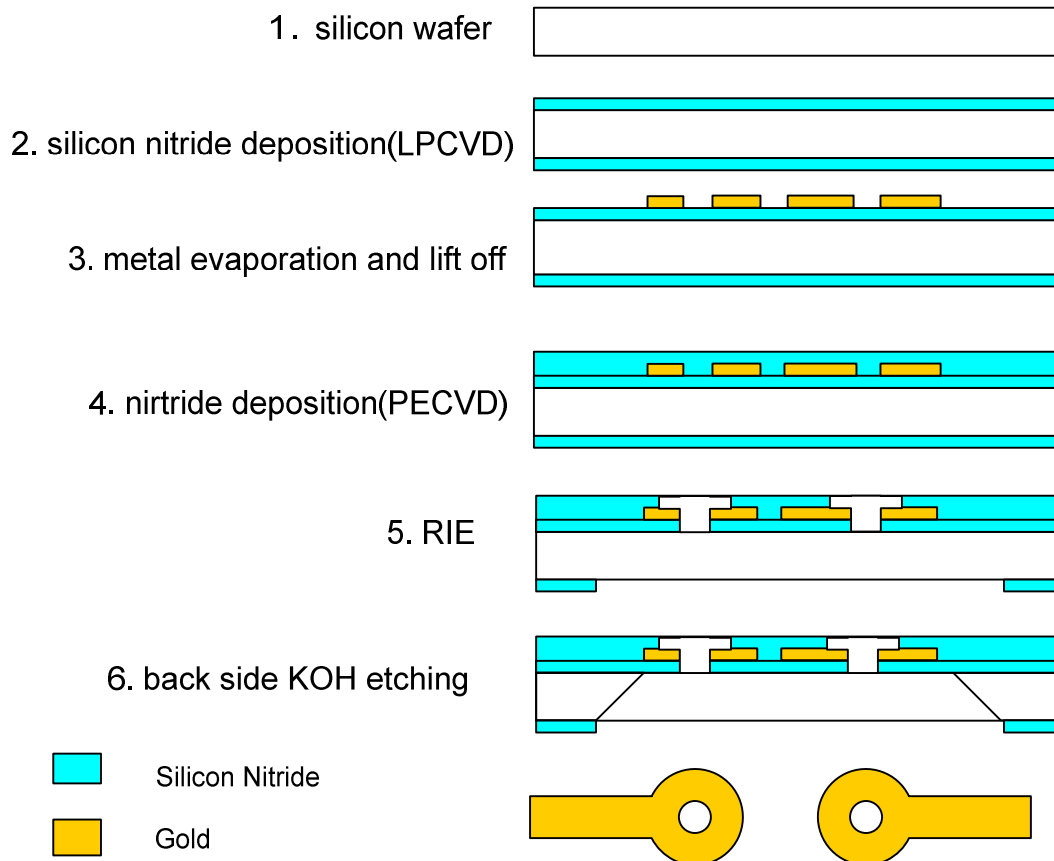


Fig. 4.4 Fabrication process for the planar electrodes on thin film design, 1-6 cross section view, the bottom picture is the top view of the patterned sensing ring electrodes with opening in the center.

The advantage of this design is that the size of the suction opening and positioning position can be precisely controlled by photolithography and RIE etching. Also, the backside alignment accuracy is not critical. The disadvantages are: 1) the planar sensing electrode area is reduced compared to the well electrodes 2) cells are positioned on a suspended thin film and thus, the device may not be so robust.

II. Planar electrodes on silicon on the top of an upright pyramid well

This method is similar to method (1), instead of letting a thin film to hold the cell and the sensing electrodes. It is possible to fabricate the electrodes on bulk silicon with a through hole. The idea is to pre-sort wafers by thickness or order a set of wafers with well-

controlled thickness. As shown in Fig. 3.10 in chapter 3, the opening of the suction hole could be well controlled if the thickness of the wafer is well controlled since in the (100) wafers the crystal plane angle is fixed. The fabrication process is very similar as shown in Fig. 3.12 in chapter 3. The advantage of this method is that the device will be robust without fragile thin films and thus can be reused many times. The disadvantage of this design is that we need silicon wafers with thickness very well-controlled. Another disadvantage is that the sensing array may not be as compact as method (1) since the pyramid shaped opening at the backside of the wafer is much larger and occupies lots of silicon die area. If there is difficulty to use the LPCVD silicon nitride process, the process can be modified to use silicon dioxide by thermal oxidation. A thick SiO₂ layer (>1.5 μm) can be grown using wet oxidation as the KOH etching mask, the etching area can be exposed by removing the SiO₂ by HF etching. Both side will be protected by photo resist when the HF etching is performed except for the etching area.

III. SOI design with well controlled silicon layer thickness

Is there a design which can keep the advantages of the well electrode design and at the same time it can be fabricated with a feasible well controlled fabrication process? The answer is yes. A design based on SOI (Silicon On Insulator) wafer makes it possible. On a SOI wafer, we can define the profile of the well size and bottom opening by the thin silicon layer on insulator, the thickness of this layer is well controlled by the wafer manufacturer. For a well to hold a single cell, the thickness is in the range of 10-15 μm. According to equation 3.2, if there is a 2 μm opening with a 15 μm silicon layer, the size of the etching square pattern on top of the silicon wafer would be:

$$L_{top} = d + 2t \times \text{ctg} \alpha = 2 + 2 \times 15 \times \text{ctg} 54.74 = 23.2 \text{mm} \quad (4.1)$$

While the opening of the sensing well is well controlled by the thin silicon wafer, the bulk silicon underneath the oxide layer may have some variations. Thus, this variation should be considered when calculating the bottom etching opening size. There are two options as shown in method 1 and method 2. We can either adopt the design similar to method 1 with a large suspension of film, or we can use the design in method 2 where each individual well has a bigger pyramid hole underneath. The overall process can be described as follows:

1. Start from a SOI wafer, with a thin Si layer thickness well controlled ($\sim 15 \mu\text{m}$) on SiO_2 . The well profile and opening is defined by this layer.
2. Silicon nitride deposition by LPCVD on both sides of the wafer
3. Spin coat photo resist and pattern with etch mask ($23.2 \mu\text{m}$ square)
4. RIE etching to expose the square for KOH etching
5. KOH etching until stop at SiO_2 layer
6. PECVD nitride deposition on top layer to insulate the exposed silicon layer
7. Metal deposition and lift-off to pattern the well electrodes and the contact pads.
8. PECVD nitride deposition again to passivate the metal electrodes
9. Pattern top layer and RIE to expose the sensing well electrodes and contact pads
10. Back side patterning with photo resist and RIE etching
11. Back side KOH etching

The advantage of this design is obvious in that it has well-electrodes with better sensing capability and automatic positioning and can be fabricated with a well-controlled process. The disadvantage is that SOI wafer is expensive and the process is a four-mask process, involved in more process steps and one more mask than the previous two processes.

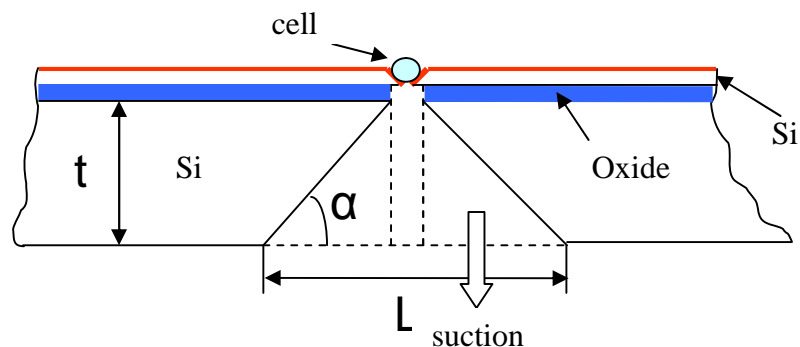


Fig. 4.5 The schematic design, etching profile of the device on SOI wafer and working principle of automatic positioning by suction

4.3.2 Horizontal approach with microchannels

One drawback of the vertical approach is that the action range or radius of the suction force may not be wide enough. If there are no cells close enough by the suction hole, the wells will not be able to be attracted to the hole. If too much suction is applied, the cells already on top of the electrode may be damaged or squeezed through. Another drawback is that the solution may dry soon and cells can stack or coagulate together. Yet, in another aspect, stimulation of exocytosis may not be fast enough. An alternative design to the vertical approach is the horizontal approach where the above problems can be overcome. Microfluidic channel allows cells to flow inside the channel with much less evaporation so that very small amount of drugs or reagents is needed. The cell can be trapped inside a microchannel for longer time and it also allows rapid exchange of extracellular fluid for cell exocytosis stimulation. Glass-glass or glass-PDMS bonded microchannels are transparent such that the cells can be seen through from both top and bottom for observation and optical detection. Glass-glass wafer bonding requires a very high temperature ($>650^{\circ}\text{C}$, fusion thermal bonding) and the channel shape or profile can not easily controlled using current etching techniques. Instead, It is relatively easy to etch

microchannels in Si wafers and anodically bonded (field assisted thermal bonding) with glass or PDMS (polydimethylsiloxane) after oxygen plasma treatment. We can also use reversible bonding with PDMS with an oxide layer to allow device reusability.

There are basically two configurations in the horizontal approach, the series configuration and parallel configuration. The series configuration is simpler in design in which one or more electrodes are patterned perpendicular to the flow channel. Electrodes can be first deposited and patterned on a glass wafer, then bond with a piece of PDMS with molded channel and injection reservoir. The simplest design can only use one electrode theoretically if the cells can be stopped right at the electrode. Then only one amplifier is needed and it cost less in hardware for amplification and data acquisition. But practically, it is very difficult to stop a cell at a 20 μm electrode in a dynamic cell flow environment inside a microchannel.

A more practical way is to adopt a parallel design with cell traps along the cell flow channel as shown in Fig. 4.6. When cells flow from top to bottom, they will be trapped at the docking positions by a lateral force from the flow solution. Multiple cell exocytosis can be measured simultaneously with a multiple channel data acquisition under this automatic cell trapping method. Thus it can greatly automate the exocytosis measurement process with high throughput. Cell-sized micro sensing electrodes are patterned at the trapping positions which have the similar size of single cells. This trapping mechanism can have a space resolution of cell secretion since the cells are placed as close as possible to the

sensing electrodes. High speed data acquisition will enable high time resolution measurement.

I. Channels created in Si wafer

Although a Si substrate is not transparent, it is relatively easy to etch channels in Si by wet etching. In addition, by anisotropic etching, the profile of the channel is easier to define and control. There is also a mature process for Si-glass or PDMS-SiO₂ bonding so we can have transparent channel on one side. Silicon is the most commonly used material in the microelectronics industry and many micromachining processes are available and, more importantly, it has the potential to integrate CMOS circuitry with the MEMS structure and thus achieve complete lab-on-a-chip devices.

Our goal here is to carry out the parallel measurement of exocytosis in microfluidic channels with automatic cell docking. In the parallel approach, two channels are created in parallel, one connected to the cell reservoir with some “notch” like features along the cell channel and the cells will be docked in those positions as the fluid flows along the channel and to the neighboring waste channel. Two or three reservoirs can be implemented, one is the cell reservoir, the other is the waste reservoir, the third one is the stimulation solution reservoir. The last one may not be needed depending on the stimulation method. Two channels from the cell reservoir and the stimulation solution reservoir meet together at some point and form the cell channel, which runs parallel to the waste channel. The two channels are connected by the middle passage in between. The passage could be small channels or a dam structure in which the whole middle part has a height slightly (2 μm) lower than the wafer surface such that the solution can flow through the dam to the other channel while

the cells are too large and thus become trapped. This kind of structure will flow cells to docking sites with a “notch” shape where electrodes are patterned underneath. By doing this not only can we realize fast fluid exchange; but also, we can realize parallel measurement of cell exocytosis.

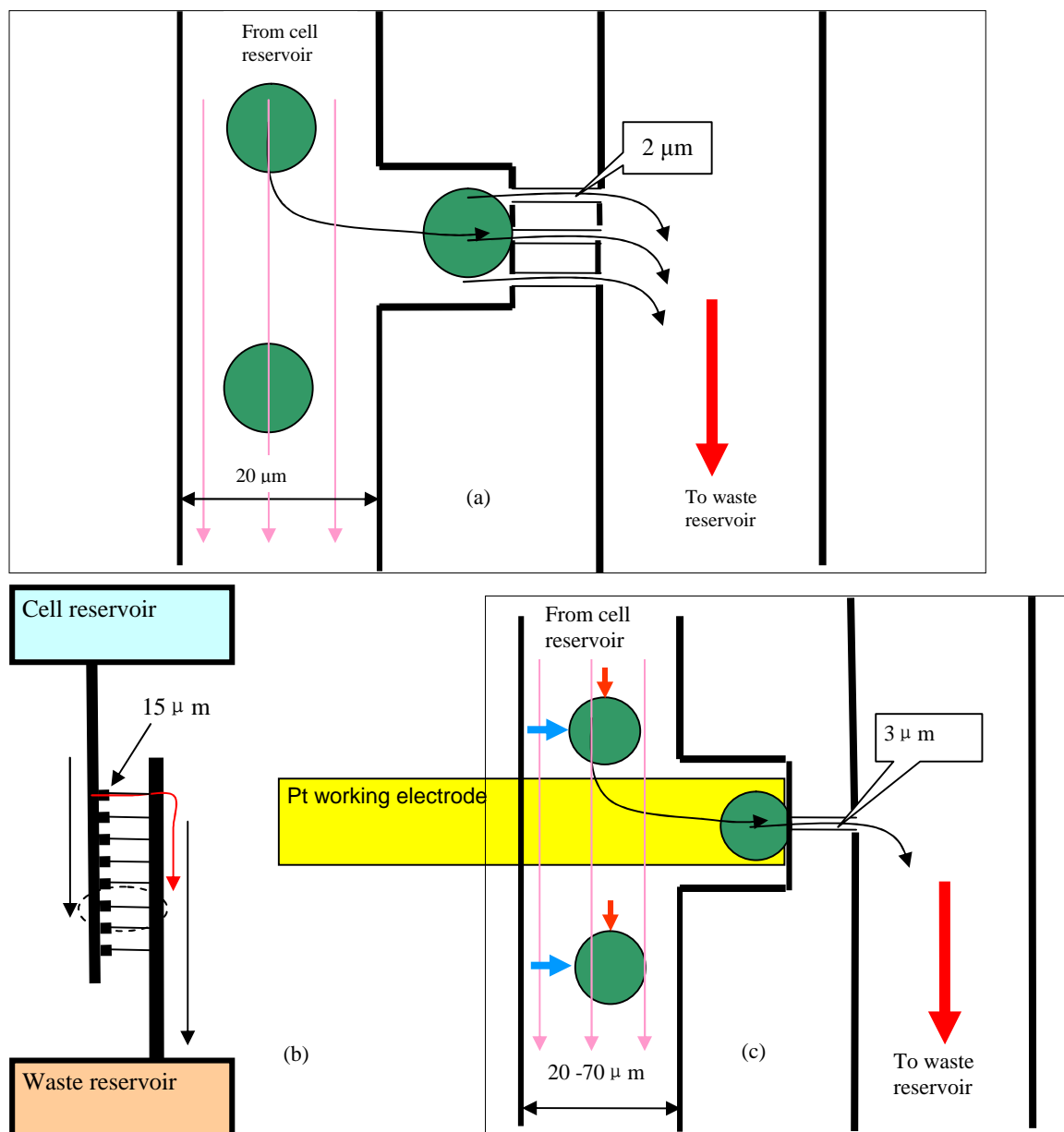


Fig. 4.6 Schematic design of parallel channel with cell docking, cell flow channel width $20\ \mu\text{m}$, cell diameter is about $10\ \mu\text{m}$ and dock width is about $15\ \mu\text{m}$. there are small channels with $2\ \mu\text{m}$ width connecting the two main channels. (a) Cell trap position with 3 passage channel, (b) simplified design with two reservoirs and the parallel running channel, (c) cell trap with one $2\ \mu\text{m}$ passage channel and a sensing electrode

1) design 1, small passage channel between the cell flow channel and the waste channel

The schematic design of the overall structure and the cell docking position with small passage channel between the two main channels is shown in Fig. 4.6. The arrows show the flow direction. The three 2 μm -wide small channels ensure solution flow even if the cell blocks on of the narrow channels. The flow also allows a stimulation solution to perfuse the cell such as a high potassium solution. Due to some crystal plane misalignment during the wafer manufacturing process, misalignment during the photolithography process and the resulted undercut in wet etching, the small passage may widen after etching. The three small channel may merge together and damage the original design in a wet etching process, so we only adopted a simplified design of only one passage channel as shown in (c). This is what we used in our actual device. The channel depth would be $2 \mu\text{m} * \text{ctg}54.74 = 1.4 \mu\text{m}$.

Fabrication process(cross section view as shown in Fig. 4.7):

- a) start with <100> 2" wafer
- b) oxidation, grow a thin SiO₂ layer(300nm)
- c) spin coat photoresist and pattern by lithography
- d) Buffered HF etching to remove SiO₂ to expose Si for KOH etching
- e) KOH etching: 1 $\mu\text{m}/\text{min}$ for 20 mins for 20 μm deep channel and reservoir.
- f) Deposit and pattern metal electrodes into channels
- g) Anodic bond to a glass slide.

A possible problem for this process is that there may be undercut at the corners of the feature. The deeper the channel, the more serious the undercut. The alternative design to avoid wet etching would be silicon dry etching like deep RIE (DRIE) or using PDMS replica molding technique to create channels in PDMS instead of silicon. Deep silicon RIE

etching (e.g. Bosch process) is very useful for MEMS fabrication. We can create channel and docking in one etch step with high quality and high aspect ratio in silicon wafer. But the DRIE equipment is extremely expensive, a state of the art system cost at least half a million dollars. The draw back of this process is that metallization is difficult at high aspect ratio deep channels. This can be resolved if the electrodes can be patterned on the glass, a much simpler process, but, we need a bonding machine with alignment capability such as EV501 anodic bonder.

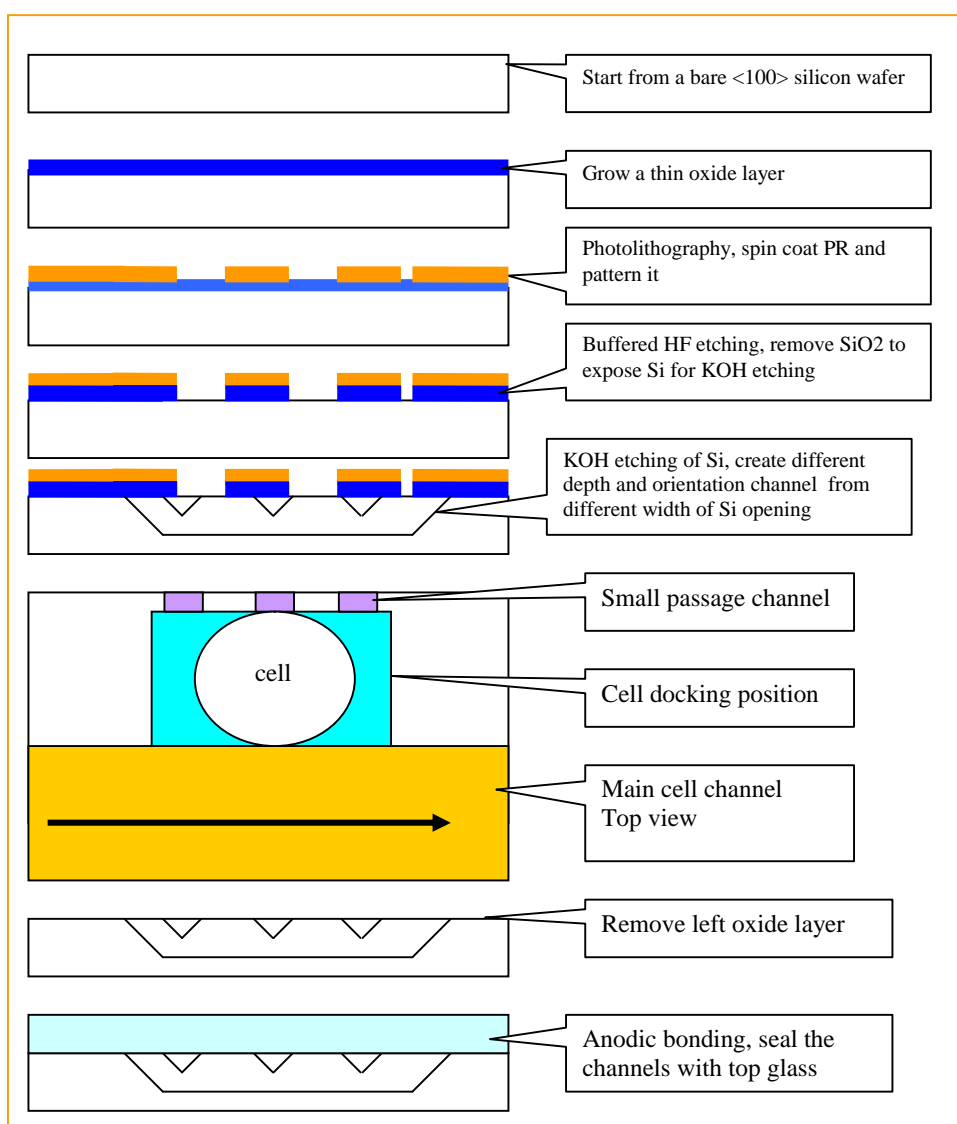


Fig. 4.7 Cross section view of the simplified fabrication process for design 1.

2) **design 2, small dam structure**

For the small channel passage design, it is possible that the small channels may be easily blocked by cell or the debris of damaged cell. In addition, flow resistance is very large due to high resistance tension in very small channels. Practically, small features as small as 2 μm are very close to the limit of contact photolithography and greatly increase the process difficulty. Other processes like wet etching have similar practical difficulty. To address these problems, an alternative design would be a dam structure. Yang et. al³¹. proposed such a structure in glass without trapping positions for cell docking as reviewed in chapter one. Here, we design an improved dam structure with special cell trapping position and sensing electrodes underneath the trapping position so that we can localize and measure single cells. In this design, instead of using one or more small channels as the connection between the cell and the waste channels, a continuous shallow dam structure is etched between the cell channel and the waste channel. The dam has a shallower depth around 2-3 μm , while the flow channel has a depth around 15 μm . Compared to the small channel passage, a continuous flow can be maintained easily all along the dam length which can be as long as the two parallel flow channels. So, even if partial width is blocked by a cell, there is still a flow going through the unblocked area thus eliminating the chances of the blockage of the channel. Also, due to larger flow passage, flow resistance is much lowered. The ideal case is that cells will be automatically brought to the docking positions without any external suction or positive pressure to maintain the flow. The schematic design of the dam structure is shown in Fig. 4.8. The fabrication is a two mask process for creating the channels and we need alignment for the two masks. Including additional processes like

metal deposition-liftoff and insulation layer for the electrodes, the whole process need four masks. We can create the dam channel first or the main channel first.

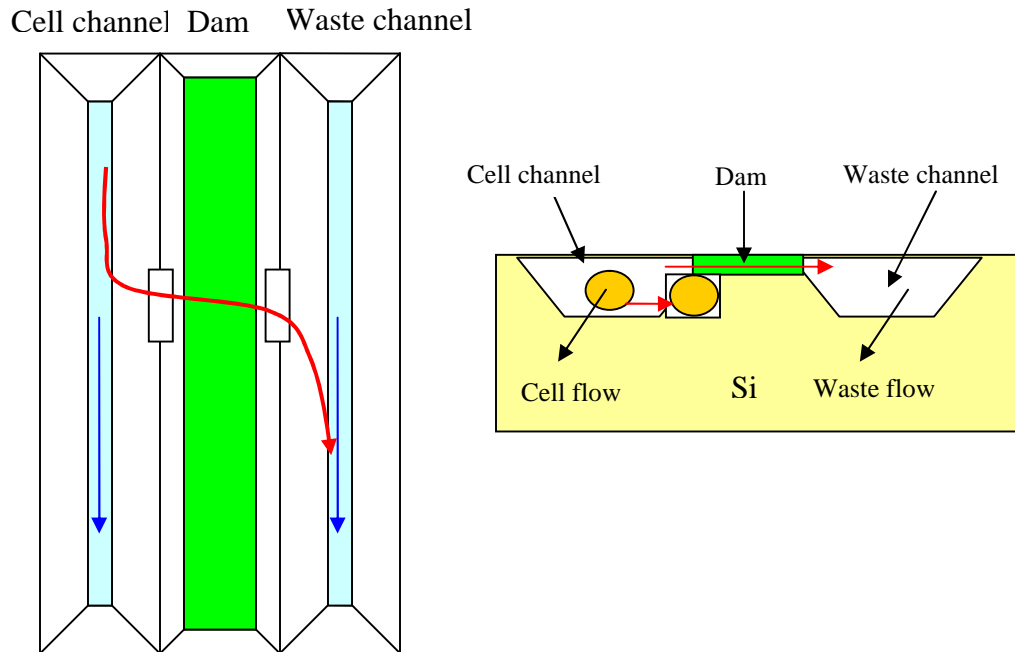


Fig. 4.8 Schematic design of the dam structure, top view and cross-section view; the profile of the channel shown is after anisotropic etching, the middle green color is the dam channel which connects two main channels, with a much shallower depths(2~3 mm)

Fabrication process for the dam structure:

- a) start from $\langle 100 \rangle$ 2" wafer
- b) grow a 300 nm silicon dioxide layer
- c) Photolithography pattern the dam structure
- d) BHF etching remove oxide layer over the dam structure
- e) KOH etching, etch the 2 μm dam structure
- f) Grow another 300 nm oxide layer to cover the dam channel
- g) Do photolithography again to pattern the reservoirs and flow channels, need align to the already etched feature
- h) BHF etching remove oxide layer over the reservoirs and flow channels
- i) KOH etching, etch the 20 μm reservoirs and flow channels
- j) Remove the remaining oxide layer

- k) Rinse wafer and check etched feature
- l) Anodic bond to the glass substrate with metal electrode already patterned or alternatively reversibly bonded to PDMS so that the chip can be more easily cleaned and reused.

II. Channels created in PDMS

PDMS (polydimethylsiloxane) is a very attractive MEMS material especially for microfluidic devices. It is optically transparent and generally considered to be inert, non-toxic and non-flammable. It has been widely used in several microfabrication or nanofabrication methods collectively known as soft lithography. PDMS has been used to fabricate microchip electrophoresis systems with amperometric detection.^{106, 107} Soft lithography is well-suited for applications in biotechnology, plastic electronics, and applications involving large or nonplanar surfaces due to the unique properties of PDMS such as biocompatibility, flexible and quick molding capability. When making a PDMS device, a master is first fabricated which is often patterned photoresist on a flat and smooth substrate like silicon or glass wafer. Many other types of molds can be created, e.g. by wet or dry etching into silicon, glass, PMMA. Whereas fabricating the master requires photolithography or etching, the replica molding step is much simpler and straight forward. The PDMS prepolymer mixture is cast over the master and the device is ready after the PDMS is cured. It is fast, repeatable and convenient. The master can be reused many times.

The advantage of channels created in PDMS is that the channels will have a well controlled profile, without the undercut problems that accompany silicon wet etching. The disadvantage is that there is aspect ratio limit for the PDMS channel or reservoir since the soft PDMS may collapse if the aspect ratio of width to height/depth is too large, Another disadvantage is that it is extremely difficult to deposit metal electrodes onto PDMS

material. High resolution alignment during PDMS bonding with other substrate may be difficult. Although we did not implement a device where microchannels are created in PDMS, we can see that PDMS process is very promising in this kind of application.

- 1) Planar electrodes are easy to deposit and pattern, pattern electrode into channels is more difficult.
- 2) By using glass substrate and transparent electrodes such as ITO and DLC, complete transparent devices can be constructed thus allow optical method to stimulate exocytosis such as caged calcium.

III. Electrodes and channels layout

One of the important purposes of the project is high throughput measurement which requires a number of sensing electrodes. One way to make full use of the die area is to design two pairs of microfluidic channel and align sensing electrodes along the right and left side as shown in Fig. 4.11. A total number of thirty electrodes are designed with 15 on each side with symmetric alignment. The contact pads occupy the most die area since there is a minimum size requirement for wire bonding. Obviously, this design can double the electrodes on similar die area as compared to the one side design shown in Fig. 4.11 (b). If more electrodes are needed, the electrodes can be laid out on top and bottom side of the two reservoirs. Some other channels of different sizes can be put in between the two channels with sensing electrodes to help establish the flow between the cell reservoir and the waste reservoir. Another idea is to adopt bigger cell flow channel with escape channel at the end. Bigger channel facilitate cell flowing, the escape channel will further facilitate flow and can release extra cells in the cell flow channel.

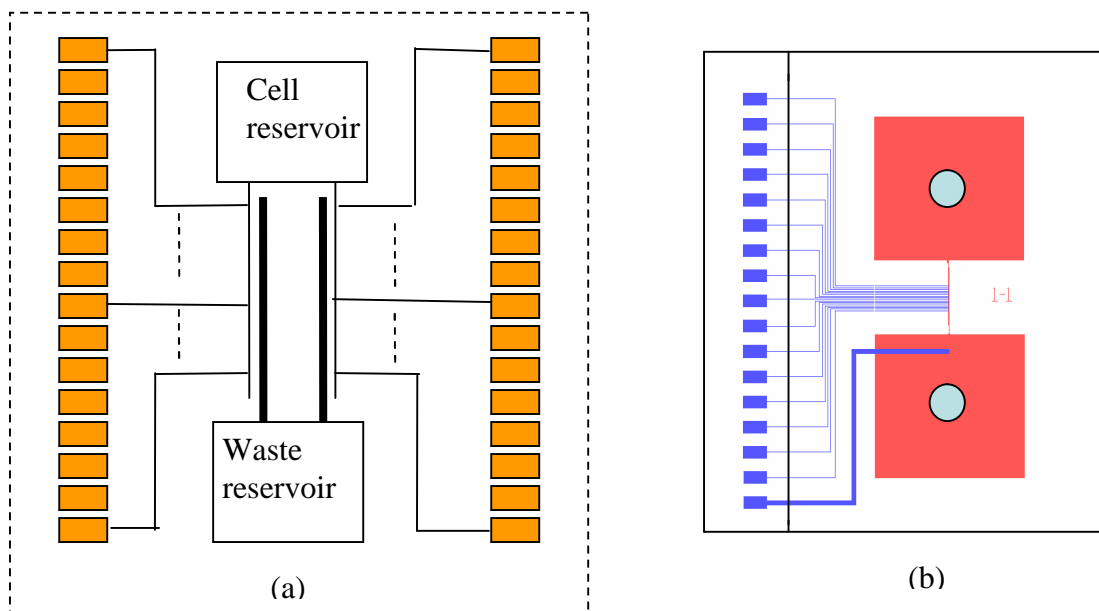


Fig. 4.9 Schematic design and electrodes layout of the device. (a) Two pairs of flow channels are designed between the two reservoirs, contact pads are aligned on both sides of the channels. (b) Only one pair of flow and waste channel, sensing electrodes and contact pads are laid out only on one side, the number is only half the right side design.

The detailed design parameters are as follows: Overall size of the die is 18mm x 18mm. The number of sensing electrodes is thirty and the wire width is 20 μm . The reservoir size is 3mm x 3 mm, distance between two reservoirs is 10 mm(center to center). The docking position size is 10 μm x 15 μm and actual size will be larger due to corner undercut in anisotropic etching. The distance between docking positions is 80 μm Although a total number of 96 docking positions are designed, only the center thirty docking positions have sensing electrodes. Four channel widths of 20, 30, 50, 70 μm are laid out to study docking and flow performance of different channel sizes. Total contact pads occupy a die area of 13mm(w) x 15.5 mm(h), contact pad size is 0.5mm x 1mm with a center to center distance or pitch of 1 mm. The two columns of contact pads for electrode connection can be designed to be compatible with the normal DIP IC package in semiconductor industry. The

actual design as a screen shot from L-Edit is shown in Fig. 4.12 and the overall layout on a 2" wafer is shown in Fig. 4.13.

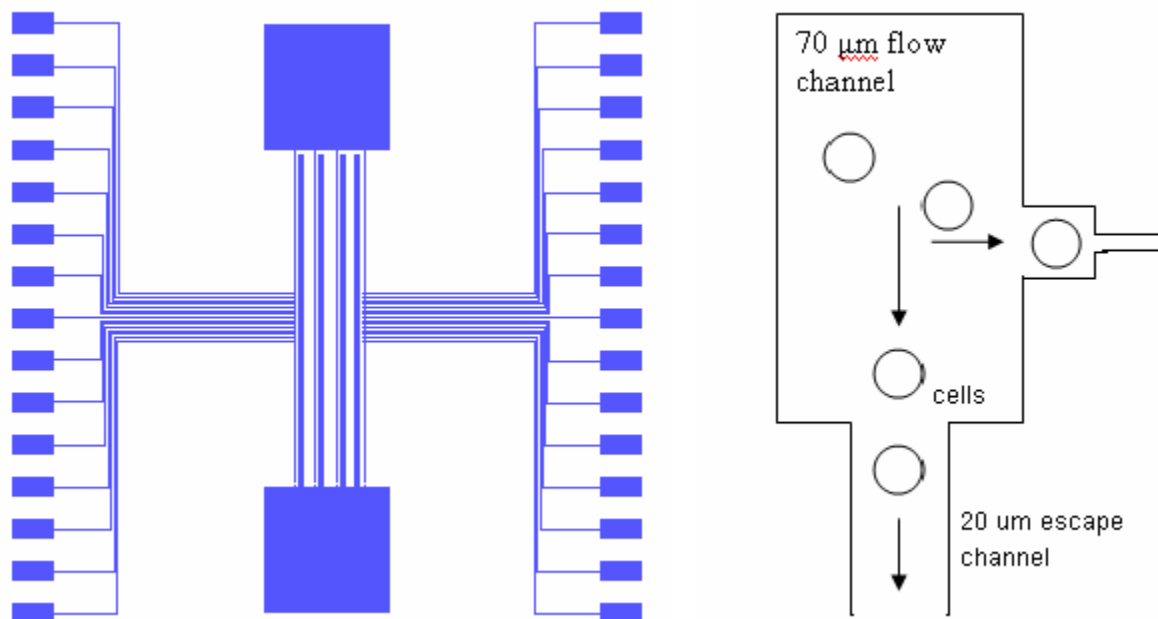


Fig. 4.10 Screen shot of the device design from CAD tool L-Edit and the idea of escape channel

IV. Bigger size with escape channels

The original idea of using 20 μm channel with 2 μm passage channel is try to control the cells flow one by one into the channel and not let the cell squeeze through the passage channel. But, there are some practical problems. The first problem is the difficulty to get the cell and solution to flow. We have seen that cells do not easily flow into a 20 μm channel and the cells are easily clogged at the entrance of the 20 μm channel. The other problem is due to the small size of the 2 μm channels, it is not easy to get a good flow of solution because of the high resistance. We will keep the 20 μm channel to try to confine the cells to flow one by one. We decided to also test larger channels with sizes of 30, 50 and 70 μm for comparison. We changed the passage channel size is changed to 4 μm .

Another change to promote docking of individual cells was to add a 20 μm cell escape channel at the bottom of the cell flow channel as shown in Fig. 4.12. The extra cells in the cell channel will leave from the escape channel while the already docked cell will remain in the docking positions. The escape channel should be small enough as not to divert too much flow from the trapping channels.

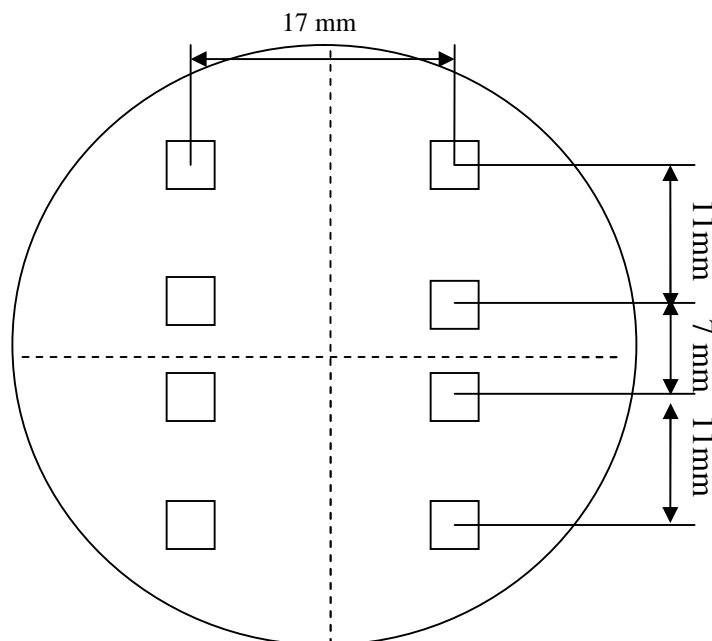


Fig. 4.11 Device layout on a 2" wafer, 4 devices are laid out.

4.3.3 Fabrication process overview

I. Oxidation

After the discussion of the possible designs, the next step is to implement the designs into practical fabrication procedures, which include many processes. Since we do not have the LPCVD silicon nitride process in our laboratory currently, we use silicon oxide layer as the mask layer and insulation layer. Thus, the first process is the oxidation process. In order to develop this process, we built a thermal furnace which is much simpler than a LPCVD

process. A Lindberg furnace with three heating zones was used to build the furnace with six inch diameter quartz tube with the maximum temperature of the furnace as 1100 °C. The furnace uses resistive heating with EuroTherm 847 temperature controller to control the heating procedure by PID control. If only pure oxygen is used, it is called dry oxidation. If only water steam is used, it is called wet oxidation and if it is a mixture of oxygen and water steam, we call it wet oxygen oxidation. The difference between the three oxidation methods lies in the oxidation speed and the film quality. Dry oxidation is the slowest but produces the best quality oxide. The schematic and the actual built thermal furnace are shown in Fig. 4.14. For wet oxidation, we can run oxygen through a bottle of water with a temperature close to the boiling point on a hotplate.

The oxidation process is a diffusion limited process since once oxide layer is formed on the surface of silicon wafer, oxygen can only react with silicon by diffusion. Oxidation involves a volume expansion ($\sim 2.2x$) and is amorphous even grow on a crystalline substrate. To study and predict the thickness of the oxide layer, many SiO₂ growth kinetics models have been proposed, among them, the most famous one is the Deal-Grove model¹⁰⁸. The Deal-Grove model can be mathematically shown in equation 4.1 with parameters given in table 4.1. By implementing the model and plotting the curves, we can look up the time need for a certain oxide thickness or vice versa at a chosen oxidation temperature. An example plot is shown in Fig. 4.15 implemented in Matlab (Mathworks Inc.), for temperatures of 1000°C, 1100°C and 1200°C.

$$x_o = \frac{A}{2} \left\{ \sqrt{1 + \frac{t+t}{A^2/4B}} - 1 \right\} \quad (4.2)$$

$$\text{Where } t = \frac{x_i^2 + Ax_i}{B}$$

$$B = C_1 e^{(-E_1/kT)}, \quad \frac{B}{A} = C_2 e^{(-E_2/kT)}$$

Table 4.1 Deal-Grove model parameters.

Ambient	B	B/A
Dry O ₂	$C_1 = 7.72 \times 10^2 \mu^2 \text{ hr}^{-1}$ $E_1 = 1.23 \text{ eV}$	$C_2 = 6.23 \times 10^6 \mu \text{ hr}^{-1}$ $E_2 = 2.0 \text{ eV}$
Wet O ₂	$C_1 = 2.14 \times 10^2 \mu^2 \text{ hr}^{-1}$ $E_1 = 0.71 \text{ eV}$	$C_2 = 8.95 \times 10^7 \mu \text{ hr}^{-1}$ $E_2 = 2.05 \text{ eV}$
H ₂ O	$C_1 = 3.86 \times 10^2 \mu^2 \text{ hr}^{-1}$ $E_1 = 0.78 \text{ eV}$	$C_2 = 1.63 \times 10^8 \mu \text{ hr}^{-1}$ $E_2 = 2.05 \text{ eV}$

To better control the thickness of the oxide layer, several precautions need to be taken. First, we have to wait until the furnace is at the right temperature before inserting the wafer boat into the tube. The wafer can be loaded into the furnace first but must stay at the entrance and wait until the desired temperature is reached. Then the wafer boat is gradually push into the heated zone. Second, oxygen flow should start after the preset temperature is reached and the wafer loaded to the position.

Since we use SiO₂ as the KOH mask, we need a thickness that can withstand the long duration (> 20 min) KOH etching. This time is calculated from a channel depth of 20μm and etching rate of 1 μm/min. The etching rate of SiO₂ at 40% KOH at 80 °C is about 20 Angstroms/min. A silicon dioxide layer of 300 nm is sufficient to withstand the etching.

According to the Deal-Grove model, 18 minutes oxidation time is needed for 300 nm oxide thickness at 1100 °C when using wet oxidation. The actual thickness of the silicon dioxide layer can be measured by ellipsometry.

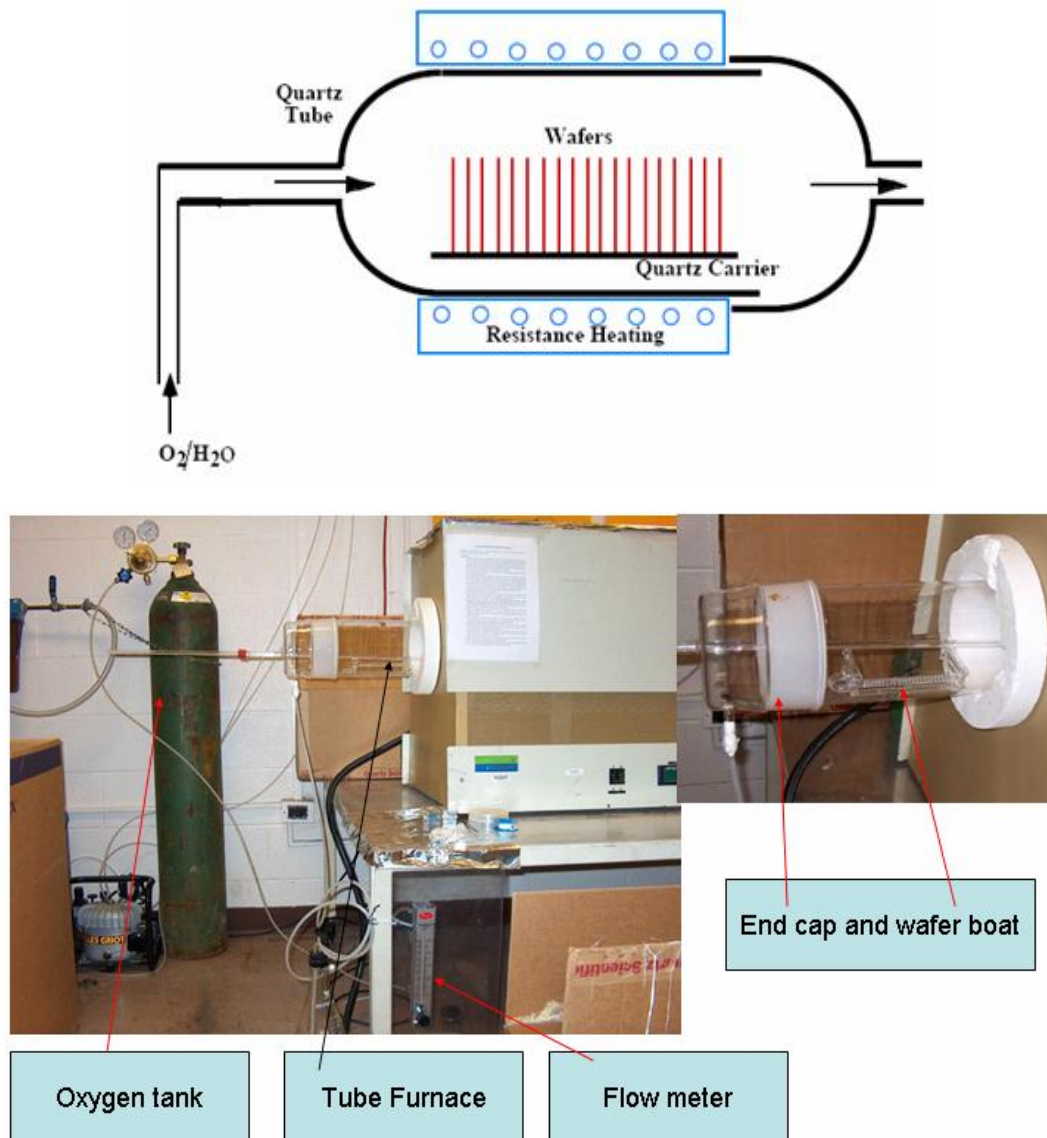


Fig. 4.12 The schematic and the actually built oxidation furnace

Ellipsometry is a non-destructive optical technique and uses polarized light to measure thin film properties such as thickness, refractive index and even dielectric properties of a

sample. The ellipsometer measures the polarization change of a reflected beam off a sample by a known polarization incident beam. The exact nature of the polarization change is determined by the sample's properties (thickness and refractive index etc). The ellipsometry is a very sensitive measurement technique which provides unequalled capabilities for thin film metrology down to a few nanometers.

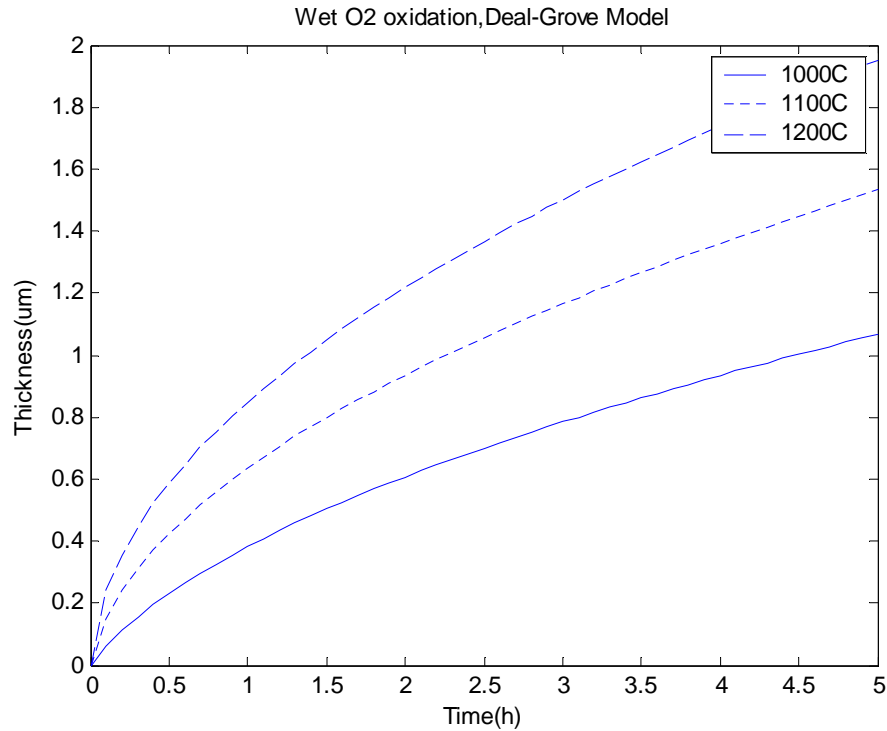


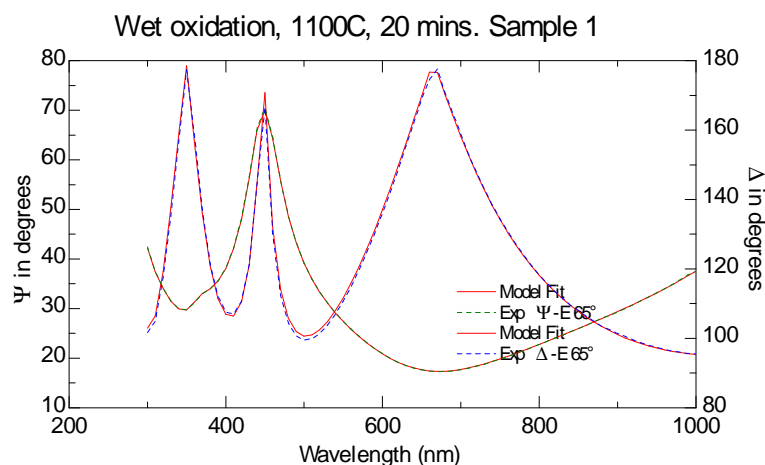
Fig. 4.13 Plot of Wet oxygen oxidation curve from the Deal-Grove model

Ellipsometry measures two parameters conventionally denoted by Ψ and Δ . The polarization state of the light incident upon the sample can be decomposed into s and p component (the s -component is oscillating parallel to the sample surface, and the p -component is oscillating parallel to the plane of incidence). R_s and R_p represent the intensity of the s and p component after reflection, the fundamental equation of ellipsometry can be represented by:

$$\rho = \frac{R_p}{R_s} = \tan(\Psi)e^{i\Delta} \quad (4.3)$$

where $\tan\Psi$ is the amplitude change upon reflection, and Δ is the phase shift. Since ellipsometry is measuring the ratio of two values (rather than the absolute values), it is very robust, accurate, and reproducible. Layer models are needed to interpret the measured Ψ and Δ data by a iterative curve fitting program to get the optical constants of the sample. The optical constants which come closest to the experimental Ψ and Δ are considered to be the correct values for the sample by least-squares minimization.

Fig. 4.16 shows the curve fitting result of two oxidized sample. From the fitting result we can get the thickness of sample1 is 291.52 ± 0.0812 nm with $MSE=11.46$ and sample 2 is 305.66 ± 0.0812 nm with a MSE of 12.19. The thickness is very closed to the desired value.



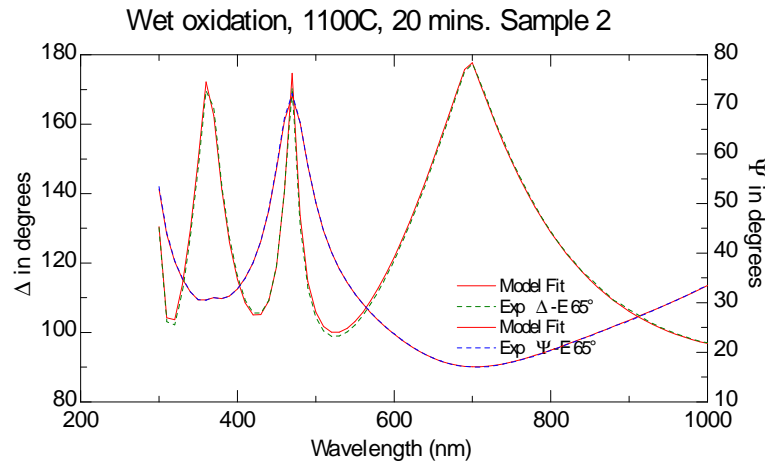


Fig. 4.14 Ellipsometry curve fitting data of two oxidized sample

II. The etching of the channels.

The first design of the etching mask is directly adopted from the design as shown in Fig. 4.6. We hoped that the docking positions and channels can be etched as desired in one step. But the actual etching result turned out to be non-ideal due to the orientation of the crystal plane in silicon wafer and the so caused undercut by KOH anisotropic etching. The convex corner at intersection of the channels will widen because there is no complete $\langle 111 \rangle$ crystal plane to serve as an etch stop (see Fig. 4.17). From the etching pictures at different times we can see that the docking positions and small $2\ \mu\text{m}$ channels will widen and merge. Before the etching reaches a useful depth around $15\text{-}20\ \mu\text{m}$, the channels are so wide such that cells can pass through freely. This one-step-etching design failed to etch the desired channel profile. Etching simulation provides an explanation of the result. Fig. 4.18 shows the simulation result by the software ACES (Anisotropic Crystalline Etch Simulation). ACES is a PC-based 3-D etch simulator from UIUC. Tilting the wafer by 45 degrees can alleviate the problem but the problem still exists. It is possible to do some etching compensation in the etching mask. We can intentionally narrow the features at the docking

position, so that during etching, it may widen to the desired width of the original design. But it is not easy to control this width since the etching is time dependent, and the simulation software just provide an estimated etching result that differs the actual result.

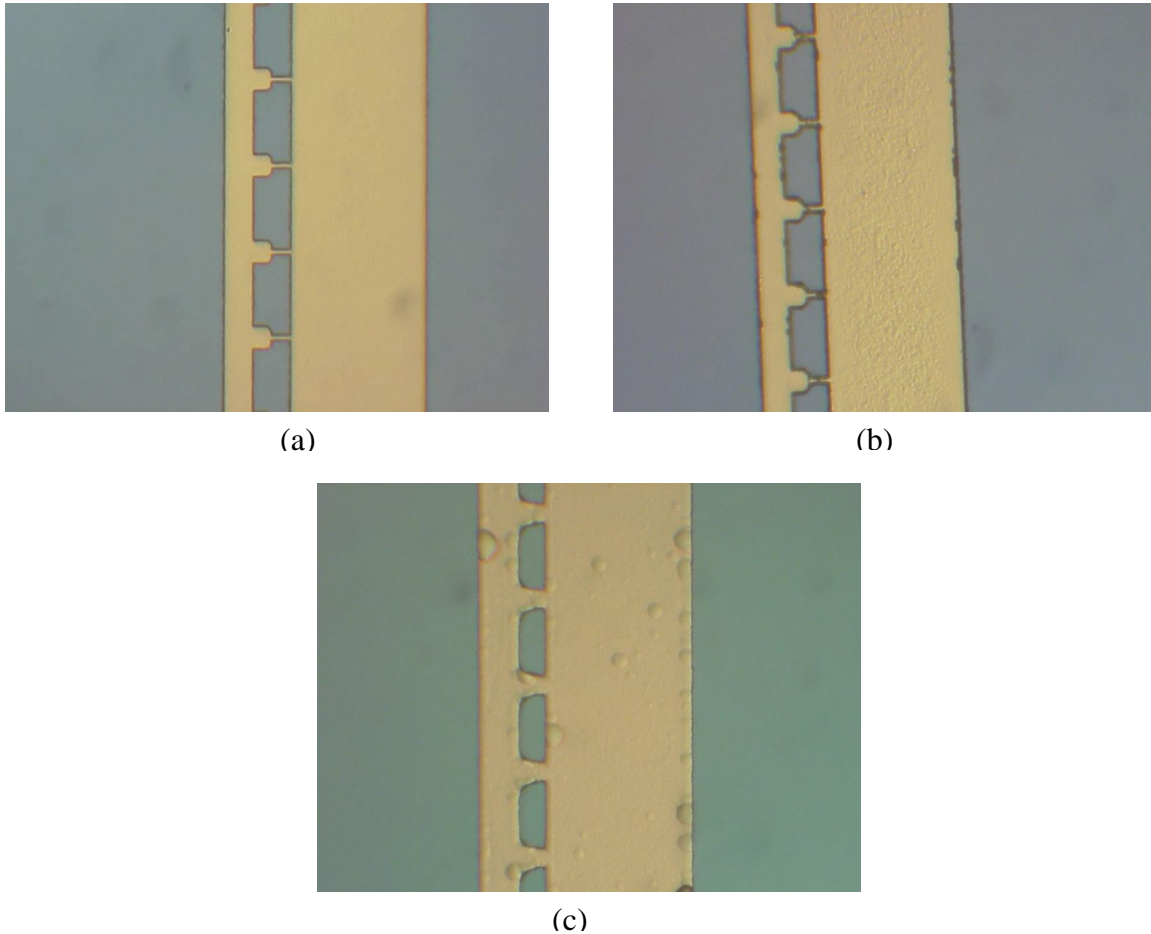


Fig. 4.15 The etching process of the “one-step-etching” design where the docking positions, channels and the 2 μm channel are laid out in one mask. (a) channels patterned on silicon wafer, grey blue is the SiO_2 masking layer. (b) After 4 minutes etching at a channel depth about 4 μm . (c) After 10 minutes etching, the docking position and the small channel merged.

Possible improvements of the etching process could be either dry etching or two-step wet etching. DRIE (Deep Reactive Ion Etching) is a very important MEMS process where high aspect ratio channels can be etched easily. Since we do not have the equipment, we have to seek some other method and two-step etching is a good alternative approach. The idea is

that we etch the small channels first, then add a protection layer by an additional oxide layer. This protection layer prevents the small channel from widening.

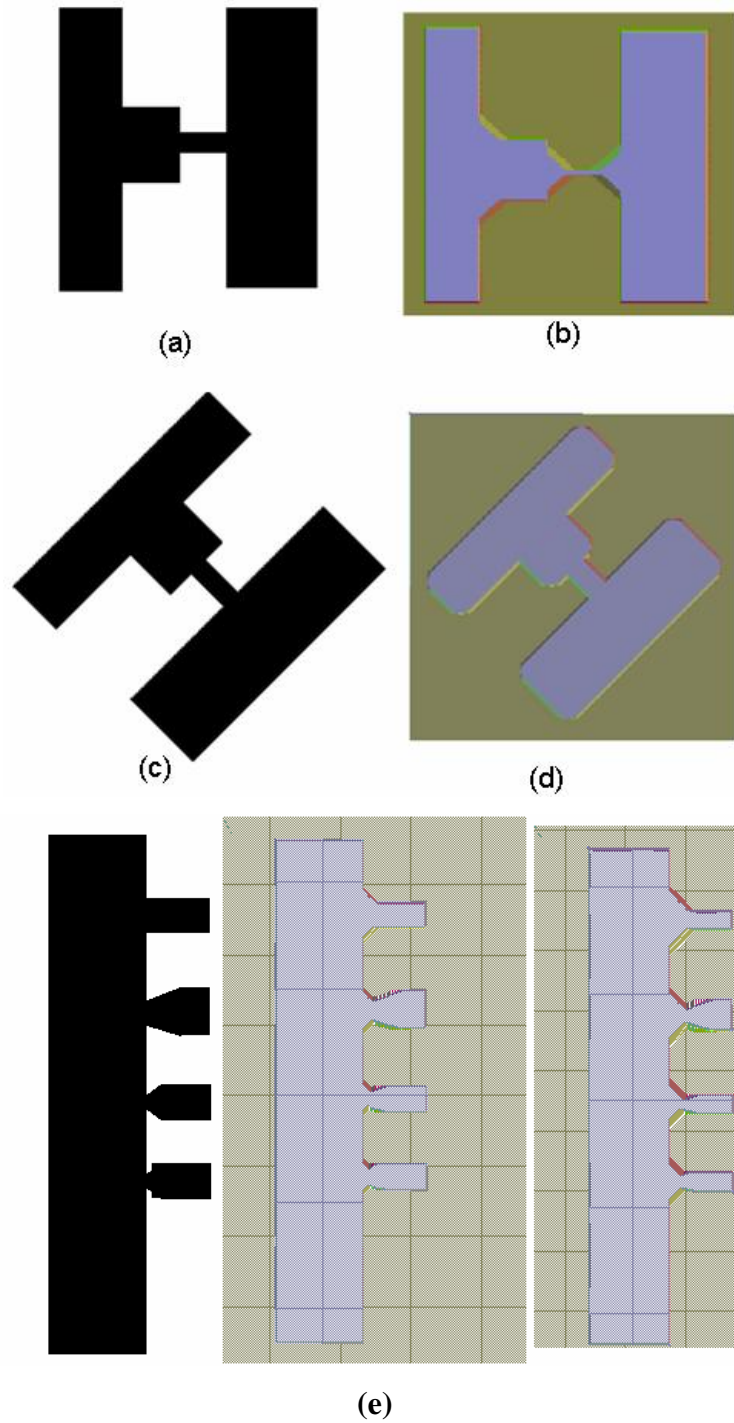


Fig. 4.16 Silicon etching simulation by AECS. Silicon wafer orientation is $\langle 100 \rangle$. (a), (b) etching mask vertical to $\langle 100 \rangle$ plane, (c), (d) etching mask tilted 45 degrees. (e) etch compensation simulation, left is the etching mask with bottle neck like compensation shapes, the middle part is the simulation etching result after 10 minutes, and the right part is the etching result after 15 minutes.

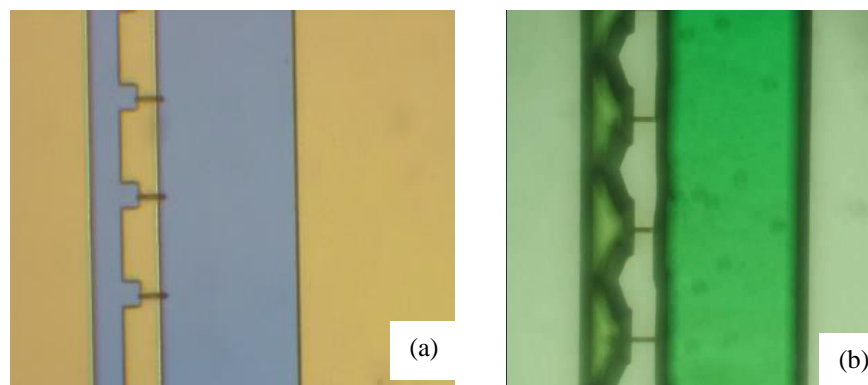


Fig. 4.17 Two-step etching to keep the small channel from widening. (a) the blue is oxide layer, the black line is the etched 2 μm channel after oxidation protection. (b) is the etched channel after dye flow test, the green dye is flowed from the left channel through the small 2 μm channels.

Two-step silicon etching is necessary to keep the profile of the design since in silicon anisotropic etching, the crystal planes are complicated at channels junctions. First, a 300 nm thick SiO_2 film is grown on a silicon wafer in a thermal oxidation furnace, then photolithography is performed using mask 1 to pattern the small 2 μm channel. Following is BOE (buffered oxide etching) etching of the SiO_2 film using 10:1 buffered HF, the 2 μm channel is then etched using KOH (40% solution by weight @ 80C, etching rate $\sim 1.2 \mu\text{m}/\text{min}$). After the first KOH etching, the wafer is oxidized again to protect the etched small 2 μm channels. The second photolithography step uses mask 2 to pattern the left channels and is aligned to the first etching. Another BOE and KOH are needed to finish the channels and reservoirs. Fig. 4.19 shows the fabricated two step etching process and the etched channels. Although the small channel is protected, the trapping position at the edge of the cell flow channel still has an undercut due to the perpendicular notch.

The fabrication of the device with dam structure is very similar to that of the small passage channel. Fig. 4.20 shows the mask layout design and the actual fabricated channels with the dam in-between. Fig. 4.21 is a screen shot from the profiler Alpha step 200 showing the depth profile of the etched channels and dam.

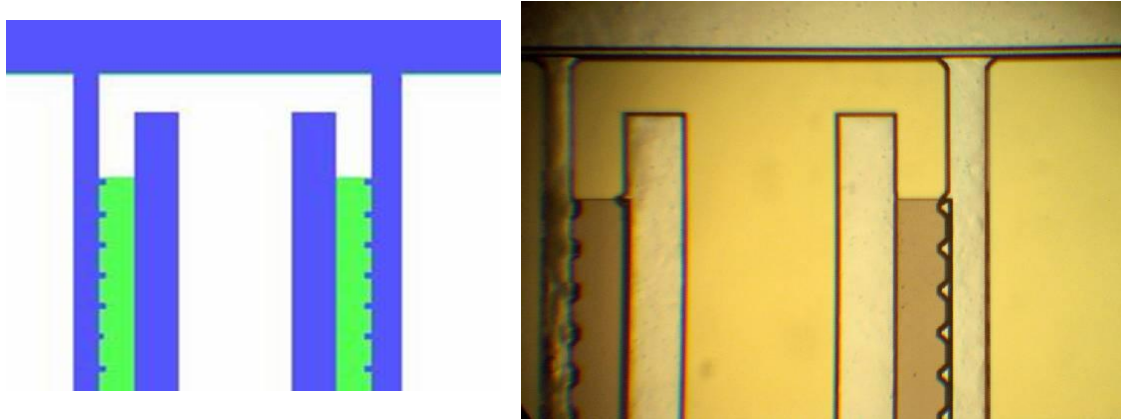


Fig. 4.18 Etching mask and the etched channel with cell trapping positions and dam structure in-between in a silicon wafer. Two pairs of channels are shown, the dam lies between the two channels with a deeper color, small notches are the cell trapping positions.

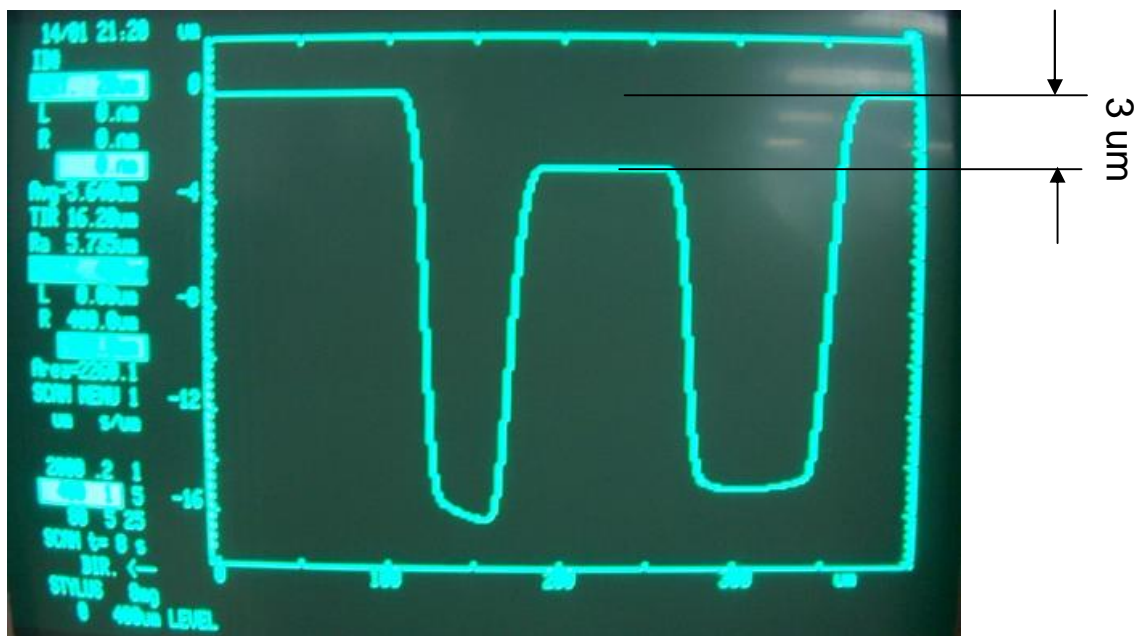


Fig. 4.19 Screenshot of the measurement result from Alpha step 200, the profile of the etched channel with the dam structure.

III. Reusability and bonding method

The bonding method of the device will determine the reusability and ease of solution flow.

The bonding of the device is among three materials: silicon, glass and PDMS.

Anodic bonding of silicon and glass.

Anodic bonding is a common and strong process for joining a silicon wafer and glass. Not all kinds of glass can be used for anodic bonding, borosilicate glass or Pyrex are commonly used since they have a thermal expansion coefficient that closely matches that of silicon. It is believed that the sodium oxide (Na_2O) content of the glass is important for anodic bonding. High temperature (200 to 500 degree Celsius) and high voltage (500 V – 1500V) are needed in the anodic bonding process. First, the silicon wafer is placed on the anode (usually at the bottom), then, glass is placed on top of the silicon wafer, and the assembly is heated to a high temperature ($\sim 400\text{ }^\circ\text{C}$). Then high voltage is applied to produce an electric field between the silicon wafer and the glass. The electric field will drive the mobile metal ions in the glass to move when the glass is softened by the high temperature. The high negative voltage pulls most of the positive metal sodium ions (Na^+) to the top to the cathode. The negative ions such as (O^{2-}) are left behind. These permanent negative ions can form a depletion region between the silicon wafer and the glass. The depletion region is a space charge region between the silicon and the Pyrex. The silicon wafer and the glass are pulled into contact with one another both by some mechanical spring force holding the bonding pieces and the strong electrostatic attraction between the silicon wafer and glass wafers, fixing them firmly in place. In addition, the electric field transports oxygen from the glass to transport to the glass-silicon interface where it could combine with silicon to form Si-O bonds between the silicon and glass. Fig. 4.26 shows the schematic anodic bonding setup. One aluminum or other metal plate are put under the silicon wafer, another

metal plate is put on top of the glass wafer in a sandwich configuration, this is to ensure that the electrical field is uniform for the entire bonding surface so that uniform bonding occurs. In addition, the top metal plate is pressed by a spring, this can apply a pushing force to assist the bonding process and provide a better electrical contact.

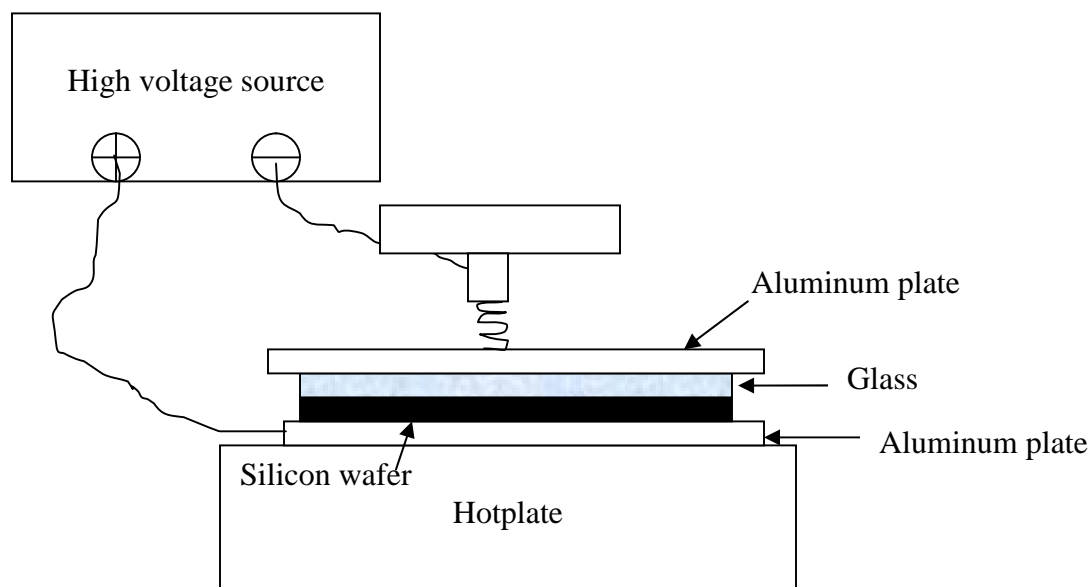


Fig. 4.20 Schematic setup of anodic bonding

Anodic bonding of silicon substrate with glass can enhance the robustness of the final device, and since the glass is hydrophilic, it is easy to flow solution into the channels. In fact, our experiments demonstrated that for relatively larger channels of 50 μm or more, we do not need extra force or pressure to flow cell solution into the channels; the solution can flow by the capillary force alone. The disadvantage is that we need the extra step removing the oxide layer and protecting the channel and electrodes inside the channels. Another disadvantage is that since the cells can get stuck inside the channels, it is not easy to clean the bonded device it is difficult to reuse the device. Due to the above reason, we decided not to use it in the final devices.

Oxygen plasma assisted bonding between Si/Glass with PDMS

Oxygen plasma treated PDMS and glass bonding is a non-reversible process. With optimized process parameters, the bonding strength can be as high as 80 psi¹⁰⁹. This bonding needs to be done right after the plasma treatment because the surface will revert to hydrophobic after a period of time. Since we do not need a very high pressure in our device and non-reversible bonded device can hardly be reused due to clean and clogging problem, this is not an option for our device.

Reversible bonding between Si/Glass with PDMS

Reusability is a very desirable property, we can use reversible PDMS for bonding to create the sealed channel. Since the bonding is reversible, after each measurement, the PDMS piece can be peeled off, both the chip and the PDMS can be rinsed, cleaned and bonded again for another measurement, thus make reuse possible and convenient. Reversible bonding does not require oxygen plasma treatment. In addition, we have to make the PDMS sticky by using less amount of curing agent and cure the PDMS at a lower temperature. The recommended ratio of PDMS to curing agent is 20:1. Curing temperature should be around 80 °C and curing time less than one hour to give satisfactory results. Experiments showed that not only can the PDMS reversible bonding provide well sealed channels, but it provides very good electrical insulation also.

4.3.4 Process integration and device Implementation

After many experiments on different design and processes, we finally implemented complete process for two microfluidic designs on silicon: The channel-trap design and the dam structure design. The flow through the small passage channel is limited due to its

small size, that's why we also choose to implement the dam structure design in which the small passage "widens" such that the flow can go from the cell channel to the waste channel at the entire overlap portion of the paired flow channels, not just at the center of the trapping sites. In this case, there is a bigger lateral flow created by the dam design which will make solution exchange easier and cell docking faster.

We selected the most feasible fabrication process that is cost-effective and achievable at our current microfabrication capability on the MU campus. The integrated process flow is shown in Fig. 4.23. The fabrication process starts from (100) orientation 50 mm wafers which allows fabrication of 4 devices are designed. First, a thin, 300 nm thick silicon dioxide film is grown in a thermal furnace as the etching mask. Then photolithography is performed using the first mask to pattern the oxide layer with a contact aligner (Model 200IR from OAI, San Jose, CA, USA). Buffered HF etching is followed to remove SiO₂ to expose the small passage channel or dam structure pattern on bare silicon surface for KOH etching. The first KOH etching depth is for 2~3 μm and then the wafers are oxidized again to protect the etched dam or small channel from being further etched. Then the second mask is used to pattern the reservoirs and flow channels. Another KOH etching step is performed to create the ~20 μm deep flow channels and the trapping sites, followed the second buffered HF etching to remove the oxide layer. A third oxidation step is used to insulate the channel from the silicon substrate. The third mask is used to pattern the electrodes and contact pads by a lift-off process followed by sputter deposition of platinum (100 nm thick with a Ti adhesion layer of 4 nm). Since we need to photolithographically pattern electrodes within the severe topography of ~20 μm deep channels, thick photoresist Clariant AZ P4620® (10 μm film) is used instead of Shipley S1813 (< 2 μm). Fig. 4.24

shows the devices fabricated on a two inch silicon wafer, we can get four devices from one wafer. Fig. 4.25 shows the patterned Pt electrodes inside the microchannels. The final step of the fabrication is die cutting. Usually the dies are cut using a diamond saw, especially if there are many dies on one wafer. Here our design has only four devices on one wafer, we can use a diamond scribe to cut the die. We first cut the wafer into half, then each half to a quarter.

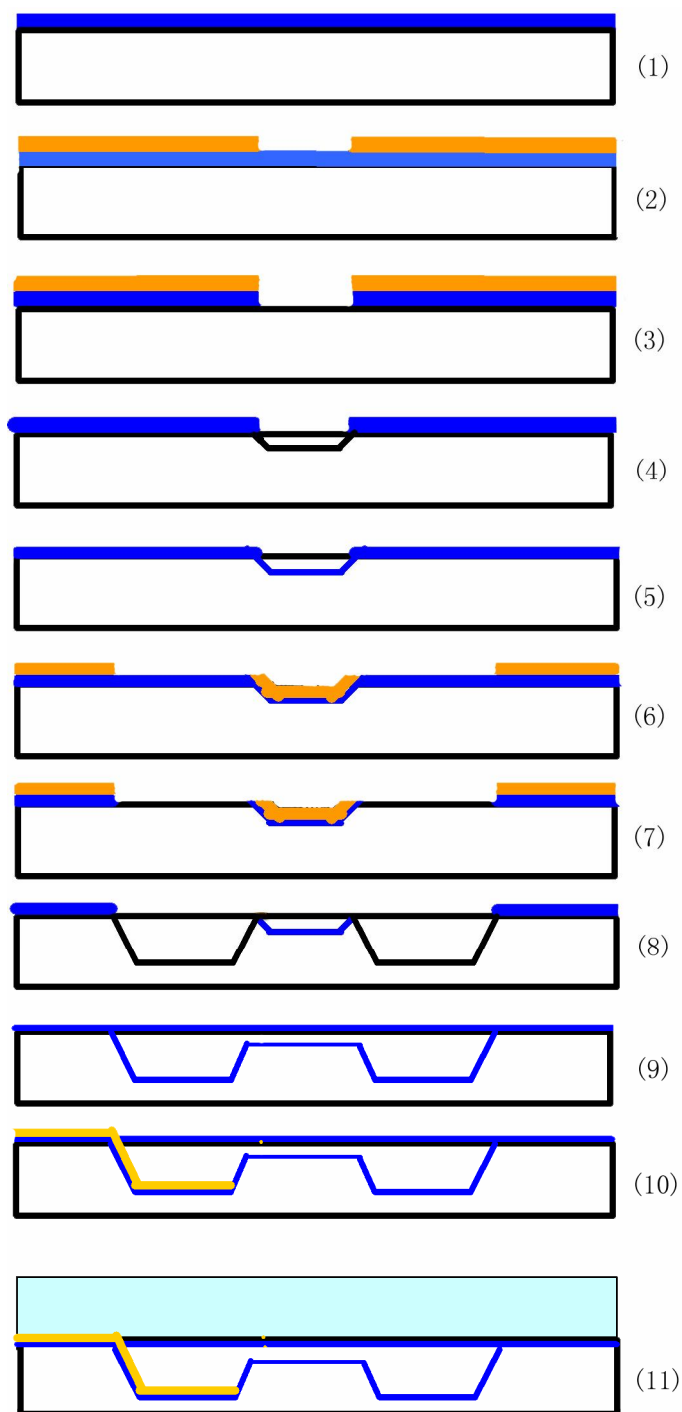


Fig. 4.21 Schematic view in cross section view for the device fabrication process. (1) Start from a bare $\langle 100 \rangle$ silicon wafer, first oxidation to grow a 300 nm oxide layer. (2) First photolithography to pattern the small passage channel. (3) Buffered HF etching, removes SiO_2 to expose Si for KOH etching. (4) KOH etching of Si, create the small passage channel or a shallow dam channel. (5) Second oxidation to protect the etched channel. (6) Second photolithography for the cell and waste channels. (7) Second buffered HF etching to remove SiO_2 to expose Si for KOH etching. (8) KOH etching, create the main channel pair and the docking sites. (9) Third oxidation to insulate channel from the substrate. (10) Metallization using lift-off process, deposit and pattern 20 μm wide electrode into the channel and the docking sites. (11) Channel bonding, seal the channels with a PDMS piece.

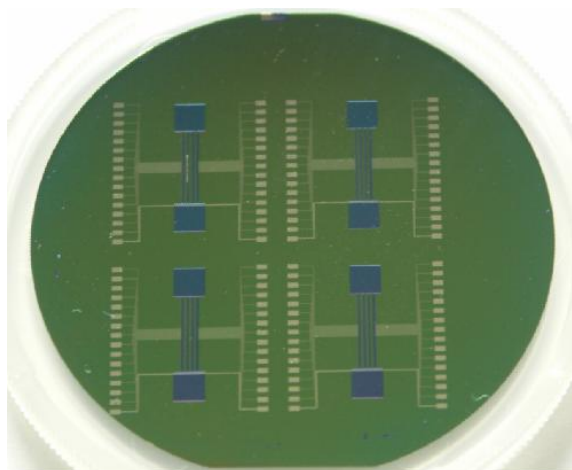


Fig. 4.22 Fabricated devices on a two inch silicon wafer, total four devices on one wafer

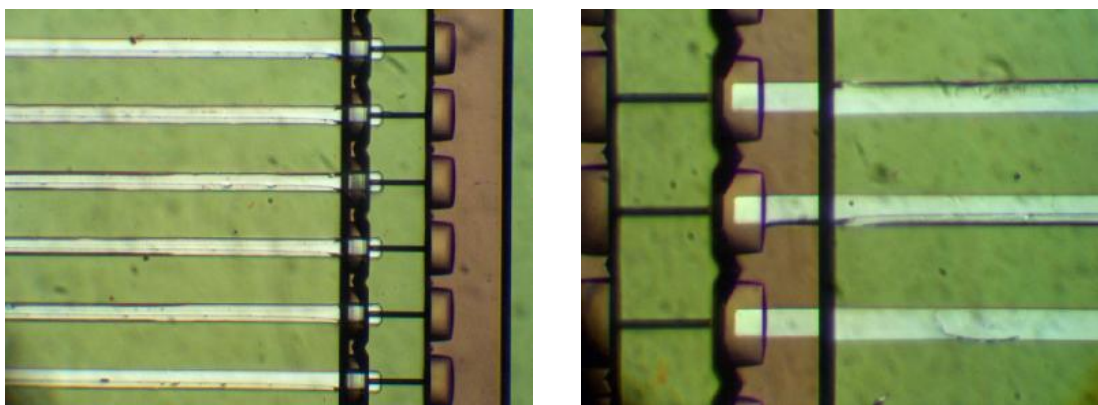


Fig. 4.23 Patterned microelectrodes inside microchannels, electrodes width is 20 μm .

4.4 Device interface and instrumentation system

The exocytosis current signal is very small like many other electrophysiological measurements. We need a high-performance instrument for the amplification of small, fast signals. These measurements must be accurate, low in noise, stable and reliable for useful and quantitative characterization of the underlying biological signal. The amplifiers must

also be able to control the current and/or voltage since we need an adjustable constant potential or voltage-clamp. In addition, we need low-pass filtering of the signal.

The basic configuration of the amplifier is an I-V (current to voltage) converter similar to a patch clamp amplifier. The working electrode is connected to the inverting input of the OP-AMP, the non-inverting input of the OP-AMP is set at a reference potential V_{ref} high enough to oxidize the analyte, usually 700 mV. The feedback in the circuit ensures that the working electrode will have the same potential as the V_{ref} . For an ideal OP-AMP, no current flow into the input, so the current I flow from the working electrode through the feedback resistor R_f . This will produce an output of the OP-AMP of $V_{ref} + IR_f$. The second stage of the circuit is a differential amplifier which subtracts V_{ref} from the output of the first stage and gives an output voltage proportional to the current from the working electrode. The schematic circuit design of the small current amplifier or “I-V” converter is shown in Fig. 4.26. This is the basic circuit that is also used in patch-clamp amplifiers.

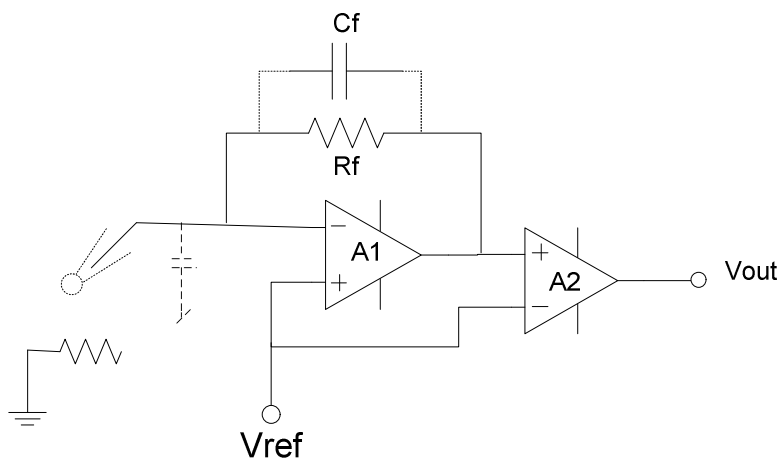


Fig. 4.24 Schematic circuit design of the small current amplifier or “I-V” converter, it is also used in the patch clamp amplifiers as the pre-amplifier or head stage.

The instrumentation system includes circuit design and computer software design. The circuit design mainly deals with amplifier, filters circuits, mainly hardware. It also includes components selection, PCB layout design, grounding and shielding etc. Software deals with data acquisition and data analysis and other control functions. The schematic configuration of the instrumentation system is shown in Fig. 4.27

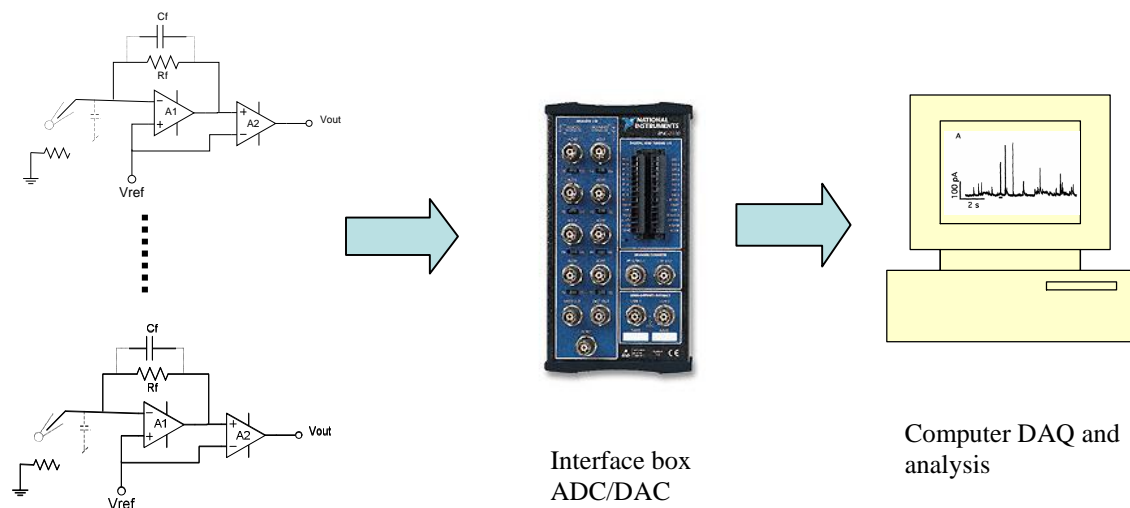


Fig. 4.25 The schematic configuration of the instrumentation system

4.4.1 Hardware Design

Since our goal is high throughput, multi-channel measurement, an array of amplifiers is needed. Due to the extremely low input current, the selection of the first stage OP-AMP is critical. The input OP-AMP needs to have low voltage noise and low bias or background current, i.e. lowest noise level from the OP-AMP side. As we discussed in section 2.4, the main noise sources are thermal noise, shot noise and $e_n c_t$ noise. Since thermal noise is mainly determined by the feedback resistor R_f , not depend on the OP-AMP, so we have only have to consider the later two. We add up equation (2.17) and (2.18) to get equation (4.4):

$$S^2_{I,Total} = S^2_{I,shot} + S^2_{I,enct} = 2I_b eB + \int_0^B (2pfC_t)^2 e_n^2 df = 2I_b eB + \frac{1}{3} (2pC_t)^2 e_n^2 B^3 \quad (4.4)$$

Where I_b is the bias current of the OP-AMP, e_n is the OP-AMP noise in unit of nV/\sqrt{Hz} and B is the bandwidth of the signal. I_b and e_n are usually specified in the OP-AMP data sheets. If we choose the bandwidth at 4 kHz, by comparing a few high performance, low bias, low noise OP-AMPs available in the market (OPA129, OPA627, OPA637, AD8671, AD8605 and AD8606), we found that OPA627 from BURR-BROWN (now TI) gives the best overall noise performance at a reasonable price.

The hardware consists of an array of amplifiers with high value feedback resistors ($G\Omega$) to amplify the small current signal due to oxidation. The amplified signal from the first stage is then fed to a filter circuit which is a fourth order Bessel filter in the Sallen key configuration. Figure 4.28 below is a schematic of a one of the amplifier & filter array elements used in the patch clamp amplifier.

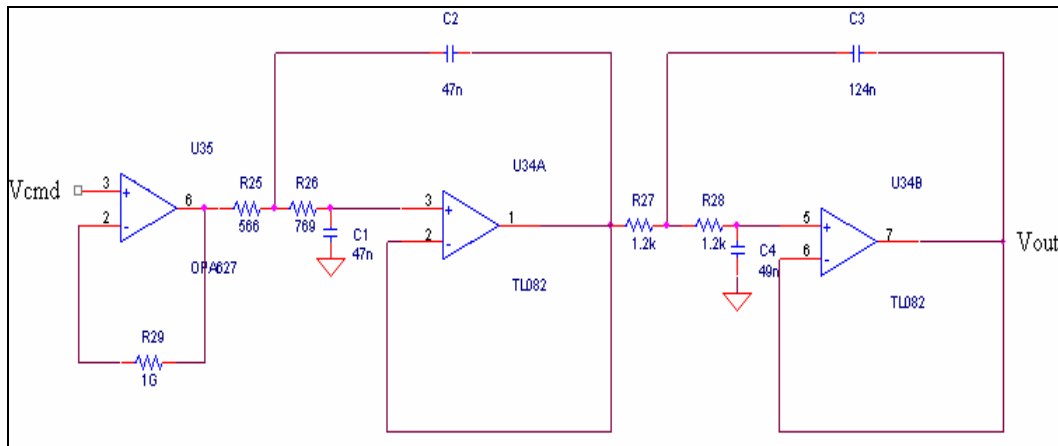


Fig. 4.26 Single Patch Clamp amplifier cell

For the critical stage the design consists of an OPA627 high speed Difet (Dielectrically isolated Field Effect Transistor) operational amplifier¹¹⁰, with typical bias current of 1 pA, and input voltage noise of $5.2 \text{ nV} / \sqrt{\text{Hz}}$ at 1 kHz bandwidth. This amplifier has very good performance characteristics and adequately meets all performance criteria required for the critical stage of the patch clamp amplifier. The current to voltage conversion is achieved using a $1\text{G}\Omega$ feed back resistor. It is important to note that the feedback resistor should have a very low parasitic capacitance C_f as it creates a low pass filter effect in the circuit as shown in Fig. 4.26. If we assume that the parasitic capacitance of the resistor be 0.1pF , then the cutoff frequency of this filter can be calculated from

$$f_0 = \frac{1}{2\pi RC} = \frac{1}{2\pi RC} \quad (4.5)$$

Given the parameters above, this give a result of 1.591 kHz. Clearly this low pass filter effect limits our signal detection capabilities at higher frequencies. It is therefore important to carefully select the feedback resistor. To further reduce parasitic capacitance picked up from the PCB board, the feed back resistor and the input pin of the IC are not directly soldered to the PCB board. Instead, the critical signal path is suspended above the board. Usually, parasitic capacitance compensation circuitry is needed in high performance instrument. Correction could also be implemented in software.

The second stage of the circuit consists of a fourth order Bessel filter. The Bessel filter was chosen as it provides a linear phase response which is useful when designing circuits requiring low signal distortion¹¹¹. It also has a steep transition band. The filter was

designed as a cascade of two second order Bessel filters with a specified cutoff frequency of 2 kHz. The configuration was a Sallen-Key configuration which is shown in Fig. 4.29.

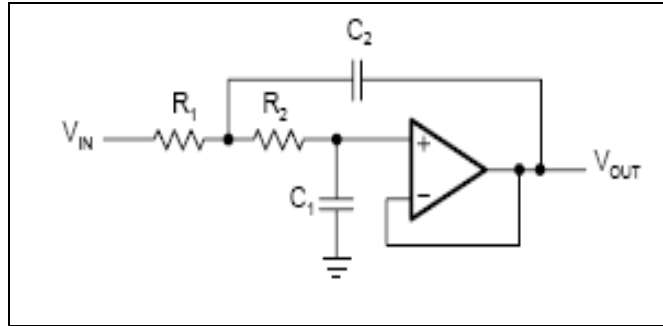


Fig. 4.27 2nd order Filter – Sallen Key Topology

The transfer function of this filter topology is given by the equation 4.6

$$A(s) = \frac{1}{1 + \omega_c C_1 (R_1 + R_2) s + \omega_c^2 R_1 R_2 C_1 C_2 s^2} \quad (4.6)$$

Coefficients for the above transfer function are given by:

$$\begin{aligned} A_0 &= 1 \\ a_1 &= \omega_c C_1 (R_1 + R_2) \\ b_1 &= \omega_c^2 R_1 R_2 C_1 C_2 \end{aligned}$$

Thus given the values for C1 and C2 the values for R1 and R2 can be calculated from:

$$R_{1,2} = \frac{a_1 C_2 \mp \sqrt{a_1^2 C_2^2 - 4b_1 C_1 C_2}}{4\pi f_c C_1 C_2} \quad (4.7)$$

Coefficients a_1 and b_1 can be obtained from filter look up tables or MATLAB using the *besself(order,cutoff freq[ω_n])* function.

From the design equations we selected C1 and C2 = 49nF to obtain the following values to complete the filter stage design.

Table 4.2 Filter Component Values

R1	560 Ω
R2	750 Ω
R3	1.2K Ω
R4	1.2K Ω
C1	49nF
C2	49nF
C3	49.9nF
C4	124nF

4.4.2 Software design

We plan to use the LabVIEW™ platform to develop the instrumentation control program using a high-speed data acquisition card. The data acquisition sampling frequency of each channel should be sufficiently fast to represent the bandwidth of the actual signal not overly fast to produce redundant data and lengthy data files. A sampling frequency of 4~10 kHz will be generally fast enough for normal conditions, considering the theoretical Nyquist frequency (2 x 2 kHz) necessary to guarantee the fidelity of the signal.

The program will show real time data acquisition waveforms just like an oscilloscope. The program should also allow data storage and retrieval for display and analysis. Comments will also be recorded for each experiment to store the information such as the experiment parameters, date, operator, sample information. It will be desirable if the program can include online and offline data analysis such as data filtering, includes peak detection and spike parameter extraction from the scanned input waveforms.

4.5 Experimental setup and device test

4.5.1 Experiment setup

After the devices are successfully fabricated, we need a suitable experimental setup to test our devices. To make the microchip device reusable, a PDMS (8mm by 16 mm, Sylgard 184, Dow Corning, Midland, MI) layer was used as the device lid to create the sealed reservoirs and channels. Good sealing is required not only for creating the microchannels but also for providing good electrical insulation between the solution inside the channels and the conduction traces outside the channels so that only the working electrode inside the channel are in contact with the solution and cells. So a high ratio of 20:1 of the PDMS monomer to the crossing-linking agent was used to make the PDMS lid soft and sticky for better sealing. Two holes are punched in the PDMS piece right above the center of the two reservoirs to facilitate the injection of solutions into the microchannels. The setup for measuring cell exocytosis is shown schematically in Fig. 4.30. Although the final goal is to implement signal amplification onto the PCB board with integrated amplifier arrays, at this first stage, we are using the standard patch-clamp amplifier (EPC-9) to test and characterize our fabricated chip. This is also convenient for data comparison with other approaches using similar instrument. So the experiment setup consists of the fabricated device, headstage, amplifier and control computer.

Devices diced from the wafers are fixed and glued into the center a PCB board with the help of a piece of double sided tape and PDMS. The working electrodes are connected to the wire traces on the PCB board through wire bonding of the contact pads on the silicon device. The PCB board not only provides a support for the chip, but also provides electrical connection and signal amplification. On the prototype PCB board, we also implemented

two amplification channels with a low noise OP-AMP I-V converter. Fig. 4.31 shows a magnified view of the device and PCB mount, (a) is a device used for experiment which is mounted onto PCB, sealed with PDMS and connected to a syringe through small tubing; (b) is a close view of one device die and (c) is the assembled device with amplifiers and filters on a PCB board. Small tubing is plugged into the reservoir through holes in the PDMS sealing piece and connected to a syringe for solution injection or withdraw. Short wires are soldered on the PCB board to connect to the contact pads on the chip and to the head stage of the EPC-9 patch-clamp amplifier (HEKA, Lambrecht, Germany). HEKA Pulse software was used for the amplifier control and data acquisition. A Ag/AgCl electrode was inserted into a reservoir as the reference electrode, for amperometric recording, a +700 mV potential was applied to the sensing microelectrode relative to the Ag/AgCl reference, and current from the sensing electrode is monitored and recorded by the computer. To minimize external electrical noise, the chip and the head stage were put inside a Faraday cage.

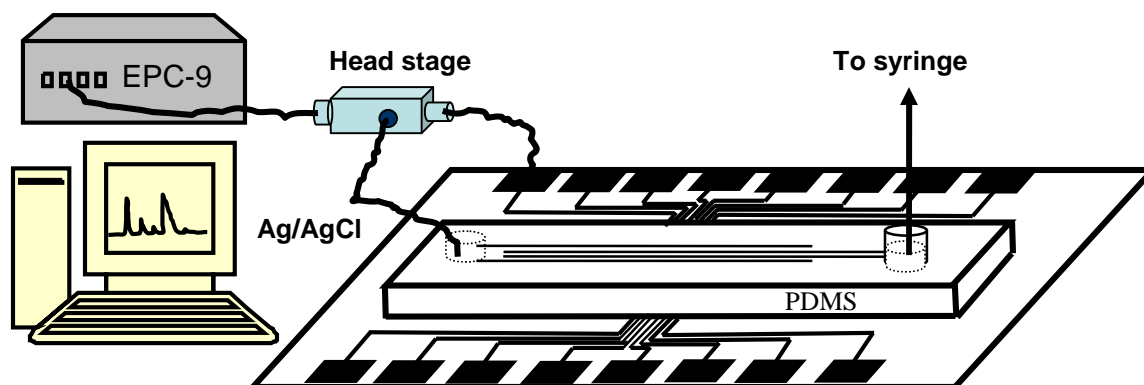
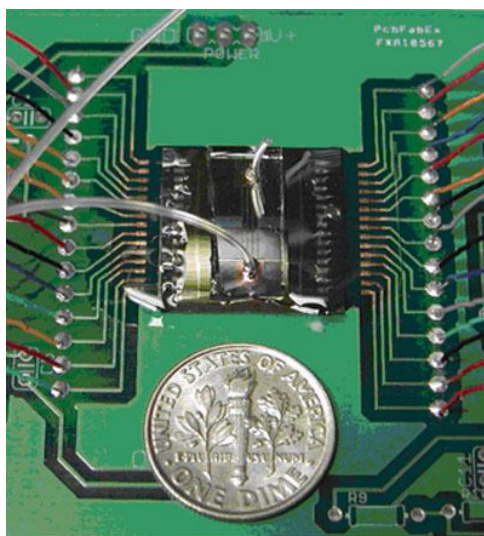


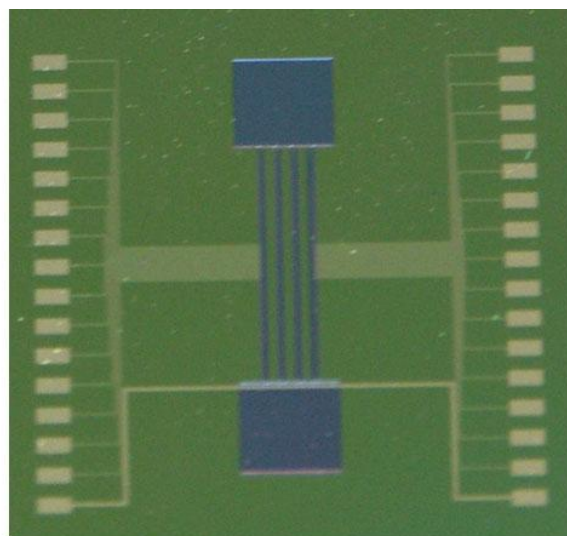
Fig. 4.28 Schematic experiment setup of the device, the device was fixed on a PCB board (not shown) and working electrodes are connected to the PCB board by wire bonding and soldered with short wires, short wires then connected to a head stage and EPC-9 patch-clamp amplifier which is controlled by HEKA pulse software.

4.5.2. Cell trapping experiments

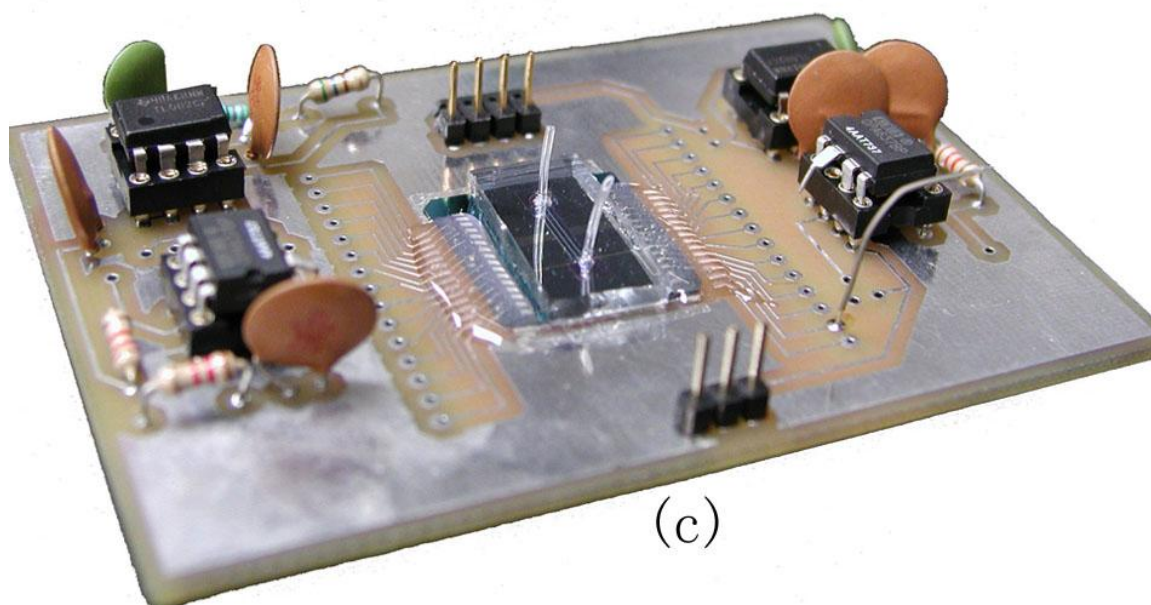
As shown in Fig. 4.32 we can trap cells at different sizes of microchannels. Some of the initial trapping experiments were done in devices where no electrodes are fabricated as in (a) and (b). The size of the channels affects the performance of cell trapping. Although the 20 μm channel ideally allows single-file cell flow, the resistance of the channel is high. A wider channel will allow cells to flow more easily into the channel and be trapped, but the trade-off is that the working electrode area will be larger and so there will be a larger background current and noise level. In the original design, the trapping sites are rectangles, which are good enough to trap and hold the cells if the shape can be kept, but due to the anisotropic nature of wet etching process we used, there is undercut at the convex angle of the patterns, so the actual trapping sites are widened and became wedge like. Although this can help cells flow into the trapping positions without any possible rupture from sharp edges, the widened trapping profile will diminish the holding capability of the trapping structure.



(a)



(b)



(c)

Fig. 4.29 The fabricated microchip device in silicon. (a) Device mounted onto a PCB board and working electrodes are connected to the small wires through wire bonding. (b) A cut device die with microchannels, reservoirs and working electrodes. (c) A whole board view of the prototype of the device with integrated amplifiers and filters on PCB board.

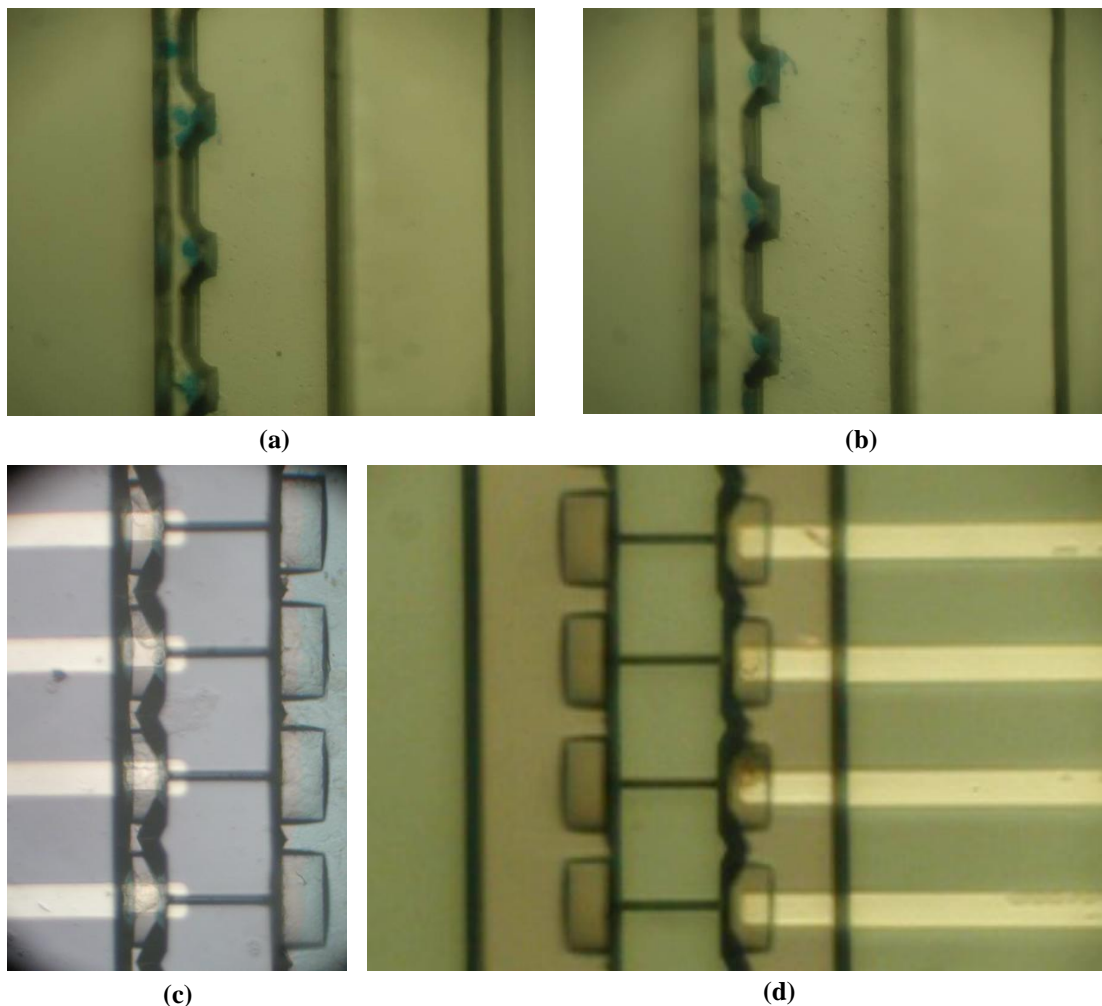


Fig. 4.30 Cell trapping experiment on different size of channels. (a) 20 μm cell flow microchannel. (b) 30 μm cell flow microchannel. Device in (a) and (b) have no working electrodes, cells are stained with Methylene blue for easier visualization. (c) cell trapped in 20 μm channel. (d) cell trapped in 70 μm channel

4.5.3 Amperometric detection of quantal exocytosis of catecholamines

Chromaffin cells were harvested from fresh bovine adrenal gland as described in chapter 2. Immediately before the experiment, cell solution with bovine adrenal chromaffin cells at a cell density of 10^6 cells/mL was mixed with an equal volume of the “high- K^+ ” solution. One to two drops of cell solution (about 4 μL) were pipetted into the cell reservoir on the chip. We put a small O-ring or short tubing at the inlet of the cell reservoir to hold more

solution if needed. Then gentle suction from the waste reservoir is applied through a syringe to let cells flow in the channel and be trapped to the trapping sites. Docked cells are checked by an upright microscope (Olympus, model BX-50WI). Cells trapped in the tapping sites are very close to the electrode due to hydrodynamic force. This is a desirable property in a trapping device since it can provide the highest time resolution for the quantal release of catecholamine from the cells. After cells are trapped at the electrodes, exocytosis events can be recorded immediately since the cells have been pre-stimulated. The “High K^+ ” stimulation depolarize the cell, which subsequently opens the voltage-gated Ca^{2+} channels on the cell membrane to allow considerable Ca^{2+} influx from the extracellular calcium bath solution. And the rise of intracellular Ca^{2+} concentration triggers exocytosis. The release of an individual vesicle causes a current spike as catecholamines are oxidized on the electrode surface. The amperometric data was acquired at a sampling frequency of 4 kHz with a low pass filter at a cut-off frequency of 1 kHz. Fig. 4.33 shows a typical recording from one working electrode. There are more example recordings shown in Fig. 4.34.

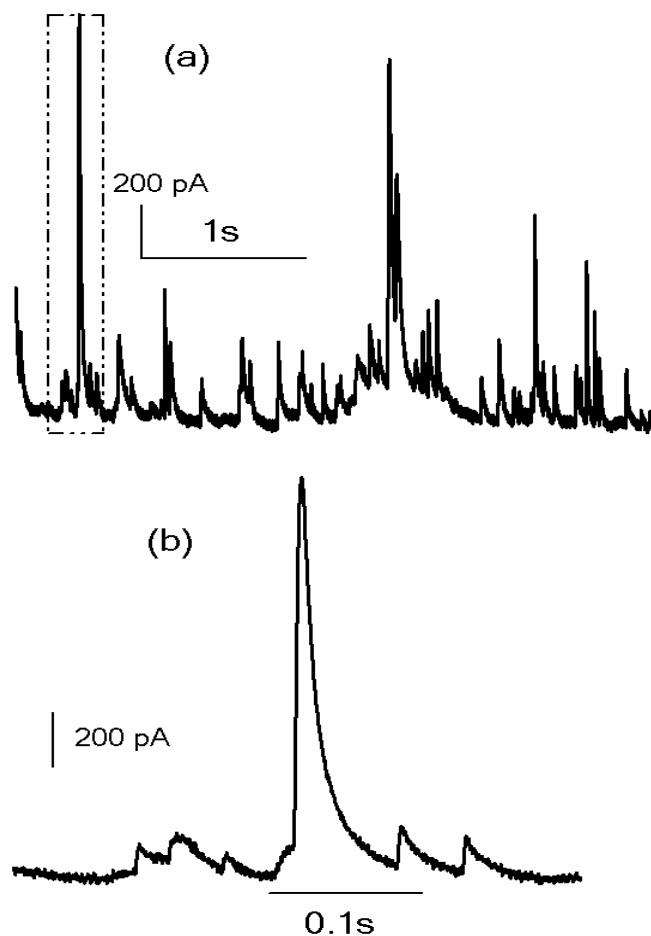


Fig. 4.31 Exocytosis recording example from the microchip device. (a) A typical exocytosis recording for a period of 4 seconds. (b) An expanded view of the dashed square region of (a) showing a spike with a clear foot signal.

We can see the high time resolution from the fast rise times of the current spikes. For example, the largest spike during this recording has an amplitude of 1497.4 pA and a 10-90% rise time of 5.1 ms, a total charge of 25.3 pC and a half width of 11.58 ms. Spike analysis was performed using software developed by F. Segura et al. The average rise time was measured to be 4.8 ms with a median value of 3.01 ms, and most of the spikes

have a rise time within a few milliseconds. Due to the overlapping of some of the spikes and the limitation of the spike detection software, although around 800 spikes in the recording are detected, many spikes are not analyzed such as those with overlapping spikes. The average amplitude of the final 622 current spikes from a continuous recording of 120 seconds is 258.2 pA and the average charge per spike is 4.29 pC. The mean half width of the spikes was measured as 11.01 ms. The average amplitude and charge per spike are bigger than that of the carbon fiber recordings previously reported^{112,113,114}. The possible reasons for the higher amplitude and larger charge per spike could be (1) larger noise background so that smaller spikes are not detected by the software such that the average value is higher (2) vesicles discharge their full contents under these experimental conditions whereas vesicles only transiently fuse and partially release their contents during “normal” carbon fiber experiments. (3) the local PH value at the working electrode surface in the limited space at a trapping site may be changed. (4) catalytic effect of platinum. These four reasons are our hypothesis at this point, since the exocytotic event is a complicated process as reviewed by Mosharov¹¹⁵ et. al, we need a lot of data and statistics to make a sound conclusion, and this makes the high throughput device desirable, which has the potential to collect large amount of data with minimum human interference.

4.5.4 Further analysis of exocytosis, events density, amplitude and background current

I. Frequency of exocytosis

High frequency of exocytotic events, around six spikes per second are observed from the developed trapping devices. This spike frequency is higher than that in many other methods.

The reason could be due to the confined environment in the trapping position where cells were under certain mechanical stress as we mentioned earlier, the other possible reason could be due to the fact that there maybe more than one cells are trapped and squeezed together. We also observed a phenomenon where both frequency and amplitude of the current spikes gradually decrease following time. A good example is shown in Fig. 4.34 which shows four traces recorded over a period of 30 minutes. It is apparent that current spikes become smaller and less frequent over time. One reason for this trend could be the depletion of available vesicles inside the chromaffin cells following a continuous stimulation; the other possible reason could be due to the gradual passivation of the working electrode.

II. Background current and noise level in amperometric measurements

The background current (or offset current) measured from the device varied over a large range from 100 pA to 1500 pA over a period of about 30 minutes, although it is relatively stable during a normal data acquisition sweep lasting between a few seconds to a minute. The background current can be as high as 1350 pA and can gradually drop to around 200 pA after about 30 minutes for a 20 μm by 80 μm platinum microelectrode. Exocytosis recordings showing slow changes in background offset current are depicted in Fig. 4.34 (a) through (d). From the figure we can see that at the beginning, background current is as high as 1.35 nA, then after a few minutes, it drops to around 1.1 nA. After about 10 minutes, the base line current is about 430 pA and finally about 180 pA after 30 minutes. While the initial quick jump current is due to the charge effects of the large parasitic capacitance from the cable and wires on the device and PCB board, which should settle down quickly in a few seconds, the possible reason for the slower change in background current could be due

to the gradual passivation of the electrode surface by the cell and solution. We need to point out that the background current is usually proportional to the electrode surface area. The background current will not affect the spike recording if the electrode will not be passivated since the spikes are added on the base line.

III. Reusability of the chip

The chips are designed for multiple uses. We know that mounting the device and wire bonding connection is not a small job, so reuse of the chip is desirable. First, by using PDMS reversible bonding, the PDMS piece can be easily peeled-off and the sealed channels can thoroughly cleaned using detergent like Micro-90 and some gentle sonication in case there is residue from the cells or medium. The working electrode is very sensitive to surface cleanness; a gentle oxygen plasma treatment is a good method to re-activate the electrode surface for the next recording. A quick way to check whether the electrode is clean or not is to run a cyclic voltammetry using potassium ferricyanide. If we can clearly see the redox peaks, then the electrode is clean and active.

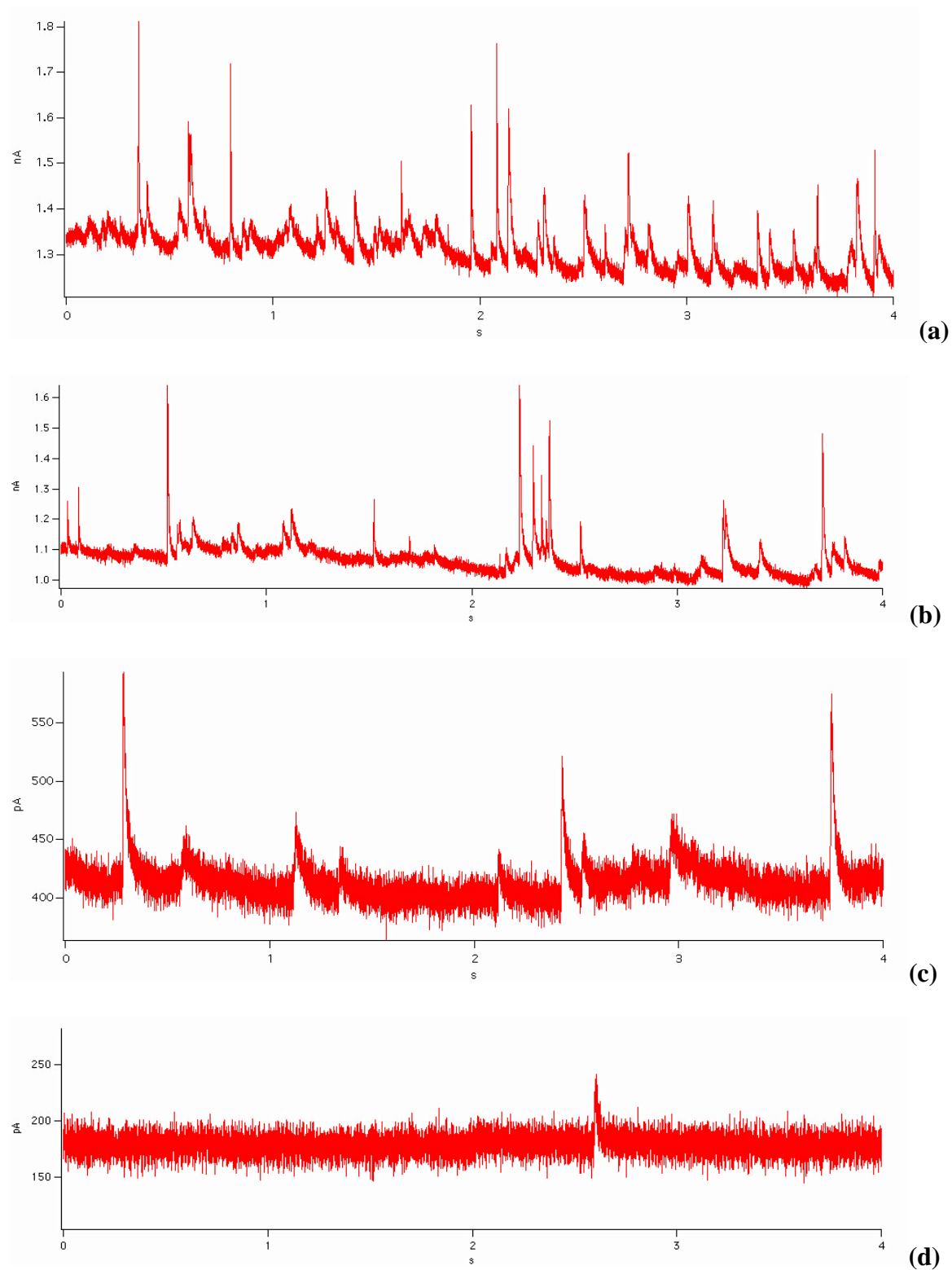


Fig. 4.32 Exocytosis recordings from the trapping device for a period of 30 minutes, each last for 4 seconds. (a) At the beginning. (b) A few minutes later. (c) After about 10 minutes (d) After around 30 minutes.

4.6 Summary

Different designs and fabrication processes of microchip devices for on-chip exocytosis measurement are discussed and compared. The microchannel based design with parallel cell docking and exocytosis recording is chosen to integrate process capabilities at the MU Center for MEMS/NMES system and Nano technology and the final prototype device are completely fabricated. Experiments demonstrated that the designed device can realize automatic cell trapping by differential forces from fluidic dynamics. Further exocytosis measurement from chromaffin cells on the developed device and test setup proved the device can not only automatically dock cells but also possible parallel recording from multiple channels. The observed higher average amplitude and current spike frequency may indicate higher sensitivity of the device and higher throughput in addition to automatic cell docking. The developed on-chip exocytosis technology can not only provide a better research tool for electrophysiology, but also show great potential in applications such as cell based sensors, and high throughput screening of new drugs.

Chapter 5 CONCLUSION AND FUTURE WORK

Fast screening of cells through microfabricated devices on an individual basis provides new opportunities for biomedical applications. It will greatly improve the speed or efficiency of cell based studies and related research in life sciences and drug discovery. In our research, prototypes of micro devices have been designed and fabricated for single cell measurement with different focus and applications. The impedance based sensor probe is aimed at fast cell screening one by one, and the electrochemical microsensor device is aimed for high throughput cell secretion measurement at single cell level. These microchip devices not only have the advantages of faster speed or higher throughput, but also have the advantage of low unit cost due to mass production, low consumption of reagents due to reduced size, and possibly better sensing performance. Processes have been developed for the fabrication of the microdevices. Prototype devices also have been tested and the test results are very promising.

The development of micro sensors not only involves process development, but also sensing mechanism and new sensing materials. We have explored new microelectrode materials for improving electrochemical detection performance of the micro devices. The developed DLC electrodes showed very promising results with low noise, relatively simple process and lower cost. It could find applications in other electrochemical sensors in addition to the ones developed here which targets more specifically on catecholamines secreted by endocrine chromaffin cells.

Of course, there is still a lot work to do if we want to develop the prototype devices into true high-throughput product with commercial potential. Areas for improvement include: a) better cell trapping capability; b) practical instrumentation system for parallel recording; c) new sensing electrode material and integration of DLC to trapping devices

5.1 Bettering cell trapping capability

After the fabrication of the microchip device for exocytosis assay, single cell trapping at multiple trapping sites have been achieved, but more tests are needed for better trapping capability. The parameters such as cell concentration, flow speed or the external force such as positive pressure for pushing or negative pressure for suction need to be optimized. The current design itself needs improvement if we continue use the wet etching process. The current cell trapping design is not perfect due to limitation of the etching process. The trapping sites profile widens due to undercut and convex corners of anisotropic wet etching. The trapped cell can come out of position and be washed away. A possible improvement for better holding capability is to use a 45 degree angle trapping sites which will hold cell better because the cell can hardly come out of the trapping sites by going against the flow direction of the solution. In addition, the 45 degree angle design also lessen the undercut during the etching at the corners. A process simulation shown in Fig. 5.1 indicates that, although the trapping sites will also widen, but due to the 45 degree design, will preserve the corners better than the previous design.

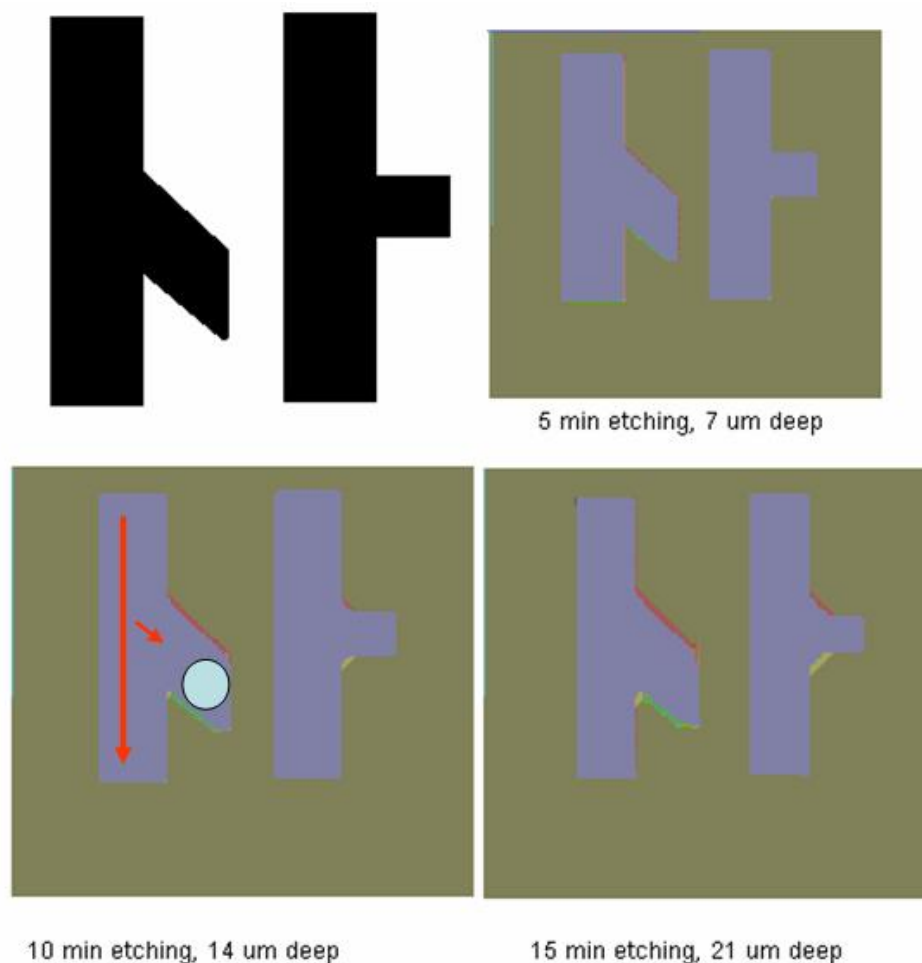


Fig. 5.1 Possible design improvement to count for undercut and widen problem in silicon anisotropic wet etching process for better cell trapping.

Another way to completely solve the under cut or widen problem is to use silicon deep RIE etching or the DRIE process. DRIE will preserve the design profile with a high aspect ratio. Of course, high aspect ratio is not friendly for electrodes patterning, so electrode deposition in high aspect ratio channels may be a challenge.

Another possible cell trapping method is using microwells to trap cells by gravity and slow cell flow. Planar electrodes can be patterned first, then the microwell can be created by a layer of thick photoresist or patterning other kind of thick polymers. Relatively big

channels can be molded by PDMS and form microchannels with well/well electrodes inside as mentioned in chapter 2. This method simplifies the fabrication process and the potential without sacrifice in trapping capability.

Our current chip uses a passive trapping mechanism along microfluidic channels. This may not be good enough for many other applications. On the other hand, due to passive trapping, without other sensing mechanism, we could not know whether a cell has been trapped on a certain sensing electrode or not, so it is desirable that some cell sensing be performed before actual data acquisition. The capacitance of the electrode may allow us to determine if a cell is nearby. We can also simply do data acquisition for all channels and discard the channel without a cell during data analysis manually or automatically, by this way, we can make the sensing simpler. Although this is a low-cost way since data processing with software is cheaper than that by hardware, but we may lose information since this method will not be able to find non-responsive cells.

5.2 A practical instrumentation system for multiple channel recording

In the prototype device test of the on-chip exocytosis measurement with or without trapping, Pt or DLC electrode, we used the commercial patch-clamp amplifiers EPC-9 for signal amplification and data acquisition. Although this instrument is popular and convenient for data comparison, the instrument is very expensive, and has a limited number of channels. So we need to develop an instrumentation system capable of multi-channel data acquisition and data analysis for real high throughput measurement. We have proposed

to develop the system using National Instruments high speed data acquisition cards and LabView platform to develop the instrumentation system. We also have initial tests using a basic amplifier circuit and prototype PCB, but we need a complete functional system to realize high throughput recordings.

5.3 Further work on DLC and new sensing electrode material

We developed the DLC microelectrode for on-chip exocytosis measurement and found that the new material is very promising. It is developed on a sputtering process and it is compatible with general microfabrication processes. Test on cell shows it is very good material for low noise exocytosis measurement. But our tests only carried out on glass substrate, we did not integrate it onto silicon trapping devices yet. In addition, the DLC process we developed needs further optimization. In addition to cell exocytosis measurement, the DLC microelectrode may show excellent sensing capability for other applications.

List of Publications

I. Journals and Conference Proceedings

1. “An Impedance Microsensor With Coplanar Electrodes and Vertical Sensing Apertures”, Hui Tang and **Yuanfang Gao**, IEEE SENSORS JOURNAL, Vol. 5, No. 6, Page 1346- 1352, Dec. 2005.
2. “Magnetron sputtered diamond-like carbon microelectrodes for on-chip exocytosis measurement”, Yuanfang Gao, Kevin Gillis, and Shubhra Gangopadhyay, in preparation.
3. “Microchip device for high throughput exocytosis measurements with automatic cell positioning”, Yuanfang Gao, Xiaohui Chen, Shantanu Bhattacharya, Arnold A. Lubguban, Kevin Gillis, and Shubhra Gangopadhyay, in preparation.
4. “Mechanics of plasma exposed SOG (Spin-on-Glass) and PDMS (Poly dimethyl Siloxane) surfaces and their impact on bond strength” , Shantanu Bhattacharya, Yuanfang Gao et. al, Applied Surface Science, accepted, Sept. 2006.
5. “Controlled Stimulation of Quantal Catecholamine Release from Chromaffin Cells Using Photolysis of Caged Ca²⁺ on Transparent Indium-Tin-Oxide Microchip Electrodes”, Xiaohui Chen, Yuanfang Gao, Maruf Hossain, Shubhra Gangopadhyay, Kevin D. Gillis.
6. “A Novel On-Chip Diagnostic Method to Measure Burn Rates of Energetic Materials”, Shantanu Bhattacharya, **Yuanfang Gao**, Steve Apperson, Rajesh Shende, Shubhra Gangopadhyay, Journal of Energetic Materials, 24: 1–15, 2006.
7. “Optimization of design and fabrication process for realization of a PDMS-Silicon DNA amplification chip”, Shantanu Bhattacharya, **Yuanfang Gao**, Venumadhav Korampally, Sheila A. Grant, Steven B Klieboeker, Keshab Gangopadhyay, Shubhra Gangopadhyay, Accepted, Journal of MEMS, Oct. 2006.
8. “Optimization of fabrication process for a PDMS-SOG-Silicon based PCR Micro Chip through system identification techniques”, Venumadhav Korampally, Shantanu Bhattacharya, **Yuanfang Gao**, Sheila Grant, Steven Kleiboeker, Keshab Gangopadhyay, Jinglu Tan, Shubhra Gangopadhyay, CBMS 2006, the 19th IEEE International Symposium on Computer-Based Medical Systems, Salt Lake City, Utah, Jun 22-23, 2006.
9. “Comparative Study of Frequency Spectrum and Amplitude of Oscillatory Potentials in Different Species of Laboratory Animals”, Bo Lei, Keqing Zhang, **Yuanfang Gao**, Kurt Hofeldt, Gang Yao, submitted to the journal of Vision Research, Nov. 2005.

10. "Self-assembled Ordered Energetic Composites of CuO Nanorods and Nanowells and Aluminum Nanoparticles with High Burn Rates", Rajesh V. Shende, Senthil Subramaniam, Steve Apperson, Shameem Hassan, Shantanu Bhattacharya, **Yuanfang Gao**, Maruf Hossain, Shubhra Gangopadhyay, Paul Render, Deepak Kappoor, Steven Nicolich, 2005 MRS Fall meeting, Boston, MA. Nov. 28- Dec. 2, 2005.
11. "Crystallization of amorphous silicon by self propagation of nano-energetic thermites", Maruf Hossain, Senthil Subramanian, Shantanu Bhattacharya, **Yuanfang Gao**, Steve Apperson, Rajesh Shende, Suchi Guha, and Shubhra Gangopadhyay, submitted to Applied Physics Letter, September, 2005.
12. "On-chip Initiation and Burn Rate Measurements of Thermite Energetic Reactions", Steve Apperson, Shantanu Bhattacharya, **Yuanfang Gao**, Senthil Subramaniam, Shameem Hassan, Maruf Hossain, Rajesh V. Shende, Shubhra Gangopadhyay, Paul Render, Deepak Kappoor, Steven Nicolich, 2005 MRS Fall meeting, Boston, MA. Nov. 28- Dec. 2, 2005.
13. "A Micro Sensing Probe for Detecting Individual Biological Cells", **Yuanfang Gao**, Venu Korampally, and Hui Tang, The 25th Annual International Conference of the IEEE Engineering in Medicine and Biology, Volume 4, 17-21, P3348-3351, Cancun, Mexico Sept. 2003.
14. "Discrete Ordinates neutron transport method via half-range and full-range weight functions", K. Ganguly and **Yuanfang Gao**, submitted to Transport Theory and Statistical Physics, June, 2004.
15. "Comparative study of frequency spectrum and energy of electroretinogram oscillatory potentials (OPs) in mammals", K.J. Hofeldt, **Yuanfang Gao**, K.Zhang, and B. Lei, Annual Meeting of Association for Research in Vision and Ophthalmology, Fort Lauderdale, Florida, April 2004.
16. "IVECO car-body visual inspection station and its control system", **Yuanfang Gao**, Xueyou Yang, et al., the 7th annual meeting on inspection technology of the Chinese Car-industry Engineering Association. Nov. 97, Hangzhou, China.

II. Presentations

17. "High throughput microchip for exocytosis measurement with automatic cell positioning", **Yuanfang Gao**, Shantanu Bhattacharya, Arnold Lubguban, Pascal Ruzigana, Kevin Gillis, Shubhra Gangopadhyay, 11th annual IBE meeting, Mar. 10-12, 2006, Tucson, Arizona.
18. "Microelectrode Surface Modification by Self-Assembled Nanoparticles", Arnold Lubguban, **Yuanfang Gao**, Rajesh Shende, Shameem Hasan, Kevin Gillis, Mark Prelas and Shubhra Gangopadhyay, 52nd MIDWEST SOLID STATE CONFERENCE, Columbia, MO, October 8-9, 2005.

19. "A novel PCR based DNA micro-analyzer", Shantanu Bhattacharya, *Yuanfang Gao*, et. al., 10th annual IBE meeting, March 2005, University of Georgia, Athens.
20. "High throughput microchip based quantal exocytosis measurement system with automatic cell positioning", *Yuanfang Gao*, Pascal Ruzigana, Shantanu Bhattacharya, Kevin Gillis, Shubhra Gangopadhyay, MU Life Science Week poster session, April 2005.
21. "A novel PCR based DNA micro-analyzer", Shantanu Bhattacharya, *Yuanfang Gao*, et. al., BMES 2005, Baltimore, MD, Sept. 28-Oct. 1, 2005.
22. "A Novel Approach to Evaluate OPs in Electroretinogram (ERG) and its Applications", *Yuanfang Gao* and Bo Lei, Presentation, Phi Zeta Research Awards, April, 2004.
23. "ERG: Analyses and Origins of Components", *Yuanfang Gao*, K.J. Hofeldt, K.Zhang, and B. Lei, MU Life Science Week poster session, April 2004.
24. "A novel PCR based DNA micro-analyzer", Shantanu Bhattacharya, *Yuanfang Gao*, et. al., 10th annual IBE meeting, March 2005, University of Georgia, Athens.
25. "A novel PCR based DNA micro-analyzer", Shantanu Bhattacharya, *Yuanfang Gao*, et. al., BMES 2005, Baltimore, MD, Sept. 28-Oct. 1, 2005.
26. "A Micro Sensing Probe for Detecting Individual Biological Cells", *Yuanfang Gao*, Venu Korampally, and Hui Tang, MU Life Science Week poster session, April 2002.

III. Patents Applications:

1. "On chip diagnostics of nanoenergetics to determine burn rate characteristics", Shubhra Gangopadhyay, Shantanu Bhattacharya, *Yuanfang Gao*, et. al. filed with MU patent disclosure, Jan, 2005, patent pending.
2. "On-Chip igniter and Method of Manufacture", Shubhra Gangopadhyay, *Yuanfang Gao*, et. al., US patent application filed Oct 28, 2005, patent pending.
3. "Reusable PCR Amplification System and Method", Shantanu Bhattacharya, Shubhra Gangopadhyay, Keshab Gangopadhyay, *Yuanfang Gao*, et. al. filed at the US Patent and Trademark Office on Friday, Dec. 16, 2005, patent pending.

VITA

Yuanfang Gao received his B.S. and M.S. degrees in precision instruments engineering from Tianjin University, Tianjin, China, in 1993 and 1998, respectively. He received his second M.S. degree in electrical engineering from the University of Toledo, Toledo, Ohio, USA in 2001 and the Ph.D. degree in electrical engineering from the University of Missouri-Columbia, Columbia, Missouri, USA in 2006.

Yuanfang Gao worked as a consumer electronics design engineer in Shenzhen Sapphire Groups from 1993 to 1995. From 1998 to 2000, he was a senior electronic engineer in telecommunications at Huawei Technologies, Ltd, Shenzhen, China. From 2002 to 2006, he was a research assistant in the Department of Electrical and Computer Engineering at University of Missouri-Columbia. And from September 2006 to December 2006, he was an intern at PDF Solutions Inc, San Diego office.

Yuanfang Gao is a student member of IEEE and his research interests include microsensors, MEMS, instrumentation, and microelectronics. His biography was published in “The Chancellor’s List”, 2004-2005.

References:

- ¹ Peng Chen, Bai Xu, Natalya Tokranova, Xiaojun Feng, James Castracane and Kevin D. Gillis, "Amperometric detection of quantal catecholamine secretion from individual cells on micromachined silicon chips", *Analytical Chemistry*, 2003. 75(3): p. 518-24.
- ² Gao, J., Yin, X. F., and Fang, Z. L., "Integration of single cell injection, cell lysis, separation and detection of intracellular constituents on a microfluidic chip," *Lab Chip*, vol. 4, no. 1, pp. 47-52, Feb.2004.
- ³ Dias, A. F., Dernick, G., Valero, V., Yong, M. G., James, C. D., Craighead, H. G., and Lindau, M., "An electrochemical detector array to study cell biology on the nanoscale," *Nanotechnology*, vol. 13, no. 3, pp. 285-289, June2002.
- ⁴ Li, P. C., de Camprieu, L., Cai, J., and Sangar, M., "Transport, retention and fluorescent measurement of single biological cells studied in microfluidic chips," *Lab Chip*, vol. 4, no. 3, pp. 174-180, June2004.
- ⁵ Matsuoka, H., Komazaki, T., Mukai, Y., Shibusawa, M., Akane, H., Chaki, A., Uetake, N., and Saito, M., "High throughput easy microinjection with a single-cell manipulation supporting robot," *J.Biotechnol.*, vol. 116, no. 2, pp. 185-194, Mar.2005.
- ⁶ Park, J., Jung, S. H., Kim, Y. H., Kim, B., Lee, S. K., and Park, J. O., "Design and fabrication of an integrated cell processor for single embryo cell manipulation," *Lab Chip*, vol. 5, no. 1, pp. 91-96, Jan.2005.
- ⁷ Pepperkok, R., Schneider, C., Philipson, L., and Ansorge, W., "Single cell assay with an automated capillary microinjection system," *Cytotechnology*, vol. 5 Suppl 1 pp. 93-98, 1991.
- ⁸ Hui Tang and Yuanfang Gao, "An Impedance Microsensor With Coplanar Electrodes and Vertical Sensing Apertures", *IEEE SENSORS JOURNAL*, Vol. 5, No. 6, Page 1346- 1352, Dec. 2005.
- ⁹ Adam T. Woolley, Kaiqin Lao, Alexander N. Glazer, and Richard A. Mathies, "Capillary Electrophoresis Chips with Integrated Electrochemical Detection", *Anal. Chem.*1998, 70,684-688.
- ¹⁰ Ulli Backofen, Frank-Michael Matysik, and Craig E. Lunte, "A Chip-Based Electrophoresis System with Electrochemical Detection and Hydrodynamic Injection", *Anal. Chem.*2002, 74,4054-4059.
- ¹¹ Zelle, M. R. "A simple single-cell technique for genetic studies of bacteria", *J. Bacteriol.* 61:345-349, 1951.
- ¹² Grover, S. C., Skirtach, A. G., Gauthier, R. C., and Grover, C. P., "Automated single-cell sorting system based on optical trapping," *J.Biomed.Opt.*, vol. 6, no. 1, pp. 14-22, Jan.2001.
- ¹³ Arthur Ashkin, "Optical trapping and manipulation of neutral particles using lasers", *Proc. Natl. Acad. Sci. USA*, Vol. 94, Biophysics pp. 4853-4860, May 1997.
- ¹⁴ Arai, F., Ng, C., Maruyama, H., Ichikawa, A., El Shimy, H., and Fukuda, T., "On chip single-cell separation and immobilization using optical tweezers and thermosensitive hydrogel," *Lab Chip*, vol. 5, no. 12, pp. 1399-1403, Dec.2005.
- ¹⁵ Goksoy, M., Enger, J., and Hanstorp, D., "Optical manipulation in combination with multiphoton microscopy for single-cell studies," *Appl.Opt.*, vol. 43, no. 25, pp. 4831-4837, Sept.2004.
- ¹⁶ Chronis, N. and Lee, L. P., "Electrothermally activated SU-8 microgripper for single cell manipulation in solution", *Journal of Microelectromechanical Systems*, vol. 14, no. 4, pp. 857-863, Aug.2005.
- ¹⁷ Alahiko ICHIKAWA, Fumihito ARAI, Hisataka MARUYAMA, Toshio FUKUDA and Tohoru KATSURAGI, "Single Cell Trap on a Chip Using In-situ Micro fabrication with Photo-Crosslinkable Resin

and Thermal Gelation”, IEEE Proceedings of International Conference on Robotics & Automation, New Orleans, AL, April 2004.

¹⁸ Jennifer W. L. Zhou and Wen J. Li, "MEMS-Fabricated ICPF Grippers for Aqueous Applications", IEEE, The 12th International Conference on Solid State Sensor, Actuators and Microsystems, Boston, June 8-12, 2003.

¹⁹ Chronis, N.; Lee, L.P., "Polymer MEMS-based microgripper for single cell manipulation", 17th IEEE International Conference on Micro Electro Mechanical Systems (MEMS), Page(s):17 – 20, 2004.

²⁰ Jager, E. W. H., Inganas, O., and Lundstrom, I., "Microrobots for micrometer-size objects in aqueous media: Potential tools for single-cell manipulation", *Science*, vol. 288, no. 5475, pp. 2335-2338, June 2000.

²¹ Boukallel, M., Gauthier, M., Piat, E., Abadie, J., and Roux, C., "Microrobots for in vitro fertilization applications," *Cell Mol.Biol.(Noisy-le-grand)*, vol. 50, no. 3, pp. 267-274, May 2004.

²² Julie Clayton, "Go with the microflow", *Nature methods*, Vol 2, No.8, p621-627, Aug. 2005.

²³ Ogura E, Abtti PJ, Morizumi T, "Measurement of human red blood cell deformity using a single micropore on a thin Si3N4 film", *IEEE Trans. Biomed Eng* 38(8), p721-725, 1991.

²⁴ Tracey, M.C.; Greenaway, F.S.; Das, A.; Kaye, P.H.; Barnes, A.J., "A silicon micromachined device for use in blood cell deformability studies", *IEEE Transactions on Biomedical Engineering*, Vol 42, Issue 8, Page(s):751 - 761 Aug. 1995.

²⁵ Lee, et al, "Single red blood cell deformability test using optical trapping in plastic microfluidic chip", 3rd IEEE/EMBS Special Topic Conference on Microtechnology in Medicine and Biology, 12-15 May 2005 Page(s):389-390.

²⁶ Shimizu et al. , "The automatic image analysis of red blood cell deformability and blood flow in microchannels with an image-intensified high-speed video camera system", *Proceedings of the 20th Annual International Conference of the IEEE Engineering in Medicine and Biology Society*, 1998.

²⁷ Ian K. Glasgow, Henry Chris Zeringue, David J. Beebe, Seong-Jun Choi, Joseph T. Lyman, Natalie G. Chan, and Matthew B. Wheeler, "Handling Individual Mammalian Embryos Using Microfluidics", *IEEE TRANSACTIONS ON BIOMEDICAL ENGINEERING*, VOL. 48, NO. 5, MAY 2001.

²⁸ Yong Huang; Ning Chen; Borninski, J.; Rubinsky, B., "A novel microfluidic cell-chip for single cell analysis and manipulation", *IEEE The Sixteenth Annual International Conference on Micro Electro Mechanical Systems*, 9-23 Jan. 2003 Page(s):403 – 406.

²⁹ Jungyul Park, Seng-Hwan Jung, Young-Ho Kim, Byungkyu Kim, Seung-Ki Lee and Jong-Oh Park, "Design and fabrication of an integrated cell processor for single embryo cell manipulation", *Lab On Chip*, 2005, 5, 91–96.

³⁰ Kwang-Seok Yun and Euisik Yoon, "Micro/Nanofluidic Device for Single-Cell-Based Assay", *Biomedical Microdevices* 7:1, 35–40, 2005.

³¹ Mengsu Yang, Cheuk-Wing Li, and Jun Yang, "Cell Docking and On-Chip Monitoring of Cellular Reactions with a Controlled Concentration Gradient on a Microfluidic Device", *Anal. Chem.* 2002, 74, pp3991-4001.

³² Anne M Taylor, Mathew Blurton-Jones, Seog Woo Rhee, David H Cribbs, Carl W Cotman, Noo Li Jeon, "A microfluidic culture platform for CNS axonal injury, regeneration and transport", *Nature Methods*, pp599-605 Vol.2 No.8 Aug, 2005.

-
- ³³ Hellmich, W., Pelargus, C., Leffhalm, K., Ros, A., and Anselmetti, D., "Single cell manipulation, analytics, and label-free protein detection in microfluidic devices for systems nanobiology", *Electrophoresis*, vol. 26, no. 19, pp. 3689-3696, Oct.2005.
- ³⁴ Medoro, G., Manaresi, N., Leonardi, A., Altomare, L., Tartagni, M., and Guerrieri, R., "A lab-on-a-chip for cell detection and manipulation," *Ieee Sensors Journal*, vol. 3, no. 3, pp. 317-325, June2003.
- ³⁵ S Zhang, L Yan, M Altman, M Lassle, H Nugent, F Frankel, D Lauffenburger, G Whitesides, A Rich, "Biological surface engineering: a simple system for cell pattern formation", *Biomaterials* 20 (1999) 1213}1220.
- ³⁶ T. Yamada, M. Placzek, H. Tanaka, J. Dodd, and T.M. Jessell, "Control of cell pattern in the developing nervous system: Polarizing activity of the floor plate and notochord", *Cell*, Vol 64, 635-647, 8 February 1991.
- ³⁷ Bohanon T, Elender G, Knoll W, Koberle P, Lee JS, Offenhausser A, Ringsdorf H, Sackmann E, Simon J, Tovar G, Winnik FM. "Neural cell pattern formation on glass and oxidized silicon surfaces modified with poly(N-isopropylacrylamide)". *J Biomater Sci Polym Ed.* 1996;8(1):19-39.
- ³⁸ Connolly, P., Clark, P., Dow, J.A.T., Curtis, A.S.G., Lind, R. and Wilkinson, C.D.W., "Extracellular electrodes for monitoring cell cultures", *Institute of Physics Short Meeting Series No. 21* (IOP Publishing, UK) (1989).
- ³⁹ Petty, R.C.; Kun, S.; Peura, R.A., "Tissue ischemia measurement using induced current impedance spectroscopy: non-contact system design", *Bioengineering Conference, 1998. Proceedings of the IEEE 24th Annual Northeast, 9-10 April 1998* Page(s):74 – 76.
- ⁴⁰ H. E.Ayliffe, A. B. Frazier, and R. D. Rabbitt, "Electric impedance spectroscopy using microchannels with integrated metal electrodes," *J. Microelectromech. Syst.*, vol. 8, pp. 50–57, Mar. 1999.
- ⁴¹ Schroeder, T.J., J.A. Jankowski, K.T. Kawagoe, R.M. Wightman, C. Lefrou, and C. Amatore. "Analysis of diffusional broadening of vesicular packets of catecholamines released from biological cells during exocytosis". *Analytical Chemistry* 64:3077-3083. 1992.
- ⁴² Robinson, I.M., J.M. Finnegan, J.R. Monck, R.M. Wightman, and J.M. Fernandez. "Colocalization of calcium entry and exocytotic release sites in adrenal chromaffin cells", *Proceedings of the National Academy of Sciences of the United States of America* 92:2474-2478, 1995.
- ⁴³ Jankowski, J.A., T.J. Schroeder, E.L. Ciolkowski, and R.M. Wightman, "Temporal characteristics of quantal secretion of catecholamines from adrenal medullary cells", *Journal of Biological Chemistry* 268:14694-14700, 1993.
- ⁴⁴ Wightman, R.M., T.J. Schroeder, J.M. Finnegan, E.L. Ciolkowski, and K. Pihel, "Time course of release of catecholamines from individual vesicles during exocytosis at adrenal medullary cells", *Biophysical Journal* 68:383-390, 1995.
- ⁴⁵ http://www.walt.med-rz.uniklinik-saarland.de/med_fak/physioll/forschung_rettig_ohne.htm
- ⁴⁶ Allen J. Bard and Larry R. Faulkner, "Electrochemical methods, Fundamentals and applicationis", John Wiley & Sons, Inc, 2001.
- ⁴⁷ John O'M. Bockris and Amulya K.N. Reddy, "Modern electrochemistry", Vol. 2, Plenum Press, New York, 1970.

-
- ⁴⁸ R. Cobbold, *Transducers for Biomedical Measurements: Principles and Applications*. New York: Wiley, 1974.
- ⁴⁹ N. Goda, N. Kataoka, J. Shimizu, S. Mohri, Y. Yamamoto, and F. Kajiya, "Evaluation of micromotion of vascular endothelial cells with estrogen in electrical cell-substrate impedance sensing (ECIS) method using a mathematical model cell-to-cell distance and cell-to-substrate distance," Proc. 3rd Ann. Inter.IEEE EMBS Special Topic Conf. On Microtechnologies in Medicine and Biology, 12-15 May 2005.
- ⁵⁰ J. Hong, D.S Yoon, S.G. Kim, T.S. Kim, S. Kim, E.Y. Pak, and K. No, "AC frequency characteristics of coplanar impedance sensors as design parameters," *Lab Chip*, 2005, 5, 270-279.
- ⁵¹ S. Gawad, K. Cheung, U. Seger, A. Bertsch, and P. Renaud, "Dielectric spectroscopy in a micromachined flow cytometer: theoretical and practical considerations," *Lab Chip*, 2004, 4, 241-251.
- ⁵² Allen J. Bard, "Electroanalytical chemistry: a series of advances", Vol. 15. Marcel Deller Inc. New York, 1989.
- ⁵³ J. Robertson *Pure and Applied Chemistry* **66**(22) 1789-1796, 1994.
- ⁵⁴ M. Hilden, J. Lee, V. Nayak, G. Ouano, and A. Wu, "Sputtered carbon on particulate media", *IEEE Transactions on Magnetics*, vol. 26, no. 1, January 1990. pp174-178.
- ⁵⁵ Sivertsen, J.M.; Geng Wang; Ga-Lane Chen; Judy, J.H.; "Evaluation of amorphous diamond-like carbon-nitrogen films as wear protective coatings on thin film media and thin film head sliders", *IEEE Transactions on Magnetics*, Volume 33, Issue 1, Part 2, Jan. 1997 Page(s): 926 – 931.
- ⁵⁶ IUPAC Compendium of Chemical Terminology, 2nd Ed. (1997).
- ⁵⁷ G. A. J. Amaratunga, V. S. Veersamy, C. A. Davis, W. I. Milne, D. R. Mckenzie, J. Yuan, M. Weiler, J. Non-Cryst. Solids 1993, 164 -166, 1119.
- ⁵⁸ C. Ronning, U. Griesmerier, M. Gross, H. C. Hofsass, R. G.Downing, G. P. Lamaze, *Diamond Relat. Mater.* 1995, 4, 666.
- ⁵⁹ Rossier, J.S., et al., "Microchannel networks for electrophoretic separations", *Electrophoresis*, 1999. 20 (4-5): p. 727-731.
- ⁶⁰ Martin, R.S., et al., "Carbon paste-based electrochemical detectors for microchip capillary electrophoresis/electrochemistry. *Analyst*, 2001. 126(3): P. 277-280.
- ⁶¹ Osbourn, D.M. and C.E. Lunte, *Cellulose acetate decoupler for on-column electrochemical detection in capillary electrophoresis*. *Anal Chem*, 2001. 73(24): p. 5961-4.
- ⁶² Wang, J. and M. Pumera, *Dual conductivity/amperometric detection system for microchip capillary electrophoresis*. *Anal Chem*, 2002. 74(23): p. 59 19-23.
- ⁶³ Wang, J., M.P. Chatrathi, and B. Tian, *Microseparation chips for performing multi-enzymatic dehydrogenase/oxidase assays: simultaneous electrochemical measurement of ethanol and glucose*. *Anal Chem*, 2001. 73(6): p. 1296-300.
- ⁶⁴ A. Zeng, E. Liu, S. N. Tan, S. Zhang, J. Gao, "Cyclic Voltammetry Studies of Sputtered Nitrogen Doped Diamond-Like Carbon Film Electrodes", *Electroanalysis* 2002, 14, No. 15-16, pp 1100-1115.
- ⁶⁵ (25) Zhou, Z.; Neher, E. *J. Physiol.* 1993, 469, 245-273.

-
- ⁶⁶ Xiuhua Sun and Kevin D. Gillis, “On-Chip Amperometric Measurement of Quantal Catecholamine Release Using Transparent Indium Tin Oxide Electrodes”, *Anal. Chem.* 2006, 78, pp 2521-2525.
- ⁶⁷ Kevin D. Gillis, “Techniques for Membrane Capacitance Measurements”, chapter 7 of “Single-channel recording”, edited by Bert Sakmann and Erwin Neher, New York : Plenum Press, c1995, 2nd edition.
- ⁶⁸ Kawagoe, K. T.; Jankowski, J. A.; Wightman, R. M. “Etched carbon-fiber electrodes as amperometric detectors of catecholamine secretion from isolated biological cells”, *Anal. Chem.* 1991, 63, 1589-1594.
- ⁶⁹ F. Segura et al. *Journal of Neuroscience Methods* 103 (2000) 151–156.
- ⁷⁰ Chow, R. H.; von Ruden, L.; Neher, E. *Nature* 1992, 356, 60-63.
- ⁷¹ Jankowski, J. A.; Schroeder, T. J.; Holz, R. W.; Wightman, R. M. *J. Biol.Chem.* 1992, 267, 18329-18335.
- ⁷² Wightman, R. M.; Jankowski, J. A.; Kennedy, R. T.; Kawagoe, K. T.; Schroeder, T. J.; Leszczyszyn, D. J.; Near, J. A.; Diliberto, E. J., Jr.; Viveros, O. H. *Proc. Natl. Acad. Sci. U.S.A.* 1991, 88, 10754-10758.
- ⁷³ Khademhosseini A, Yeh J, Eng G, Karp J, Kaji H, Borenstein J, Farokhzad OC, Langer R, “Cell docking inside microwells within reversibly sealed microfluidic channels for fabricating multiphenotype cell arrays”, *Lab Chip.* 2005 Dec;5(12):1380-6. Epub 2005 Oct 13.
- ⁷⁴ Giaever, I. and Keese, C.R., "Use of electric fields to monitor the dynamical aspect of cell behavior in tissue culture," *IEEE Transactions on Biomedical Engineering*, BME-33(2):242-247, 1986.
- ⁷⁵ E.W. H. Jager, O. Inganas, and I. Lundstrom, “Microrobots for micrometer-size objects in aqueous media: Potential tools for single-cell manipulation,” *Science*, vol. 288, no. 5475, pp. 2335–2338, Jun. 2000.
- ⁷⁶ N. Manaresi, A. Romani, G. Medoro, L. Altomare, A. Leonardi, M. Tartagni, and R. Guerrieri, “A CMOS chip for individual cell manipulation and detection,” *IEEE J. Solid-State Circuits*, vol. 38, no. 12, pp. 2297–2305, Dec. 2003.
- ⁷⁷ M. Ozkan, T. Pisanic, J. Scheel, C. Barlow, S. Esener, and S. N. Bhatia, “Electro-optical platform for the manipulation of live cells,” *Langmuir*, vol. 19, no. 5, pp. 1532–1538, Mar. 2003.
- ⁷⁸ A. Nagy, M. Gertsenstein, K. Vintersten, and R. Behringer, *Manipulating the Mouse Embryo: A Laboratory Manual*, 3rd ed. Woodbury, NY: Cold Spring Harbor Lab. Press, 2002.
- ⁷⁹ R. A. Yotter, L. A. Lee, and D. M. Wilson, “Sensor technologies for monitoring metabolic activity in single cells—Part I: Optical methods,” *IEEE Sensors J.*, vol. 4, no. 4, pp. 395–411, Aug. 2004.
- ⁸⁰ L. L. Sohn, O. A. Saleh, G. R. Facer, A. J. Beavis, R. S. Allan, and D. A. Notterman, “Capacitance cytometry: Measuring biological cells one by one,” *PNAS*, vol. 97, no. 20, pp. 10 687–10 690, Sep. 2000.
- ⁸¹ Y. Sun and B. J. Nelson, “Biological cell injection using an automous microrobotic system,” *Int. J. Robot. Res.*, vol. 21, no. 10, pp. 861–868, 2002.
- ⁸² M. D. Antonik, P. N. P. D’Costa, and J. H. Hah, “A biosensor based on micromechanical interrogation of living cells,” *IEEE Eng. Med. Biol. Mag.*, vol. 16, no. 2, pp. 66–72, Feb. 1997.
- ⁸³ W. Groner and E. Simson, *Practical Guide to Modern Hematology Analyzers*. New York: Wiley, 1995.
- ⁸⁴ M. Safali, B. Celasun, and O. Gunhan, “DNA cytometry in pleomorphic adenomas with cytologyctypia,” *Anal. Quant. Cytol. Histol.*, vol. 24, no. 6, pp. 325–330, Dec. 2002.

-
- ⁸⁵ A. Buhmeida, H. Backman, and Y. Collan, "DNA cytometry in diagnostic cytology of the prostate gland," *Anticancer Res.*, vol. 22, no. 4, pp. 2397–2402, Jul. 2002.
- ⁸⁶ U. D. Larsen, G. Blankenstein, and J. Branebjerg, "Microchip coulter particle counter," in *Proc. Int. Conf. Solid-State Sensors and Actuators*, 1997, pp. 1319–1322.
- ⁸⁷ M. Koch, A. G. R. Evans, and A. Brunnschweiler, "Design and fabrication of a micromachined coulter counter," *J. Micromech. Microeng.*, vol. 9, no. 2, pp. 159–161, 1999.
- ⁸⁸ O. A. Saleh and L. L. Sohn, "Quantitative sensing of nanoscale colloids using a microchip coulter counter," *Rev. Sci. Instrum.*, vol. 72, no. 12, pp. 4449–4451, Dec. 2001.
- ⁸⁹ M. J. Madou, *Fundamentals of Microfabrication*, 2nd ed. Boca Raton, FL: CRC, 2002.
- ⁹⁰ C. Fuller, J. Hamilton, H. Ackler, P. Krulevitch, P. Gascoyne, F. Becker, A. Eldredge, J. Yang, and B. Boser, "Microfabricated multi-frequency particle impedance characterization system," in *Proc. Micro TAS*, 2000, pp. 265–268.
- ⁹¹ H. E. Ayliffe, A. B. Frazier, and R. D. Rabbitt, "Electric impedance spectroscopy using microchannels with integrated metal electrodes," *J. Microelectromech. Syst.*, vol. 8, pp. 50–57, Mar. 1999.
- ⁹² S. Gawad, L. Schild, and P. Renaud, "Micromachined impedance spectroscopy flow cytometer for cell analysis and particle sizing," *Lab on a Chip*, vol. 1, no. 1, pp. 76–78, 2001.
- ⁹³ A. Y. Fu, C. Spence, A. Scherer, F. H. Arnold, and S. R. Quake, "A microfabricated fluorescence-activated cell sorter," *Nature Biotechnol.*, vol. 17, pp. 1109–1111, Nov. 1999.
- ⁹⁴ G. B. Lee, C. H. Lin, and G. L. Chang, "Multi-cell-line micro flow cytometers with buried SU-8/SOG optical waveguides," in *Proc. MEMS*, 2002, pp. 503–506.
- ⁹⁵ F. Lefebvre, M. Ouafitouh, B. Nongaillard, and E. Radziszewski, "Biological cells detection using high frequency ultrasounds," in *Proc. IEEE Ultrasonics Symp.*, 1993, pp. 1019–1022.
- ⁹⁶ S. M Sze, "Semiconductor Devices: Physics and Technology", John Wiley and Sons (WIE); 2nd edition, November 1981.
- ⁹⁷ J. G. Webster, *Medical Instrumentation: Application and Design*, 3rd ed. New York: Wiley, 1998.
- ⁹⁸ R. Cobbold, *Transducers for Biomedical Measurements: Principles and Applications*. New York: Wiley, 1974.
- ⁹⁹ L. A. Geddes, *Electrodes and the Measurement of Bioelectric Events*. New York: Wiley, 1972.
- ¹⁰⁰ Leu, T. S., Chen, H. Y., and Hsiao, F. B., "Studies of particle holding, separating, and focusing using convergent electrodes in microsorters," *Microfluidics and Nanofluidics*, vol. 1, no. 4, pp. 328–335, Oct.2005.
- ¹⁰¹ Medoro, G., Manaresi, N., Leonardi, A., Altomare, L., Tartagni, M., and Guerrieri, R., "A lab-on-a-chip for cell detection and manipulation," *Ieee Sensors Journal*, vol. 3, no. 3, pp. 317–325, June2003.
- ¹⁰² Gray, D. S., Tan, J. L., Voldman, J., and Chen, C. S., "Dielectrophoretic registration of living cells to a microelectrode array (vol 19, pg 1765, 2004)," *Biosensors & Bioelectronics*, vol. 19, no. 12, pp. 1765–1774, July2004.
- ¹⁰³ Neher, E. and A. Marty, "Discrete changes of cell membrane capacitance observed under conditions of enhanced secretion in bovine adrenal chromaffin cells", *Proceedings of the National Academy of Sciences of the United States of America* 79:6712–6716, 1982.

-
- ¹⁰⁴ Xiaojun Feng, Szaro BG, Castracane J. “**Study of cell secretion using MEMS-based arrays**”, *SPIE-Int. Soc. Opt. Eng. Proceedings of SPIE - the International Society for Optical Engineering*, vol.5345, no.1, 2003, pp.35-42. USA.
- ¹⁰⁵ Xiaojun Feng, Tokranova N, Bai Xu, Peng Chen, Gillis K, Castracane J. “Micro-array development for cell secretion studies”, *SPIE-Int. Soc. Opt. Eng. Proceedings of SPIE - the International Society for Optical Engineering*, vol.4982, 2003, pp.37-44. USA.
- ¹⁰⁶ Adam T. Woolley, Kaiqin Lao, Alexander N. Glazer, and Richard A. Mathies, “Capillary Electrophoresis Chips with Integrated Electrochemical Detection”, *Analytical Chemistry*, 1998, vol. 70, 684-688.
- ¹⁰⁷ Ulli Backofen, Frank-Michael Matysik, and Craig E. Lunte, "A Chip-Based Electrophoresis System with Electrochemical Detection and Hydrodynamic Injection", *Analytical Chemistry*, 2002, vol. 74, 4054-4059.
- ¹⁰⁸ Stephen Campbell, “The science and engineering of microelectronics fabrication”, 2nd edition, Oxford University Press, 2001.
- ¹⁰⁹ Shantanu Bhattacharya, J.M. Berg, S. Gangopadhyay, “Studies on surface wettability of PDMS and glass under oxygen plasma treatment and correlation with bond strength”, *Journal of Microelectromechanical Systems*, Vol.14, No.3, June 2005.
- ¹¹⁰ <http://focus.ti.com/docs/prod/folders/print/opa627.html>
- ¹¹¹ <http://focus.ti.com/lit/ml/sloa088/sloa088.pdf>
- ¹¹² Chow, R. H.; von Ruden, L.; Neher, E. *Nature* 1992, 356, 60-63.
- ¹¹³ Jankowski, J. A.; Schroeder, T. J.; Holz, R. W.; Wightman, R. M. *J. Biol.Chem.* 1992, 267, 18329-18335.
- ¹¹⁴ Wightman, R. M.; Jankowski, J. A.; Kennedy, R. T.; Kawagoe, K. T.; Schroeder, T. J.; Leszczyszyn, D. J.; Near, J. A.; Diliberto, E. J., Jr.; Viveros, O. H. *Proc. Natl. Acad. Sci. U.S.A.* 1991, 88, 10754-10758.
- ¹¹⁵ “Analysis of exocytotic events recorded by amperometry”, Eugene V Mosharov, and David Sulzer, *Nature Methods*, Vol2, No.9, Sept. 2005, p651-658.